Transactions of the ASME

EDITORIAL STAFF
Mng. Dir., Publ., J. J. FREY
Director, Technical Publishing, JOS. SANSONE
Managing Editor, CORNELIA MONAHAN
Editorial Production Assistant, BETH DARCHI

FLUIDS ENGINEERING DIVISION
Technical Editor
FRANK M. WHITE (1984)
Executive Secretary
L. T. NELSON (1984)
Calendar Editor
M. F. ACKERSON

Associate Editors
Fluid Machinery
BUDUGUR LAKSHMINARAYANA (1982)
WILLIAM E. THOMPSON (1984)
Fluid Measurements
THEODORE R. HEIDRICK (1984)
Fluid Mechanics
SHLOMO CARMI (1984)
CHARLES DALTON (1983)
KIRTI N. GHIA (1984)
BRIAN E. LAUNDER (1982)
Fluid Transients
M. HANIF CHAUDHRY (1983)
Polyphase Flow
PAUL H. ROTHE (1983)
OKITSUGU FURUYA
Review Articles
KENNETH E. HICKMAN (1982)

FOREIGN CORRESPONDENTS
Europe and Russia
JACQUES CHAUVIN
Europe and Russia
JOHN H. HORLOCK
India and Middle East
ARUN PRASAD
Japan and China
YASUTOSHI SENOO

BOARD ON COMMUNICATIONS
Chairman and Vice President
MICHAEL J. RABINS

Members-at-Large
W. BEGELL, J. CALLAHAN, M. HELMICH, D. KOENIG, M. KUTZ, F. LANDIS, J. W. LOCKE, J. ORTLOFF, C. PHILLIPS, K. REID

OFFICERS OF THE ASME
President, ROBERT B. GAITHER
Executive Director and Sec'y, BURKE E. NELSON
Treasurer, ROBERT A. BENNETT

The Journal of FLUIDS ENGINEERING (USPS 278-480) is edited and published quarterly at the offices of The American Society of Mechanical Engineers, United Engineering Center, 345 E. 47th St., New York, N. Y. 10017. Cable Address, "Mechaneer," New York. Second-class postage paid at New York, CHANGES OF ADDRESS must be received at Society headquarters seven weeks before they are to be effective. Please send old label and new address.
PRICES: To members, $30.00, annually; to nonmembers, $60.00. Single copies, $20.00 each. Add $5.00 for postage to countries outside the United States and Canada.
STATEMENT from By-Laws. The Society shall not be responsible for statements or opinions advanced in papers or . . . printed in its publications (B7.1, Par. 3).

INDEXED by the Engineering Index, Inc.

Journal of Fluids Engineering

Published Quarterly by The American Society of Mechanical Engineers

VOLUME 104 • NUMBER 2 • JUNE 1982

A New Instrument in Cavitation Research: The Cavitation Susceptibility Meter

D. M. Oldenziel
Research Scientist,
Pumps and Industrial
Circulations Branch,
Delft Hydraulics Laboratory,
The Netherlands

The rate of cavitation in liquid flow appears to be linked to the concentration and size distribution of gas bubbles and "weak" nuclei in the liquid used, as well as to the dissolved gas content. Consequently, the onset of cavitation is related to the tensile strength of the liquid, rather than the vapor pressure. The tensile strength of the liquid depends on the amount of gas in gas pockets (i.e., gas bubbles and gas absorbed at solid particles) suspended in the liquid and the shape of these gas pockets. An instrument will be described, which measures the tensile strength in a direct way. In this method a sample of liquid is made to pass through a pressure well, the minimum pressure of which can be adjusted.

Introduction

In practical flow situations the liquid is not pure; gas bubbles and small impurities are embedded within the fluid. Small gas bubbles stay in suspension for a long time, because the relative motion in upward direction due to gravity is opposed by transport in the downwards direction by turbulent diffusion. However, at quiet places in the top of closed circuits, bigger bubbles can collect. Jet entrainment, cavitation, and strong turbulence at a gas-liquid interface result in bubbles being dispersed within the liquid.

The size distribution of bubbles changes in time because of diffusion of gas across the gas-liquid interfaces. This process takes a relatively long time (typically tens of seconds) and depends on the dissolved gas and absolute pressure.

The concentration of solid particles, e.g., dust, sand particles, and organisms, is very uncertain. The density of the impurities differs from that of the liquid in general and can be higher as well as lower. Some of these particles in the liquid have a certain amount of gas entrapped in their crevices, as described by the model of Harvey et al. [1]. This amount of gas depends on geometry and contact angle between gas-liquid interface and the solid wall. It is also related to the dissolved gas content and pressure. In the situation that the gas bubbles are coated with certain surface-active materials, as discussed in the model of Fox and Herzfeld [2], diffusion across the interface can be limited significantly.

Cavitation can be divided into two main types, namely travelling bubble cavitation (clouds, bubbles) and attached cavitation (spots, sheets). The first type of cavitation consists of exploding and imploding bubbles in the low pressure regions of streamlined bodies or in the shear flow behind nonstreamlined objects. The second type of cavitation can maintain itself and needs only a weak nuclei to start. Very recently Van der Meulen [3] gave a clear description of types of cavitation on two-dimensional hydrofoils. The way in which the weak nuclei and gas bubbles become involved in a certain cavitation process depends on the type of cavitation.

Especially during the last decade, measurements of weak nuclei in a liquid have become very important. Many investigators have developed instruments to detect the nuclei concentration and their size distribution. Keller [4] measured the nuclei size distribution applying the Mie-scatter method. When a nucleus passes through a control volume of high light intensity it scatters light, the intensity of which is proportional to the geometrical cross section within certain limits. Also Kümmel [5] and Gates and Billet [6] describe such an optical detection system.

Peterson [7], Oosterveld and Van Renesse [8], and Katz [9] measured bubbles and other impurities with a high speed holographic technique. The holograms obtained are used to produce a 3-dimensional image of the contents of the original volume. The typical exposure time is 10 ns. These investigators found both analytically and experimentally that about 20 μm was the smallest bubble size that could be reliably distinguished from a solid particle.

Peterson et al. [10] describes combined measurements to correlate cavitation inception and nuclei spectrum.

Silberman et al. [11] measured the cavitation susceptibility by counting exploding bubbles in a known pressure field. An axisymmetrical standard body was used to count the bubble collapses acoustically with a pressure sensor in the body. The number of collapses per unit of time depends on the absolute pressure and is a measure for the bubble size distribution.

It is also possible to detect bubbles acoustically using their very sharp resonance frequency of radial volume oscillations. Schiebe and Killen [12] used the acoustic tone burst attenuation technique and tried to measure the bubble size distribution in water. A review of acoustic detection methods

Contributed by the Fluids Engineering Division and presented at the Winter Annual Meeting at the Symposium on Cavitation Inception, New York, N.Y., December 2-7, 1979, of THE AMERICAN SOCIETY OF MECHANICAL ENGINEERS. Manuscript received by the Fluids Engineering Division, February 11, 1980; revised manuscript received June 8, 1981.

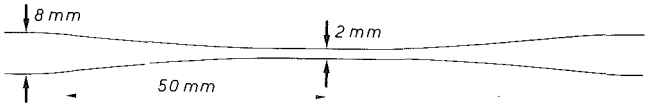

Fig. 1 Shape of venturi tube. The difference between actual shape and the hyperbolic cosine is ±1.5 percent of the measured diameter for $x < 3 \times 10^{-2}$ m. The uncertainty in the throat diameter is ± 10 μm.

has been written by Scarton and McDonald [13]. The problem with all these active acoustic techniques is that in relatively small structures reflection causes a great amount of noise in the detected signal.

Another method is the application of an acoustic doppler system described by Jansen [14]. In the detection volume of about one cm^3 the amplitude of the reflected signal is a measure of the bubble concentration, and the doppler shift gives their velocity. In this way the bubble transportation can be measured very sensitively. In Godefroy et al. [15] this acoustic method is compared with some other methods during combined cavitation measurements at the Delft Hydraulics Laboratory.

Determination of Tensile Strength

By the term "tensile strength" of the liquid used we mean the minimum tensile stress in liquid at which nuclei start to explode (the liquid ruptures). This property will be referred to as the "cavitation susceptibility" in this paper. Measurements of the cavitation susceptibility are based on bubble explosions in a prescribed pressure well. The geometry chosen for this purpose is a small venturi tube made of glass in which the minimum pressure can be controlled by adjusting the discharge.

If the diameter of the venturi tube is $d(x)$ and the diameter of the tube at both ends d_0 the pressure as a function of location x is given by

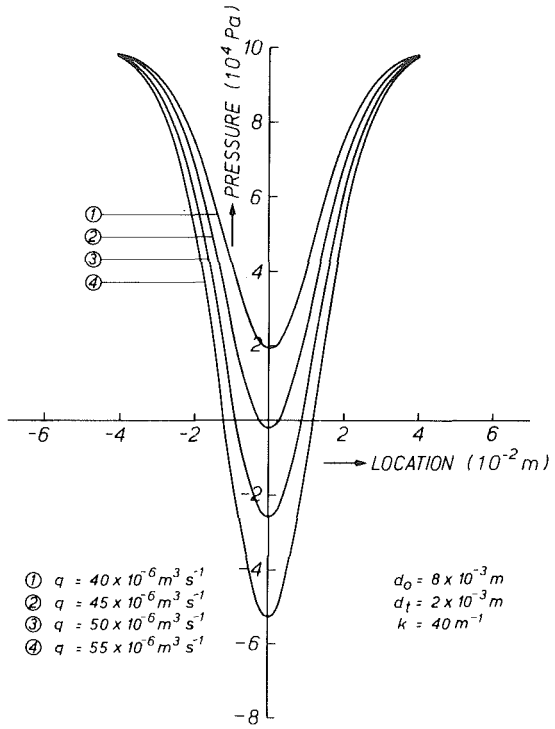

Fig. 2 Pressure wells caused by the venturi throat

$$p(x) = p_0 - 8\frac{\rho q^2}{\pi^2 d_0^4}\left[\frac{d_0^4}{d^4(x)} - 1\right] \tag{1}$$

where $p(x)$ is the local pressure in the venturi throat and p_0 is the pressure in the tube at the upstream side of the venturi; q denotes the discharge in the system. There is no friction in-

Nomenclature

A_1 = sensitive area of photodiode (m^2)
D = diffusion coefficient of air in water ($m^2 s^{-1}$)
d_0 = pipe diameter of venturi system (m)
d_s = inlet diameter of venturi system (m)
d_t = diameter of venturi throat (m)
$d(x)$ = local diameter in venturi tube (m)
f = expression for friction coefficient (1)
k = contraction factor of venturi tube (m^{-1})
l_s = radial excursion of bubble near the inlet venturi system (m)
n_s = bubble concentration (m^{-3})
p = pressure at certain location ($kg\ m^{-1} s^{-2}$)
p_0 = pressure at the upstream side of venturi tube ($kg\ m^{-1}\ s^{-2}$)
p_c = cavitation susceptibility ($kg\ m^{-1} s^{-2}$)
p_t = pressure at the location of the venturi throat ($kg\ m^{-1}\ s^{-2}$)
p_v = vapor pressure ($kg\ m^{-1} s^{-2}$)
$p(x)$ = local pressure in venturi tube ($kg\ m^{-1} s^{-2}$)
Δp = characteristic pressure difference near the minimum of pressure well ($kg\ m^{-1} s^{-2}$)
$|\nabla p|$ = absolute value of pressure difference near inlet of venturi system ($kg\ m^{-2} s^{-2}$)
q = discharge ($m^3 s^{-1}$)
R = bubble radius (m)
t = time (s)
t_c = characteristic time lapse for bubble explosion (s)
t_s = time of residence near inlet of venturi system (s)
$U(R)$ = output voltage of photodiode as function of bubble radius ($kg\ m^2 A^{-1} s^{-3}$)
u = velocity at certain location (ms^{-1})
u_0 = undisturbed water velocity (ms^{-1})
u_r = relative bubble velocity (ms^{-1})
u_s = water velocity at inlet of venturi system (ms^{-1})
u_t = water velocity in venturi throat (ms^{-1})
$u(x)$ = local water velocity (ms^{-1})
u' = water velocity in radial direction (ms^{-1})
u_r' = relative bubble velocity in radial direction (ms^{-1})
V_b = volume of bubble (m^3)
x = coordinate along axis of venturi system (m)
β = numerical constant (1)
δ_t^* = displacement thickness near the venturi throat (m)
$\delta^*(x)$ = displacement thickness in venturi tube (m)
ν = kinematic viscosity of water ($m^2 s^{-1}$)
ρ = density of water ($kg\ m^{-3}$)
σ = cavitation number related to vapor pressure (1)
σ' = cavitation number related to cavitation susceptibility (1)
τ = coefficient in optical cross-section of bubble (1)

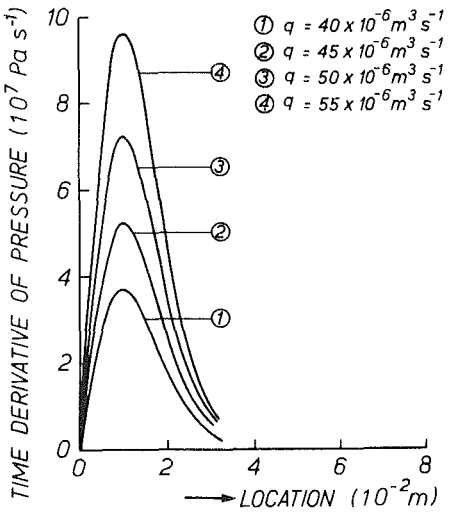

Fig. 3(*a*) Pressure gradient as a function of location in venturi tube with discharge as parameter

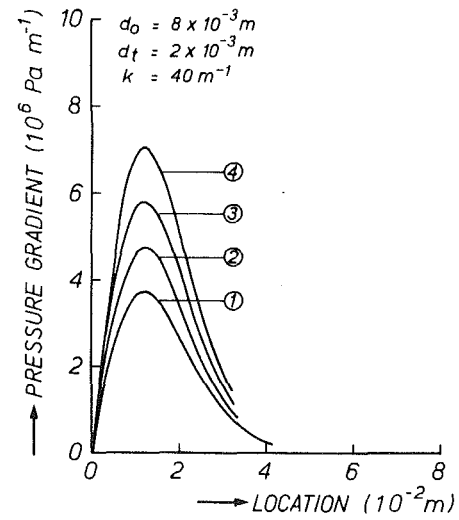

Fig. 3(*b*) Time derivative of pressure as a function of location in the venturi tube with discharge as parameter

volved up to now and equation (1) is based on the Bernoulli equation using

$$u(x) = \frac{4q}{\pi d^2(x)} \tag{2}$$

The function $d(x)$ is given, with sufficient accuracy in respect to practical design, by

$$d(x) = d_t \cosh(kx) \tag{3}$$

where d_t equals the diameter of the venturi throat. The shape of a typical venturi tube has been drawn in Fig. 1. The shape factor k is about 40 m^{-1} and the values chosen for the throat diameter and the tube diameter are $d_t = 2 \times 10^{-3}$ m and $d_0 = 8 \times 10^{-3}$ m, respectively. For these values and different discharges, the pressure as a function of x is given in Fig. 2. The pressure at the upstream side of the venturi tube is $p_0 = 10^5$ Pa.

With regard to bubble dynamics it is very important to know the pressure gradient as a function of time as well as a function of location. The pressure change as a function of place is given by

$$\frac{dp}{dx} = -\rho u \frac{du}{dx} = \frac{32\rho q^2 k \sinh(kx)}{d_t^4 \pi^2 \cosh^5(kx)} \tag{4}$$

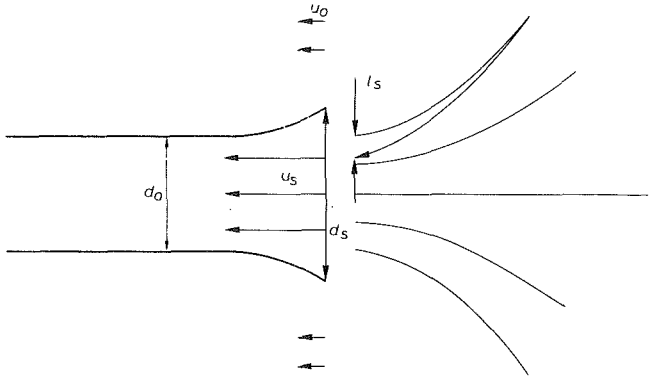

Fig. 4 Sketch of relative bubble motion near inlet of venturi system

For different values of q this function is drawn in Fig. 3(*a*). The pressure change as felt by an observer moving with the liquid is - as shown in Fig. 3(*b*):

$$\frac{dp}{dt} = \frac{dp}{dx}\frac{dx}{dt} = 128\rho \frac{q^3 k \sinh(kx)}{d_t^6 \pi^3 \cosh^7(kx)} \tag{5}$$

Based on these basic equations some additional remarks should be made to achieve a better picture of the real processes. Attention will be paid to the influence of friction, the condition at the inlet of the venturi system and the behavior of bubbles near the venturi throat.

In equation (1) a certain boundary layer growth at the wall of the venturi tube has been neglected. Introducing a displacement thickness $\delta^*(x)$ the pressure as a function of location is given by

$$p(x) = p_0 - \frac{8\rho q^2}{\pi^2 d_0^4}\left[\frac{d_0^4}{\{d(x) - 2\delta^*(x)\}^4} - 1\right] \tag{6}$$

Expanding the first term between the brackets in series, which is allowed because $\delta^*(x) << d(x)$, the pressure at the throat of the venturi can be given by:

$$p_t = p_0 - \frac{8\rho q^2}{\pi^2 d_t^4}\left[1 - \left(\frac{d_t}{d_0}\right)^4 + 8\frac{\delta_t^*}{d_t} + \ldots\right] \tag{7}$$

δ_t^* is the boundary layer thickness at the location of the venturi throat. Computation of the boundary layer thickness, based on the three dimensional Thwaites method as described by Crabtree et al. [16] gives a displacement thickness $\delta_t^* \sim 40$ μm. This means the pressure in the throat of the venturi is about 15 percent lower than the pressure obtained with zero displacement thickness. It is obvious that the pressure gradient is not much affected by the existence of a thin boundary layer so the shape of the curves as drawn in Fig. 2 and Fig. 3 is about the same, however, only at the upstream side of the venturi throat. The position of the minimum pressure is located somewhat at the downstream side of the venturi throat at a distance $x \sim k^{-1}\sinh^{-1}(4\delta_t^*/d_t)$.

Not only in the contraction part of the venturi tube but also near the inlet of the venturi system, pressure gradients exist. At the inlet the liquid will be accelerated or decelerated and this has consequences in taking representative samples.

Liquid sampling for the venturi tube can be estimated as follows: When the liquid velocity u_s in the inlet of the venturi system is not equal to the velocity of the liquid u_0 far from the inlet, a pressure gradient appears. In Fig. 4 the situation is schematized. When the diameter of the cylindrical inlet is d_s, then the pressure gradient is about

$$|\nabla p| \sim \frac{\rho|u_s^2 - u_0^2|}{2d_s} \tag{8}$$

The velocity u_s is determined by the discharge in the venturi

system, so only d_s and u_0 are free parameters. The error in the bubble concentration of the liquid sample depends on the radial excursion of a bubble l_s near the inlet and is expressed by

$$\frac{\delta n_s}{n_s} = 1 - \frac{(d_s - l_s)^2}{d_s^2} \tag{9}$$

where n_s is the bubble concentration near the inlet. When only the radial components of the velocities are considered the relative bubble motion is given by [17]

$$\frac{1}{2}\rho V_b(\mathbf{u}_r + \mathbf{u}) \cdot \nabla u_r'$$

$$= \rho V_b\left(\mathbf{u} - \frac{1}{2}\mathbf{u}_r\right) \cdot \nabla u' - \frac{4\pi\nu\rho}{3\beta} R u_r' \tag{10}$$

where β is a numerical constant. The value of β depends on the flow field around the bubble and equals ~ 0.3. The primes denote the components in radial direction. Using equation (8) the first term at the right-hand side of equation (10) can be written by:

$$|\rho V_b\left(\mathbf{u} - \frac{1}{2}\mathbf{u}_r\right) \cdot \nabla u'| \sim + V_b |\nabla p|$$

$$+ \frac{1}{2}\rho V_b \left| u_r' \frac{u_s - u_0}{d_s} \right| \tag{11}$$

When $(u_s - u_0)/d_s << 2\nu/\beta R^2$ the friction force dominates and $u_r' << u'$. The time in which the bubble velocity is governed by the pressure gradient near the inlet is given by:

$$t_s = \frac{2d_s}{u_s + u_0} \tag{12}$$

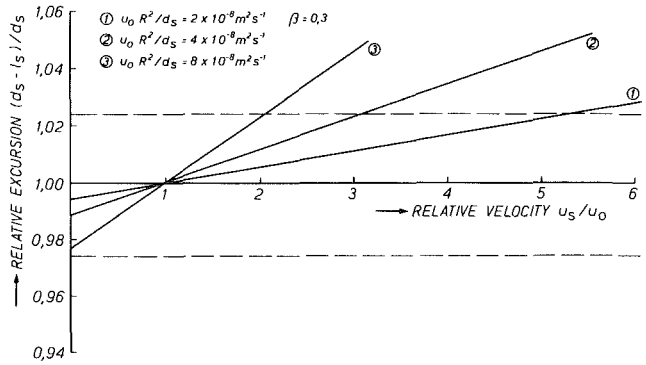

Fig. 5 Radial bubble excursion as a function of inlet velocity with diameter of suction opening as a parameter

Using equation (10), (11), and (12) the radial excursion of a bubble with radius R is given by

$$l_s = \frac{\beta R^2}{\nu}(u_0 - u_s) \tag{13}$$

In Fig. 5 the relative excursion $(d_s - l_s)/d_s$ is plotted as a function of u_s/u_0 with $u_0 R^2/d_s$ as parameter. Between the two horizontal broken lines the error δn_s is smaller than 5 percent.

Also at the upstream side of the venturi throat the very high pressure gradient introduces a relatively high slip velocity of the bubble. This may affect the amount of gas inside the bubble by diffusion, and thus may change the tensile stress necessary, causing the bubble to explode. Applying equation (10) together with known parameters giving the time scale and pressure gradient, the relative bubble motion can be estimated. A computation of the rate of gas transport across the bubble surface, using an expression, based on potential flow around the bubble and which is only valid for Peclet numbers $\mathrm{Pe} = u_r R/D >> 1$ (see e.g. Levich [18]) turns out that mass transport can be neglected. Only for very small bubbles should the increase of the bubble radius become significant, but then $\mathrm{Pe} < 1$ and the rate of gas transport is much smaller by the lack of convection.

The measurement of the tensile strength of a liquid sample is based on bubble explosions in the throat of the venturi in principle, and that makes it necessary that the bubbles reach a detectable size. The time available for explosion is limited and a characteristic time is given by

$$t_c = \frac{1}{u_t^2 k}\sqrt{\frac{\Delta p}{\rho}} \tag{14}$$

in which u_t is the liquid velocity in the throat of the venturi and Δp is a certain pressure difference between the pressure in the throat and the pressure at some distance from the location of the throat. Taking $\Delta p \sim 1000$ Pa, which value has the same order of magnitude as the error in the determination of the cavitation susceptibility, $u_t \sim 10\ \mathrm{ms}^{-1}$ and $k \sim 40\ \mathrm{m}^{-1}$ the time available for bubble explosion is at least $2{,}5 \times 10^{-4}$ s. With the assumption that the radial velocity of the bubble wall is about $1\ \mathrm{ms}^{-1}$, a value which is reached some microseconds after the start of the explosion, the maximum bubble radius will be about 250 μm. This is a detectable size.

Description of Apparatus

An experimental setup of the venturi system is shown in Fig. 6. The discharge was determined by measuring the

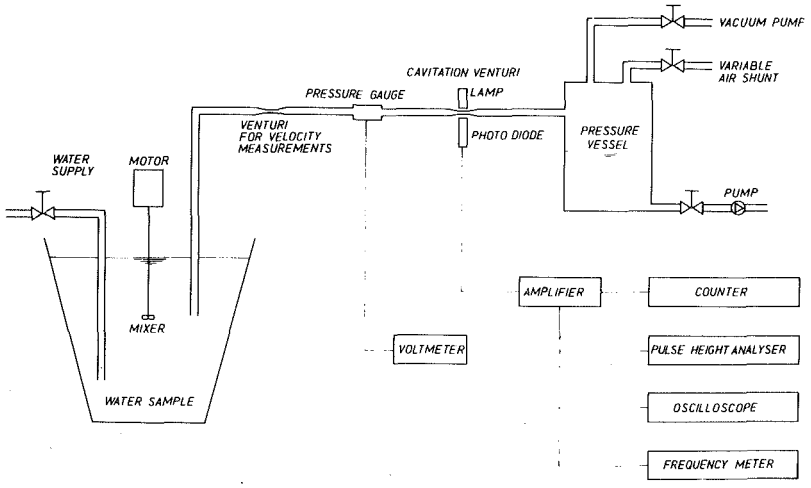

Fig. 6 Experimental setup of the cavitation susceptibility meter

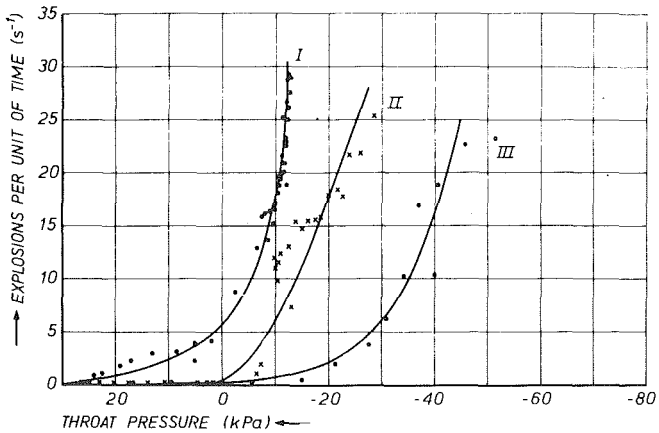

Fig. 7 Relations between throat pressure and number of exploded bubbles. The uncertainty in the throat pressure is ± 2000 Pa (systematic error). The statistical error in the counted number of explosions is $\pm\sqrt{0.1x}$, where x represents the value along the vertical axis.

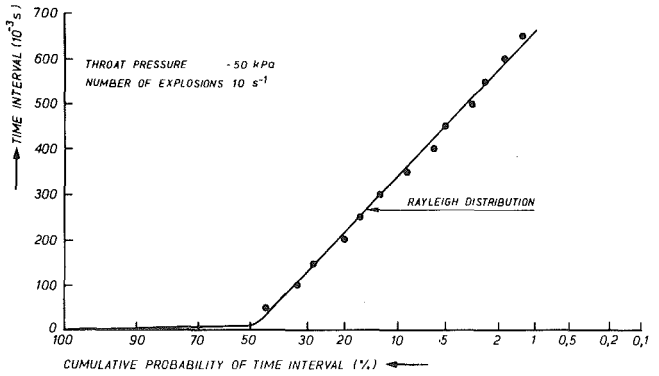

Fig. 8 Statistical distribution of time interval between bubble explosions. The uncertainty in the measurement of the time interval (vertical axis) is ±2 ms. The plots are based on a total of about 500 events (bubble explosions). The repeatability is two times the diameter of the black dots.

pressure drop over a second venturi tube at the upstream side of the cavitation venturi tube. The throat of this venturi tube was much wider than the throat of the cavitation venturi tube so, here, bubbles did not explode at all. The upstream pressure was determined by the water level in the vessel where different water samples were prepared.

The determination of boundary layer effects in the contraction of the venturi tube was carried out by measuring the pressure in the throat of the venturi directly. For this purpose the venturi tube was cut at the throat and the pressure in the free jet at the exit was measured. Applying Bernoulli's equation with the known pressure difference over one half of the venturi tube, the pressure drop due to friction was analyzed. The experimental values found in this way are slightly lower than predicted by theory.

The exploding bubbles in the throat of the glass venturi tube were detected optically with the so-called shadow method, i.e., the light source and the photo diode were situated in-line. When a bubble passed the detection center the output signal of the photo diode was given by

$$U(R) = U(0)[A_1 - \tau\pi R^2] \tag{15}$$

In this equation $U(0)$ denotes the output voltage when there are no bubbles at all. A_1 is the sensitive area of the photo diode and had a value of about 3 mm^2. τ is a coefficient in the optical cross section of the bubble and is known but depends on the optical configuration. Hooper and Uzunovic [19] give some optical characteristics of spherical bubbles and drops in liquids. The optical detection system was situated at the downstream side of the throat at a distance of 5 mm. This situation made it sure that the exploding bubbles were large enough to be detected.

This detection system had a threshold because not all particles should be counted. Dust, sand particles, and other impurities which give no bubble explosions don't act as cavitation nuclei, so it is not allowed to detect them. Using a threshold corresponding to a bubble with a radius of 100 μm all the bubble explosions were detected but only water samples could be used with particles having a radius smaller than about 100 μm.

Figure 7 shows some measured values. On the horizontal axis the throat pressure has been plotted, determined from equation (7) with measured values of q and p_0.

Step by step this pressure was lowered, and for each constant pressure value the number of exploding bubbles per second was counted. This quantity is plotted on the vertical axis of Fig. 7. Just before these experiments, water in a vessel with a capacity of 60×10^{-3} m^3 was agitated heavily. The first experiment (I) was carried out about a quarter of an hour after agitating, the second (II) and third (III) experiments were carried out after a period of one half hour and one hour respectively.

Two dynamic effects give complications during the measurement of the cavitation susceptibility of water. The first one is the appearance of sheet cavitation in the diffusor of the venturi tube and is supposed to be related to flow separation. This type of cavitation occurs at certain pressures and velocities, and introduces hysteresis effects. When sheet cavitation starts, the velocity in the venturi system decreases to a certain stationary value but the throat pressure is nearly the vapor pressure. Sheet cavitation can also disappear suddenly and the throat pressure decreases again. The second effect is the generation of additional bubble explosions due to the pressure shock wave generated by the previous bubble implosion. Determining the time intervals between the pulses statistically, it appears that many bubbles explode at a fixed time after a bubble implosion, as shown in Fig. 8 where the time interval has been plotted as a function of its cumulative probability.

The number of bubble explosions per unit of time cannot exceed a certain value. When many bubbles explode the increase of pressure in the diffusor of the venturi tube is removed and the throat pressure is limited. The maximum number of bubble explosions depends on the throat pressure: in the case of vapor pressure in the throat, hundreds of bubbles per second can pass the throat and when the throat pressure is very low no more than about 20 bubbles per second can explode.

The accuracy in the determination of the throat pressure depends on different factors. The most important ones are the statistical errors in the discharge δq and the systematic errors in the throat diameter δd_t and friction coefficient δf. This friction coefficient is defined by $f = (1 + 8\delta_t^*/d_t)$. The error in the measurement of upstream pressure is very small. The error in the throat pressure δp_t is given by:

$$\delta p_t = \left[p_0^2\left(\frac{\delta p_0}{p_0}\right)^2 + \left(\frac{8\rho f q^2}{\pi^2 d_t^4}\right)^2\left\{\left(\frac{2\delta q}{q}\right)^2 + \left(\frac{\delta f}{f}\right)^2 + \left(\frac{4\delta d_t}{d_t}\right)^2\right\}\right]^{1/2} \tag{16}$$

In fact the throat pressure is determined by the difference of two large quantities, as given by the two terms at the right-hand side of equation (1). Especially when the upstream pressure is high the absolute error is large. When the reader would like to have more detailed information, he is referred to Oldenziel [20].

Discussion

The advantage of using the cavitation susceptibility meter is the direct determination of the tensile strength of a water sample (i.e., the tensile strength of impurities imbedded in the liquid). Optical systems can only give information about the cencentration and size distribution of particles. Only more fruitful knowledge is obtained when it is sure that the particles are bubbles because the dynamics of bubbles is supposed to be known. Otherwise the correlation between tensile strength and nuclei population is most indirect and is found by making a comparison between the pressure at which a certain type of cavitation starts and the measured nuclei population. However, in a statistical point of view it is obvious that large particles and high concentrations of those particles give a shift in cavitation inception reaching a value close to vapor pressure.

The cavitation susceptibility meter only gives the tensile strength of the weakest impurities. It is not possible to test all the nuclei because at a certain number of bubble explosions per unit of time the venturi throat starts to choke. The determination of the tensile strength of the particles is carried out in a cumulative way.

The theoretical considerations about relative motion in the venturi system are based on the behavior of small bubbles, dispersed in the liquid. As a matter of fact, however, the tensile strength of liquid is normally related to solid particles, having some amount of gas absorbed (e.g. entrapped in a crevice). The mean density of these weak nuclei is expected to be different from that of water in general, but this difference would be smaller than in the case of gas bubbles. So the values of relative particle motion are smaller than estimated, using spherical bubbles.

There are no reasons to suppose that nuclei are affected by diffusion of gas during their motion in the venturi system between the sampling point and venturi throat. The pressure in this section is hardly different from the pressure in the water outside the venturi system. Due to pressure fluctuations only rectified difference could occur. However it has been estimated that this process does not have a detectable effect. The reason is that the travelling time is too short.

In the case of unfiltered city water in the closed test rig for valves at the Delft Hydraulics Laboratory it was found that the cavitation susceptibility was about -120 kPa. After the water in the test rig was filtered with a 5 μm filter it was found that the cavitation susceptibility was significantly lower, having a value of about -280 kPa.

The rate of cavitation is normally given as a function of the dimensionless expression

$$\sigma = \frac{p - p_v}{\frac{1}{2}\rho u^2} \tag{17}$$

in which p and u are the pressure and the velocity, respectively, at a location where the flow is well described and where no cavitation occurs. The vapor pressure p_v is determined by measuring the water temperature. In case of cavitation inception measurements, it should be very useful replacing p_v by p_c expressing the measured value of the cavitation susceptibility

$$\sigma' = \frac{p - p_c}{\frac{1}{2}\rho u^2}. \tag{18}$$

References

1 Harvey, E. N., McElroy, W. D., and Whitely, A. H., "On Cavity Formation in Water," *J. Applied Phys.*, Vol. 18, No. 2, Feb. 1947, pp. 162–172.

2 Fox, F. E., and Herzfeld, K. F., "Gas Bubbles With Organic Skin as Cavitation Nuclei," *J. Acoustical Soc. Am.*, Vol. 26, No. 6, Dec. 1954, pp. 984–989.

3 Meulen, J. H. J. van der, "Studies of NACA 16-012 and NACA 4412 Hydrofoils," *Symposium on Naval Hydrodynamics*, Tokyo, Oct. 1980.

4 Keller, A. P., "Experimental and Theoretical Investigation into Problems Modeling Cavitation," Ph.D. thesis, Tech. Univ. München, Germany, 1973.

5 Kümmel, K., "Theoretische, und Experimentelle Untersuchungen über die Rolle der Strömungs keime bei der Entstehung von Flüssigkeitskavitation," Ph.D. thesis, Tech. Univ. Darmstadt, Germany, Nov. 1977.

6 Billet, M. L., and Gates, E. M., "A Comparison of Two Optical Techniques for Measuring Cavitation Nuclei," *International Symposium on Cavitation Inception*, ASME, New York, Dec. 1979.

7 Peterson, F. B., "Hydrodynamic Cavitation and Some Considerations of the Influence of Free Gas Content," *Proceedings 9th Symposium on Naval Hydrodynamics*, Paris, Aug. 1972.

8 Oosterveld, N. B., and Renesse, R. L. van, "Holographic Determination of the Bubble Spectrum in a Cavitation Tunnel," Service of Applied Physics, Delft, Report No. TPD 1973-0-1, Sept. 1973.

9 Katz, J., "Construction and Calibration of an Holographic Camera Designed for Microbubbles Observation in Cavitation Research," Caltech Report No. Eng. 183-4, 1979.

10 Peterson, F. B., Danel, F., Keller, A. P., and Lecoffre, Y., "Comparative Measurements of Bubble and Particulate Spectra by Three Optical Methods," *Proceedings 14th International Towing Tank Conference*, Rep. of Cavitation Committee, 1975.

11 Silberman, E., Schiebe, F. R., and Mrosla, E., "The Use of Standard Bodies to Measure the Cavitation Strength of Water," Univ. of Minnesota, Minneapolis, St. Anthony Falls Hydraulic Lab., Report. No. 141, Sept. 1973.

12 Schiebe, F. R., and Killer, J. M., "An Evaluation of Acoustic Technique for Measuring Gas Bubble Size Distributions in Cavitation Research," Univ. of Minnesota, Minneapolis, St. Anthony Falls Hydraulic Lab., No. 120, 1971.

13 Scarton, H. A., and McDonald, J. F., "A Review of the Acoustic Detection of Boiling in Nuclear Reactors," *Proceedings of Noise and Fluids Engineering Symposium*, Atlanta, Dec. 1977.

14 Jansen, R. H. J., "The In-Situ Measurement of Sediment Transport by Means of Ultrasound Scattering," Delft Hydraulics Laboratory, Publ. No. 203, July 1978.

15 Godefroy, H. W. H. J., Jansen, R. H. J., Keller, A. P., Lecoffre, Y., Oldenziel, D. M., and Renesse, R. L. van, "Comparison of Measuring and Control Methods of the Water Quality with Respect to Cavitation Behaviour," Delft Hydraulics Laboratory, Jan. 1981.

16 Crabtree, L. F., Küchemann, D., and Sowerby, L., "Three-Dimensional Boundary Layers," in *Laminar Boundary Layers*, edited by L. Rosenhead, 1963, pp. 430–432.

17 Voinov, O. V., "Force Acting on a Sphere in an Unhomogeneous Flow of an Ideal Incompressible Fluid," *Zhurnal Prikladnoi Mekhanika i* Tekhnicheskoi Fizuki, 4, July - Aug. 1973, pp. 182–184.

18 Levich, V. G., *Physico-Chemical Hydrodynamics*, Prentice Hall, Englewood Cliffs, N.J., 1962, (trans. from Russian).

19 Hooper, F. C., and Uzunovic, R. I., "Some Optical Characteristics of Spherical Vapor Bubbles in Liquids," *Proceedings Society Photo-Optical Instrumentation Engineers*, 16th Annual technical meeting, San Mateo, 1972, pp. 31–38.

20 Oldenziel, D. M., "Bubble Cavitation in Relation to Liquid Quality," Ph.D thesis, Tech. Univ. Twente, Delft Hydraulics Laboratory, Publ. No. 211, May 1979.

W. F. Z. Lee
Manager of Research,
Municipal & Utility Division.
Mem. ASME

D. C. Blakeslee
Development Engineer,
Municipal & Utility Division.
Assoc. Mem. ASME

R. V. White
Staff Vice President,
Strategic Development.

Rockwell International Corporation,
Pittsburgh, Pa. 15208

A Self-Correcting and Self-Checking Gas Turbine Meter

A new metering concept of a self-correcting and self-checking turbine meter is described in which a sensor rotor downstream from the main rotor senses and responds to changes in the exit angle of the fluid leaving the main rotor. The output from the sensor rotor is then electronically combined with the output from the main rotor to produce an adjusted output which automatically and continuously corrects to original meter calibration accuracy. This takes place despite changes in retarding torques, bearing wear and/or upstream conditions occurring in field operations over those which were experienced during calibration. The ratio of the sensor rotor output to the main rotor output at operating conditions is also automatically and continuously compared with that at calibration conditions. This provides an indication of the amount of accuracy deviation from initial calibration that is being corrected by the sensor rotor. This concept is studied theoretically and experimentally. Both the theory and test results (laboratory and field) confirm the concept's validity and practicability.

Introduction

In recent years, the turbine meter has gained wide acceptance in the measurement of flows because of its simplicity, reliability, repeatability, accuracy, and range. However, the turbine meter will deviate from its calibration accuracy if there is a large change in retarding torques (both fluid and nonfluid) during field operation from those at calibration [1, 2, 3]. This may occur during field service as a result of bearing wear, severe contamination, change of running clearances, etc. Also, turbine meters are sensitive to any swirl or severely distorted velocity profile that exists at the rotor inlet [4, 5]. For high accuracy flow measurement, these effects must be reduced to an insignificant level. This is usually accomplished by proper installation practices as described in reference [6]. However, there are instances where the installation effect may be significant. In these cases, the meter may not operate at its calibration accuracy.

This paper presents the theory and a first-order analysis of a new turbine-type flow meter with self-checking and self-correcting capabilities that automatically compensate for variations in retarding torque and inlet flow swirls and preserve the calibration accuracy. Further, the amount of compensation can be monitored to give an on-line indication of meter performance deterioration, thus enabling effective maintenance measures to be implemented before meter failure occurs. It consists of two sequential turbine rotors—the main rotor and the sensor rotor. The free-running sensor rotor, which is placed downstream from the main rotor, senses and responds to changes in the exit angle of fluid leaving the main rotor. The pulse output from the sensor rotor is then electronically combined with the pulse output from the main rotor to produce an adjusted output which automatically and continuously corrects to the original meter calibration accuracy. This takes place despite changes in retarding torques, bearing wear, and/or upstream conditions occurring in field operations (as compared to those experienced during calibration). The ratio of the sensor rotor output to the main rotor output at operating conditions is also automatically and continuously compared with that at calibration conditions. This provides an indication of the amount of accuracy deviation from initial calibration accuracy that is being corrected by the sensor rotor. The results from both laboratory and field tests are presented, discussed, and compared with the theory.

Theory and Analysis

Conventional Gas Turbine Meter. Consider a turbine meter with helically twisted high solidity blading such as commonly

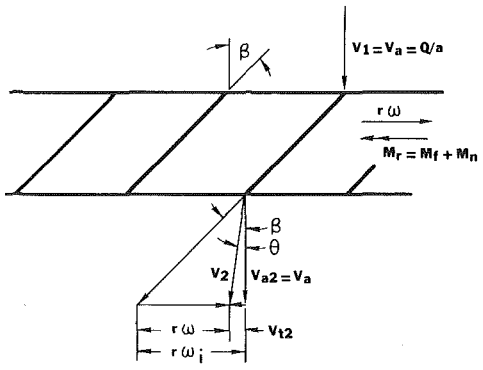

Fig. 1 Conventional turbine meter velocity diagrams

Contributed by the Fluids Engineering Division for publication in the JOURNAL OF FLUIDS ENGINEERING. Manuscript received by the Fluids Engineering Division, November 3, 1980.

used in measurement of low mach number steady-state flow with uniform velocity distribution. It is assumed that the meter performance depends upon some average flow condition which exists at the root mean square radius of the inner and outer radii of the effective flow passage of the rotor.

A. Effects of Retarding Torque. Figure 1 shows the velocity diagram of rotor blading at radius r with no inlet swirl. Flow at the rotor inlet is assumed to be axial. From conservation of angular momentum,

$$r\,\rho\,Q\,V_{t2} = M_r \text{ or } V_{t2} = M_r/r\,\rho\,Q \tag{1}$$

The flow angle at the rotor exit (hereafter called exit angle) is therefore

$$\tan\theta = V_{t2}/V_{a2} = V_{t2}/V_a$$
$$= (M_r/r\,\rho\,Q)/V_a = M_r/(r/a)\rho\,Q^2 \tag{2}$$

The ideal nonslip rotor speed is

$$r\omega_i = V_a\tan\beta = \frac{Q}{a}\tan\beta \tag{3}$$

From Fig. 1,

$$r\omega = r\omega_i - V_{t2} \tag{4}$$

Substituting (1) and (2) into (4)

$$\omega = \omega_i - \frac{V_{t2}}{r} = \omega_i - \frac{V_a}{r}\tan\theta = \omega_i - \frac{M_r}{r^2\rho\,Q} \tag{5}$$

If meter accuracy is defined to be proportional to (ω/ω_i), then

$$\text{Meter Accuracy} \propto \left(\frac{\omega}{\omega_i}\right) = 1 - \frac{M_r}{(r/a)\tan\beta\,\rho\,Q^2} = 1 - \left(\frac{\tan\theta}{\tan\beta}\right) \tag{6}$$

Hence, meter accuracy is dependent on θ only.

The relationship between the change in meter accuracy from calibration $\Delta(\omega/\omega^*)$ and change in exit angle $(\Delta\theta)$ due to change in retarding torque (ΔM_r) can be readily obtained from equation (6):

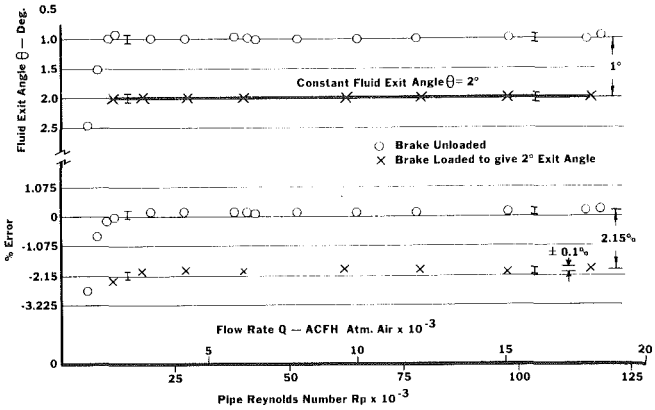

Fig. 2 Relationship between meter registration and exit angle 4 in. turbine meter with hysteresis brake

$$\text{Percent Change in Meter Accuracy from Calibration} = \Delta\left(\frac{\omega}{\omega^*}\right)\times 100 \text{ percent}$$
$$= \Delta\left(\frac{\omega}{\omega_i}\right)\left(\frac{1}{\omega^*/\omega_i}\right)\times 100 \text{ percent}$$
$$= -C(\Delta\theta)\ (\Delta\theta \text{ in degrees}) \tag{7}$$

where

$\frac{\omega^*}{\omega_i}$ = meter angular speed at calibration with reference to ideal speed ω_i

$$C = \left(\frac{100\pi}{180}\right)\left(\frac{\sec^2\theta^*}{\tan\beta}\right)\left(\frac{1}{\omega^*/\omega_i}\right)$$

practically constant independent of flow rate, line pressure, and exit angle except at low Reynolds numbers

(8)

θ^* = exit angle at calibration

Nomenclature

A = percent adjustment by sensor rotor
ΔA = percent deviation from calibration
$\Delta\bar{A}$ = percent deviation from calibration mean
a = cross-sectional area of the effective annular flow passage at rotor blading
C = proportional constant between percent change in meter accuracy from calibration and change in exit angle in degrees
K = meter factor in pulses/volume
M_f = total fluid retarding torque
M_n = total nonfluid retarding torque
M_r = total retarding torque
N = percent registration
ΔN = change in percent registration from calibration value
P = pulses from rotating rotor
Q = volume flow rate at flowing conditions
Q_b = volume flow rate at base conditions
R_p = pipe Reynolds number
r_i = inner radius of annular flow passage at rotor blading
r_0 = outer radius of annular flow passage at rotor blading
r = root mean square of r_i and r_0
U = total volume passing through the meter
V = absolute gas velocity
V_a = axial component of V
V_t = tangential component of V
W = swirl velocity in tangential direction
α = swirl angle from axial direction of meter at radius r
β = blade angle of main rotor at radius r
γ = blade angle of sensor rotor at radius r
δ = fluid angle of deviation from blade angle at blade exit
θ = fluid exit angle of main rotor for axial inlet flow, or fluid deflection angle of main rotor for nonaxial inlet flow
$\Delta\theta$ = change in exit angle from calibration value
ρ = mass density of gas at flowing conditions
ω = actual angular velocity of rotor
ω_i = ideal nonslip angular velocity of main rotor at zero inlet swirl
$\Delta\omega$ = $\omega_i - \omega_m$ = rotor slip of main rotor

Subscripts

1 = conditions existing at main rotor inlet
2 = conditions existing at main rotor exit (assumed also at sensor rotor inlet)
3 = conditions existing at sensor rotor exit
m = quantities related to main rotor
s = quantities related to sensor rotor
a = quantities related to self-adjusted turbine meter

Superscript

* = quantities related to calibration conditions

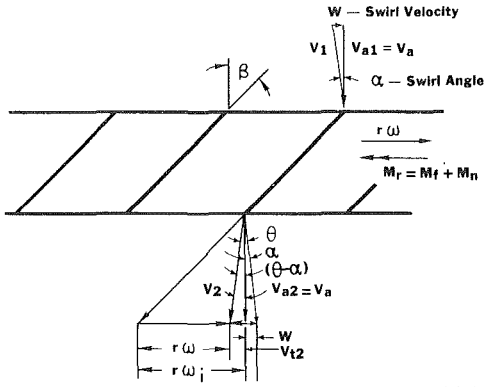

Fig. 3 Conventional turbine meter velocity diagrams with inlet swirl

From the above analysis it is seen that when the total retarding torque $M_r = M_f + M_n$ (such as fluid drag and/or bearing friction) changes during field operation from that at calibration, both the exit angle θ and the meter accuracy will deviate with corresponding amounts from the calibration values as given by equation (7). Laboratory tests were performed to confirm that changes in meter accuracy (due to changes in retarding torque) are proportional to changes in the exit angle in a very definitive and predictable manner, at least in the turbulent flow range. Figure 2 shows such a test result in air at atmospheric pressure of a 4 in. (100 mm) turbine meter equipped with a hysteresis brake. The brake exerts an external load on the rotor through a magnetic coupling to simulate the increase of rotor-bearing friction in field operation. It shows that the percent error curve of the meter at various flow rates at calibration is practically parallel to its fluid exit angle curve except at very low flow rates. Loading of the rotor by means of the hysteresis brake until a constant exit angle of 2 deg was obtained at various flow rates results in a practically constant accuracy curve except at very low flow rates. It also tends to verify the equation (8) which estimates the percent change in meter accuracy per degree change in exit angle θ. For the 4 in. (100 mm) test meter: $\beta = 45$ deg, $(\omega^*/\omega_i) \simeq 0.87$[1], and θ^* (exit angle at calibration) $\simeq 1$ deg. Equation (8) gives 2.01 percent decrease in meter accuracy from calibration for each degree increase of exit angle θ as compared favorably with 2.15 percent from test data of Fig. 2. Further testing confirms that the value of C is practically independent of flow rate, line pressure and percentage of rotor slip tested.

B. Effects of Inlet Swirl. Figure 3 shows the velocity diagram of a conventional turbine meter with inlet swirl. The swirl is expressed as a swirl tangential velocity W assumed in the direction of rotor rotation, with a swirl angle α where

$$\tan\alpha = W/V_a = W/(Q/a) \tag{9}$$

This inlet velocity V_1 at angle α with respect to the axial direction will deflect through an angle θ when passing through the rotor to produce a driving torque to overcome the total retarding torque M_r; i.e.,

$$r\,\rho\,Q(V_{t2} + W) = M_r \text{ or } V_{t2} = \frac{M_r}{r\,\rho\,Q} - W \tag{10}$$

The exit angle from the rotor is $(\theta - \alpha)$. The rotor speed $r\omega$ becomes from Fig. 3:

$$r\omega = r\omega_i - V_{t2} = r\omega_i - V_a \tan(\theta - \alpha).$$

Note that ω_i is the ideal rotor angular velocity at zero inlet swirl.

[1] This numerical evaluation is based on a "straight-through" flow cross-sectional area at rotor blading, not the effective flow cross-sectional area "a" to yield the real value of the ideal nonslip rotor speed ω_i as defined by equation (3). Therefore this value of 0.87 should not be used to determine the percent rotor slip due to retarding torque at calibration.

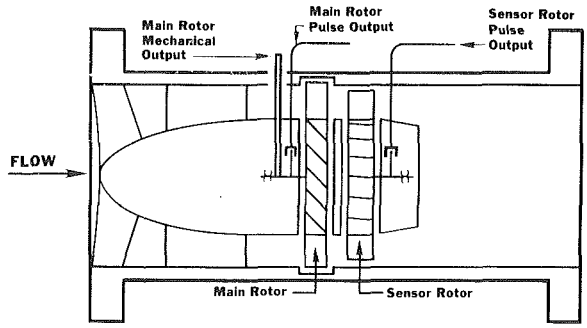

Fig. 4 Schematic drawing of a self-adjusting turbine meter

$$\text{Meter Accuracy} \propto \left(\frac{\omega}{\omega_i}\right) = 1 - \frac{\tan(\theta-\alpha)}{\tan\beta}$$

$$= 1 - \left[\frac{M_r}{(r/a)\tan\beta\,\rho\,Q^2} - \left(\frac{\tan\alpha}{\tan\beta}\right)\right] \tag{11}$$

Hence, meter accuracy is dependent on inlet swirl angle α as well as retarding torque M_r or θ.

Self-Adjusting Turbine Meter. In the previous discussion it is shown that the conventional turbine meter is sensitive to changes in both retarding torque and inlet flow conditions.

After considerable analysis and experimentation, it was determined that a constant meter accuracy could be accomplished by placing a second, free-running rotor (sensor rotor) downstream of the original rotor (main rotor); see Fig. 4. This sensor rotor is designed to have essentially the same root mean square radius and effective flow area as the main rotor. The sensor rotor blading is inclined in the same direction as that of the main rotor relative to the rotor shaft. The sensor rotor blade angle γ is considerably smaller than the main rotor blade angle β, but larger than the exit angle θ at calibration conditions. Consequently, within the operating range of the meter, the sensor rotor rotates in the same direction as the main rotor and at a designed speed of about 10 percent of the main rotor. This new metering system will henceforth be called a "self-adjusting turbine meter" as explained in the following.

Figure 5 shows the velocity diagrams for both rotor elements at radius r of the self-adjusting turbine meter. Under total retarding torque $(M_r)_m$, the axial inlet gas leaves the main rotor with an exit angle θ as previously described. The gas inlet angle to the sensor rotor may be less than the exit angle θ from the main rotor. For the sake of simplicity and clarity in analysis and as a first-order approximation, the gas inlet angle to the sensor rotor will be assumed to be equal to the exit angle θ from the main rotor as shown in Fig. 5. This may be justified as: (1) the primary interest here is the change of meter accuracy due to change of exit angle θ; (2) the meter accuracy will be determined by direct calibration; and (3) test results with three different distances between the two rotors (0.11 in., 0.29 in., and 0.52 in. for a 4 in. test meter) show practically no difference in meter accuracy curves. With the sensor rotor subjected to its total retarding torque $(M_r)_s = (M_f)_s + (M_n)_s$, the gas will enter the sensor rotor with an inlet angle equal to θ and leave it with an exit angle $(\theta + \theta_s)$ where θ_s is the gas deflection angle through the sensor rotor to overcome the retarding torque $(M_r)_s$. Since the free-running sensor rotor operates at about 1/10 of the main rotor speed, it develops much less fluid retarding torque $(M_f)_s$ and thrust load than those on the main rotor. The sensor rotor also carries no upshaft loading and has smaller bearings than those of the main rotor. Therefore, it is reasonable to assume that the total retarding torque $(M_r)_s$ on the sensor rotor is small (by at least an order of magnitude) in comparison with the

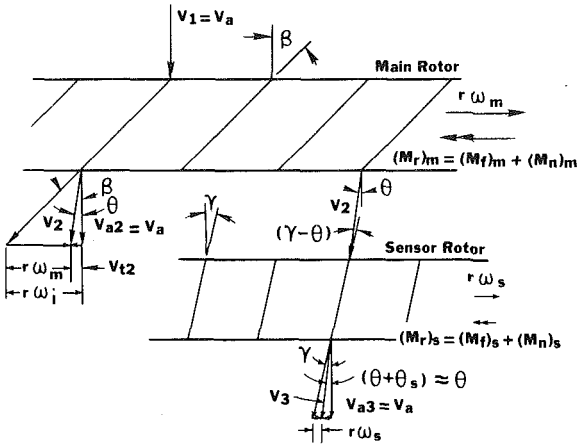

Fig. 5 Self-adjusting turbine meter velocity diagrams

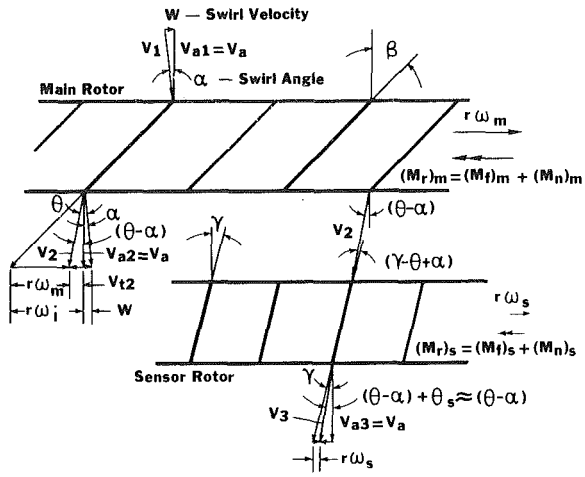

Fig. 6 Self-adjusting turbine meter velocity diagrams with inlet swirl

total retarding torque $(M_r)_m$ on the main rotor at the same operating condition. Therefore, the gas deflection angle θ_s through the sensor rotor should be small in comparison with the gas deflection angle or exit angle θ of the main rotor and $(\theta + \theta_s) \simeq \theta$ for all practical purposes.

For Fig. 5, the main rotor angular speed ω_m is given by equation (5):

$$\omega_m = \omega_i - \frac{V_a}{r}\tan\theta = \frac{V_a}{r}\tan\beta - \frac{V_a}{r}\tan\theta$$

The sensor rotor angular speed is given by:

$$\omega_s = \frac{V_a}{r}\tan\gamma - \frac{V_a}{r}\tan(\theta+\theta_s) \simeq \frac{V_a}{r}(\tan\gamma - \tan\theta) \qquad (12)$$

If the meter accuracy of this self-adjusting turbine meter is defined as proportional to the difference between the main rotor angular speed ω_m and the sensor rotor angular speed ω_s both in terms of ideal main rotor angular speed ω_i:

$$\text{Meter Accuracy of Self-Adjusting Meter} \propto \frac{(\omega_m - \omega_s)}{\omega_i} = \left(\frac{\omega_m}{\omega_i}\right) - \left(\frac{\omega_s}{\omega_i}\right)$$

$$= \left[1 - \frac{\tan\theta}{\tan\beta}\right] - \left[\frac{\tan\gamma}{\tan\beta} - \frac{\tan\theta}{\tan\beta}\right]$$

$$= 1 - \left(\frac{\tan\gamma}{\tan\beta}\right) \qquad (13)$$

It is seen that meter accuracy is independent of θ.

A comparison between equation (13) of a self-adjusting turbine meter and equation (6) of a conventional turbine meter indicates that a self-adjusting turbine meter replaces the variable exit angle θ with a constant sensor rotor blade angle γ. Therefore, a self-adjusting turbine meter with a sensor rotor of blade angle γ is, in effect, equivalent to a conventional turbine meter operating continuously at a constant exit angle equal to the sensor rotor blade angle γ.

Equation (13) implies that any change in the main rotor retarding torque $(M_r)_m$ will change its angular speed ω_m (thus the registration of the main rotor) and its exit angle θ. The sensor rotor senses this change in exit angle θ and will change its angular speed by an absolute amount equal to the change in the main rotor speed. The self-adjusting meter accuracy (which is determined by the difference of the rotor speeds) will, therefore, remain constant and equal to the meter accuracy obtained by original calibration.

Response to Inlet Swirl. Figure 6 shows the velocity diagrams at radius r of the self-adjusting turbine meter where the inlet flow has a swirl. The swirl is expressed as a swirl tangential velocity W assumed in the direction of main rotor rotation, with a swirl angle α where $\tan\alpha = W/V_a = W/(Q/a)$.

As shown previously in the case of a conventional turbine meter, the rotor speed $r\omega_m$ of the main rotor is from Fig. 6: $r\omega_m = r\omega_i - V_{t2} = r\omega_i - V_a\tan(\theta - \alpha)$, or

$$\frac{\omega_m}{\omega_i} = 1 - \frac{\tan(\theta-\alpha)}{\tan\beta} \qquad (14)$$

As discussed previously in the case of axial flow, the gas inlet angle to the sensor rotor will be assumed to be equal to the exit angle $(\theta - \alpha)$ from the main rotor as shown in Fig. 6. With the sensor rotor subjected to its total retarding torque $(M_r)_s$, the gas will enter the sensor rotor with an angle equal to $(\theta - \alpha)$ and leave it with an exit angle $(\theta - \alpha + \theta_s)$ where θ_s is the gas deflection angle through the sensor rotor to overcome retarding torque $(M_r)_s$. As previously discussed, $\theta_s << \theta$ and, therefore, can be neglected.

With this simplification, the sensor rotor speed becomes from Fig. 6:

$r\omega_s = V_a\tan\gamma - V_a\tan(\theta-\alpha)$, or

$$\frac{\omega_s}{\omega_i} = \frac{\tan\gamma}{\tan\beta} - \frac{\tan(\theta-\alpha)}{\tan\beta} \qquad (15)$$

Therefore, for the self-adjusting turbine meter when metering flow with an inlet swirl of swirl angle α:

$$\text{Meter Accuracy of Self-Adjusting Meter} \propto \frac{(\omega_m - \omega_s)}{\omega_i} = \left(\frac{\omega_m}{\omega_i}\right) - \left(\frac{\omega_s}{\omega_i}\right)$$

$$= \left[1 - \frac{\tan(\theta-\alpha)}{\tan\beta}\right] - \left[\frac{\tan\gamma}{\tan\beta} - \frac{\tan(\theta-\alpha)}{\tan\beta}\right]$$

$$= 1 - \left(\frac{\tan\gamma}{\tan\beta}\right) \qquad (16)$$

Hence, the meter accuracy is independent of swirl angle α.

A comparison between equation (16) with inlet swirl and equation (13) without inlet swirl indicates that the self-adjusting turbine meter will have the same meter accuracy (same as that determined by original calibration) with or without inlet swirl. In other words, it has the ability of self-correcting for inlet swirl also. This is accomplished because, as seen from Fig. 6 and equation (16), any change in the main rotor speed due to the presence of inlet swirl will result in a corresponding change in the fluid exit angle from the main rotor. This change in the exit angle of the main rotor will cause a change in the sensor rotor speed by an absolute amount equal to the change in the main rotor speed.

Self-Checking. The amount of deviation of the main rotor's

accuracy from its calibration value that is being corrected by the sensor rotor is indicative of the amount of change in condition of the rotors (such as change in bearing friction), and/or response to change in flow and installation conditions in the field from those at calibration. The knowledge of these changes can be used to provide an early warning of a deteriorating condition well before meter failure occurs.

The percent deviation from calibration of the main rotor ΔA can be determined from the change of rotor speed ratio (ω_m/ω_s) from its calibration value $(\omega_m/\omega_s)^*$ as follows. Let ω_a be the adjusted angular speed of the self-adjusting turbine meter. From equation (13)

$$\omega_a = \omega_m - \omega_s \tag{17}$$

From the self-correcting feature of the self-adjusting turbine meter

$$\omega_a = \omega_a{}^* = \omega_m{}^* - \omega_s{}^* \tag{18}$$

Then percent deviation from calibration of main rotor ΔA becomes

$$\Delta A = \left[\left(\frac{\omega_m}{\omega_a}\right) - \left(\frac{\omega_m}{\omega_a}\right)^*\right] \times 100$$

$$= \left[\frac{100}{\left(\frac{\omega_m}{\omega_s}\right) - 1}\right] - \left[\frac{100}{\left(\frac{\omega_m}{\omega_s}\right)^* - 1}\right] = A - A^* \tag{19}$$

Where

$$\left[\frac{100}{\left(\frac{\omega_m}{\omega_s}\right) - 1}\right] = \left(\frac{\omega_s}{\omega_a}\right) \times 100 = \text{percent adjustment by sensor rotor in field} = A$$

$$\left[\frac{100}{\left(\frac{\omega_m}{\omega_a}\right)^* - 1}\right] = \left(\frac{\omega_s{}^*}{\omega_a{}^*}\right) \times 100 = \text{percent adjustment by sensor rotor at calibration} = A^*$$

It may also be expressed in terms of percent registration N

$$\Delta A = \left[\frac{100}{\left(\frac{N_m}{N_s}\right) - 1}\right] - \left[\frac{100}{\left(\frac{N_m}{N_s}\right)^* - 1}\right] \tag{20}$$

The parameter ΔA provides a measure of the amount of correction being performed.

Note that since the sensor rotor rotates in the same direction as the main rotor, the self-checking parameter will indicate the sum of the main rotor error and the sensor rotor error (although with proper design, the probability of sensor rotor error is very small).

Tests

Test Setup. To bring rotor speed information out of the meter's measuring module, both rotors are equipped with electrical pulse generating devices that feed this information into an electronic unit.

A microprocessor in the electronic unit performs the following self-correcting and self-checking calculations:

A. Adjusted Volume - Self-Correcting Equation (13)

$$U_a = \left(\frac{P_m}{K_m}\right) - \left(\frac{P_s}{K_s}\right) \tag{21}$$

B. Percent Deviation From Calibration Mean - Self-Checking Equation (19)

$$\Delta\bar{A} = \left[\frac{100}{\left(\frac{P_m/K_m}{P_s/K_s}\right) - 1}\right] - \left[\frac{100}{\left(\frac{P_m/K_m}{P_s/K_s}\right)^* - 1}\right]$$

$$= \left[\frac{100}{\left(\frac{P_m/K_m}{P_s/K_s}\right) - 1}\right] - \bar{A}^* \tag{22}$$

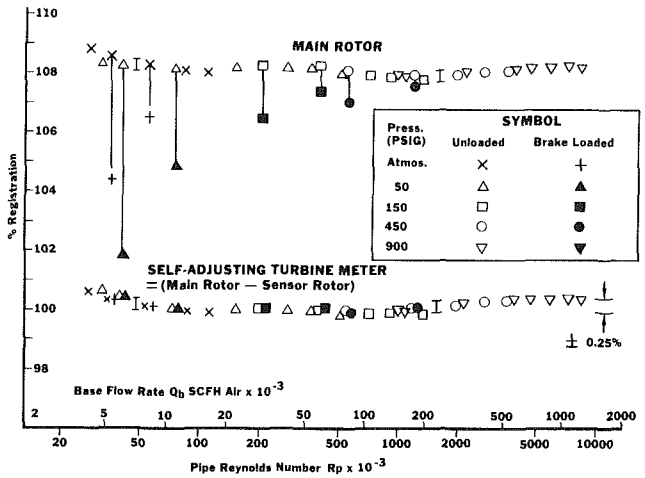

Fig. 8 Self-correction for mechanical drag 4 in. self-adjusting turbine meter

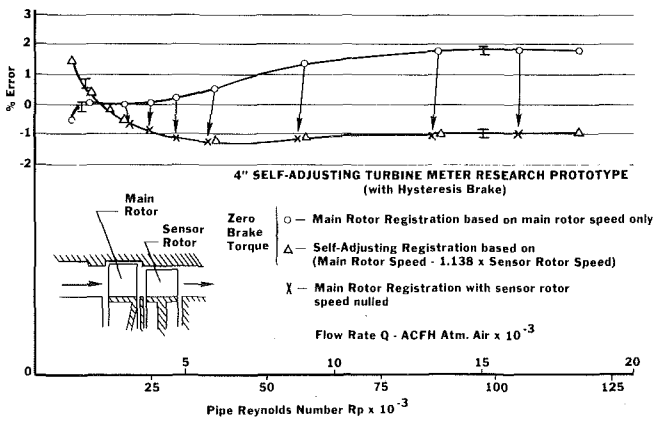

Fig. 7 Experimental verification of the self-adjusting turbine meter concept

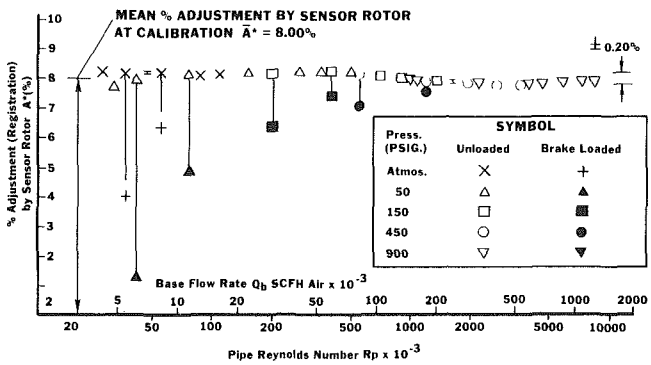

Fig. 9 Self-correction for mechanical drag—sensor rotor adjustment 4 in. self-adjusting turbine meter

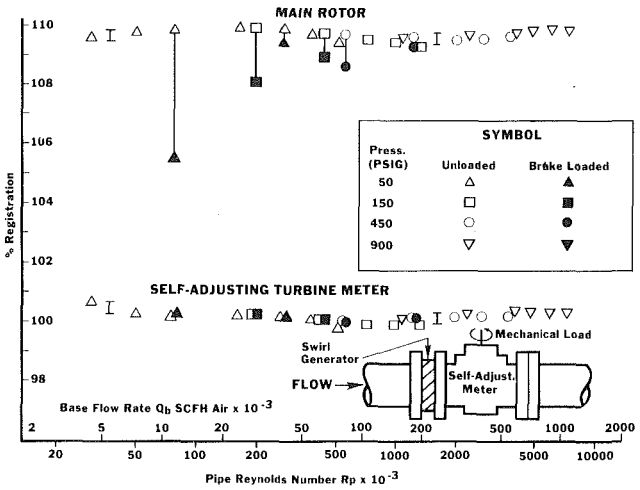

Fig. 10 Self-correction for swirl and mechanical drag 4 in. self-adjusting turbine meter

where

$\Delta\bar{A}$ = percent deviation from calibration mean

$$\bar{A}^* = \left[\frac{100}{\left(\frac{\overline{P_m/K_m}}{P_s/K_s} \right)^* - 1} \right] = \text{mean value of the percent adjustment of the sensor rotor at calibration over the meter's operating range}$$

The meter factors K_m and K_s for both rotors and the mean value of the percent adjustment of the sensor rotor at calibration $\bar{A}^*$ are determined from calibration data, and their values are fed into the electronic unit's memory as meter constants.

Laboratory Testing. Figure 7 shows test data in atmospheric air of a 4 in. (100 mm) self-adjusting turbine meter research prototype with an adjustable hysteresis brake on its main rotor. The blade angle γ of the sensor rotor is very small (approximately 2 deg). At each flow rate, the meter was first tested as a self-adjusting turbine meter with the hysteresis brake set at zero torque. Both the main rotor registration (based on main rotor speed only) and the self-adjusting registration (based on main rotor speed - 1.138 × sensor rotor speed) were determined by calibration and plotted. Then, the hysteresis brake torque loading on the main rotor was increased to slow down the main rotor speed and increase the exit angle θ until the sensor rotor speed was zero. The main rotor registration, which was based on this main rotor speed when the sensor rotor speed was nulled, was determined and plotted. Since the sensor rotor had a very small angle γ and very low friction, it can be stated that the null condition of the sensor rotor under this test meant that the exit angle θ from the main rotor equaled the sensor rotor blade angle γ. From the test results as shown in Fig. 7, it is seen that the meter accuracy curve of the self-adjusting meter is practically identical to the meter accuracy curve of the main rotor (or a conventional turbine meter) operating at a constant exit angle equal to the sensor rotor blade angle γ of the self-adjusting turbine meter. Similar results were obtained when tested at higher line pressures. These test results experimentally verify the concept that a self-adjusting turbine meter, of Fig. 5, with a sensor rotor of blade angle γ, has, in effect, the same meter accuracy curve as a conventional turbine meter of Fig. 1 operating continuously at the constant exit angle $\theta = \theta^* = \gamma$. The value of this constant exit angle is determined indirectly, but very accurately, by direct calibration.

Figures 8 and 9 show typical performance of a self-adjusting turbine meter with changes in retarding torque on the main rotor at various pressures and flow rates.

The filled and open symbols on the figure represent the conditions with and without application of retarding torque on the main rotor. From Fig. 8 it is seen that the application of retarding torque causes a decrease in the main rotor registration. For a conventional turbine meter this would result in a corresponding error in flow rate measurement. However, the registration for the self-adjusting meter shows no change with retarding torque, implying that the effect of retarding torque on the main rotor is adequately corrected for.

Figure 9 shows the magnitude of the adjustment factor with and without retarding torque applied to the main rotor.

Figure 10 shows the typical performance of the self-adjusting turbine meter in self-correcting for inlet swirl and for the combined effect due to inlet swirl and change in retarding torque at various pressures and flow rates. As shown in Fig. 10, the swirl is created by a swirl generator in the form of a 45 deg turbine rotor blading placed directly at test meter inlet. In this series of testing, the test meter was the same one used in Figs. 8 and 9. The test meter has integral straightening vanes like those in a conventional turbine meter. From the test results plotted in Fig. 10 with swirl compared with those in Fig. 8 without swirl, it is seen that the main rotor increases its registration by roughly 1.6 percent depending upon pressure and flow rate. However, the sensor rotor registration is also increased by the same amount, resulting in practically the same self-adjusting meter registration $N_a = N_m - N_s = N_a{}^*$ with and without swirl over a wide range of pressures and flow rates. Therefore the meter self-corrects for swirl as expected from equation (16).

Field Testing. Six 4 in. (100 mm) self-adjusting turbine meters have been placed for field test at six different sites throughout the United States and Canada since November, 1979.

Results of the field testing to date, based upon installation tests, monthly readings (of both adjusted and unadjusted volumes), chart records and trimonthly engineering checkups (including visual inspection of the meter inside and spin tests of both rotors) have shown that the meters are performing their self-correcting and self-checking functions equally well in the field as in the laboratory.

Conclusion

A new metering concept of a self-correcting and self-checking turbine meter has been studied theoretically and experimentally. Both the theory and the test results (laboratory and field) confirm the concept's validity and practicability. With the use of microprocessor-based digital electronics, the meter is capable of retaining its calibration accuracy in field operation despite bearing wear, changes in other retarding torques and upstream flow conditions, and the combination of these. It is also capable of self-checking its own mechanical and electrical conditions and indicating the amount of percent deviation from the calibration mean. Theory and test data also show that this self-adjusting turbine meter (with a sequential main rotor-sensor rotor system) may constitute an excellent transfer standard similar to the twin turbine-meter transfer standard package used by NBS in their Measurement Assurance Programs (MAPs) for fluid flow [7].

Acknowledgments

The authors wish to express their indebtedness to their colleagues within Rockwell International whose contributions make this paper possible. They also would like to acknowledge the kind cooperation received from the

following companies which provided direct support for the field test programs reported in this paper: Alberta Gas Trunk Line Company, Ltd.; Columbia Gas Transmission Corporation; Michigan Wisconsin Pipe Line Company; Natural Gas Pipeline Company of America; TransCanada Pipelines, Ltd.; and United Gas Pipe Line Company.

References

1 Thompson, R. E., and Gray, J., "Turbine Flowmeter Performance Model," ASME *Journal of Basic Engineering*, Vol. 92, No. 4, Dec. 1970, pp. 712-723.

2 Rubin, W., Miller, R. W., and Fox, W. G., "Driving Torques in a Theoretical Model of a Turbine Meter," ASME *Journal of Basic Engineering*, Vol. 87, No. 2, June 1965, p. 413.

3 Lee, W. F. Z., and Evans, H. J., "Density Effect and Reynolds Number Effect on Gas Turbine Flowmeter," ASME *Journal of Basic Engineering*, Vol. 87, No. 4, Dec. 1965, pp. 1043-1057.

4 Hutton, S. P., "The Effect of Inlet Flow Conditions on the Accuracy of Flowmeters," Conference on Component Interactions in Fluid Flow Systems, Institution of Mechanical Engineers, March 7, 1974, Paper C40/74, pp. 1-8.

5 Bellinga, H., and Stronk, H. B., "The Practical Application of Flow Straighteners with Turbine Flowmeters for Gas," VII IMEKO Congress, London 10-14, May 1976.

6 A.G.A. Transmission Measurement Committee Report No. 7, "Measurement of Fuel Gas by Turbine Meters," 1981.

7 Mattingly, G. E., Pursley, W. C., Paton, R., and Spencer, E. A., "Steps Toward an Ideal Transfer Standard for Flow Measurement," FLOMEKO Symposium on Flow, Groningen, The Netherlands, Nov. 1978.

J. E. McAllister
Research Engineer,
Savannah River Laboratory,
E.I. du Pont de Nemours & Co.,
Aiken, S. C.
Assoc. Mem. ASME

F. J. Pierce
Professor,
Mechanical Engineering,
Virginia Polytechnic Institute
and State Univ.,
Blacksburg, Va. 24061
Mem. ASME

M. H. Tennant
Research Engineer,
Savannah River Laboratory,
E.I. du Pont de Nemours & Co.,
Aiken, S. C.
Mem. ASME

Direct Force Wall Shear Measurements in Pressure-Driven Three-Dimensional Turbulent Boundary Layers

Unique, simultaneous direct measurements of the magnitude and direction of the local wall shear stress in a pressure-driven three-dimensional turbulent boundary layer are presented. The flow is also described with an oil streak wall flow pattern, a map of the wall shear stress-wall pressure gradient orientations, a comparison of the wall shear stress directions relative to the directions of the nearest wall velocity as measured with a typical, small boundary layer directionally sensitive claw probe, as well as limiting wall streamline directions from the oil streak patterns, and a comparison of the freestream streamlines and the wall flow streamlines. A review of corrections for direct force sensing shear meters for two-dimensional flows is presented with a brief discussion of their applicability to three-dimensional devices.

Introduction

Recent studies provide the first simultaneous *direct* force measurements of wall shear stress magnitude and direction in a three-dimensional turbulent boundary layer. Coupled with corresponding velocity and pressure field information, these data provide a unique means for direct verification of three-dimensional prediction techniques and near-wall similarity models. Since the velocity and pressure measurements in three-dimensional flows are common, emphasis will be placed on these unique measurements of wall shear stress in a three-dimensional flow. Details of the instrumentation for these wall shear measurements are given in reference [1].

Only *direct* force measurements of wall shear stress can provide the means for verifying a three-dimensional near-wall similarity model [2, 3, 4]. Direct measurements, i.e., with a force sensing, floating element device, are necessary because indirect techniques (heat elements, Preston tubes, and the like) require a valid three-dimensional near-wall similarity law *and* calibration in a three-dimensional flows as a prerequisite for their use. To date, no three-dimensional near-wall similarity models have been verified, nor has any indirect diagnostic device been calibrated in a three-dimensional flow. The use of any indirect wall shear sensing device in a three-dimensional flow using a two-dimensional calibration assumes, *a priori* and without justification, that the near wall flow is identical for the two and three-dimensional cases. This presumes the near-wall similarity models are the same for both two- and three-dimensional flows and to date this has not been verified as such – either by experiment or analysis. One of the single largest concerns over such an assumption at this time is that the two-dimensional similarity law is a scalar law, while the near-wall flow in the three-dimensional case appears to show a strong vector character all the way to the wall itsef [5, 6, 7, 8].

Since the direction of wall shear stress in a three-dimensional flow cannot be determined *a priori*, a direct determination of wall shear stress direction as well as magnitude is required. Regions of collateral flow near the wall formerly presumed to exist have more recently been questioned both experimentally [5, 6] and analytically [7, 8]. Hence it is highly questionable to assume that the direction of the velocity vector measured near the wall is in the direction of the shear stress *at* the wall. Similarly, use of heated elements for determining wall shear direction is questionable because they typically respond to some average direction over the thermal boundary layer. While analysis shows that miniature or fine wire flush surface heat meter effects penetrate the flow over very small distances in two-dimensional flows [9], the effects of the turning of the local wall flow vector down to the wall in three-dimensional flows have not been predicted.

Background

In the last fifty years over fifty investigators have reported the measurement of wall shear stress in incompressible turbulent boundary layers. All but nine of these investigations [10–18] have dealt with two-dimensional flows.

Two-Dimensional Flows. For two-dimensional flows, about two thirds of the wall shear stress measurements have been made with relatively simple indirect techniques. The remainder used floating element devices to measure wall shear stress directly. In essence, in this direct method of

Contributed by the Fluids Engineering Division for publication in the JOURNAL OF FLUIDS ENGINEERING. Manuscript received by the Fluids Engineering Division, June 30, 1980.

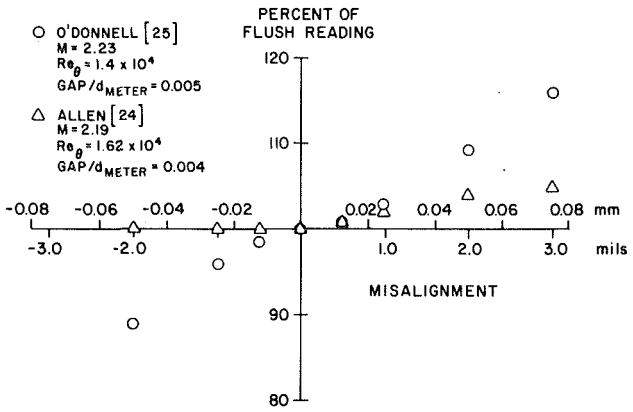

Fig. 1 Misalignment errors for two-dimensional direct force sensing shear meters

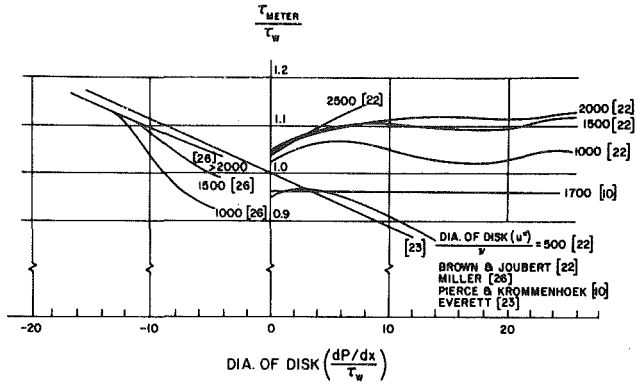

Fig. 2 Pressure gradient errors for two-dimensional direct force sensing shear meters

measurement, a small area of the wall is isolated and the force acting on that area is measured.

Errors associated with floating element devices have been catalogued and studied [10, 19–25]. The largest errors appear to be as a result of element misalignment and the pressure gradient imposed on the element. Two experimental studies have been made concerning errors induced by floating element misalignment [24, 25]. Both these studies were carried out in two-dimensional supersonic flows. Figure 1 shows a comparison of the results of these two studies. Allen's [24] results do not include discrete data points. The values shown in Fig. 1 were estimated from his graphical results for comparison with the results of O'Donnell [25]. While some researchers [19, 20, 21] have noted similar behavior in subsonic flows, little supporting data have been reported.

Four experimental studies of pressure gradient effects on floating elements have been reported [10, 22, 23, 26]. Figure 2 shows a comparison of the results of these studies. In these experiments the wall shear stress inferred from the law of the wall, a momentum balance, or some indirect measurement technique was assumed to be exact. The wide scatter among these results makes practical application very difficult, if not impossible.

From the results shown in Figs. 1 and 2, an argument could be made that no more exacting values of wall shear stress can be measured than those measured by a floating element device. For example, errors due to misalignment shown in Fig. 1 can be minimized by design. Additionally, it should be clear that the alleged "errors" in Fig. 2 incorporate the uncertainties associated with the two-dimensional law of the wall and its constants [27], or with the various indirect measurement technique themselves, as well as possible errors due to any floating element device.

Three-Dimensional Flows. For three-dimensional flows, a number of studies have reported wall shear results for indirect diagnostic devices/techniques that have been calibrated or validated only in two-dimensional flows. Since essentially all such devices/techniques are based on the well established existence of near-wall, similarity in a wide range of two-dimensional flow circumstances, their use in a three-dimensional flow presumes *a priori* that the two-dimensional near-wall similarity law is valid in the three-dimensional flow. Differences between the collateral and scalar two-dimensional flow and the skewed three-dimensional flow with its strong vector character are ignored in such an assumption. While

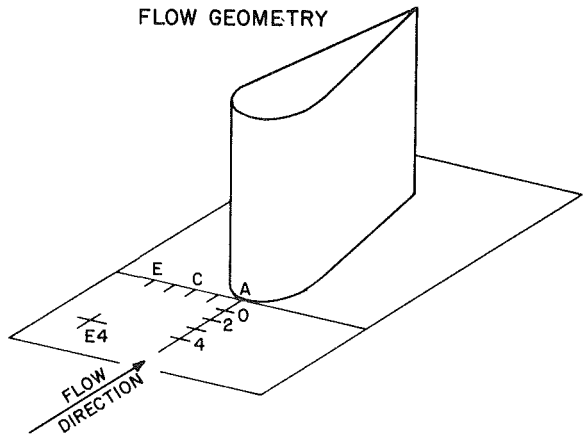

Fig. 3 Flow geometry and station designation

such differences may be minimized when ultra miniature devices or techniques penetrate the flows minimally, serious questions must be raised with Preston tubes, rakes, fences, etc. which see a changing velocity direction (as well as magnitude) in a three-dimensional flow. Pierce and Krommenhoek [10] made direct force measurements of local wall shear stress in a three-dimensional flow with a floating element device. The experiment was limited and only five direct force measurements were reported. Allowing element movement in only one direction, their floating element device was aligned using a directionally sensitive heated element. No supporting data concerning the velocity or pressure fields were reported.

Application of misalignment or pressure gradient corrections obtained for two-dimensional devices to floating element measurements in three-dimensional flows is questionable. Since misalignment can be limited to less than 0.025 mm, even direct application of the results of Fig. 1 results in small corrections. There appears to be no reason to suspect these corrections to be larger in three-dimensional flows than two-dimensional flows. Direct application of pressure gradient corrections is complicated since the pressure gradient and wall shear stress vector directions are rarely coincident in three-dimensional flows. The obvious lack of agreement in Fig. 2 is also difficult to reconcile. An independent study is currently in progress to evaluate the effects of pressure gradients on the floating element measurements reported in this three-dimensional flow. No corrections were applied to the results presented here.

Nomenclature

P = pressure
x = distance
u^* = shear velocity τ_w/ρ
τ_w = wall shear stress
τ_{meter} = wall shear stress per mechanical meter
ν = kinematic viscosity
U = freestream
U/ν = unit Reynolds number

Flow Geometry and Instrumentation

Flow in a forward quadrant of a cylinder with a trailing edge placed normal to the floor of a wind tunnel as shown in Fig. 3 was studied. This geometry was chosen because: 1) a wide range of skewing could be studied, 2) the configuration represents a large class of pressure-driven, three-dimensional flows, and 3) this geometry has been studied earlier, giving some opportunity for comparisons (e.g., East and Hoxey [11]). The cylinder has a diameter of 12.7 cm, is 25.4 cm high, and has a tapered trailing edge giving an overall length of 29.2 cm.

The body was placed in the test section of a large, open circuit, 0.61 × 0.91 m (2 × 3 ft) wind tunnel. The wind tunnel can provide air speeds up to about 26 m/sec with a freestream turbulence level of <0.6 percent at the test section. Locations for data measurement are designated by two symbols (see Fig. 3). The first symbol is alphabetic and represents a line parallel to the tunnel axis, with the centerline of the body designated with the symbol A. The second symbol is numeric and respresents the location along the tunnel axis, in inches, with the leading portion of the body designated with the symbol 0. Measurement stations were placed on a 2.54 cm grid.

A floating element omnidirectional direct force sensing wall shear meter was designed for the simultaneous measurement of the magnitude and direction of wall shear stress vectors. Details of the meter's design, characteristics of operation, and calibration (both static and dynamic) are discussed in reference [1]. Owing to its delicate nature, the meter was held stationary while the body was moved relative to the meter location. Velocity profiles were measured with a small claw probe whose tip consisted of three stainless steel tubes each of 0.50 mm OD.

Results and Discussion

Wall shear stress results are shown in Fig. 4. Two sets of data are reported. The first set (Tennant), at a tunnel unit Reynolds number of about 1.45 × 10^6/m, was taken nearly 18 months before the second set (McAllister) which was at a unit Reynolds number of about 1.30 × 10^6/m. The only differences between the Tennant and McAllister data sets are that McAllister's data were at a lower wind tunnel velocity resulting from a tunnel-fan interface modification which was made between their two sets of measurements, and the omnidirectional meter's readout instrumentation was improved. Tennant's study, including his data in Fig. 4, included over one hundred direct force wall shear measurements, and McAllister's study, including his data in Fig. 4, included nearly two hundred such measurements. There is an uncertainty estimate for both the magnitude and direction of each of the wall shear stress vectors in Fig. 4 and these uncentainty values were used to define the small curvilinear rectangle at the tip of each of the shear stress vectors. The uncertainties were calculated after reference [28].

As noted above, the two sets of data in Fig. 4 are not directly comparable since they were obtained at different tunnel unit Reynolds numbers. The larger wall shear stress magnitude of Tennant's data is a result of a 12 percent higher unit Reynolds number. For comparison purposes it is noted that extensive measurements in a nominally two-dimensional flow indicated wall shear for the higher Reynolds number tunnel conditions at 20 percent higher than for the lower speed conditions. It is noted that the pseudo two-dimensional, nominally symmetric flow at station A7 shown in Fig. 4 reflects an equal difference. It is not possible to predict shear magnitude differences between the readings in the fully three-dimensional flow. Agreement between the wall shear stress angles is generally within uncertainty bands, although it should be noted that these angles would also be expected to change slightly for a change in the wind tunnel unit Reynolds number. Note that the largest differences appear near the separation horseshoe vortex where measurements are very difficult because of larger fluctuations in the detected wall shear. Overall, each data set gives similar results for the two different unit Reynolds numbers showing the repeatability of the omnidirectional meter between the two studies. Repeatability of measured data within each study was generally well within the indicated uncertainty bands.

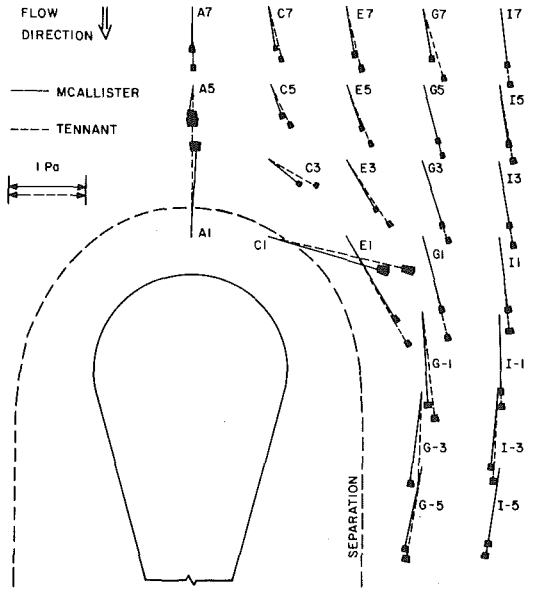

Fig. 4 Wall shear vectors by direct force measurements for a pressure driven flow. $U/\nu = 1.45 \times 10^6$/m for Tennant; $U/\nu = 1.30 \times 10^6$/m for McAllister. Uncertainty intervals at 15:1.

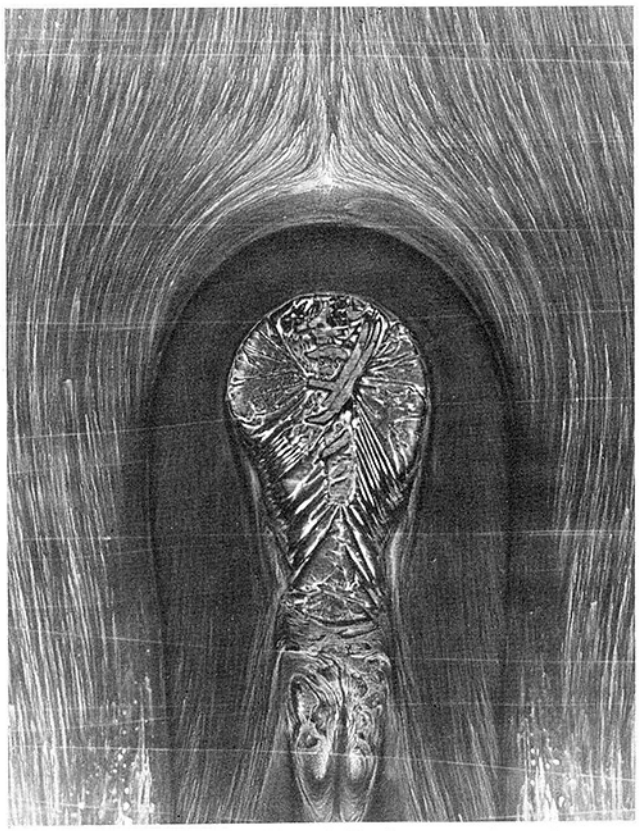

Fig. 5 Wall streak photograph showing separation region

As the leading edge of the body as approached, a reversal of the wall shear direction was noted near station A3. A complete flow reversal was recorded at station Al with a very high local shear stress identified with the horseshoe vortex behind the upstream separation sheet. The separation line shown in Fig. 4 is based on wall oil streak patterns obtained with finely ground titanium dioxide particles suspended in a diesel fuel-mineral oil mix and shown in Fig. 5. The liquid-particle mixture was applied with a hard rubber roller as a very thin film of only a few thousandths of an inch of thickness, and, in a relatively thick boundary layer as in this case, it is assumed they represent the wall flow or limiting wall streamlines with good accuracy. It appears that station C1 is also within the separation vortex. The shear vector direction indicates a significant downstream wall flow component develops in a relatively short distance from the symmetry plane. This separated flow near the cylinder-floor corner appears to be very complex and is being investigated by LDV techniques in a subsequent study. In the unseparated region the wall shear appears well behaved as its angle turns first away from the body as the flow approaches and moves around the cylinder, and then turns toward the body as the flow reverses direction to follow the trailing edge.

Omitting the singular zero pressure gradient case, the pressure gradient wall shear vector orientations in two-dimensional flows are limited. These vectors may be directed in the same sense or in the opposite sense, but they are always collinear and may be treated in a scalar sense. The three-dimensional case is more complex as the following technique confirmed. A plate containing fifty-four static pressure taps was placed in the floor of the wind tunnel to provide a map of the wall pressure field surrounding the cylinder. From this pressure map, pressure gradients could be estimated. Using a calibrated pressure transducer and scanning device, static pressure measurements were made and fitted to various higher order equations with a least-square method. These equations were differentiated to obtain estimates of the pressure gradients. Details of the instrumentation and method of estimation are given elsewhere [29].

Figure 6 shows a map of the pressure gradient field for both sets of data. Considering the uncertainty in differentiating experimental data, the agreement is considered to be very good. McAllister's results are preferred because the method of estimation used for that data was more refined. The relative direction of the pressure gradient and wall shear vectors vary from nearly collateral along the centerline (the A) stations to nearly orthogonal at station G-1. These results confirm the anticipated difficulties in the application of any pressure gradient corrections such as those in Fig. 2 to three-dimensional flow measurements.

Recent experiments [5, 6] and analyses [7, 8] in pressure-driven flows do not support the assumption of a collateral near-wall layer in three-dimensional turbulent flow as

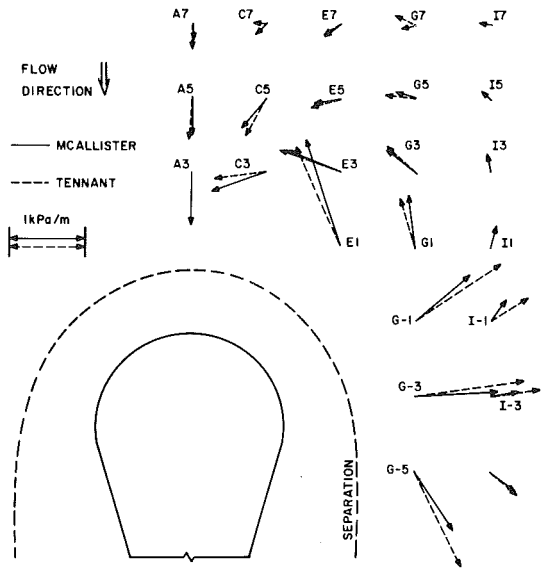

Fig. 6 Pressure gradient map. Estimated uncertainties of magnitude ±10 percent; direction ±5 deg both at 15:1.

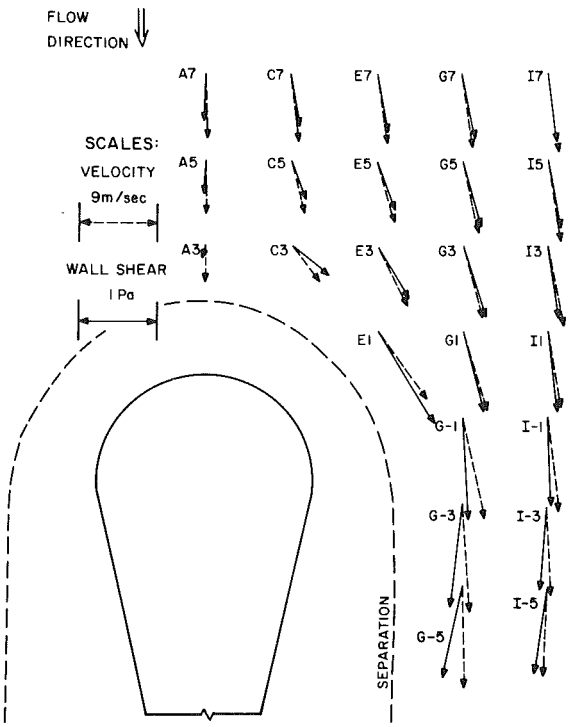

Fig. 7 Wall shear directions and nearest wall velocity directions. Velocity magnitude ±3, direction ±1 deg both at 20:1. Wall shear uncertainties are shown in Fig. 4.

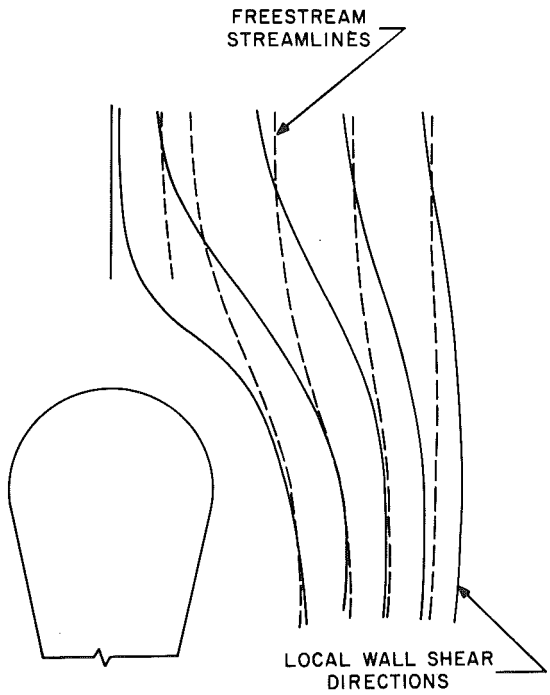

Fig. 8 Local wall shear directions and freestream directions

Table 1 Comparison of flow angles[a]

Station	Shear meter	Velocity probe [b]	Oil streaks
A7	− 0.9 deg	1.3 deg	+ 0.5 deg
A5	− 1.8	1.7	
C7	7.5	6.8	7.0
C5	20.3	14.2	20.5
C3	52.3	39.1	47.0
E7	10.1	8.4	10.0
E5	18.8	14.7	18.0
E3	31.7	26.6	31.5
E1	31.1	36.2	32.5
G7	9.4	9.1	10.5
G5	13.7	12.7	16.0
G3	16.9	16.5	16.5
G1	14.7	17.8	15.5
G-1	3.9	13.1	5.5
G-3	− 6.9	3.9	− 4.0
G-5	−11.9	2.0	−10.5
I7	6.4	7.6	7.0
I5	8.2	9.0	8.0
I3	9.3	11.0	9.0
I1	6.9	10.0	7.3
I-1	1.5	7.2	4.0
I-3	− 4.6	1.1	− 3.0
I-5	− 8.1	− 2.7	− 7.0

[a] Tunnel inlet unit Reynolds number of 1.30×10^6/m

[b] Probe OD = 0.25 mm (0.020 in.) with the probe on the wall

suggested by polar representations of velocity profiles. Thus the assumption that the limiting wall streamline direction or the wall shear stress direction can be taken as the flow direction indicated by a small velocity probe very near the wall is at best highly suspect. Figure 7 compares the velocity vector direction at 0.25 mm (0.010 in.) from the wall and the wall shear stress direction for the McAllister data. The wall shear stress and nearest wall velocity vector angles can differ significantly, for example, in this experiment at station C3 the angles differ by over 13 deg, with this difference well outside any reasonable uncertainties for both measurements. The boundary layer at profile C3 is nominally five inches thick and the velocity probe indicated a monotone increasing skew relative to the freestream direction of 32 deg at the nearest wall velocity reading. The oil streak pattern indicated an additional 13 deg of turning at the wall. One would expect a smaller angle difference with a smaller probe since it could be placed closer to the wall, but in this case, with a nominally five inch boundary layer, the ratio of the boundary layer thickness to the probe diameter is about 250, a relatively larger value in such work. These results are consistent with studies noted earlier which indicate that the velocity vector changes direction continuously to the wall. Since the measurements of local wall shear stress direction can be significantly different than the typical nearest wall velocity direction, the common practice of inferring the limiting wall streamline angle from the latter, can yield significant errors for at least some flow conditions.

Limiting wall streamline directions were measured from the oil streak pattern shown in Fig. 5 and the results are shown in Table 1. With only a few exceptions, there is excellent agreement between the oil streak directions and the direct force wall shear directions, and as noted above, these directions are different from those of the nearest wall velocity indicating further turning of the velocity vector down to the wall.

The strong agreement between the oil streak limiting wall streamline directions and the direct force wall shear directions suggests that any pressure gradient effects on the direct force sensing shear meter affected the wall shear direction minimally, if at all. The results in Table 1 are interesting from another point of view. It has been suggested, at least informally, that the demonstrated *use* of miniature, dual sensor, buried wire flush mounted heat meters in a three-dimensional turbulent flow by Higuchi and Peake [18] in effect validates the use of such devices for quantitative results in other such three-dimensional flows. It has been inferred that the smallness of such miniature heat meter sensors would result in a minimal thermal penetration into the skewed near-wall flow so that limiting wall streamline directions would be well predicted. The comparison of wall flow angles measured by oil streak patterns and the dual element heat sensor (calibrated in a two-dimensional flow) reported in reference [18] show consistent and typical differences ranging from about 5 deg to as much as 15 deg. Based on the high degree of agreement found in this study between the wall flow angles measured from the oil streak patterns and the wall shear direction measured by the direct force sensing shear meter, at this point in time it would seem somewhat presumptuous to assume that such miniature heat sensors do in fact report limiting wall streamline directions accurately. Parenthetically, it is also noted that the wall shear magnitude values reported in reference [18] were based on a two-dimensional calibration using a Preston tube. No validation of this two-dimensional calibration was attempted in any three-dimensional flow.

Finally, Fig. 8 shows the relative orientations of the freestream streamline directions and the local wall shear stress directions. The local wall shear directions were taken from the direct measurements which agreed well with the oil streak pattern. The freestream lines were constructed from velocity direction measurements made over the wall shear measurement locations. As expected, the collinear upstream character of these two families is quickly lost when significant freestream streamline curvature begins with the corresponding pressure-driven secondary flow in the boundary layer. The figure also suggests that if one identifies wall streamlines with the local wall shear stress, then those wall streamlines appear to turn substantially less than the freestream streamlines. An ultimate return toward parallelism appears downstream when the freestream streamlines lose their curvature. The freestream streamlines in the lower quadrant of Fig. 8 tend to become parallel with the body centerline, rather than follow the body contour. This behavior appears to relate to the thickening of the separation horseshoe vortex as it wraps itself around the body as evidenced by the nearly constant width shown for the downstream portions of the separation line in Fig. 5. The influence of this separation vortex in the freestream flow in close proximity to the body, particularly in the regions downstream of the 90 deg plane on the body, remains to be determined in further work in this three-dimensional, separated flow.

Acknowledgments

This research was initiated by a grant from the National Science Foundation and continued with a subsequent grant from NASA-Ames.

References

1 Tennant, M. H., Pierce, F. J., and McAllister, J. E., "An Omnidirectional Wall Shear Meter," ASME JOURNAL OF FLUIDS ENGINEERING, Vol. 102, Mar. 1980, pp. 21–25.

2 Nash, J. F., and Patel, V. C., *Three-Dimensional Turbulent Boundary Layers*, SBC Technical Books, 1972.

3 Chandrashekhar, N., "Some Studies on Three-Dimensional Turbulent Boundary Layers," Ph.D dissertation, Department of Applied Mechanics, Indian Institute of Technology, Madras, India, Oct. 1974.

4 van den Berg, B., "The Law of the Wall in Two- and Three-Dimensional Turbulent Boundary Layers," National Aerospace Laboratory, The Netherlands, TR 72111 U, Jan. 1973.

5 Rogers, B. K., and M. R., Head, "Measurement of Three-Dimensional

Turbulent Boundary Layers," *The Aero. Journal of the Royal Aero. Society*, Vol. 73, Sept. 1969, pp. 796–798.

6 Hebbar, K. S., and Melnik, W. L., "Wall Region of a Relaxing Three-Dimensional Incompressible Turbulent Boundary Layer," *Journal of Fluid Mechanics*, Vol. 52, Part 1, 1978, pp. 33–58.

7 Pierce, F. J., and East, J. L., "Near-Wall Collateral Flow in Three-Dimensional Turbulent Boundary Layers," *AIAA Journal*, Vol. 10, No. 3, Mar. 1972, pp. 334–336.

8 Klinksiek, W. F., and Pierce, F. J., "A Finite Difference Solution of the Two- and Three-Dimensional Incompressible Turbulent Boundary Layer Equations," ASME JOURNAL OF FLUIDS ENGINEERING, Vol. 95, Sept. 1973, pp. 445–458.

9 Rubesin, M. W., Okuno, A. F., Mateer, G. G., and Brosh, A., "A Hot-Wire Surface Gage for Skin Friction and Separation Detection," NASA TM X62, 465, Ames Research Center, 1975.

10 Pierce, F. J., and Krommenhoek, D. H., "Wall Shear Stress Diagnostics in Three-Dimensional Turbulent Layers," Interim Technical Report No. 2, ARO-D Project 6858E, Virginia Polytechnic Institute and State University, Sept. 1968.

11 East, L. F., and Hoxey, R. P., "Low-Speed Three-Dimensional Turbulent Boundary Layer Data," Parts 1 and 2, Aeronautical Research Council R & M 3653, Mar. 1969.

12 Prahlad, T. S., "Wall Similarity in Three-Dimensional Turbulent Boundary Layers," *AIAA Journal*, Vol. 6, No. 9, 1968, pp. 1772–1774.

13 Power, J. L., "Wall Shear Stress and Mean-Velocity Measurements in a Three-Dimensional Turbulent Boundary Layer," Naval Ship and Development Center Report 4056, Sept. 1973.

14 Prahlad, T. S., "Yaw Characteristics of Preston Tubes," *AIAA Journal*, Vol. 10, No. 3, Mar. 1972, pp. 357–359.

15 Hebbar, K. S., and Melnik, W. L., "Measurements in the Near-Wall Region of a Relaxing and Three-Dimensional Low Speed Turbulent Air Boundary Layer," University of Maryland, T. R. No. AE-76-1, July 1976.

16 Vagt, J. D., and Fernholz, H., "Use of Surface Fences to Measure Wall Shear Stress in Three-Dimensional Layers," *The Aeronautical Quarterly*, Vol. 24, 1973, pp. 87–91.

17 McCroskey, W. J., and Durbin, E. J., "Flow Angle and Shear Stress Measurements Using Heated Films and Wires," ASME *Journal of Basic Engineering*, Vol. 94, Mar. 1972, pp. 46–52.

18 Higuchi, H., and D. J. Peake, "Bi-Directional, Buried-Wire Skin Friction Gage," NASA TM 78531, Ames Research Center, 1978.

19 Smith, D. W., and Walker, J. H., "Skin-Friction Measurements in Incompressible Flow," NACA TN 4231, Mar. 1958.

20 Morsy, M. G., "An Instrument for the Direct Measurement of the Local Shear Stress on Circular Cylinder," *Journal of Physics, Part E-Scientific Instruments*, Vol. 7, Feb. 1974, pp. 83–86.

21 Furuya, Y., I. Nakamura, H. Osaka, and H. Honda, "The Spanwise Non-Uniformity of Nominally Two-Dimensional Turbulent Boundary Layer II—Wall Shear Stress and Flow Field," *JSME Bulletin*, Vol. 18, July 1975, pp. 673–680.

22 Brown, K. C., and Joubert, P. N., "The Measurement of Skin Friction in Turbulent Boundary Layers with Adverse Pressure Gradients," *Journal of Fluid Mechanics*, Vol. 35, Part 4, 1969, pp. 732–757.

23 Everett, H. U., "Calibration of Skin Friction Balance Discs for Pressure Gradient," Defense Research Laboratory, DRL-426, CF-2708, Aug. 1958.

24 Allen, J. M., "Experimental Study of Error Sources in Skin Friction Balance Measurements," ASME JOURNAL OF FLUIDS ENGINEERING, Vol. 99, Mar. 1977, pp. 192–204.

25 O'Donnell, F. B., Jr., "A Study of the Effect of Floating-Element Misalignment of Skin-Friction-Balance Accuracy," Defense Research Laboratory, DRL-515, CR-10, Mar. 1964.

26 Miller, B. L. P., "The Measurement of Wall Shearing Stress in Turbulent Boundary Layers," Ph.D. thesis, University of Leicester, Great Britain, Aug. 1972.

27 Pierce, F. J., and D. S., Gold, "Near-Wall Velocity Measurements for Wall Shear Inference in Turbulent Flows," *Flow Measurement in Open Channels and Closed Conduits*, NBS Special Publication 484, Vol. 2, Oct. 1977, pp. 621–648.

28 Kline, S. J., and McClintock, F. A., "Describing Uncertainties in Single-Sample Experiments," *Mechanical Engineering*, Jan. 1953, p. 3.

29 Nelson, D. J., "Pressure and Velocity Fields in a Relaxing Three-Dimensional Turbulent Boundary Layer," M.S. thesis, Virginia Polytechnic Institute and State University, Blacksburg, Va., Aug. 1979.

J. E. McAllister
Research Engineer,
Savannah River Laboratory,
E. I. du Pont de Nemours & Co.,
Aiken, S. C. 29801
Assoc. Mem. ASME

F. J. Pierce
Professor, Mechanical Engineering,
Virginia Polytechnic Institute
and State University,
Blacksburg, Va. 24061
Mem. ASME

M. H. Tennant
Research Engineer,
Savannah River Laboratory,
E. I. du Pont de Nemours & Co.,
Aiken, S. C. 29801
Mem. ASME

Preston Tube Calibrations and Direct Force Floating Element Measurements in a Two-Dimensional Turbulent Boundary Layer

Preston tubes provide a convenient means of estimating local wall shear stress. Practical difficulties arise from a lack of calibration data obtained in turbulent boundary layer flows and from the wide choice of calibration equations available mainly from pipe flow calibrations. The results of an experimental study comparing a large number of direct force local wall shear stress measurements in a near-zero pressure gradient two-dimensional turbulent boundary layer flow are presented. The results indicate that there is consistent and excellent agreement between the Patel intermediate calibration formula and the direct force measurements. Typical differences among the direct force measurements and several other proposed calibration equations are also shown.

Introduction

Preston tubes provide a convenient means of estimating local wall shear stress in two-dimensional flows because of their ease in construction and use and their general applicability over a fairly wide range of pressure gradients [1-19]. Practical difficulties arise from a lack of calibration data in turbulent boundary layers and from the wide choice of calibration curves and equations available mainly from pipe flow calibrations. Only one calibration equation based on direct force local wall shear measurements is available for boundary layer flows [14] and this relationship is in modest disagreement with the more frequently recommended calibration equations obtained from fully developed pipe flow measurements. Table 1 shows the more frequently cited calibration equations while Table 2 shows the different conditions under which the equations in Table 1 were determined.

Since the different calibration equations in Table 1 generally give different results, usually outside the range of expected experimental scatter, direct measurements of local wall shear stress would be of great value in any attempt to verify which calibration equation best predicts a given wall shear. It should be noted that in Table 1 only the study by Smith and Walker [14] used a floating element or direct wall shear measuring device as a standard for their Preston tube calibration. In a study devoted to transpired boundary layers [5], it was noted that the Patel [18] intermediate range equation agreed well with some zero transpiration wall shear data. While no results were shown and the extent of the measurements is not detailed, DePooter, Brundrett, and Strong [5] reported that their Preston tube measurements using the intermediate Patel equation consistently agreed with floating element direct measurements to within ±2 percent.

The results presented in this note are intended to compare all the calibration curves in Table 1 with direct wall shear stress measurements in a low speed, incompressible, two-dimensional turbulent boundary layer in a near-zero pressure gradient over a modest unit Reynolds number range.

Apparatus

The direct force sensing, mechanical omnidirectional floating element device used to provide direct wall shear measurements utilizes a 2.86 cm diameter floating element with a lip thickness of 0.635 mm and a uniform gap between the element and housing of 0.127 mm. The sensing element is supported on a 21.6 cm long, 1.59 mm diameter steel rod. A 10,000 centistoke fluid is used to damp element vibrations. Two Bently-Nevada eddy current proximeters with probes locate the element position for the simultaneous recording of both the local shear stress magnitude and direction. Additional details are provided in Tennant, Pierce, and McAllister [20]. The data reported here were obtained in an open circuit tunnel where room air enters a 3.66 × 2.44 m inlet section with a filter pad, flow straighteners, and multiple screens (open area of approximately 70 percent) followed by a 16 to 1 contraction designed for zero acceleration at exit into a 0.91 × 0.61 m rectangular tunnel with nominal 3 mm diameter rods as boundary layer trips at the tunnel inlet with the test section 5 m downstream of these trips.

Contributed by the Fluids Engineering Division for publication in the JOURNAL OF FLUIDS ENGINEERING. Manuscript received by the Fluids Engineering Division, May 7, 1981.

Table 1 Preston tube calibration equations

Investigator	Calibration Formula	
Preston [11]	$y^* = 0.1505 + 0.5x^*$	$2 \le x^* < 4.1$
	$y^* = -1.396 + 0.875x^*$	$4.1 \le x^* \le 6.5$
Head and Rechenberg [12] as given by Ferriss [13]	$y^* = -1.467 + 0.889x^*$	$5.14 \le x \le 6.94$
Ferriss [13]	$y^* = -1.422 + 0.881x^*$	$4.79 \le x^* \le 6.38$
Smith and Walker [14]	$y^* = -1.366 + 0.877x^*$	$5.0 \le x^* \le 7.5$
N.P.L. Staff [15]	$y^* = -1.353 + 0.875x^*$	$5.25 \le x^* \le 7.20$
Patel [18]	$y^* = 0.5x^* + 0.037$	$x^* < 2.90$
	$y^* = 0.8287 - 0.1381x^* + 0.1437x^{*2} - 0.006x^{*3}$	$2.9 \le x^* < 5.60$
	$x^* = y^* + 2\log_{10}(1.95y^* + 4.10)$	$5.6 \le x^* < 7.6$
Bertelrud [16]	$\frac{P_T - P}{\tau_w} = 38.85x^* - 88.53$	$4.80 < x^* < 7.72$

Table 2 Conditions under which the Preston tube calibration equations were obtained

Investigator	Flow Type	Standard Used	Pressure Gradients Present	Tube Sizes (diameter)
Preston [11]	Pipe	Pipe pressure drop	$\frac{dP}{dx} > 0, < 0$	0.740 to 3.084 mm (0.02915 to 0.1214 in.)
Head and Rechenberg [12]	Pipe	Sublayer fence	$\frac{dP}{dx} = 0, > 0, < 0$	0.597 to 9.520 mm (0.0235 to 0.3748 in.)
Ferris [13]	Channel	Sublayer fence	$\frac{dP}{dx} = 0, > 0$	0.914 to 2.870 mm (0.036 to 0.113 in.)
Smith and Walker [14]	Flat Plate	Floating element device	$\frac{dP}{dx} = 0$	0.762 and 3.091 mm (0.0300 and 0.1217 in.)
Staff of the N.P.L. [15]	Flat Plate	Wake-traverse method and Stanton tubes	$\frac{dP}{dx} = 0$	1.194 to 3.175 mm (0.047 to 0.125 in.)
Patel [18]	Pipe	Pipe pressure drop	$\frac{dP}{dx} = 0, > 0, < 0$	0.597 to 12.649 mm (0.0235 to 0.498 in.)
Bertelrud [16]	Pipe	Pipe pressure drop	no mention	0.599 to 18.999 mm (0.0236 to 0.748 in.)

The Preston tubes were individually mounted on 12.7 cm diameter aluminum disks with the tube opening centered on the disk. The opening of each stainless steel tube was hand-crafted in order to insure a smooth, round entrance free of burrs. The tubes were approximately 3.81 cm long and they were epoxied to the aluminum disk. Tubes with outside diameters of 0.46, 0.71, 0.91, and 2.11 mm were used. The inside diameters were 0.241, 0.394, 0.584, and 1.60 mm, respectively. Except for the largest tube, the static pressure taps were located 1.27 cm from the tube opening in a line transverse to the direction defined by the tube axis. In preliminary testing of the three smaller tubes, static pressure tap locations as close as 0.64 cm to the Preston tube produced the same results as the taps located at the 1.27 cm distance. For the largest diameter Preston tube, the static pressure tap was 2.54 cm from the Preston tube opening. Static pressure taps closer than 1.27 cm gave readings dependent on this separation distance, while readings with the static pressure taps located from 1.6 cm up to 3.2 cm gave identical results.

The Preston tube measurements were made with a Datametrics model 1400 electronic digital manometer using a Gould Type 590 D-10W-2P1-V1-4D transducer. This system gave a least count of 25.4 μm of water.

Nomenclature

D = Preston tube outer diameter
h = channel height
P = static pressure
P_T = total pressure
$\Delta P = P_T - P$
U = tunnel inlet freestream velocity

$$x^* = \log_{10}\left(\frac{\Delta P D^2}{4\rho\nu^2}\right)$$

$$y^* = \log_{10}\frac{(\tau_w D^2)}{4\rho\nu^2}$$

ν = kinematic viscosity
ρ = density
τ_w = wall shear stress
$\Delta = \frac{\nu}{\rho u_\tau^3}\frac{dp}{dx}$ Patel parameter

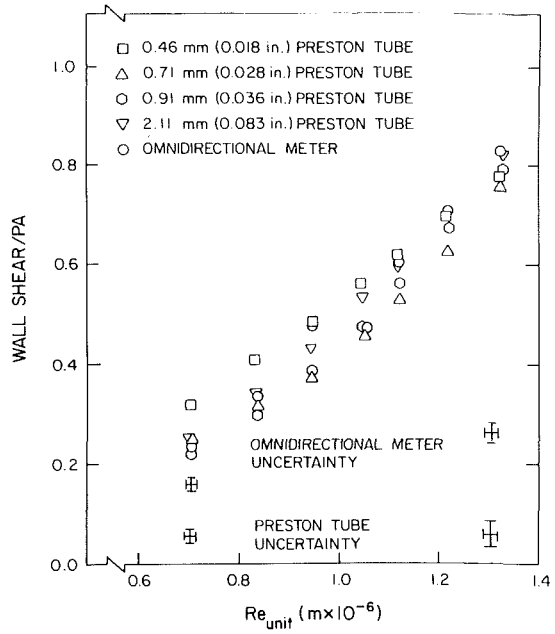

Fig. 1 Preston tube results using the Preston [11] calibration equations

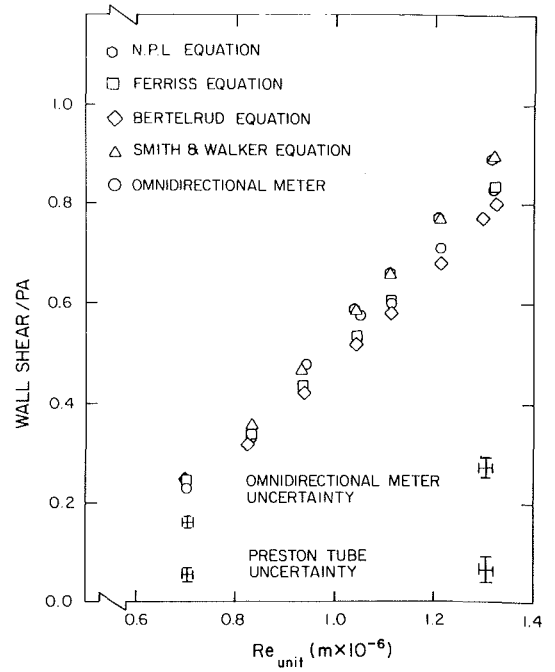

Fig. 2 Preston tube results for the 2.11 mm tube using the NPL [15], Ferriss [13], Bertelrud [16], and Smith and Walker [14] calibration equations

Data Uncertainties

The uncertainties in the direct force, omnidirectional meter data and in the Preston tube data were determined using a Kline-McClintock-type [21] analysis and typical data uncertainties are shown in Figs. 1–4. These uncertainties are estimated at nominal 20:1 odds.

Results

The direct force and indirect wall shear data were obtained at different times over a limited range of tunnel speeds. Detailed velocity profile measurements indicated a nominally two-dimensional turbulent boundary layer about 10 cm thick existed in the test section with a freestream turbulence level of 0.6 percent. Data were taken over a unit Reynolds number range, $\mathrm{Re}/L = U/\nu$, of 0.6×10^6 to 1.4×10^6/m which corresponded to an R_θ range of 7.5×10^3 to 12.8×10^3 and a near constant shape factor range of $H = 1.34$ to 1.32. The Patel parameter, Δ, was nearly zero varying from -1.85×10^{-3} to -3.15×10^{-4}. Freestream velocities varied from 12.9 to 24.4/m s. These velocity profile measurements indicated consistent and repeatable transverse test section variations in the local skin friction from +3.5 to −9.3 percent of the mean test section value at each unit Reynolds number over the full range of running conditions. These variations are consistent with such transverse nonuniformities as reported in the carefully documented work of Bradshaw [22], Furuya and Osaka [23], and Furuya, et al. [24], de Bray [25], and Favre and Gaviglio [26]. Though these transverse variations were consistent and repeatable, the shear force measurements were made consecutively at the same physical location maintaining a careful control of not only the inlet unit Reynolds number for similitude, but keeping the flow conditions nearly identical as well. Only the barometric pressure was a free variable and this varied very little over most of the data.

Wall shear stresses calculated from the various Preston tube calibration equations and compared to the direct force measurements for this small pressure gradient flow are shown in Figs. 1–4. Figure 1 compares the four different sizes of Preston tubes to the original Preston tube calibration equations. It is clear that the tube size is not properly accounted for in these calibration equations. Figure 2 compares the N.P.L., the Ferriss, the Bertelrud, and the Smith and Walker calibration equation results to the direct force measurements. Figure 3 shows the results of the Patel intermediate range formula for the range of unit Reynolds numbers of this study. There was substantially more data available at the higher unit Reynolds numbers than could be shown in Fig. 3. These data, in the range of the boxed area in Fig. 3, are shown in Fig. 4 in an expanded scale. From these figures it is evident that the intermediate range Patel calibration equation gives much better agreement with the direct force wall shear measurements than the Preston, N.P.L., Bertelrud, and Smith and Walker calibration equations. The Ferriss formula appears to offer the same level of agreement with the direct wall shear data as the Patel equations but the Ferriss formula is severely limited in its applicable range. The N.P.L. and the Smith and Walker wall shear values are generally higher than the direct force wall shear values. While the Bertelrud results are generally lower, the choice of dependent variable in this equation leads to overall wall shear uncertainties for this calibration equations that are smaller than for the other equations. Bertelrud purposely used different variables for his calibration equation given in Table 1 because Head and Ram [17] showed these variables to be less sensitive to the Preston tube data inputs than the x^* and y^* variables used by most other investigators. A close examination of the Patel and Bertelrud results in Figs. 2 and 3 indicates that although both agreed with the direct wall shear data within experimental uncertainty, the Patel calibration gives overall better agreement. As in reference [5], all the Preston tube data in this study also fell into the x^* range covered by the intermediate Patel calibration formula so that results for only the intermediate formula are shown in Figs. 3 and 4.

A least squares regression analysis using Gauss-Jordan reduction with maximum pivot strategy [27] was completed for all 75 Preston tube and for all 113 direct force wall shear values. Various order polynominals were fitted and while third order curves gave slightly better fits in terms of residuals, the (even slight) "waviness" that higher order curves suggested was rejected. The second order fits showed the Preston tubes to read about 4–5 percent low at the lower

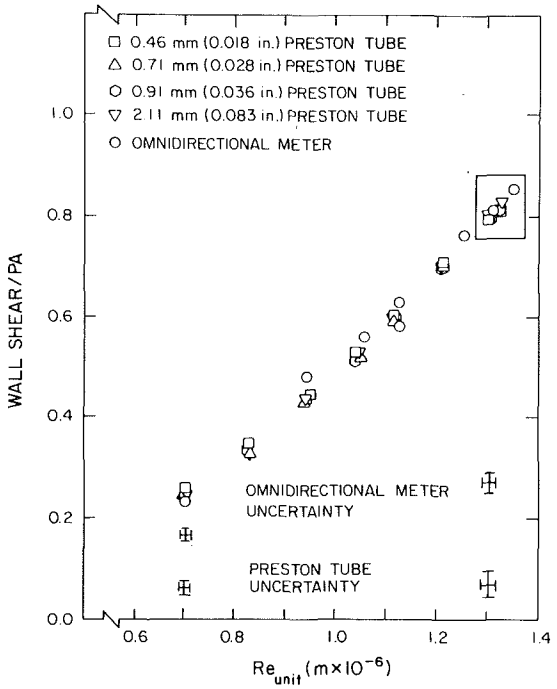

Fig. 3 Preston tube results using the Patel [18] intermediate calibration equation

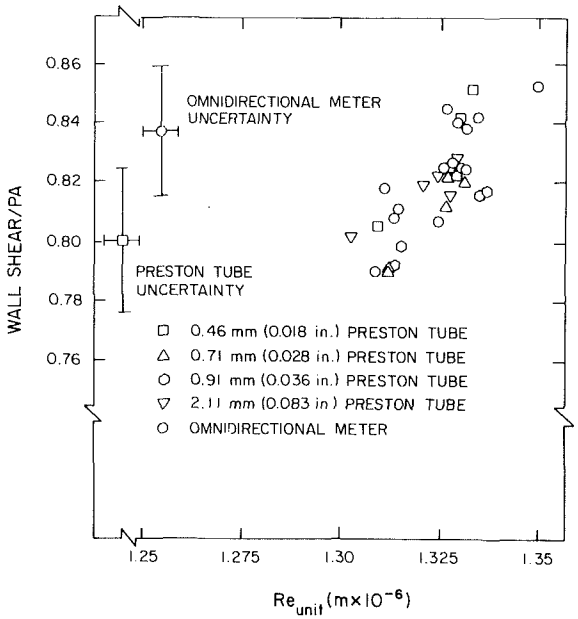

Fig. 4 Details of Preston tube and direct force shear measurements at the high unit Reynolds number range

unit Reynolds number and this decreased to a nearly zero difference at the highest Re/L values of Fig. 3. It is noted that the large majority of both Preston tube and shear meter data was in the highest Re/L interval where the two sets of shear values agreed best (nearly perfect) in the least squares sense.

It is also noted that for near zero pressure gradient flow Brown and Joubert [8] reported a generally 4–5 percent higher reading for their mechanical shear meter results compared to their Preston tube results, with this difference apparently persisting over the full larger Re/L range of their work. The more recent work of Frei and Thomann [28] used a mechanical shear meter in circular cross section flows with a circumferential sensing element. The expected local transverse wall shear variations recorded by Preston tubes required that such data be averaged for comparison with the direct force measurements; hence comparisons of individual Preston tube readings were not made. While data are not presented in detail, for a near zero pressure gradient flow Fig. 6 in Frei and Thomann appears to show the majority of the direct force wall shear readings to be slightly (but only slightly) higher than the averaged Preston tube results with these differences less than the 4–5 percent reported by Brown and Joubert and noted here for the lower Re/L range of these data.

Brown and Joubert [8] identified these small differences with their mechanical shear meter and attributed them to slight secondary forces on the floating element, possible slight misalignment, and the roughening effect of the gap. Interestingly enough, the Frei and Thomann [28] results showing generally better agreement between the mechanical meter and Preston tube results used an innovative method of minimizing the meter gap effect by sealing the gap using the surface tension of glycerine. The gap was essentially sealed and except for miniscus effects (and possible very slight misalignment) the flow sensed a continuous surface in the neighborhood of the floating section. On the other hand, the very large quantity of data over the high Re/L interval in this study showed excellent agreement between the shear meter and the Preston tubes, and this is not unlike the circumferential averaging required of the Frei and Thomann Preston tube data.

Thus it would appear that in two-dimensional near-zero pressure gradient flows, while Preston tubes in the range of the intermediate Patel calibration formula and direct force measurements agree very well, carefully taken direct force measurements tend to be, on a point by point comparison, up to 4–5 percent high and with some consistency. It would also appear that minimizing the shear meter slot or gap size or the effect of this gap as with a liquid film tends to reduce this difference, as did the averaging of a large quantity of data under nominally given flow conditions.

Conclusions

An experimental study comparing extensive direct force local wall shear stress measurements in a near zero pressure gradient, two-dimensional turbulent boundary layer over a range of unit Reynolds numbers from about 0.6×10^6 to 1.4×10^6/m, to shear stresses calculated for a series of four different size Preston tubes for several calibration equations is presented.

The results indicate that the intermediate range pipe flow calibrations of Patel consistently reduce the Preston tube data from a range of four tube sizes to wall shear values which generally agree very well with the direct force local wall shear values from the direct force sensing, omnidirectional wall shear meter. For the range of Re/L reported here regression fits of the data showed the Preston tube results 4–5 percent low at the lower Re/L interval of data, with these differences essentially vanishing at the high Re/L interval where in fact the large majority of the data was obtained. The findings of Preston tube readings slightly lower than direct force measurements are consistent with the results of Brown and Joubert [8] and Frei and Thomann [28].

Acknowledgments

This project was supported by a grant from NASA Ames with Mr. Joseph G. Marvin monitoring the grant.

References

1 Bertelrud, A., "Skin Friction Measurement Techniques in Incompressible Turbulent Flow—A Literature Survey," Aeronautical Research Institute of Sweden, FFA Rept. AU-726, 1972 (available from NTIS as N73-17246).

2 Allen, J. M., "Evaluation of Preston Tube Calibration Equations in Supersonic Flow," *AIAA Journal*, Vol. 11, No. 11, Nov. 1973, pp. 1461–1462.

3 Bertelrud, A., "Pipe Flow Calibration of Preston Tubes of Different Diameters and Relative Lengths Including Recommendations on Data Presentation for Best Accuracy," Aeronautical Research Institute of Sweden, FFA Rept. 125, Sept. 1974 (available from NTIS as N75-15000).

4 Simpson, R. L., and Whitten, D. G., "Preston Tubes in the Transpired Turbulent Boundary Layer," *AIAA Journal*, Vol. 6, No. 11, Sept. 1968, pp. 1776–1777.

5 Depooter, K., Brundrett, E., and Strong, A. B., "The Calibration of Preston Tubes in Transpired Turbulent Boundary Layers," ASME JOURNAL OF FLUIDS ENGINEERING, Vol. 100, Mar. 1978, pp. 10–16.

6 Bradshaw, P., and Galea, R. V., "Step-Induced Separation of a Turbulent Boundary Layer in Incompressible Flow," *Journal of Fluid Mechanics,* Vol. 27, Part 1, 1967, pp. 111–130.

7 Sigalla, A., "Measurements of Skin Friction in a Plane Turbulent Wall Jet," *Journal of the Royal Aeronautical Society,* Vol. 62, Dec. 1958, pp. 873–877.

8 Brown, K. C., and Joubert, P. N., "The Measurement of Skin Friction in Turbulent Boundary Layers with Adverse Pressure Gradients," *Journal of Fluid Mechanics,* Vol. 35, Part 4, 1969, pp. 737–757.

9 Prahlad, T. S., "Yaw Characteristics of Preston Tubes," *AIAA Journal,* Vol. 10, No. 3, Mar. 1972, pp. 357–359.

10 Power, J. L., "Wall Shear Stress and Mean-Velocity Measurements in a Three-Dimensional Turbulent Boundary Layer," Naval Ship Research and Development Center, Report 4056, Sept. 1973 (available at AD 768297).

11 Preston, J. H., "The Determination of Turbulent Skin Friction by Means of Pitot Tubes," *Journal of the Royal Aeronautical Society,* Vol. 58, Feb. 1954, pp. 109–121.

12 Head, M. R., and Rechenberg, I., "The Preston Tube as a Means of Measuring Skin Friction," *Journal of Fluid Mechanics,* Vol. 14, Part 1, 14, Part 1, 1962, pp. 1–17.

13 Ferriss, D. H., "Preston Tube Measurements in Turbulent Boundary Layers and Fully Developed Pipe Flow," A.R.C. 26 678, 1965 (available as AD 479412).

14 Smith, D. W., and Walker, J. H., "Skin-Friction Measurements in Incompressible Flow," NACA TN 4231, Mar. 1958.

15 Staff of the N.P.L., "On the Measurement of Local Surface Friction on a Flat Plate by Means of Preston Tubes," N.P.L. Report No. 3185, May 1958.

16 Bertelrud, A., "Preston Tube Calibration Accuracy," *AIAA Journal,* Vol. 14, No. 1, Jan. 1976, pp. 98–100.

17 Head, M. R., and Ram, V. V., "Simplified Presentation of Preston Tube Calibration," *Aeronautical Quarterly,* Vol. 22, Part 3, Aug. 1971, pp. 295–300.

18 Patel, V. C., "Calibration of the Preston Tube and Limitations on Its Use in Pressure Gradients," *Journal of Fluid Mechanics,* Vol. 23, Part 1, 1965, pp. 185–208.

19 Miller, B. L. P., "The Measurement of Wall Shearing Stress in Turbulent Boundary Layers," Ph.D. thesis, University of Leicester, Great Britain, Aug. 1972.

20 Tennant, M. H., Pierce, F. J., and McAllister, J. E., "An Omnidirectional Wall Shear Meter," ASME JOURNAL OF FLUIDS ENGINEERING, Vol. 102, Mar. 1980, pp. 21–25.

21 Kline, S. J., and McClintock, F. A., "Describing Uncertainties in Single-Sample Experiments," *Mechanical Engineering,* Jan. 1953, pp. 3–8.

22 Bradshaw, P., "The Effect of Wind-Tunnel Screens on Nominally Two-Dimensional Boundary Layers," *Journal of Fluid Mechanics,* Vol. 22, 1965, pp. 679–687.

23 Furuya, Y., and Osaka, H., "The Spanwise Non-Uniformity of Nominally Two-Dimensional Turbulent Boundary Layer (1st Report Characteristics of Spanwise Velocity Distribution)," *Bulletin of the Japan Society of Mechanical Engineers,* Vol. 18, 1975, pp. 664–672.

24 Furuya, Y., Nakamura, I., Osaka, H., and Honda, H., "The Spanwise Non-Uniformity of Nominally Two-Dimensional Turbulent Boundary Layer (2nd Report Wall Shear Stress and Flow Field)," *Bulletin of the Japan Society of Mechanical Engineers,* Vol. 18, 1975, pp. 673–680.

25 deBray, B. G., "Some Investigations into the Spanwise Non-Uniformities of Nominally Two-Dimensional Incompressible Boundary Layers Downstream of Gauge Screens," ARC R&M3578, 1967.

26 Favre, A., and Gaviglio, J., "Turbulence et Perturbations dans la Couche Limite d'une Plaque Plane," AGARD Report 278, Apr. 1960.

27 Carnahan, B., Luther, H. A., and Wilkes, J. O., *Applied Numerical Methods,* Wiley, 1969, p. 577.

28 Frei, D., and Thomann, H., "Direct Measurements of Skin Friction in a Turbulent Boundary Layer with a Strong Adverse Pressure Gradient," *Journal of Fluid Mechanics,* Vol. 101, Part 1, 1980, pp. 79–95.

B. G. Shivaprasad
Visiting Assistant Professor.

R. L. Simpson
Professor of Mechanical Engineering.

Southern Methodist University,
Dallas, Texas 75275

Evaluation of a Wall-Flow Direction Probe for Measurements in Separated Flows

The upstream-downstream flow direction intermittency γ_{pu} is an important parameter that can quantitatively describe the stages of flow separation. This paper gives an improved design for a wall-flow-direction probe. Intermittency measurements made using this modified probe show agreement within experimental uncertainties with direct measurements made using a LDV, although both the unmodified and modified probe designs produce results that are consistently higher than those for the LDV.

Introduction

Separation is a commonly observed phenomenon that has eluded a clear and general description. Recently [1] a well-defined terminology was proposed. "Separation" must mean the entire process of "departure" or "breakway" or the breakdown of a boundary-layer flow. An abrupt thickening of the rotational flow region next to a wall and significant values of the normal-to-wall velocity component must accompany breakway, else this region will not have any significant interaction with the freestream flow.

A set of quantitative definitions on the detachment state near the wall were proposed for two-dimensional mean flows [1]: *incipient detachment* occurs with instantaneous backflow 1 percent of the time; *intermittent transitory detachment* occurs with instantaneous backflow 20 percent of the time; *transitory detachment* occurs with instantaneous backflow 50 percent of the time; and *detachment* occurs where $\bar{\tau}_W = 0$. Thus, γ_{pu}, the fraction of time the flow moves in a downstream direction, is a descriptive parameter for identifying these stages and should be documented in all separated flow experiments.

Although the LDV is a versatile technique for separated flow measurements, a simpler and less expensive technique using hot-wire sensors can be used to measure γ_{pu}. Rubesin et al. [2] demonstrated that the wake from a heater wire can heat either an upstream or downstream hot-wire sensor to determine the flow direction. Later Eaton et al. [3] developed this "thermal tuft" technique and built electronic circuitry for making use of this probe for the measurement of γ_{pu} in separated flows behind a backward facing step and diffuser. Ashjaee and Johnston [4] made extensive use of this probe in their transitory stall studies in diffusers. Since the thermal tuft provides continuous signals rather than discrete signals as provided by the L.D.V., it is more suited for measurements in unsteady flow where signal averaging is required for each phase of a flow cycle.

None of these early investigations compared thermal tuft measurements of γ_{pu} with values deduced from a LDV. One purpose of this paper is to present such comparisons. Another purpose is to present test results for a modified thermal tuft design that eliminates the insensitivity of the earlier designs to crossflows.

Modified Probe Design

The configuration of the sensors and heater wires is shown in Fig. 1. Sensor-1 detects flow moving downstream and sensor-2 detects the upstream flow. The lines joining the ends of the central heater wire to the sensor wire tips form the boundaries of regions with an included angle of 45.2 deg shown on either side of the streamwise axis. Any crossflow

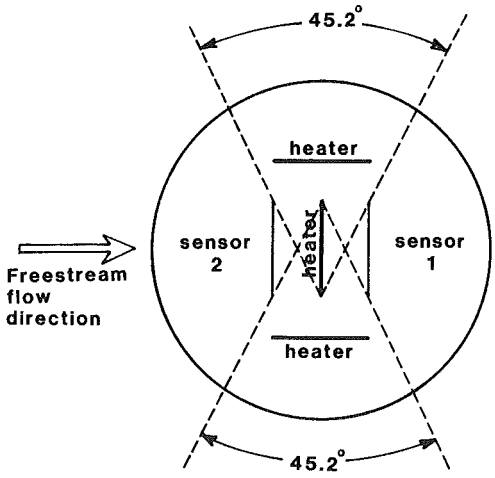

Fig. 1 Schematic planview of the modified "thermal tuft" or downstream-upstream flow direction intermittency probe. Sensors and central heater are 6 mm long 2.5 mm apart; 5 mm long side heaters are 2.5 mm from end of sensors.

Contributed by the Fluids Engineering Division for publication in the JOURNAL OF FLUIDS ENGINEERING. Manuscript received by the Fluids Engineering Division, March 25, 1981.

remaining in these regions and passing over the central heater wire will miss the sensor wires. Thus a probe containing only the central heater wire fails to sense crossflows occurring over a total angle of 90 deg. Significant instantaneous crossflows occur in detached flows, so γ_{pu} measurements with such a probe are erroneous to some extent. The present design eliminates this drawback with the additional use of the two side heater wires shown in Fig. 1.

The probe consists essentially of three heater wires of chromel, 0.254 mm in diameter, silver-soldered to the tips of silver-plated copper prongs of 0.81 mm diameter and two 0.025 mm diameter platinum-10 percent rhodium sensor wires, soldered to the tips of gold-plated copper prongs of 0.45 mm diameter to form the configuration shown in Fig. 1. All the prongs were passed through holes drilled in a plexiglas cylindrical plug and then glued to its inner surface. The heights of the prongs above the surface of the plug were adjusted such that the centers of all the wires lie in a single plane parallel to and 1.22 mm above the surface of the plug.

Similar to the pulse-wire anemometer probe of Bradbury and Castro [5], for good sensitivity the heater wires of thermal tuft must be sufficiently far from the sensor wires so that thermal conduction within the fluid is small compared to convection at low velocities. Bradbury and Castro found that the Peclet number based on the lowest fluid velocity to be detected and the distance between heater and sensor wires should be greater than 50 for good sensitivity to the velocity. In the present design and that of Eaton et al., the closest spacing between heater and sensor wires is 2.5 mm. Thus for a Peclet number of 50, these designs have good sensitivity of the direction of fluid motions greater than 1/2 ms^{-1}. With less sensitivity, the thermal tuft can also detect the direction of smaller flow velocities, since it only needs some difference between sensor wire temperatures for proper operation.

Test Flow and Instrumentation

The probe was tested in steady and unsteady mean two-dimensional separated turbulent shear flows produced by adverse pressure gradients. The separated flow was located on the lower wall of the diverging portion of a constant width, varying height, converging-diverging channel, 4.9 meters long. There was active boundary layer control on the side and top walls. The mean velocity at the throat was maintained constant for both the flows at approximately 22 mps with a momentum thickness Reynolds number of approximately 2600 for both cases. Detailed descriptions of this wind tunnel and LDV hot-wire anemometer measurements on these flow are given by Simpson et al. [6, 7]. Aluminum bushings for the interchangeable plexiglas probe and dummy plugs were fixed in the bottom test wall of the tunnel at the required measuring locations to produce a smooth flush surface.

The instrumentation essentially consisted of a flow direction detector and a true integrating voltmeter. The electronic circuit design of the flow direction detector is the one used by Eaton et al. [3]. The reference voltage E_{ref} to the detector was from a highly stable d-c power supply (Hewlett Packard Model 6213A) and was approximately 5 volts. The two sensors were connected to the input stage of the detector which is essentially a Wheatstone bridge network. By keeping the wires taut while soldering, the sensor resistances were kept within 0.1 ohm of one another at approximately 2.3 ohms.

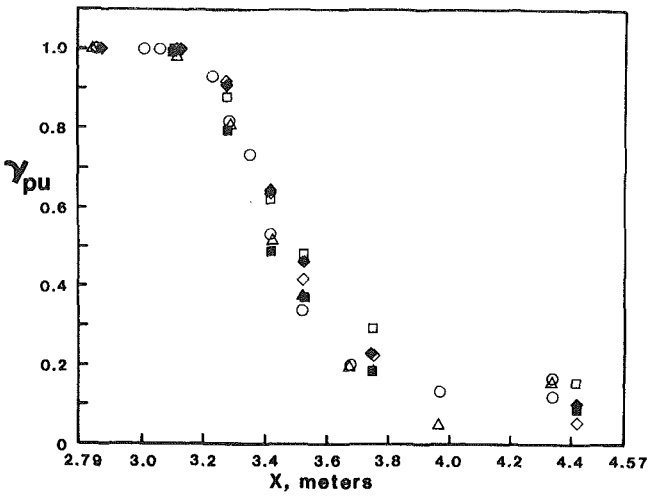

Fig. 2 Fraction of time that the flow 1.2 from the wall is in the downstream direction: ○, LDV direct measurement; △, LDV U and u′ measurements and equation (2). Thermal tuft without side heaters: □, orientation 1; ■, reversed or orientation 2. Thermal tuft with side heaters: ◇, orientation 1; ◆, reversed or orientation 2.

To adjust for this small difference in sensor resistances the probe was mounted in the flow with the heater current turned off and an input offset adjusting potentiometer was turned till the output signal fluctuated between zero and the reference voltage. The measured γ_{pu} values were not very sensitive to this adjustment. In fact, adjusting this potentiometer to obtain always either zero or the reference voltage for the output signal produced only a change within ± 0.02 in the γ_{pu} values.

During measurements the 3 amps heater current supplied by a battery charger produced a total heat dissipation of 2 watts. This heater current was much higher than the minimum value at which γ_{pu} ceases to be dependent on the heater current. Also, this large heater current made the γ_{pu} values less sensitive to the input offset resistance adjustment.

The output voltage from the detector was time averaged using a voltage-controlled oscillator and a digital counter. γ_{pu} was then computed using the equation

$$\gamma_{pu} = \frac{E - E_0}{E_{ref} - E_0} \tag{1}$$

where E_{ref} and E_0 are the voltages corresponding to forward and back flow, respectively, and E is the average voltage measured by the true integrating voltmeter.

A single point uncertainty analysis of γ_{pu} using the method of Kline and McClintock [8] yielded a value of $\pm$ 0.06 at 20:1 odds and includes the ± 4 deg uncertainty in the visual alignment of the probe with the freestream direction. For the directly measured LDV values for γ_{pu}, Simpson et al. [6] give an expression, $\pm 0.1 \exp(-U^2/2u'^2)$, for computing its uncertainty. This expression yields uncertainties in the range of ± 0.07 to ± 0.1 for all the streamwise locations where the data are presented.

Experimental Results

Data were obtained with the modified three-heater-wire

Nomenclature

E = time-averaged voltage from detector
E_{ref}, E_0 = high and low voltages from detector
U = streamwise mean velocity
u' = RMS streamwise fluctuation
γ_{pu} = fraction of time flow moves in downstream direction
$\bar{\gamma}_{pu}$ = time-averaged γ_{pu} over an unsteady flow cycle
$\hat{\gamma}_{pu}$ = phase-averaged γ_{pu} for an unsteady flow cycle
γ_{pw} = fraction of time the flow moves in the spanwise direction

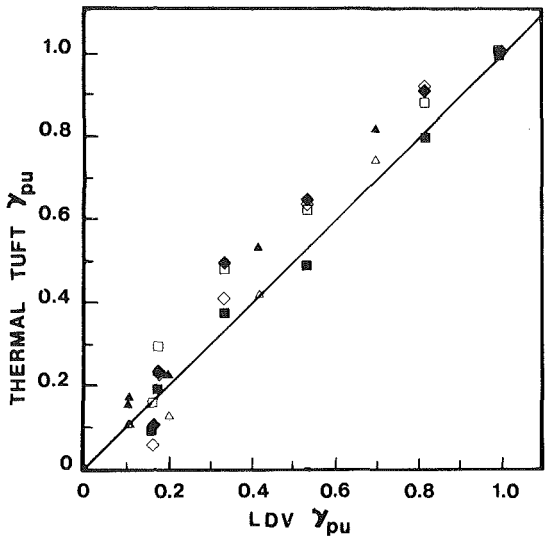

Fig. 3 Comparison of thermal tuft and LDV results for γ_{pu}. Steady flow, thermal tuft without side heaters: □, orientation 1; ■, orientation 2. Steady flow, thermal tuft with side heaters: ◇, orientation 1; ◆, orientation 2. Unsteady flow with side heaters: △, orientation 1; ▲, orientation 2.

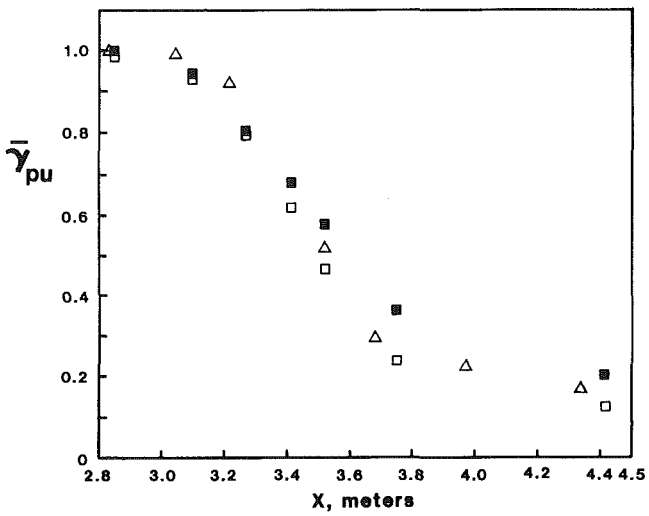

Fig. 4 Distribution of the cycle-averaged mean value of γ_{pu} or $\bar{\gamma}_{pu}$ for the unsteady flow. Thermal tuft: □, orientation 1; ■, orientation 2. △, LDV U and u' measurements and equation (2).

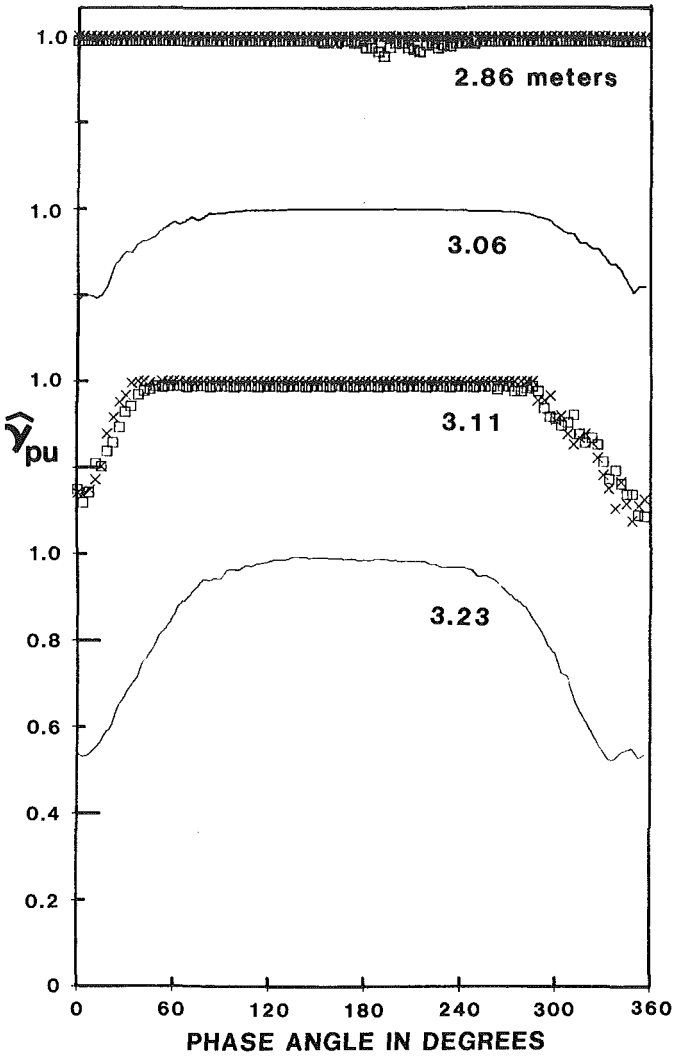

Fig. 5 $\hat{\gamma}_{pu}$ or phase-averaged γ_{pu} for the sinusoidally varying freestream velocity flow of Simpson et al. [7]. Thermal tuft: □, orientation 1; x, orientation 2. Solid line obtained from phase-averaged U and u' LDV measurements and equation (2). Note displaced ordinates.

design described above. Other data were obtained with the side heater wires disconnected so that the probe behaved like the unmodified design of earlier investigations. Figure 2 gives a comparison of the distributions of γ_{pu} obtained using the intermittency probe and the LDV for the steady flow. There are two types of γ_{pu} data obtained from the LDV measurements. One from a direct measurement of the fraction of time that the flow moves downstream and the other computed by using values of the mean velocity U and the rms value of the turbulent fluctuations u'. This computation uses the relation given by Simpson [8]

$$\gamma_{pu} = \frac{1}{2}\left[1 + \text{erf}\left(\frac{U}{\sqrt{2}u'}\right)\right] \tag{2}$$

that is derived from a Gaussian velocity probability distribution. In that work, he obtained good agreement between the directly measured values of γ_{pu} with an LDV and those obtained using equation (2). The two types of LDV results for the present steady flow also show a reasonable agreement. The uncertainty of γ_{pu} obtained from equation (2) is ± 0.03 at 20:1 odds.

Thermal tuft data were always taken for two possible orientations of the probe by turning it through 180 deg. The difference in results is due to slight imbalances in the detection circuit and the possible asymmetry in the construction of the probe. It can be seen that when using three heater wires the agreement between the data for the two orientations is within the limits of uncertainty. When using the unmodified one heater wire design the data for the two orientations also agree within the limits of uncertainty at all locations except one. However, the difference at most of the locations is larger than for the modified design with three heater wires since during the time crossflows are present, the output randomly indicates forward or backward flow. The possibility of the result being inaccurate depends on the duration of time that crossflows occur within the two 45.2 deg angles shown in Fig. 1. For the present flow, the good agreement between the LDV data and the data obtained with one heater wire only suggests that there is little crossflow present, but does not contradict the theoretical usefulness of side heaters in flows with larger crossflows.

Figure 3 shows that γ_{pu} values from the thermal tuft are consistently 0.05 to 0.1 higher than the LDV data for values

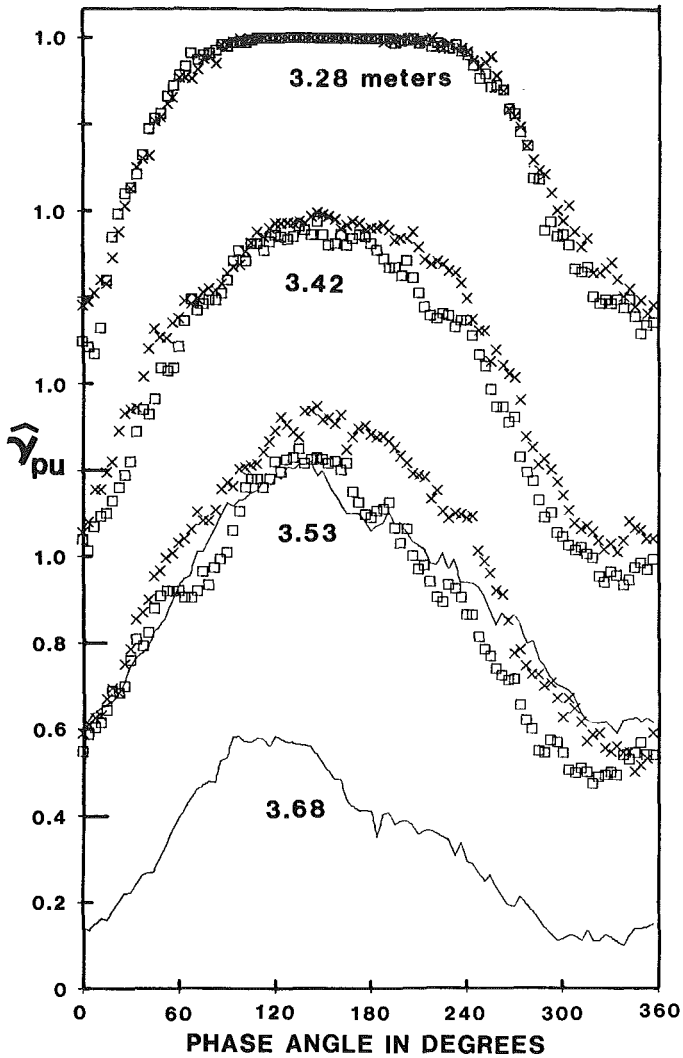

Fig. 6 $\hat{\gamma}_{pu}$ or phase-averaged γ_{pu} for the sinusoidally varying freestream velocity flow of Simpson et al. [7]. Thermal tuft: □, orientation 1; x, orientation 2. Solid line obtained from phase-averaged U and u' LDV measurements and equation (2). Note displaced ordinates.

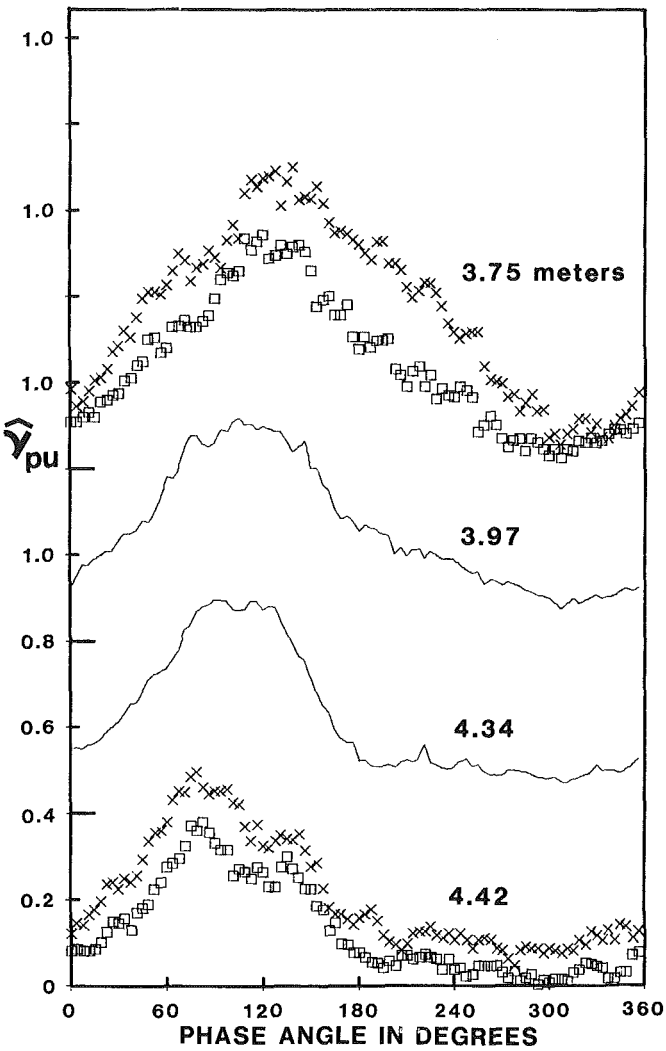

Fig. 7 $\hat{\gamma}_{pu}$ or phase-averaged γ_{pu} for the sinusodially varying freestream velocity flow of Simpson et al. [7]. Thermal tuft: □, orientation 1; x, orientation 2. Solid line obtained from phase-averaged U and u' LDV measurements and equation (2). Note displaced ordinates.

not near zero or unity. This difference can be explained qualitatively. The portions of the flow that move in the downstream direction have a higher velocity on the average than the portions of the flow that move in the upstream direction [6]. This means that flow in the downstream direction moves more quickly over the probe and can change the sensed flow direction quicker than the reversed flow. In other words, during the times which the flow changes direction the signal tends to be biased in favor of the downstream flow direction. For γ_{pu} values near zero or unity, there are less frequent changes in the flow direction and the LDV and thermal tuft values are in better agreement. Nevertheless, the agreement within the estimated uncertainty limits between the directly measured LDV data and the data from the modified probe provides a direct check of this measurement technique for the first time.

Figure 4 gives the distributions of the mean value of γ_{pu} ($\bar{\gamma}_{pu}$) for the 0.6 Hz periodic unsteady separating flow [7] obtained using the modified probe and those computed from equation (2) using the U and u' values obtained from LDV. Figures 5–7 give similar distributions for the phase-averaged values of γ_{pu}, ($\hat{\gamma}_{pu}$). The phase averaging was done over 200 cycles of the free-stream velocity variation, which Simpson et al. [7] showed to be sufficiently large. In all the figures the data obtained from the two orientations agree within the limits of uncertainty. At the 2.86 meters and 3.53 meters locations from the test wall leading edge, the phase-averaged distributions of γ_{pu} show good agreement between the two measurement methods, while at other stations where only the trends can be compared they do seem to agree well. This suggests that the thermal tuft can be used to measure phase-averaged values of γ_{pu} within the uncertainty and bias mentioned above.

Comments on the Measurement of Spanwise Intermittency

Some measurements of the spanwise intermittency, γ_{pw}, or the fraction of time that the flow moves in the spanwise direction, were also made with this probe with the sensor wires parallel to the mainstream flow directions. However, the results only indicated the high sensitivity of the γ_{pw} values to the asymmetry in the construction of the probe. γ_{pw} values obtained for orientation 2 were always higher, the disparity increasing as one moves upstream. In fact, γ_{pu} also showed higher values for orientation 2 almost everywhere, but the disparity was well within the limits of uncertainty. This could be attributed to the nonuniform heating along the length of the side heaters. The disparity between the intermittency obtained for the two orientations was particularly high for the γ_{pw} measurements, because during those measurements the

side heaters that were perpendicular to the mainstream flow direction were principally cooled by flow in that direction. For this reason the disparity was greater at the upstream locations than the downstream ones, because the crossflows were smaller and the flow along the streamwise direction was higher. Thus the measurement of γ_{pw} seems to be much more difficult and involves a careful and precise construction of the probe.

Conclusions

The modified design of the wall-flow-direction probe presented here uses additional heater wires to make it more sensitive to crossflows. Results obtained with this probe are in agreement within experimental uncertainties with direct measurements of upstream-downstream intermittency obtained with a LDV and provide support for the use of this probe in detecting flow reversals. However, for γ_{pu} values not near zero or unity, the thermal tuft produces values that are 0.05 to 0.1 higher than the LDV values. Also, the use of this probe for measuring the flow direction intermittency in the spanwise direction where the velocities are small seems to be possible only with a careful construction of the probe.

This flow-direction probe is insensitive to the flow direction when the thermal wakes of the heaters do not pass over the sensor wires. Larger or more heater wires could be used to partially alleviate this problem but more flow interference would undoubtedly result. In trying to optimize the probe configuration for a given application, the size of the thermal wakes and the spacing between wires should be selected to minimize periods of flow-direction insensitivity.

Acknowledgments

This work was supported by the Experimental Fluid Dynamics Branch of NASA-Ames under Grant NSG-2354.

References

1 Simpson, R. L., "A Review of Some Phenomena in Turbulent Flow Separation," ASME JOURNAL OF FLUIDS ENGINEERING, Vol. 103, Dec. 1981.

2 Rubesin, M. W., Okuno, A. F., Mateer, G. G., and Brosh, A. "A Hot-Wire Surface Gage for Skin Friction and Separation Detection Measurements," NASA TM X-62, 465, 1975.

3 Eaton, J. K., Jeans, A. H., Ashjaee, J., and Johnston, J. P. "A Wall-Flow-Direction Probe for Use in Separating and Reattaching Flows." ASME JOURNAL OF FLUIDS ENGINEERING, Vol. 101, 1979, pp. 364-366.

4 Ashjaee, J., and Johnston, J. P. "Straight Walled Two-Dimensional Diffusers-Transitory Stall and Peak Pressure Recovery," ASME JOURNAL OF FLUIDS ENGINEERING, Vol. 102, 1980, pp. 275-282.

5 Bradbury, L. J. S., and Castro, I. P. "A Pulsed Wire Technique for Velocity Measurements in Highly Turbulent Flow," *J. Fluid Mechanics*, Vol. 49, 1971, pp. 657-691.

6 Simpson, R. L., Chew, Y.-T., and Shivaprasad, B. G. "The Structure of a Separating Turbulent Boundary Layer," *J. Fluid Mechanics*, Vol. 113, 1981, pp. 23-73.

7 Simpson, R. L., Chew, Y.-T., and Shivaprasad, B. G. "Measurements of Unsteady Turbulent Boundary Layers with Pressure Gradients," Department of Civil and Mechanical Engineering Report WT-6, Southern Methodist University, 1980; submitted to *J. Fluid Mechanics*.

8 Kline, S. J., and McClintock, F. A. "Describing Uncertainties in Single Sample Experiments," *Mechanical Engineering*, Vol. 75, 1953, pp. 3-8.

9 Simpson, R. L., "Interpreting Laser and Hot-Film Anemometer Singles in a Separating Boundary Layer," *AIAA Journal*, Vol. 14, 1976, pp. 124-126.

K. R. Sreenivasan
Applied Mechanics,
Mason Laboratory,
Yale University,
New Haven, CT 06520

R. Narasimha
Department of Aeronautical Engineering,
Indian Institute of Science,
Bangalore, India

Equilibrium Parameters for Two-Dimensional Turbulent Wakes

The parameters characterizing a plane turbulent wake in its equilibrium state of development are determined through careful experiment and analysis.

1 Introduction

It is useful to consider the development of two-dimensional turbulent wakes in terms of the parameters

$$\Delta \equiv \delta(x\theta)^{-1/2} \tag{1}$$

and

$$W \equiv (w_0/U)\,(x/\theta)^{1/2} \tag{2}$$

defined by Narasimha and Prabhu [1]. (The notation is explained in the inset to Fig. 1: θ is the momentum thickness, see equation (3) below.) It is expected that in the limit of small defect ratios $w_0/U \to 0$, the above two parameters tend asymptotically to certain constant values, say Δ^* and W^*, which are universal numbers characteristic of the plane equilibrium wake. (Following [1], we define an equilibrium wake as one in which the mean velocity and turbulent stresses exhibit similarity with *identical* length and velocity scales.)

As experiments can only be conducted at finite w_0/U, it is clear that an accurate determination of Δ^* and W^* may call for extrapolation of measured data to the limit $w_0/U = 0$. Because it was incidental to their work, Narasimha and Prabhu [1] did not attempt such an extrapolation; a preliminary estimate suggested that the numbers quoted by them may require a correction whose magnitude could not be assessed because the measurements were not sufficiently extensive. Other data on wakes, surveyed elsewhere [2, 3] do not permit a definitive determination of the parameters, because of too much scatter or two-dimensional momentum imbalance, or because w_0/U was not sufficiently small. It was therefore thought worthwhile to conduct carefully a new series of experiments with the sole objective of obtaining reliable values for Δ^* and W^*. The primary objective of this work is thus the accurate determination of the equilibrium wake parameters Δ^* and W^* through independent measurements and analysis.

2 The Experiments

Measurements were made in an open-circuit suction-type wind tunnel with a contraction ratio of about 10, and a test-section of about 30 cm square and 4.27 m long. Less than 1.5 percent variation in wind speed along the test section was attained by applying suitable divergence for the boundary layer growth. More details of the wind tunnel can be found in [4]. A two-dimensional wake was created behind a twin plate configuration (see inset to Fig. 1) at a freestream velocity of 21.3 ms^{-1}. The freestream turbulence level at this speed was about 0.15 percent.

It was determined that in the region of measurement the wake was in equilibrium. Although it is known ([3]; [5], Chapter 7) that the wake behind a circular cylinder requires a streamwise distance of as much as 1000 diameters to attain the equilibrium state, the twin-plate wake generator used here seems to be efficient in producing equilibrium wake in much shorter distances (of the order of 200 θ). Detailed measurements [4] of the root-mean-square streamwise and normal velocity fluctuations, as well as of the Reynolds shear stress, confirm this conclusion.

All mean velocity measurements were made with a pitot-static tube. Constant current hot-wire measurements wtih adequate frequency compensation showed that the maximum value of u'/U (where u' is the root-mean-square streamwise velocity fluctuation) ranged from about 4 percent at the closest measuring station ($x/\theta \simeq 130$) to about 1.6 percent at

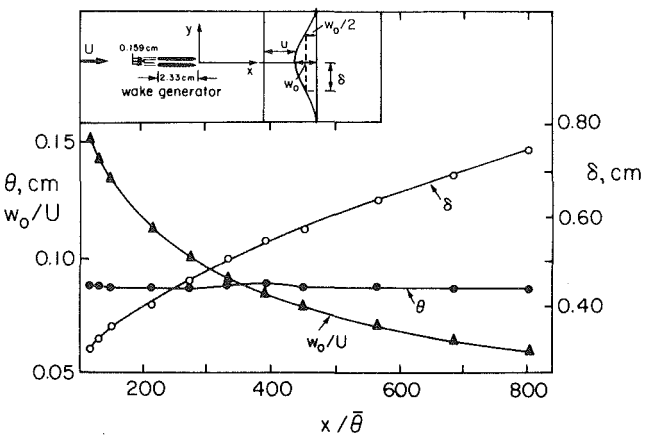

Fig. 1 Variation with the streamwise distance of the center-line wake-defect ratio w_0/U (▲), momentum thickness θ (•) and the half-defect thickness δ (o). The inset shows the wake generator and describes the notation. Average momentum thickness $\bar{\theta}$ = 0.874 mm.

Contributed by the Fluids Engineering Division for publication in the JOURNAL OF FLUIDS ENGINEERING. Manuscript received by the Fluids Engineering Division, January 26, 1981.

the farthest measuring station ($x/\theta \simeq 810$). No corrections possibly necessitated by these turbulence levels were attempted for the pitot-static measurements; simple estimates with the use of Bernoulli's equation were not higher than about 0.4 percent. The wake profiles were found to be very closely symmetric, but all parameters were evaluated using the complete velocity profile rather than one half of it.

The data on the normalized centerline wake defect w_0/U and the wake half-thickness δ are shown plotted in Fig. 1. Also shown is the momentum thickness θ evaluated here as

$$\theta = \int_{-\infty}^{+\infty} \frac{u}{U}\left(1-\frac{u}{U}\right)dy = \int_{-\infty}^{+\infty} \frac{w}{U}\left(1-\frac{w}{U}\right)dy, \qquad (3)$$

$w(y)$ being the defect velocity distribution. It is seen that θ is a constant to within ± 1 percent (except at $x = 35.08$ cm, where the departure from the mean is 1.7 percent). The mean value $\bar{\theta}$ of θ is 0.874 mm (with a standard deviation of 0.007 mm). There is therefore no need to make any convergence corrections of the type described by Prabhu and Narasimha [6].

For the analysis to be made in Section 3, we shall need the parameters I_1 and I_2, where

$$I_n = \int_{-\infty}^{+\infty} (w/w_0)^n d(y/\delta), n = 1, 2. \qquad (4)$$

The values of I_1 and I_2 obtained from measured velocity profiles at various stations are shown in the upper part of Fig. 2. There is no discernible trend with w_0/U over the range covered in the experiments; this result is to be expected if the defect velocity profiles show similarity. The mean values and the 95 percent confidence intervals are:

$$I_1 = 2.061 \pm 0.010, \; I_2 = 1.505 \pm 0.020. \qquad (5)$$

3 Analysis

From equation (3) and the definitions of I_1 and I_2, it follows that

$$(W\Delta)^{-1} = U\theta/w_0\delta = I_1 - (w_0/U)I_2. \qquad (6)$$

Measured values of the quantity $U\theta/w_0\delta$, also plotted against w_0/U in Fig. 2, follow equation (6) (with I_1, I_2 from equation (5)) quite closely. This result is, of course, not surprising, because it serves only to confirm the well-known fact that wake-defect velocity profiles are indeed self-similar to a very good approximation as long as w_0/U is not large.

The self-preserving solution for the development of a shallow (i.e., linear) plane constant-pressure wake may be written [1] as

$$\frac{U^2\delta^2}{M^2} = \frac{1}{U^2 w_0^2} = \frac{2K_1}{M}\frac{x}{U} + K_2, \qquad (7)$$

where K_1 and K_2 are constants and

$$M = U^2 w_0 \delta = U^3 (w_0\delta/U\theta)\theta. \qquad (8)$$

Substituting for M from equation (8), dividing throughout by x and noting from equation (6) that in the limit of vanishing defect $U\theta/w_0\delta \to I_1$, equation (7) can be reduced to asymptotic statements of the form

$$\Delta \equiv \delta(x\theta)^{-1/2} = \Delta^* + o(1), \qquad (9)$$

$$W \equiv (w_0/U)(x/\theta)^{1/2} = W^* + o(1). \qquad (10)$$

It is not possible to estimate precisely the $o(1)$ terms in equations (9) and (10) on the basis of linear theory alone. However, equation (6) suggests that we should expect corrections of $O(w_0/U)$; Townsend ([5], p. 137) has argued, on the basis of the energy equation, that a term of $O(x^{1/2})$ should appear on the right of equation (7), which implies a term of $O(w_0/U)$ on the right of equations (9) and (10). It is therefore a reasonable assumption to put

$$\Delta = \Delta^* + \alpha(w_0/U) + o(w_0/U), \qquad (11)$$

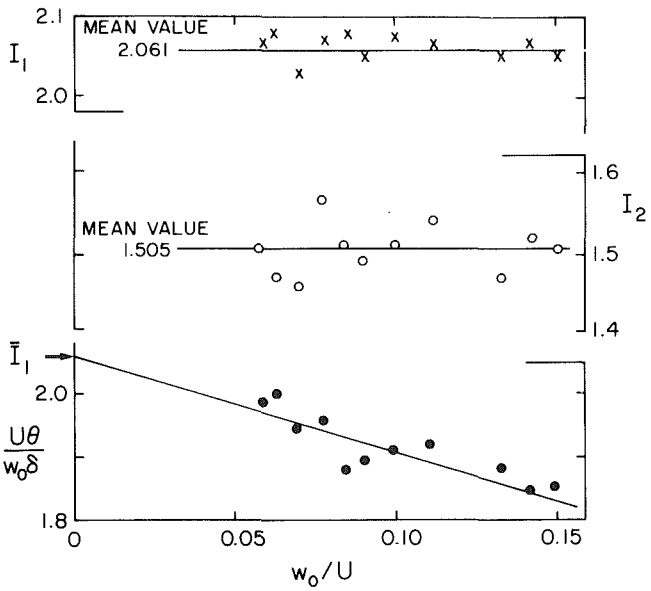

Fig. 2 Variation of the flow parameters I_1, I_2, and $U\theta/w_0\delta$ with the wake-defect ratio. The mean values of I_1 and I_2 are 2.061 and 1.505, respectively. The straight line in the lowermost part of the figure is given by $I_1 - I_2(w_0/U)$, with $I_1 = 2.061$ and $I_2 = 1.505$.

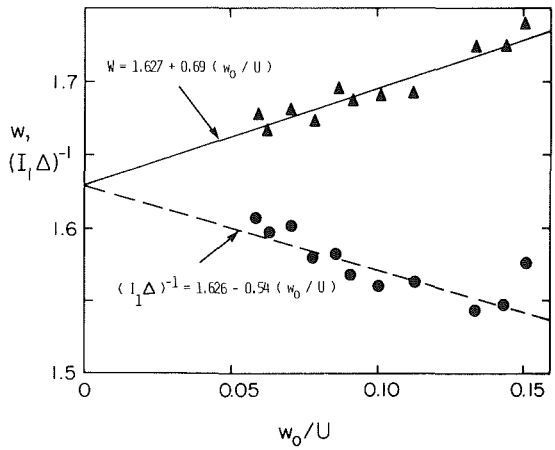

Fig. 3 Variation of the measured quantities W (▲) and $(I_1\Delta)^{-1}$ (•) with the wake defect ratio. ——, $W = 1.627 + 0.69\,(w_0/U)$; – –, $(I_1\Delta)^{-1} = 1.626 - 0.54\,(w_0/U)$.

$$W = W^* + \beta(w_0/U) + o(w_0/U), \qquad (12)$$

where α and β are some constants. It follows from equations (11) and (12) that

$$(W\Delta)^{-1} = (W^*\Delta^*)^{-1}[1 - (\alpha/\Delta^* + \beta/W^*)w_0/U] + o(w_0/U), \qquad (13)$$

and from comparison with equation (6) that

$$(W^*\Delta^*)^{-1} = I_1, \qquad (14)$$

$$\alpha/\Delta^* + \beta/W^* = I_2/I_1. \qquad (15)$$

For later convenience, we also note that

$$(I_1\Delta)^{-1} = W^* - \alpha(W^*/\Delta^*)(w_0/U) + o(w_0/U). \qquad (16)$$

As experiments give us I_1 and I_2 and a series of data points for $W(x)$ and $\Delta(x)$, we can determine the four parameters W*, Δ^*, α and β, by making a best fit of equations (11) and (12) or equivalently of equations (16) and (12) to the experimental data. This leaves equations (14) and (15) to be used as checks. Between them, equations (12), (14), (15), and (16) provide such strong constraints and checks that the parameters can be determined to a very good accuracy.

Figure 3 shows W and $(I_1\Delta)^{-1}$ plotted against w_0/U.

According to equations (12) and (16), these data should lie on straight lines intersecting on the axis $w_0/U = 0$, with the common intercept equal to W^*. This feature is the obvious advantage of using equation (16) instead of equation (11). Linear regression analysis gives

$$W = 1.627 + 0.688\ (w_0/U) \tag{17}$$

and

$$(I_1\Delta)^{-1} \simeq 1.626 - 0.542(w_0/U); \tag{18}$$

from equations (18) and (5), it follows that

$$\Delta \simeq 0.298 + 0.099(w_0/U). \tag{19}$$

As expected, the intercepts of equations (17) and (18) on the (w_0/U) axis are both practically the same, lending great force to the present analysis.

As further checks on accuracy (see equations (14) and (15)), we see from equations (17)-(19) that

$$(W^*\Delta^*)^{-1} \simeq 2.063, \tag{20}$$

in excellent agreement with the mean value from direct measurements of I_1. Similarly,

$$\frac{\alpha}{\Delta^*} + \frac{\beta}{W^*} \simeq 0.755, \tag{21}$$

which agrees with the ratio $I_2/I_1 \simeq 0.73$ to within about 3½ percent.

4 Discussion and Conclusion

It may be considered that the discrepancy of 3½ percent in this last consistency check is too large, considering the precision with which the equilibrium parameters have been deduced earlier in Section 3. However, there is a relatively large uncertainty associated with the numerical values of α and β because they show nontrivial sensitivity to small perturbations in the measured wake parameters. Thus, the numerical values of α and β are not as reliable as those of I_1, I_2, W^*, and Δ^*; on the other hand, the accuracy of W^* and Δ^* is adequately proved by the check concerning $(W^*\Delta^*)^{-1}$. However, in view of the other uncertainties such as possible errors due to finite turbulence level in pitot-static tube measurements, etc., it is considered that the equilibrium wake parameters (except perhaps I_1) cannot here be quoted to an accuracy better than about 1 in 100. The best estimates from the present measurements and analysis therefore are:

$$\Delta^* = 0.30 \pm 0.005, W^* = 1.63 \pm 0.02,$$

$$I_1 = 2.06 \pm 0.01, I_2 = 1.51 \pm 0.02.$$

In each case, the error estimates correspond to 95 percent confidence intervals.

These values are quite close to the values[1] quoted by Narasimha and Prabhu [1] ($\Delta^* = 0.298$, $W^* = 1.595$, $I_1 = 2.05$, and $I_2 = 1.50$). In the sense that the wakes of Narasimha and Prabhu [1] had finite defect, this close agreement may be somewhat of a coincidence. Nevertheless, the contribution of this note has not been in giving new values for equilibrium parameters but in confirming, through careful analysis and experiment, the suggestion of reference [1].

Acknowledgment

We are indebted to Dr. Prabhu for many useful discussions.

[1] Due to a misprint in [1] the value quoted for W^{*2} appears as 2.34 instead of 2.54.

References

1 Narasimha, R., and Prabhu, A., "Equilibrium and Relaxation in Turbulent Wakes," *Journal of Fluid Mechanics*, Vol. 54, 1972, pp. 1-17.

2 Sreenivasan, K. R., "Data on Constant-Pressure Two-Dimensional Turbulent Wakes," *Rep. 74 FM5*, Department of Aeronautical Engineering, Indian Institute of Science, Bangalore, 1974.

3 Sreenivasan, K. R., "Approach to Self-Preservation in Plane Turbulent Wakes," *A.I.A.A. Journal*, Vol. 19, 1981, pp. 1365-1367.

4 Prabhu, A., "Non-equilibrium Wake Flows," *Ph.D. thesis*, Department of Aeronautical Engineering, Indian Institute of Science, Bangalore, 1971.

5 Townsend, A. A., *The Structure of Turbulent Shear Flow*, 1st ed., University Press, Cambridge, U.K., 1956.

6 Prabhu, A., and Narasimha, R ., "Turbulent Non-Equilibrium Wakes," *Journal of Fluid Mechanics*, Vol. 54, 1972, pp. 19-38.

Laminar Boundary Layer Near the Rotating End Wall of a Confined Vortex

W. J. Shakespeare
Bell Telephone Laboratories,
Holmdel, N.J. 07733

E. K. Levy
Lehigh University,
Bethlehem, Pa.

The results of an experimental and theoretical investigation of the fluid mechanics in a confined vortex are discussed with particular emphasis on behavior away from the axis of symmetry and near the end walls. The vortex is generated in a rotating cylindrical chamber with an exit opening in one end. Both end walls rotate. For the range of flow rates and swirl ratios ($1 \leq S \leq 5$) of interest here, the flow field far from the end walls behaves as inviscid and irrotational; and the end wall boundary layers are thin and laminar. Measurements and calculations of tangential and radial velocity in the end wall region show the development of a secondary flow resulting in a strong velocity "overshoot" in the radial component. Results illustrating the nature of the velocity variations on the end walls are presented; and it is shown that the mass flow rate through the end wall boundary layers, while only a small fraction of the total flow, increases with increasing swirl and with decreasing total flow rate through the chamber.

I Introduction

The geometry of interest is shown in Fig. 1. The chamber has impervious top and bottom end walls which rotate with the porous cylindrical surface. Fluid enters the chamber uniformly in the radial direction, moves inward toward the center line, and flows out through the exit opening in the top end wall.

When a vortex exists with axis perpendicular to a surface, a boundary layer forms to provide a smooth transition from the freestream tangential velocity to the velocity of the surface. The region of reduced tangential velocity near the wall gives rise to an imbalance in centrifugal forces inducing a radially inward movement of fluid near the wall.

Such flow patterns have been the subject of numerous investigations for a confined vortex with both rotating cylindrical walls [1, 2, 3, 4] and tangential fluid injection [7, 8, 9, 10] and for the cases of an infinite rotating fluid over infinite and finite surfaces [11, 12, 13, 14]. The classic illustration of the induced radial velocity near a infinite stationary surface with a fluid in rigid body rotation is given by Boedewadt [16]. In this case a similarity solution is possible. However, it is the more usual situation not to have a self similar flow. For example, Hoffmann [11] has shown that no similarity solutions of the boundary layer equations exist for the case of a potential vortex over a stationary flat surface with a sink on the axis of symmetry.

Investigations of end wall boundary layers in confined vortex flow bearing the closest resemblence to the geometry of interest include experiments by Ying and Chang [2] and Wan and Chang [1] with rotating cylindrical surfaces and stationary end walls, experiments by Kotas [7] in a stationary chamber with tangential fluid injection, and experiments and analysis by Farris et al. [4] with an annular chamber with rotating inner and outer cylinders with one end wall stationary and one rotating. In addition, Hornbeck [9] and Wormley [10] performed analyses for end wall boundary layers in short cylindrical stationary vortex chambers with tangential fluid injection.

This study is concerned with the flow in the end wall boundary layers in a confined vortex with rotating end walls, where the ratio of tangential to radial velocity at the cylindrical wall is of order unity. Aside from the study by Farris et al. [4] for an annular chamber, the authors are not aware of any other investigations which considered the rotating end

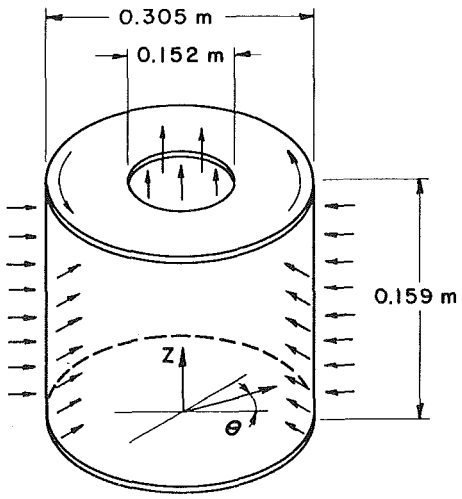

Fig. 1 Confined vortex chamber

Contributed by the Fluids Engineering Division for publication in the JOURNAL OF FLUIDS ENGINEERING. Manuscript received by the Fluids Engineering Division, June 30, 1980.

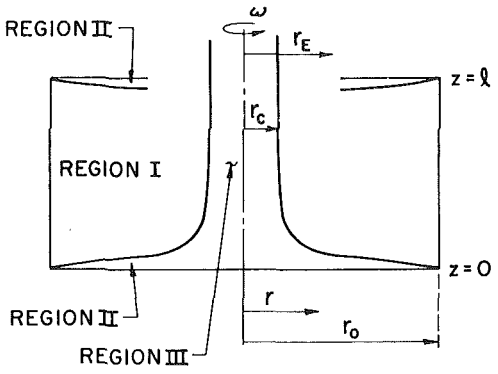

Fig. 2 Regions of the flow

wall case; and for the stationary end wall geometries which have been studied, very few results exist for S near unity.

An interesting review of the confined vortex literature was published by Lewellen in 1971 [15]. In that study, he recommended dividing the flow into three regions as shown in Fig. 2:

(*i*) Main Region (Region I)
(*ii*) End Wall Boundary Layers (Region II)
(*iii*) Viscous Core (Region III)

The emphasis in this paper is on Region II; however, because of coupling between the regions it is also important to understand the general behavior of the other regions. It has been found [5] that the main part of the flow field [Region I] can be adequately described by an inviscid irrotational model subject to the condition that there is a radial position at which the radial velocity is zero. This position marks the boundary of the viscous core, Region III. References [5 and 6] include experimental and theoretical results on the effects of chamber geometry and operating conditions on the dimensions of the viscous core and on the velocity variations in Region I.

Results are presented in this paper on hot fiber anemometer measurements of tangential and radial velocity in the bottom end wall boundary layer region for a range of swirl ratios from 1 to 5 and for values of Re_N of 5×10^3 and 10^4. Solutions of the laminar boundary layer equations using a finite difference approach are obtained, and comparisons are presented between the analysis and experiments.

II Theory

A. Analysis of the Main Flow (Region I). Reference [5] contains a detailed description of experimental and analytical work for Region I in the range of $5 \times 10^3 \leq \mathrm{Re}_N \leq 10^4$ and $1 \leq S \leq 5$. Those results indicate that the flow can be modeled as inviscid and irrotational. Since the Region I flow provides the boundary conditions for Region II, the theoretical approach used is reviewed here.

Assuming the flow in Region I is inviscid and irrotational, the velocity potential ϕ must satisfy the equation

$$\nabla^2 \phi = 0$$

where the velocity vector $\vec{v} = \nabla \phi$. In cylindrical coordinates, this is

$$\frac{1}{r}\frac{\partial}{\partial r}\left(r\frac{\partial \phi}{\partial r}\right) + \frac{1}{r^2}\frac{\partial^2 \phi}{\partial \Theta^2} + \frac{\partial^2 \phi}{\partial z^2} = 0 \tag{1}$$

where the three velocity components are

$$u = \frac{\partial \phi}{\partial r}$$

$$v = \frac{1}{r}\frac{\partial \phi}{\partial \Theta} \tag{2}$$

$$w = \frac{\partial \phi}{\partial z}$$

Letting

$$\phi(r,\Theta,z) = \phi_1(r,z) + \phi_2(\Theta) \tag{3}$$

Equation (1) becomes

$$\frac{1}{r}\frac{\partial}{\partial r}\left(r\frac{\partial \phi_1}{\partial r}\right) + \frac{\partial^2 \phi_1}{\partial z^2} = 0 \tag{4}$$

and

$$\frac{1}{r^2}\frac{\partial^2 \phi_2}{\partial \Theta^2} = 0 \tag{5}$$

Equation (5) was solved by direct integration to yield a free vortex

$$v = \frac{\text{constant}}{r}$$

With the boundary condition

$$v = \omega_0 r_0 \text{ at } r = r_0$$

this becomes

$$v = \frac{\omega_0 r_0^2}{r} \tag{6}$$

Equation (4) was solved numerically using second order finite differences, with mesh size 20×20 in the $r-z$ plane subject to the boundary conditions

$$\phi(r_0,z) = 1$$
$$u(r_c,z) = 0$$

Nomenclature

l = chamber length
$\dot{m}$ = mass flow rate
$\dot{m}_{BL}$ = mass flow rate through end wall boundary layer
$\dot{m}_T$ = total mass flow rate through chamber
Q = volumetric flow rate
p = pressure
P = $p/\rho u_0^2$
r = radial coordinate
R = r/r_0
Re_N = radial Reynolds number, $\rho u_0 r_0/\mu$
Re_T = tangential Reynolds number, $\rho v_0 r_0/\mu$
S = swirl $\frac{v_0}{u_0}$
u = radial velocity
U = $\frac{u}{u_0}$
v = tangential velocity
V = $\frac{v}{u_0}$
w = axial velocity
W = $\frac{w}{u_0}$
z = axial coordinate
Z = $\frac{z}{r_0}$
δ = boundary layer thickness
Θ = Azimuthal coordinate
ϕ = velocity potential
ρ = density
ω = angular velocity of chamber
Δ = dimensionless axial distance used for matching main flow to end wall boundary layer
μ = absolute viscosity

Subscripts

c = core
0 = outer radius of chamber
E = Exit

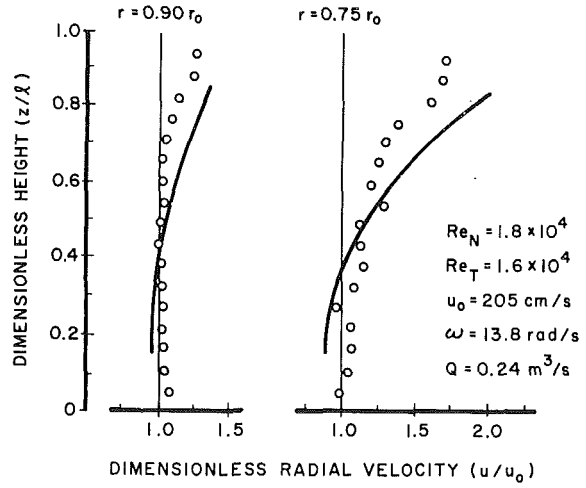

Fig. 3 Radial velocity profiles. $r_0/l = 1$

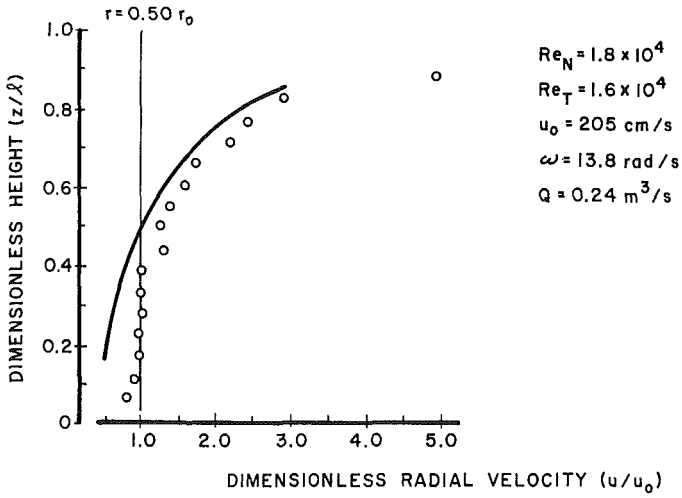

Fig. 4 Radial velocity profiles

$$w(r,0) = 0$$

$$w(r_E < r < r_0, l) = 0$$

$$w(r_c < r < r_E, l) = \frac{\dot{m}}{\rho\pi[r_E^2 - r_c^2]}$$

The core size, r_c, used in the analysis was based on measured exit plane velocity profiles. A complete description of these measurements is contained in reference [6]. However, the calculated velocities in most of Region I are relatively insensitive to the assumed core radius.

Some results of the potential flow analysis for Region I along with sample hot fiber anemometer data are presented in Figs. 3-6. Figures 3, 4, and 5 show the axial variations of radial velocity

$$\text{at } \frac{r}{r_0} = 0.9,\ 0.75,\ \text{and } 0.50$$

and radial variations of tangential velocity

$$\text{at } \frac{z}{l} = 0.06,\ 0.28,\ 0.50,\ \text{and } 0.89.$$

A comparison of the predicted and observed radial and tangential velocities at a height of 0.00763m above the bottom end wall, are shown in Fig. 6 as a function of radial position. The radial velocities and radial pressure gradient near the bottom end wall must be calculated numerically for a discrete series of positions. To permit use of these results as free-stream boundary conditions for an end wall boundary layer

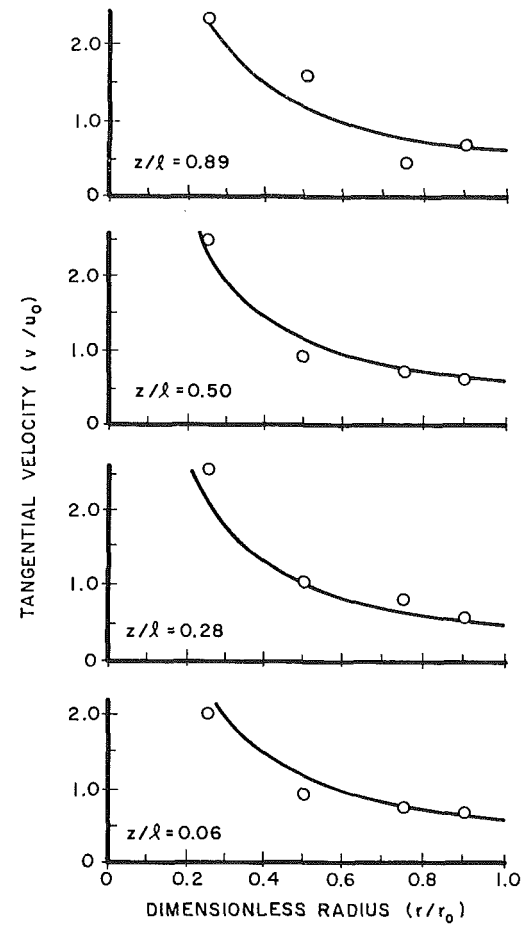

Fig. 5 Radial variation of tangential velocity ($Re_N = 1.8 \times 10^4$; $Re_T = 1.6 \times 10^4$)

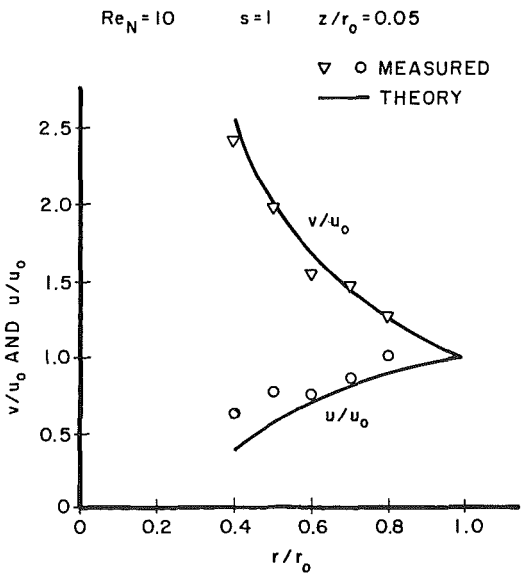

Fig. 6 Comparison of radial and tangential velocities at $\frac{z}{r_0} = 0.05$

analysis, the values have been smoothed using a cubic spline. The results of this smoothing process for radial velocity and pressure gradient will hereinafter be denoted as u_I and $(\partial p/\partial r)_I$, respectively.

B. Analysis of End Wall Boundary Layers (Region II). The major assumptions used in modelling the end wall boundary layers are as follows:

- Thin end wall boundary layers exist for both the tangential and radial velocity components. This is confirmed by the velocity measurements in Regions I and II.
- The end wall flow is laminar.
- The pressure gradient and velocity distribution calculated from the potential flow model for Region I and the experimentally determined viscous core size serve as the boundary conditions for the parabolic viscous flow equations used to calculate the velocity variations in the boundary layers.

The starting point for the analysis is the dimensionless form of the Navier Stokes equations in cylindrical coordinates.

$$U\frac{\partial U}{\partial R} - \frac{V^2}{R} + W\frac{\partial U}{\partial Z} = -\frac{\partial P}{\partial R} + \frac{1}{\mathrm{Re}_N}\left(\frac{\partial^2 U}{\partial R^2} + \frac{1}{R}\frac{\partial U}{\partial R} - \frac{U}{R^2} + \frac{\partial^2 U}{\partial Z^2}\right) \tag{7}$$

$$U\frac{\partial V}{\partial R} + \frac{UV}{R} + W\frac{\partial V}{\partial Z} = \frac{1}{\mathrm{Re}_N}\left(\frac{\partial^2 V}{\partial R^2} + \frac{1}{R}\frac{\partial V}{\partial R} - \frac{V}{R^2} + \frac{\partial^2 V}{\partial Z^2}\right) \tag{8}$$

$$U\frac{\partial W}{\partial R} + W\frac{\partial W}{\partial Z} = -\frac{\partial P}{\partial Z} + \frac{1}{\mathrm{Re}_N}\left(\frac{\partial^2 W}{\partial R^2} + \frac{1}{R}\frac{\partial W}{\partial R} + \frac{\partial^2 W}{\partial Z^2}\right) \tag{9}$$

$$\frac{\partial U}{\partial R} + \frac{U}{R} + \frac{\partial W}{\partial Z} = 0$$

For the problem under consideration, there is assumed to be a boundary layer of thin axial extent which reduces equations (7)–(9) to

$$U\frac{\partial U}{\partial R} - \frac{V^2}{R} + W\frac{\partial U}{\partial Z} = -\frac{\partial P}{\partial R} + \frac{1}{\mathrm{Re}_N}\left(\frac{\partial^2 U}{\partial Z^2}\right) \tag{10}$$

$$U\frac{\partial V}{\partial R} + \frac{UV}{R} + W\frac{\partial V}{\partial Z} = \frac{1}{\mathrm{Re}_N}\left(\frac{\partial^2 V}{\partial Z^2}\right) \tag{11}$$

$$U\frac{\partial W}{\partial R} + W\frac{\partial W}{\partial Z} = -\frac{\partial P}{\partial Z} + \frac{1}{\mathrm{Re}_N}\left(\frac{\partial^2 W}{\partial Z^2}\right) \tag{12}$$

subject to the boundary conditions

$$U(1,Z) = -1 \qquad U(R,0) = 0 \tag{13}$$

$$V(1,Z) = S \qquad V(R,0) = SR \qquad V(R,\Delta) = \frac{S}{R}$$

$$W(1,Z) = 0 \qquad W(R,0) = 0$$

The radial pressure gradient and radial velocity at $Z = \Delta$ above the surface are available from the analysis for Region I. Hence

$$\frac{\partial p}{\partial R} = \left(\frac{\partial P}{\partial R}\right)_I \quad U(R,\Delta) = U_I \tag{14}$$

In this analysis, values for the quantity Δ were chosen to be greater than the dimensionless end wall boundary layer thickness.

A numerical, marching, implicit, finite difference technique was used to obtain a solution to equations (10), (11), and the continuity equation.

In an attempt to minimize the number of grid positions needed for an accurate solution to the equations, the finite differences in the cross-stream direction were written with variable grid spacing. Other investigators [9] have noted that the problems of stability associated with the marching procedure can be minimized using "upwind" differences to represent the convective terms. Equations (10) and (11) become at the position $i+1, j$:

$$U_{i,j}\left(\frac{U_{i,j} - U_{i+1,j}}{\Delta R}\right) - \frac{V_{i,j}}{R_{i+1}}\left(V_{i+1,j}\right) + W_{i,j}\left(\frac{U_{i+1,j+1} - U_{i+1,j-1}}{(1+a)\Delta Z}\right) = -\left(\frac{\partial P}{\partial R}\right)_I + \frac{1}{\mathrm{Re}_N}\left(\frac{aU_{i+1,j+1} - (1+a)U_{i+1,j} + U_{i+1,j-1}}{\frac{a}{2}(1+a)\Delta Z^2}\right) \tag{10a}$$

$$U_{i,j}\left(\frac{V_{i,j} - V_{i+1,j}}{\Delta R}\right) + \frac{U_{i,j}V_{i+1,j}}{R_{i+1}} + W_{i,j}\left(\frac{V_{i+1,j+1} - V_{i+1,j-1}}{(1+a)\Delta Z}\right) = \frac{1}{\mathrm{Re}_N}\left(\frac{aV_{i+1,j+1} - (1+a)V_{i+1,j} + V_{i+1,j-1}}{\frac{a}{2}(1+a)(\Delta Z)^2}\right) \tag{11a}$$

where "a" is the grid spacing ratio $(\Delta Z)_j/\Delta Z_{j+1}$.

When the values of U and V have been determined for all j at $i+1$, the continuity equation may be used to determine the axial velocities:

$$\frac{U_{i,j} - U_{i+1,j}}{\Delta R} + \frac{U_{i+1,j}}{R_{i+1}} + \frac{W_{i+1,j+1} - W_{i+1,j}}{\Delta Z} = 0$$

Since the pressure has been assumed to be uniform through the boundary layer, equations (10), (11) and continuity have been solved for the unknown U, V, and W. Equation (12) is not needed. The equations have been written such that computation begins at $R = 1$ and proceeds radially inward toward the centerline. Fifty axial grid points have been used with a grid spacing ratio $a = 0.9$ and streamwise steps of 0.005. Since 20 axial grid points were used in Region I, the computed free-stream values closest to the wall are at $Z = 0.05$, which was chosen as the value of Δ in the end wall analysis.

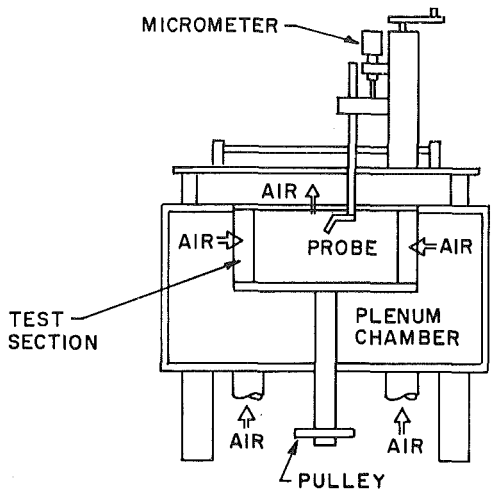

Fig. 7 Experimental apparatus

III Experiments

The experimental apparatus (Fig. 7) consists of a porous cylindrical chamber 0.305 m in diameter and 0.159 m high,

with impervious top and bottom end walls. The bottom wall is attached to a shaft which is driven by a variable speed electric motor. Air is supplied to the plenum chamber which completely surrounds the cylinder and is sealed by a teflon ring and metal sheet to the top wall of the chamber and to the shaft on the bottom. The top end wall contains the exit opening, 0.152 m in diameter and is constructed of 19 mm thick plexiglass. The cylinder is completely surrounded by honeycomb sections so that air is accelerated to the proper tangential velocity before reaching the distributor. The distributor in turn is wrapped with cloth to provide a pressure drop large enough to ensure even distribution of the air flow. The air supply system is capable of delivering approximately 0.378 m^3/s (800 scfm) to the chamber which is capable of angular velocities up to 42 s^{-1} (400 rpm). The angular velocity of the chamber is determined by a calibrated strobe light focused on a mark on the chamber drive shaft. The air flow rate is determined with a pitot static probe oriented in the direction of flow at the supply duct centerline. Air flow calibration is carried out by measuring the dynamic pressure at a number of radial positions in the supply duct, computing the velocities, and then integrating the velocity profiles for various flow rates.

Measurements of the radial and tangential velocities in the end wall region were made using a DISA hot fiber anemometer probe. The probe was mounted on a traversing mechanism. Fine vertical positioning with accuracy ± 0.025 mm was accomplished with a micrometer mounted on the vertical carriage (Fig. 7).

The component of velocity perpendicular to the end wall is small in the immediate vicinity of the wall. In addition, to determine the three-dimensional velocity vector, at least one of the sensor positions must lie outside of a plane parallel to the wall. The sensor itself is 2.5 mm in length. Therefore, the practical method of measurement in Region II is to assume that the velocity is two-dimensional and to make traverses with the sensor in two perpendicular positions in a plane parallel to the end wall, and the probe body vertical.

In any vortex flow, the potential for probe interference with the flow must be considered. In most previously studied confined vortex flows, the swirl was so large that it was very difficult to obtain accurate measurements with an invasive probe. However, in the present experiments, except in the viscous core region, the local radial velocity was large enough to sweep the probe wake away from the measuring position, permitting accurate measurements. The validity of this procedure was confirmed by calculating the ratio of radial to tangential velocity along with known values for the growth of a wake to insure that the wake did not intersect the measuring position.

The experimental procedure was as follows. The probe in one orientation was moved vertically in steps of 1.27 mm from a height of 12.7 mm above the plate. The last two steps were 0.6 mm. Traverses were made at $R=0.8$, 0.7, 0.6, 0.5, and 0.4.

Experimental results with theoretical predictions superimposed are shown in Figs. 8 through 15. The radial velocity profiles for $Re_N = 10^4$ and $S=1$ with an aspect ratio of $r_0/l=1$ [Fig. 8] show a typical boundary layer profile at $R=0.8$. At that location, the boundary layer thickness of the radial component is approximately $Z=0.04$. As the radius decreases, an inflection point develops with a velocity overshoot occurring at about $R=0.50$. This overshoot becomes more pronounced at smaller radii.

The tangential velocity increases from the value $v=\omega r$ on the plate to the free-stream velocity $v=v_0/r$ over a vertical distance $Z=0.02$. Note also that the overshoot in radial velocity occurs within the boundary layer for tangential velocity [Fig. 9].

Figure 10 shows radial velocities for $Re_N = 10^4$ and $S=2$.

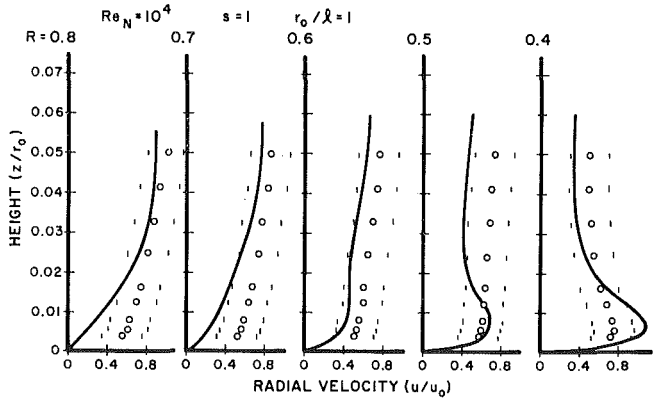

Fig. 8 Bottom end wall boundary layer. $Re_N = 10^4$, $S=1$, $r_0/l=1$

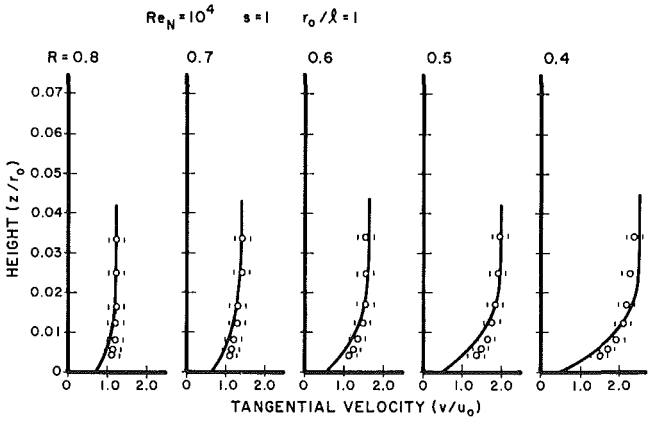

Fig. 9 Bottom end wall boundary layer. $Re_N = 10^4$, $S=1$, $r_0/l=1$

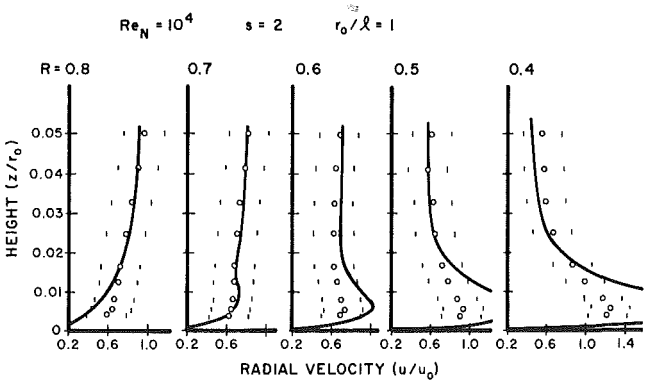

Fig. 10 Bottom end wall boundary layer. $Re_N = 10^4$, $S=2$, $r_0/l=1$

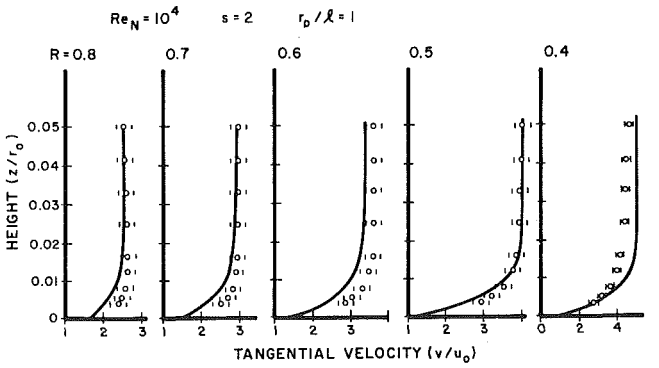

Fig. 11 Bottom end wall boundary layer. $Re_N = 10^4$, $S=2$, $r_0/l=1$

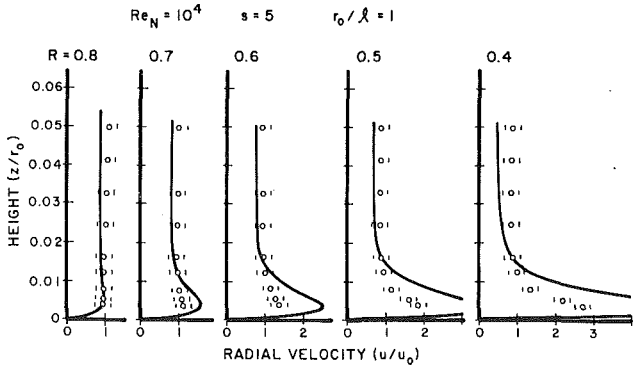

Fig. 12 Bottom end wall boundary layer. $Re_N = 10^4$, $S = 5$, $r_0/l = 1$

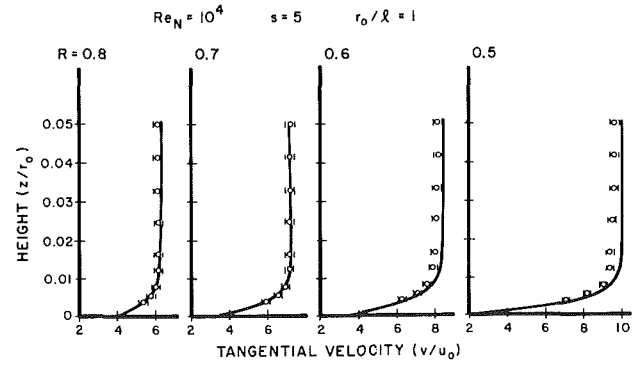

Fig. 13 Bottom end wall boundary layer. $Re_N = 10^4$, $S = 5$, $r_0/l = 1$

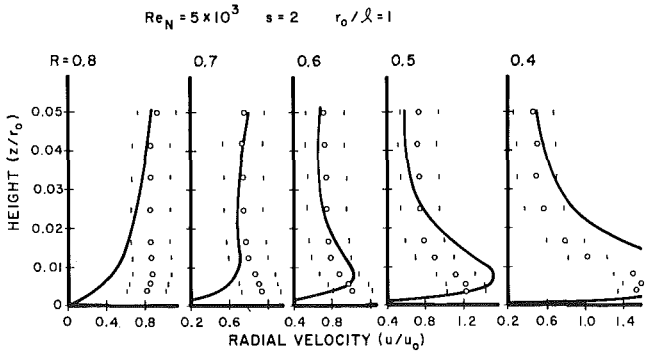

Fig. 14 Bottom end wall boundary layer. $Re_N = 5 \times 10^3$, $S = 2$, $r_0/l = 1$

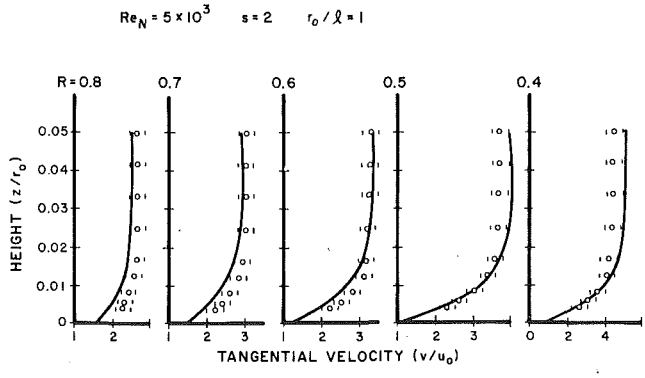

Fig. 15 Bottom end wall boundary layer. $Re_N = 5 \times 10^3$, $S = 2$, $r_0/l = 1$

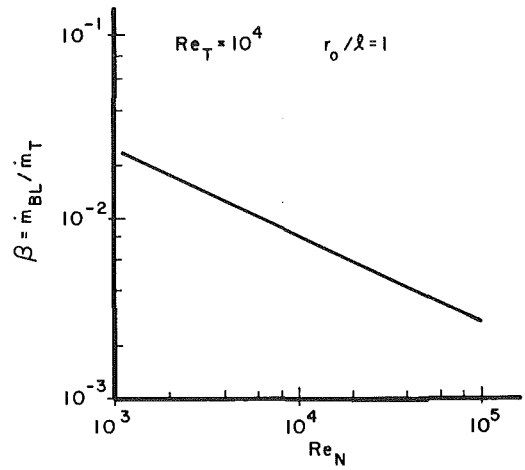

Fig. 16 Variation of flow rate through boundary layer with radial Reynolds number

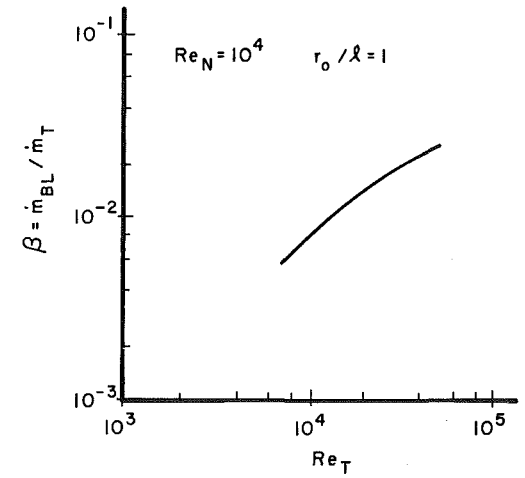

Fig. 17 Variation of flow rate through boundary layer with tangential Reynolds number

At larger swirl, the position of the first noticeable overshoot is at a larger radius, and the magnitude of the overshoot is greater. With increased swirl the velocity overshoot also occurs closer to the wall, and this is apparently the result of the thinner tangential boundary layer as shown in Fig. 11.

Figures 12 and 13 show the boundary layers for $Re_N = 10^4$ and $S = 5$. In this case overshoot begins almost immediately at $r = 0.80$, the layers are quite thin ($\delta/r_0 \sim 0.01$), and the peak radial velocity is about 12 times the free-stream velocity.

Figures 14 and 15 are for the conditions $Re_N = 5 \times 10^3$ and $S = 2$. The decrease in Reynolds number from $Re_N = 10^4$ to 5×10^3 at constant swirl results in a thickening of the tangential boundary layer and an outward displacement of the velocity overshoot.

In general, while the agreement between the measured and predicted tangential velocities is very good, the radial profiles do not agree nearly so well. There are a number of possible reasons. Measurements were not made in the region near the axis of symmetry close to the bottom end wall; and there may be some interaction between the end wall boundary layer and the core which has not been accounted for in the theory. The theory assumes a core radius which is uniform with height and although the effect of core radius on the velocities in Region I has been found to be small, it is not known whether this assumption is also valid for the end wall boundary layer. Finally, the boundary layer approximations imply that the radial diffusion terms $\partial^2/\partial r^2$ are small. An order of magnitude check on these terms shows that they are ap-

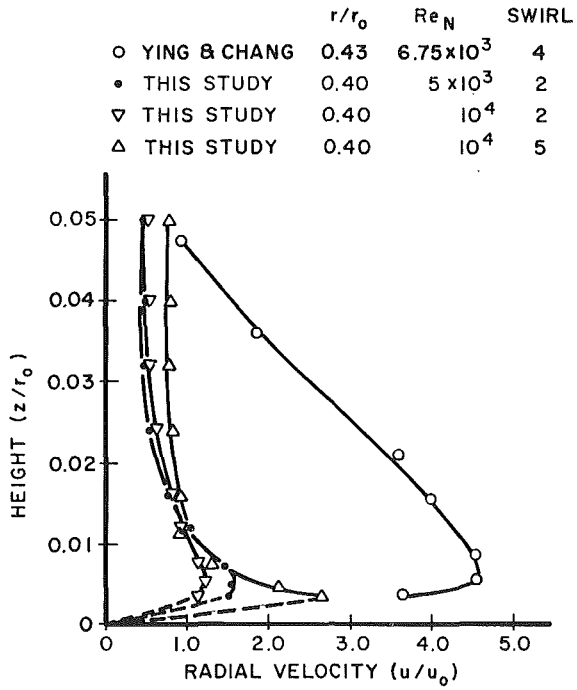

Fig. 18 Comparison of radial velocity profiles

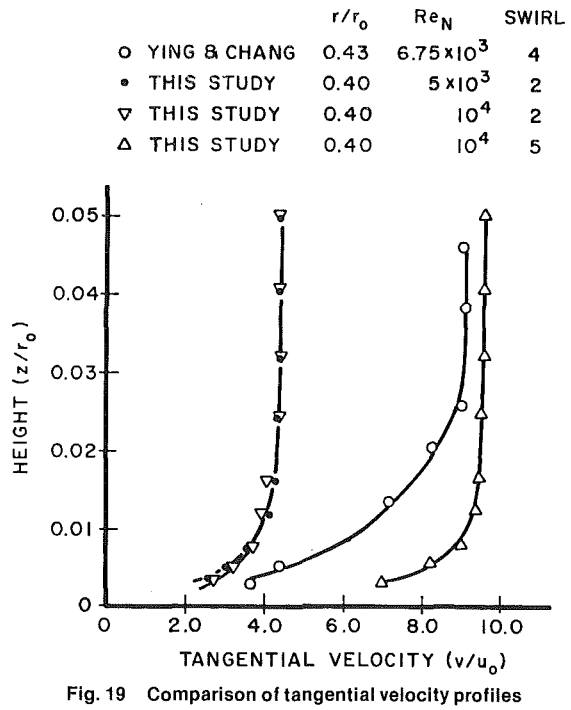

Fig. 19 Comparison of tangential velocity profiles

proximately 10 percent of the value of the $\partial^2/\partial Z^2$ terms. It is possible that this is large enough to account for some of the disagreement.

IV Discussion and Conclusions

Summarizing the results, at high flow rate with swirl ratios of order unity, the confined vortex of Fig. 1 possesses a region where the fluid behaves inviscidly and irrotationally and has boundary layers at the end walls which occupy less than 5 percent of the chamber height. The wall region is characterized by a radial velocity overshoot which increases in magnitude with increasing swirl. The thickness of the wall layer decreases with increasing radial Reynolds number.

In general, over the range of conditions studied, the data for tangential velocity agree very well with the theory. In addition, the radial velocity data show the same qualitative behavior as the theory, i.e., velocity overshoot at the appropriate positions, approximately correct boundary layer thickness, and the correct trends with changing conditions.

As discussed above, the analysis is valid only at radii larger than the core radius. In addition, the wall boundary layers must be thin with only a small fraction of the total flow passing through the wall layers. This is substantiated by Figs. 16 and 17 which give values of the quantity $\beta = \dot{m}_{BL}/\dot{m}_T$ as functions of Re_N and Re_l. These results, obtained from the theory, show that β increases with swirl and decreases with Re_N, with values in the range from 3×10^{-3} to 3×10^{-2}.

The only other experimental work known to the authors which is in the same approximate range of Re_N and Re_l is by Ying and Chang [2] for the case of a stationary end wall. The minimum swirl in their study was 4.0 and the chamber aspect ratio was $r_0/l = 0.63$. Because of differences in end wall conditions, only qualitative comparisons are possible. These are shown in Figs. 18 and 19 for $r/r_0 = 0.43$, $S = 4$ and $Re_N = 6.75 \times 10^3$ for the Ying and Chang data and at $r/r_0 = 0.4$, $S = 2$ and 5, and $Re_N = 5 \times 10^3$ and 10^4 for the present study. The radial profiles [Fig. 18] show essentially the same shape. However, in the stationary end wall case, there is a much larger velocity overshoot and the boundary layer for radial velocity is much thicker. The tangential profiles in Fig. 19 also suggest a thicker boundary layer for tangential velocity in the stationary end wall case.

References

1 Wan, C. A., and Chang, C. C., "Measurement of the Velocity Field in a Simulated Tornado Like Vortex Using a Three-Dimensional Velocity Probe," *J. Atm. Sci.*, Vol. 29, No. 1, 1972, p. 116.

2 Ying, S. J., and Chang, C. C., "Exploratory Model Study of Tornado - Like Vortex Dynamics," *J. Atm. Sci.*, Vol. 27, No. 1, 1970, p. 3.

3 Pao, H. P., "A Numerical Computation of a Confined Rotating Flow," ASME *Journal of Applied Mechanics*, Vol. 41, No. 2, June 1974, p. 480.

4 Farris, G. J., Kidd, G. J., Lock, D. W., and Textor, R. E., "A Theoretical and Experimental Study of Confined Vortex Flow," ASME *Journal of Applied Mechanics*, Vol. 36, No. 4, 1969, p. 687.

5 Levy, E. K., Shakespeare, W. J., Tabatabaie-Raissi, A., and Chen, C. J., "Particle Elutriation from Centrifugal Fluidized Beds," AIChE 72nd Annual Meeting, San Francisco, Nov. 1979.

6 Shakespeare, W. J., "An Experimental and Theoretical Study of the Confined Vortex with High Flow Rate," Ph.D dissertation, Lehigh University, 1979.

7 Kotas, T. J., "An Experimental Study of the Three-Dimensional Boundary Layer on the End Wall of a Vortex Chamber," *Proc. R. Soc. London*, Series A., Vol. 352, 1976, p. 169.

8 Savino, J. M., and Keshock, E. G., *Experimental Profiles of Velocity Components and Radial Pressure Distributions in a Vortex Contained in a Short Cylindrical Chamber*, NASA, TN D-3072, 1965.

9 Hornbeck, R. W., *Viscous Flow in a Short Cylindrical Vortex Chamber with a Finite Swirl Ratio*, NASA, TN D-5132, 1969.

10 Wormley, D. N., "An Analytical Model for the Incompressible Flow in Short Vortex Chambers," ASME *Journal of Basic Engineering*, Vol. 91, No. 2, 1969, p. 264.

11 Hoffmann, J. A., "Similarity Solutions for the Interaction of a Potential Vortex with Free Stream Sink Flow and a Stationary Surface," ASME Journal of Engineering Materials and Technology, Vol. 96, No. 1, 1974, p. 49.

12 Burggraf, O. R., Stewartson, K., and Belcher, R., "Boundary Layer Induced by a Potential Vortex," *Physics of Fluids*, Vol. 14, No. 9, 1971, p. 1821.

13 Kuo, H. L., "Axisymmetric Flows in the Boundary Layer of a Maintained Vortex," *J. Atm. Sci.*, Vol. 28, No. 1, 1971, p. 20.

14 Rogers, M. H., and Lance, G. N., "The Boundary Layer on a Disk of Finite Radius in a Rotating Fluid," *Quart. J. Mech. and Appl. Math.*, Vol. XVII, Part 3, 1964, p. 319.

15 Lewellen, W. S., *A Review of Confined Vortex Flows*, NASA CR 1772, 1971.

16 Schlichting, H., *Boundary-Layer Theory*, 6th edition, McGraw-Hill, N.Y., 1968.

Scaling Parameters for a Time-Averaged Separation Bubble

A. J. Smits
Assistant Professor,
Department of Mechanical and Aerospace Engineering,
Princeton University,
Princeton, N.J. 08540

A splitter plate is placed in the wake of a two-dimensional bluff body. The splitter plate is long enough for the separated flow behind the body to reattach on the splitter plate. The time-averaged properties of this "closed" separation bubble are investigated under a wide range of kinematic conditions. It is found that blockage reduces the base pressure coefficient (C_{p_b}) and the distance to reattachment (l) but the relationship between l and C_{p_b} is not obvious. The pressure distribution in the separated zone, scaled on C_{p_b} and l, can be described by a universal curve. The usefulness of a slotted wall in reducing blockage effects on bluff body flows is shown to be limited in that the wall porosity affects only some properties of the separation bubble.

Introduction

When the splitter plate is placed in the wake of a two-dimensional bluff body it tends to suppress the strong eddying motions normally observed and thereby reduces the body drag. When the splitter plate is very long compared to the characteristic width of the bluff body the separated flow in the wake of the body reattaches on the splitter plate and a "closed" separation bubble results. The flow geometry is similar to that considered by Arie and Rouse [1] and Ranga Raju and Garde [2], and it is shown in Fig. 1.

Although this flow is part of an important class of separated flows the choice of this particular configuration was somewhat arbitrary. The principal concern of this study is to determine the effect of the experimental arrangement on the behaviour of a typical separation bubble. For instance, it is well known that blockage has a major influence on the base pressure coefficient [2], and other parameters like the splitter plate length and thickness may also be important. By varying the geometrical proportions of the experiment over a wide range this study aims to provide the information necessary for comparing calculations with experiment, and one experiment with another. The chief parameters of the time-averaged separation bubble are the distance to reattachment l and the base pressure coefficient C_{p_b}, where $C_{p_b} = (p_b - p_\infty)/\frac{1}{2}\rho U_\infty{}^2$. U_∞ and p_∞ are the free stream velocity and static pressure respectively, ρ is the density of the fluid and p_b is constant over the area of the base [1]. Other properties that may be used to describe the separation bubble include the maximum height of the separation streamline h and l_p, the distance along the splitter plate to the position of maximum pressure.

In a recent review Smits [3] found that l and C_{p_b} appear to depend on a number of parameters which may be split into three groups. The first group is associated with the nature of the bluff body and includes the characteristic body dimension D and the angle between the separation streamline and the freestream direction at the point of separation α [4]. The second group is related to splitter plate geometry such as its length L and thickness t. The final group is associated with the test facility, for example, the height of the working section H and its width W, the porosity of the walls and the shape of the cross-section.

In the cases considered here the splitter plate is long enough for the mean reattachment line to lie on the splitter plate and, since the boundary layer thickness at separation is much less than the diameter of the body, viscous effects are not expected to be important [5].

Dimensional analysis leads to

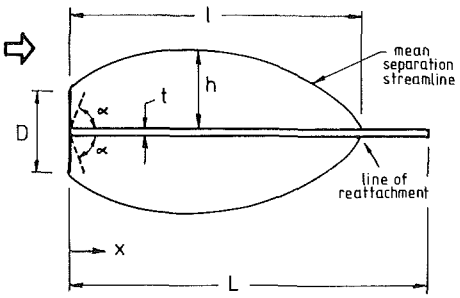

Fig. 1(a) Notation for bluff plate/splitter plate combination

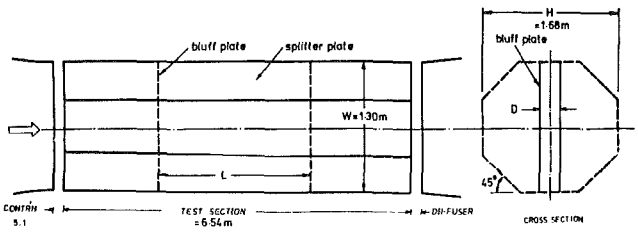

Fig. 1(b) Tunnel working section layout

Contributed by the Fluids Engineering Division and presented at the Winter Annual Meeting, Washington, D.C., November 15–20, 1981, of THE AMERICAN SOCIETY OF MECHANICAL ENGINEERS. Manuscript received by the Fluids Engineering Division, January, 1981 Paper No. 81-WA/FE-20.

$$C_{p_b}, \frac{l}{D} = f_{1,2}\left[\alpha, \epsilon, \frac{t}{D}, \frac{L}{D}, \frac{W}{D}\right] \quad (1)$$

where ϵ is a blockage parameter, given by

$$\epsilon = g\left[\frac{D}{H}, \tau, P, F\right] \quad (2)$$

τ is a parameter associated with the shape of the tunnel cross-section and was not varied "in this" investigation. P and F are relevant for a slotted wall tunnel, where P is the wall porosity parameter and F is the slotted tunnel geometry factor [6]. Note that ϵ is assumed to be independent of x.

In the present study the functional dependence expressed by equations (1) and (2) is investigated experimentally. The experimental details are described in Section 2, the results are presented and discussed in Section 3 and the conclusions are summarized in Section 4.

2 Apparatus and Experimental Technique

The wind tunnel working section is octagonal, measuring 1.68m × 1.30m with a length of 6.54m (see Fig. 1). The walls are slotted along the entire length, with an open-to-closed ratio of 4.9 percent. The adjustable side walls were set so that the longitudinal pressure gradient in the absence of the model was negligible.

The bluff plates were metal and 1.5mm thick. The edges were considered sufficiently thin and sharp and were not further bevelled. The splitter plates were plywood. These were mounted vertically and where they met the floor and ceiling of the working section the slotted walls were taped up to prevent end leakage and hence reduce secondary flows. Pressure tappings were located at 23 positions along each splitter plate and the leads were recessed so that no protrusions occurred on either face of the plate.

Altogether 25 separate cases were tested and the details for all bluff plates and splitter plates used are given in Table 1. Series A, B, and C were tested in the slotted-wall working section as described above. For Series D all the slots were taped up to give a conventional plain-wall working section.

The pressure coefficient C_p was measured relative to the reference static pressure. The reference static pressure and reference velocity were measured using static tappings located in the settling chamber and near the exit of the contraction. These tappings were calibrated against a standard NPL Pitot-static tube placed in the centre of the empty working section at the mid-chord position. Conditions at the reference static tappings were taken to be equivalent to free stream conditions. The distance downstream to the point of reattachment (l) was found by extrapolating the skin friction coefficient C_f upstream to zero. The results of Bradshaw and Wong [5] suggest that this is a reasonable procedure even when departures of the inner-layer behaviour from that of a conventional boundary layer occur. All skin friction coefficients were measured by Preston tubes of 1.06mm diameter using the calibration of Patel [7].

Velocities and pressure within the separation bubble were measured using a square edged circular Pitot tube and a disc static probe with a rounded edge. These were calibrated against the standard NPL Pitot-static tube mentioned above. A disk static head was chosen instead of a static tube because the reading is almost completely independent of flow angle in the plane of the disc and is almost constant for angles of inclination less than about ±5 percent in the plane perpendicular to this (8). Thus yaw errors should be small and pitch errors negligible.

Velocity measurements were only made at one position, at $x/l = 0.5$, and two overlapping traverses were made, one with the probe facing upstream and one with the probe facing downstream. A curve was interpolated between the two traverses to determine y_0, the distance above the splitter plate

Table 1 Experimental cases considered. Note, for splitter plate a L = 1781 mm, t = 12.4 mm; for splitter plate b L = 891 mm, t = 6.2 mm. See Fig. 1 for notation.

Slotted wall working section (I)

Series A: Splitter plate a, α=90°, symbol ○ (9 cases):
D = 25.6, 31.9, 41.5, 50.7, 63.1, 82.7, 108.2, 139.3, 178 mm.

Series B: Splitter plate a (4 cases):
(1)α = 58°, D = 172.9 mm, symbol ⬡ (II)α = 46°, D = 171.7 mm, symbol △ (III)α = 30°, D = 165.5 mm, symbol ▽ (IV)α = 30°, D = 106.7 mm, symbol ▽ .

Series C: Splitter plate b, α = 90°, symbol ⊘ (6 cases):
D = 25.6, 31.9, 41.5, 53.8, 69.8, 89 mm.

Plain wall working section (II)

Series D: Splitter plate a, α = 90°, symbol ● (5 cases):
D = 31.9, 63.1, 108.2, 139.3, 178 mm.

Nomenclature

b = shear layer thickness
C_f = skin friction coefficient
C_p = static pressure coefficient $(=(p-p_\infty)/\frac{1}{2}\rho U_\infty^2)$
C_{p_b} = base pressure coefficient
$\tilde{C}_p$ = static pressure coefficient $(=(p-p_e)/\frac{1}{2}\rho U_e^2)$
D = dimension of bluff plate in y-direction
F = slotted tunnel geometry factor
h = maximum height of the separation streamline
H = height of tunnel working section (y-direction)
l = reattachment length
l_p = distance to the point of maximum pressure
L = length of splitter plate
p = static pressure
p_b = static pressure over base of bluff plate
P = wall porosity parameter
t = splitter plate thickness
u,v = x- and y-component of the velocity fluctuation
U,V = x- and y-component of the flow velocity
W = width of the tunnel working section (z direction)
x = coordinate along the splitter plate, that is, in the streamwise direction
y = coordinate normal to the splitter plate, that is, in the cross-stream direction
y_0 = distance to the point of zero mean velocity, normal to the splitter plate, at $x/l = 0.5$
z = coordinate in the transverse direction
α = angle between the separation streamline and the freestream direction at the separation point
ϵ = blockage parameter
ν = kinematic viscosity
ρ = density

Subscripts

e = conditions outside the shear layer at the point of separation
∞ = freestream conditions
m = measured value, as different from true value

Table 2 Statement of experimental uncertainty

parameter	estimated error	main source of error
C_p	$\pm$ 0.005	inaccuracy of inclined manometer and day-to-day reproducibility
ℓ	$\pm$ 3%	inaccuracy in determining C_f, and uncertainty in extrapolating C_f values to zero.
ℓ_p	$\pm$ 3%	uncertainty in locating peak value of C_p.
y_o	$\pm$ 3%	difficulty in extrapolation, use of pressure probes in regions of high turbulence intensity.
y_m	$\pm$ 5%	uncertainty in locating minimum value of static pressure, limitations on disc static probe.
$\frac{U_{max}-U_{min}}{U_\infty}$	+0%, -5%	uncertainty in determining velocity within the separated region.

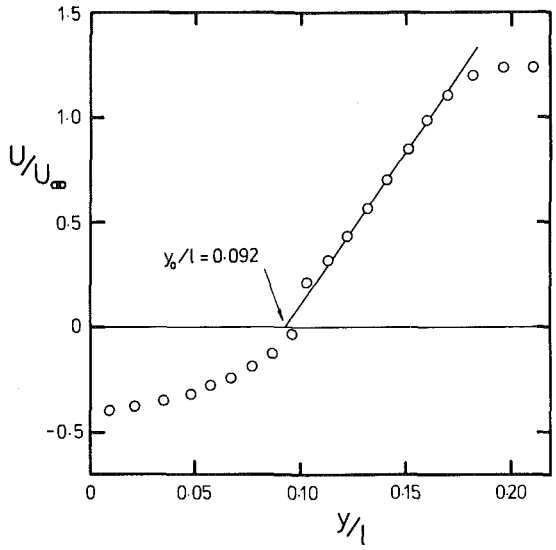

Fig. 2 Velocity profile at x/l = 0.5 for α = 46 deg, D = 171.7 mm (Series B in Table 1)

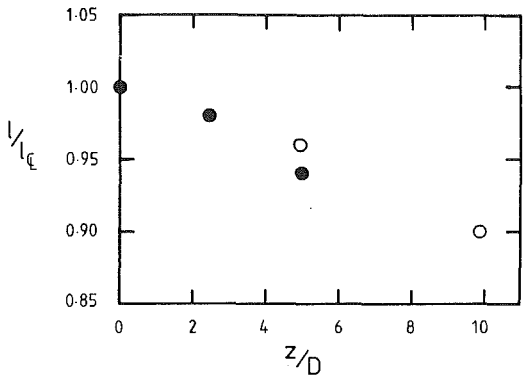

Fig. 3 Transverse variation of reattachment length normalized by centerline value.
○, Case (i): W/D = 31.3, D = 41.5 mm (Series C in Table 1).
●, Case (ii): W/D = 15.7, D = 82.7 mm (Series A in Table 1).

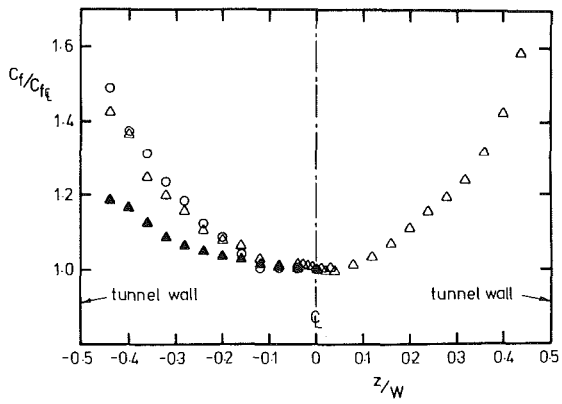

Fig. 4 Transverse variation of C_f normalized by centreline value. Case (i) and (ii) are given in Fig. 3.
○, Case (i) x/l = 1.50;
△, Case (ii) x/l = 1.43;
▲, Case (ii) x/l = 2.29

to the point of zero mean velocity. Typical results are given in Fig. 2. The dynamic pressure was related directly to the velocity U, neglecting the contribution due to the normal velocity V. This seems a reasonable assumption at $x/l = 0.5$. y_0 was chosen as a measure of the bubble height instead of h because it was felt that y_0 could be determined more accurately and more easily.

The effect of turbulence on the measurement of the total pressure is to give a reading that is too high by an amount $1/2\ \rho\overline{u^2}$ [9]. The reading of a static tube in turbulence is different from the true reading by an amount $1/2\ n\rho\ (\overline{v^2} + \overline{w^2})$ where the value of n depends on the ratio of tube diameter to turbulence length scale, and ranges from $+1$ to -1 [10]. The effect of turbulence on a disc static probe is not known with certainty but is believed to be small. In analogy with the static tube the error in static pressure is probably given by an expression such as $1/2\ n\rho\overline{w^2}$ if the disk is aligned in the $x-y$ plane. In the shear layer all three components of turbulence have similar values and the error in the measurement of mean velocity can then be written approximately as $m\overline{u^2}/U_m{}^2$ where the likely limits on m are $0 < m < 1$.

Note that the effect of turbulence on the mean velocity measurement should not affect the estimate of y_0 significantly, as long as the error is similar for the two overlapping traverses. The error in the measurement of mean velocity increases as the velocity tends to zero, and it may be seen from Fig. 2 that the inferred velocity is higher than the true velocity, as expected. By comparing the velocities measured by the two traverses, and using the turbulence results given by Arie and Rouse [1] it was estimated that in the region near the point of zero velocity a reasonable value for n was 0.5. If this applies outside this region then the uncertainty in $(U_{max} - U_{min})/U_\infty$ may be estimated, and it is given in Table 2.

For the bluff plate of height 82.7mm, with splitter plate a (Series A in Table 1), the Reynolds number based on D and U_∞ was systematically varied from 62,000 to 193,000. No change in the splitter plate pressure distribution could be distinguished. Consequently, although the actual tests covered a Reynolds number range of 42,000 to 290,000 it was assumed that the effect of viscosity on the data could be neglected.

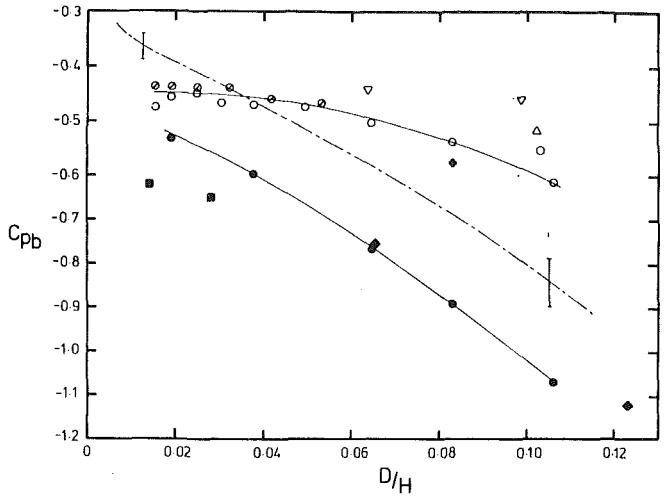

Fig. 5 Base pressure coefficient versus blockage ratio
+, Arie and Rouse (1)
◆, Ranga Raju and Garde (2)
■, Roshko and Lau (14)
—-, Good and Joubert (13) (only mean line shown, error bars indicate scatter).
For other symbols see Table 1.

3 Results and Discussion

The results presented here are subjected to the experimental uncertainty summarized in Table 2.

3.1 Three-Dimensionality of the Separation Bubble. The reattachment length l depends on the transverse position and, when nondimensionalized by the centre-line value, scales with the characteristic body dimension D. Figure 3 shows that this scaling is almost linear. In contrast, the variation of skin friction coefficient downstream of the reattachment point appears to scale with the tunnel width (Fig. 4). The apparent inconsistency of Figs. 3 and 4 may be resolved by noting that the departure from two-dimensionality decreases downstream of the reattachment point. This has also been observed by Smits, Baskaran, and Joubert [11] downstream of the separation bubble found in the lee of a two-dimensional "hill." A preliminary flow visualization study of the present configuration [3] showed that some of the fluid in the recirculation region enters the secondary separation bubble found just near the bluff plate. This fluid is transported laterally and expelled into the flow at the junction of the side wall and the splitter plate. In plan view a complex eigenvalue critical point is observed near this junction (using the terminology of [12]) and the downstream influence of this critical point spreads rapidly across the splitter plate. This may be the mechanism whereby transverse variations are reduced, although this remains purely speculative.

3.2 The Effect of Splitter Plate Length. Arie and Rouse [1] used a splitter plate of length 10D, "which had been found by observation to be longer than the eddy by a sufficient amount for the size of the latter to be unaffected by a further lengthening of the plate." For case $D = 178$mm of Series D of the present experiments ($L = 10$D, $l = 7.3D$) the splitter plate was lengthened by 52 percent and all measurements repeated. The only parameter affected was the distance to reattachment and this only increased by 7 percent. Other parameters describing the bubble shape were unchanged thus substantially verifying the conclusion of Arie and Rouse. In every case considered in the present study $l < 10$D and the effect of splitter plate length on the separation bubble was neglected. Some influence of the splitter plate length could be detected on the pressure distribution downstream of the reattachment point, and this is further discussed below.

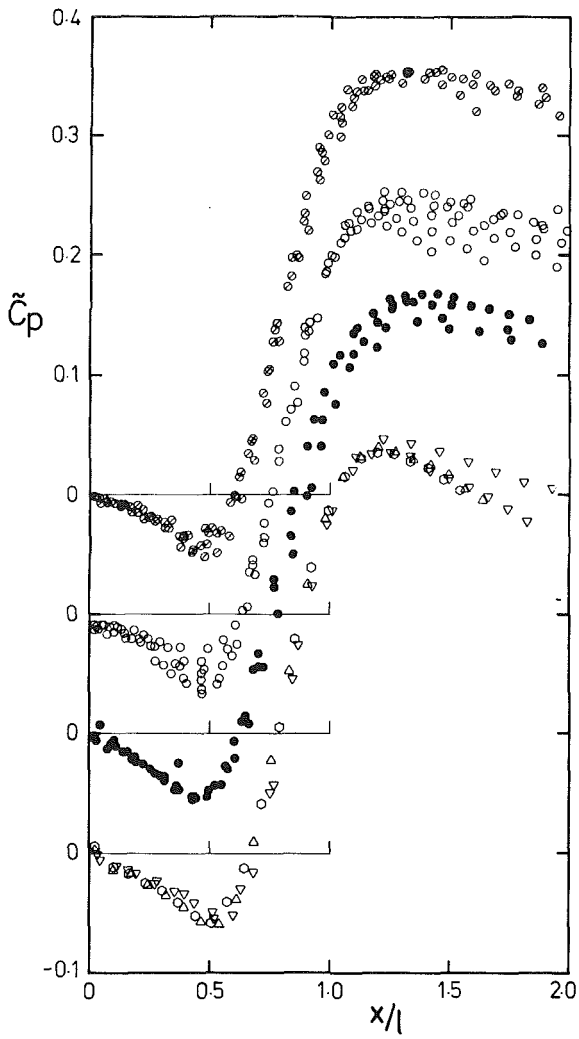

Fig. 6 Pressure coefficient (normalized by base pressure) along splitter plate. For symbols see Table 1.

3.3 Base Pressure Coefficient. Figure 5 shows that for normal bluff plates ($\alpha = 90$ deg) the base pressure coefficient is a strong function of the blockage ratio D/H and the porosity of the tunnel wall. The plain wall results agree well with the results of Ranga Raju and Garde [2], and a similar trend is observed for the fence flows of Good and Joubert (13). In the present experiments, as the blockage becomes negligible, all results appear to asymptote to a common value of -0.45, and this indicates that the efforts of Arie and Rouse [1] to account for blockage effects were not entirely successful.

For the angled bluff plates ($\alpha < 90$ deg) the effect of blockage on C_{p_b} decreases as α decreases and becomes very small for $\alpha = 30$ deg, which was the smallest value of α considered.

3.4 The Pressure Distribution in the Separation Bubble. Roshko and Lau [14] postulated that the reattachment pressure rise will depend on the nature of the accelerated flow near the tip of the bluff plate and the length of the separation bubble. Let the pressure p_e and the velocity U_e refer to the flow conditions just outside the separated zone near the point of separation. A new pressure coefficient $\tilde{C}_p$ may be defined, where

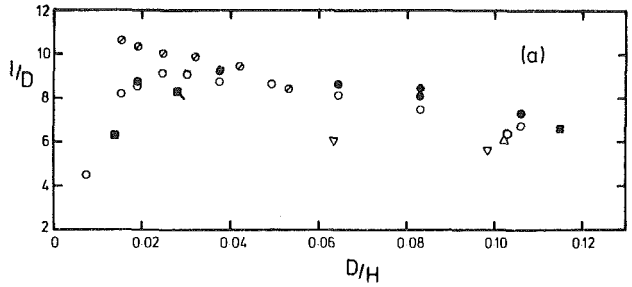

Fig. 7 Distance to reattachment versus blockage ratio
+, Arie and Rouse (1)
×, Good and Joubert (13)
▪, Roshko and Lau (14) t/d = 0.31
■, (14) t/d = 0.63.
For other symbols see Table 1.

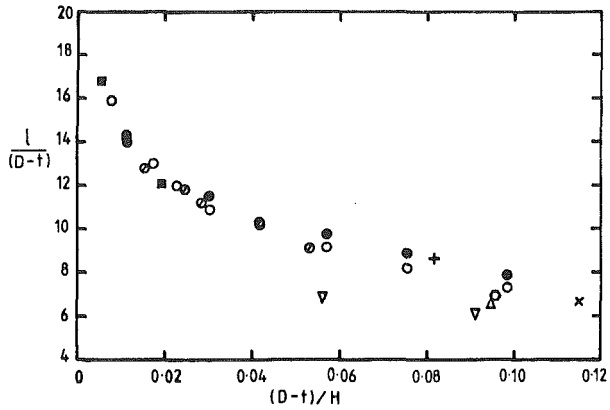

Fig. 8 As Fig. 7 using the effective base height (*D-t*) instead of *D*

$$\tilde{C}_p = \frac{p - p_e}{1/2\rho U_e^2} \tag{3}$$

Now p_e will be nearly equal to the base pressure, and $\tilde{C}_p$ may be written as

$$\tilde{C}_p = \frac{C_p - C_{p_b}}{1 - C_{p_b}} \tag{4}$$

When the measured pressure distributions are plotted using $\tilde{C}_p$ and x/l (Fig. 6) we find that the data indeed collapse onto a single curve for $x < l$, providing strong support for the arguments of Roshko and Lau.

3.5 The Shape of the Separation Bubble. Figure 7 shows that, at least for $D/H > 0.4$, the reattachment length decreases with blockage. However, for $D/H < 0.4$ the results diverge into two sets. The decrease in the reattachment length shown by one set indicates the effect of splitter plate thickness – as t/D increases the decrease in l/D becomes progressively more rapid. For the other set of results t/D is always small and the effect of splitter plate thickness is not so obvious. These results suggest that the reattachment length might scale with an effective base height like $(D\text{-}t)$. Figure 8 shows that this collapses all data for $\alpha = 90$ deg onto a single curve (excluding the case for $t/d = 1$), which monotonically decreases with increasing blockage. The decrease in reattachment length is accompanied by an increase in the bubble "aspect ratio," y_0/l (Fig. 9).

Note that for zero blockage the results for both $l/(D\text{-}t)$ and y_0/l asymptote to values considerably different to those found by Arie and Rouse [1], indicating once again that they could not account successfully for the effects of blockage.

Another interesting result from Figs. 8 and 9 is that the bubble shape is independent of the wall porosity. This implies that the presence of the tunnel wall acts purely as a geometrical constraint, scaling with D/H. Since the base pressure coefficient is a strong function of the wall porosity (see Fig. 5) it appears that no simple relationship exists between the base pressure and the reattachment length. A similar conclusion was found by Castro and Fackrell [15] in a study of bluff bodies in boundary layers.

The steady state bubble shape (and base pressure) may be regarded as resulting from a balance between the rate of entrainment of fluid from the bubble into the turbulent mixing layer along the long bubble boundary, and the rate of reversal of fluid back into the bubble by the pressure rise near reattachment [13]. Flow visualization experiments at low Reynolds numbers revealed that the vortex sheet leaving the bluff plate initially rolls up in a Kelvin-Helmholtz-like instability [20]. Downstream the vortices were seen to pair, triple and even quadruple. This seems to be the mechanism for the rapid growth of the shear layer and bears many

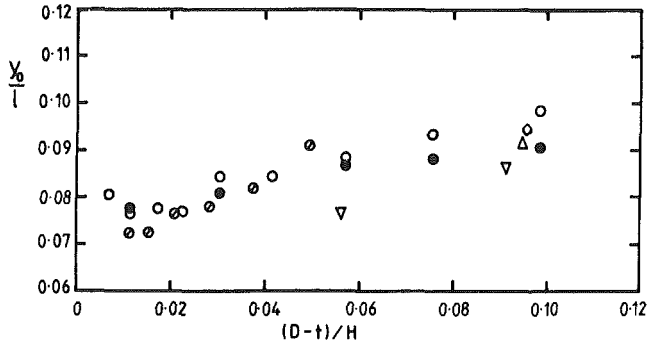

Fig. 9 Height to point of zero mean velocity (at $x/l = 0.5$) versus blockage ratio. For symbols see Fig. 7 and Table 1.

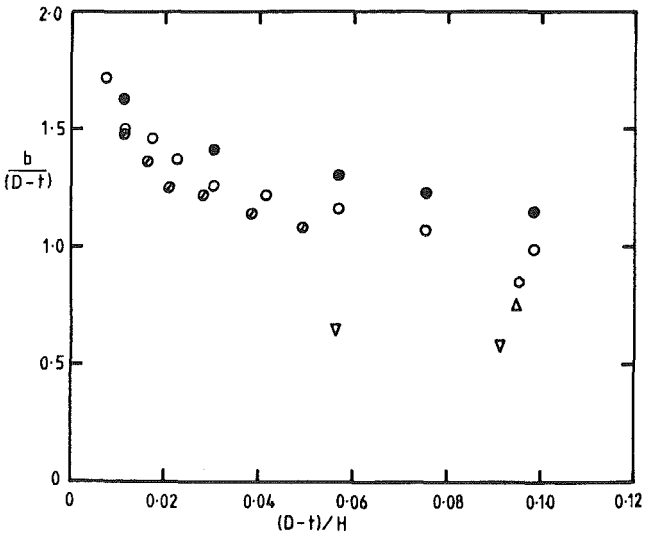

Fig. 10 Shear layer thickness at $x/l = 0.5$ versus blockage ratio. For symbols see Fig. 7 and Table 1.

similarities to the structure of the simple miximg layer [16]. If this vortex "amalgamation" is caused by small differences in the initial vortex formation combined with the presence of a large velocity gradient (as suggested by Winant and Browand [16]) then increasing the velocity gradient in the shear layer would tend to increase the rate of amalgamation.

It is now tentatively suggested that the main effect of blockage is to increase all gradients in the y-direction. A shear layer thickness may be defined by

$$b = \frac{U_{max} - U_{min}}{(\partial U/\partial y)_{max}}$$

and Fig. 10 shows a strong decrease in this shear layer thickness measured at $x/l = 0.5$ as the blockage increases. Increasing the gradients normal to the splitter plate will stimulate the turbulent mixing process in the separated shear layer and therefore decrease the distance to reattachment. The strong connection that exists between the shear layer thickness and the reattachment length is obvious from a comparison of Figs. 10 and 8. This enhanced mixing process, which was observed in the flow visualization, should cause a greater mass flow back into the bubble. Since the reattachment pressure rise is nearly constant (see Fig. 6) this may explain the increase in the bubble aspect ratio (Fig. 9).

3.6 Flow Characteristics Downstream of Reattachment. Downstream of reattachment the pressure continues to rise to a maximum value at $x = l_p$, and then falls almost linearly to a given value at the trailing edge of the splitter plate. Both the maximum value and the value at the trailing edge, relative to the conditions near the separation point, are approximately constant for all cases considered (see Fig. 6). It appears that the conditions in the wake of the bluff-body/splitter-plate combination are also determined by the nature of the flow approaching separation, and that the pressure distribution over the entire combination is affected by blockage in a similar fashion. Thus it seems that the base pressure is still the relevant scaling variable for the static pressure but for $x > l_p$ the longitudinal length scale is affected by the length of the splitter plate.

The observation that the point of maximum pressure occurs downstream of the reattachment point has been noted in a number of similar situations [13], [14], [17], [18], [19].

Consider the mean two-dimensional streamwise momentum equation:

$$\bar{U}\frac{\partial \bar{U}}{\partial x} + \bar{V}\frac{\partial \bar{U}}{\partial y} = -\frac{1}{\rho}\frac{\partial \bar{p}}{\partial x} - \left(\frac{\partial \overline{u^2}}{\partial x} + \frac{\partial \overline{uv}}{\partial y}\right) + \nu \nabla^2 \bar{U}. \quad (5)$$

In the absence of turbulent and viscous stresses the point of maximum pressure would coincide with the reattachment point. An order of magnitude analysis of equation (5), using the measurements of references [1], [5], [18], and [19], shows that not too close to the wall the viscous stress gradients are small compared to turbulent stress gradients and may be neglected at the Reynolds numbers under consideration. Thus it appears that the flow downstream of reattachment is maintained by turbulent stress gradients. In addition, the shear stress gradient is larger than the normal stress gradient, although not by an order of magnitude.

Fig. 11 indicates that the ratio l_p/l generally decreases with increasing blockage but two data points, from the plain wall tests, reverse this trend at higher blockage ratios. This may be due to an inappropriate choice of length scale, but a length scale which collapsed this data could not be found. Increasing blockage has already been observed to cause an increase in y_0/l (Fig. 9), while inspection of Figs. 8 and 10 shows that b/l increases. Both results suggest an increase in the spreading rate of the shear layer approaching reattachment. Downstream of reattachment this could cause $\partial \overline{uv}/\partial y$ to diminish but $\partial \overline{u^2}/\partial x$ to increase. Since the shear stress gradient is probably dominant this argument might provide reasons for the observed decrease of l_p/l, but the plain wall results remain unexplained. No satisfactory explanation seems possible without further detailed measurements.

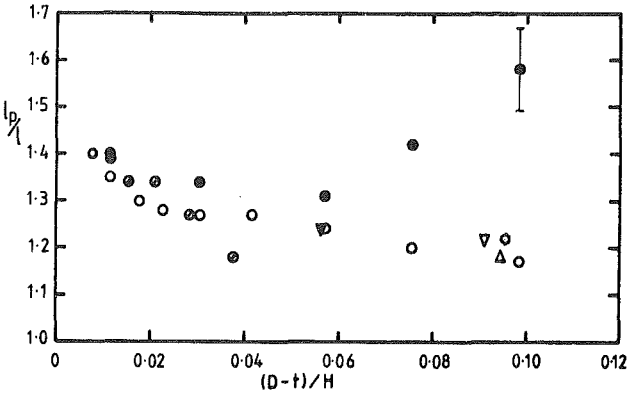

Fig. 11 Distance along splitter plate to point of maximum pressure versus blockage ratio. For symbols see Fig. 7 and Table 1. Error bars indicate uncertainty when outside the limits given in Table 2.

4 Summary of Conclusions

(1) The pressure distribution along the splitter plate scales with the base pressure, and for $x < l$ the reattachment length is the appropriate length scale, confirming the work of Roshko and Lau [14]. Only when $x > l$ does the splitter plate length enter as a variable.

(2) The thickness of the splitter plate changes the effective base height from D to $(D - t)$.

(3) No simple relationship between C_{pb} and l is apparent.

(4) Blockage confines the shear layer which increases all gradients in the y-direction. This enhances the turbulent mixing process in the shear layer, and increases the entrainment of fluid in the separated zone back in to the shear layer. This may be related to the increased vortex amalgamation observed in the flow visualization under conditions of increasing blockage, and results in a shorter reattachment length and a higher zero velocity point.

(5) The point of maximum pressure occurred downstream of the point of reattachment indicating that turbulent stress gradients are important.

(6) The usefulness of a slotted wall in reducing blockage effects on bluff body flows seems limited.

Although porous walls allow the pressure distribution to approach the infinite stream conditions more closely, the blockage dependence of the separation bubble shape and scale is independent of wall porosity.

Acknowledgments

The author wishes to thank Dr. A. E. Perry and Dr. D. I. Pullin for many useful discussions, and Dr. M. C. Good for his comments on an earlier draft. The work was financially supported by the Australian Research Grants Committee and NERDDC.

References

1 Arie, M., and Rouse, H. "Experiments on Two-Dimensional Flow over a Normal Wall," *Journal of Fluid Mechanics*, Vol. 1, 1956, pp. 129–141.

2 Ranga Raju, K. G., and Garde, R. J., "Resistance of an Inclined Plate Placed on a Plane Boundary in Two-Dimensional Flow," ASME *Journal of Basic Engineering*, Vol. 92, Mar. 1970, pp. 21–31.

3 Smits, A. J., "A Critical Preliminary Review of Literature Relating to Bluff Bodies with Splitter Plates," Report FM 10, Dept. of Mech. Eng., University of Melbourne, 1979.

4 Tanner, M., "Reduction of Base Drag," in *Progr. Aerospace Sci.*, Vol. 16, 1975, pp. 369–384.

5 Bradshaw, P., and Wong, F. Y. F., "The Reattachment and Relaxation of a Turbulent Shear Layer," *Journal of Fluid Mechanics*, Vol. 52, 1972, pp. 113–135.

6 Smits, A. J., and Baskaran, V., "Two-Dimensional Solid Blockage in a Slotted Wall Wind Tunnel," *Proc. Seventh Australasian Hydraulics and Fluid Mechanics Conference*, Brisbane, Aug. 1980, pp. 131–134.

7 Patel, V. C., "Calibration of the Preston Tube and Limitations on its Use

in Pressure Gradients," *Journal of Fluid Mechanics*, Vol. 23, 1965, pp. 185–208.

8 Bradshaw, P., *Experimental Fluid Mechanics*, Pergamon Press, 1964.

9 Chue, S. H., "Pressure Probes for Fluid Measurement," *Progr. in Aero. Sciences*, Vol. 16, 1975, pp. 147–223.

10 Toomre, A. "Effect of Turbulence on Static Pressure Measurements," Brit. A.R.C. 22010, 1960.

11 Smits, A. J., Baskaran, V., and Joubert, P. N., "Measurements in a Turbulent Boundary Layer over a Two-Dimensional Hill," *Proceedings Third Symposium on Turbulent Shear Flows*, University of California, Davis, Sept. 1981.

12 Perry, A. E., and Fairlie, B. D., "Critical Points in Flow Patterns," *Adv. in Geophysics*, B18, p. 299.

13 Good, M. C., and Joubert, P. N., "The Form Drag of Two-Dimensional Bluff Plates Immersed in Turbulent Boundary Layers," *Journal of Fluid Mechanics*, Vol. 31, 1968, pp. 547–582.

14 Roshko, A., and Lau, J. C., "Some Observations on Transition and Reattachment of a Free Shear Layer in Incompressible Flow," *Proc. of the 1965 Heat Transfer and Fluid Mech. Inst.*, 1965, pp. 157–167.

15 Castro, I. P., and Fackrell, J. E., "A Note on Two-Dimensional Fence Flows, with Emphasis on Wall Constraint," *Journal of Industrial Aerodynamics*, Vol. 3, 1978, pp. 1–20.

16 Winant, C. D., and Browand, F. K., "Vortex Pairing: the Mechanism of Turbulent Mixing-Layer Growth at Moderate Reynolds Number," *Journal of Fluid Mechanics*, Vol. 63, 1974, pp. 237–256.

17 Nash, J. F., Quincey, V. G., and Callinan, J., "Experiments on Two-Dimensional Base Flows at Subsonic and Transonic Speeds," Aero. Res. Council, Rep. and Mem 3427, 1963.

18 Mueller, T. J., Korst, H. H., and Chow, W. L., "On the Separation, Reattachment and Redevelopment of Incompressible Turbulent Shear Flow," ASME *Journal of Basic Engineering*, Vol. 86, June 1964, pp. 221–226.

19 Ota, T., and Itasaka, M., "A Separated and Reattached Flow on a Blunt Flat Plate," ASME JOURNAL OF FLUIDS ENGINEERING, Vol. 98, Mar. 1976, pp. 79–86.

20 Smits, A. J., "A Visual Study of a Separation Bubble," *Proc. Inter. Symp. on Flow Visualization*, Bochum, Sept. 1980, pp. 204–208.

On the Analysis of Turbulent Boundary Layers on Slender Cylinders

J. A. D. Ackroyd
Lecturer,
Department of the Mechanics of Fluids,
University of Manchester,
Manchester, England

An earlier analysis of turbulent flow along a cylinder in a uniform stream by White is corrected. The analysis has been extended to include turbulent flow along a cylinder extruding through an orifice into a fluid at rest. The analyses are compared with the available data for drag and, except in the case of the cylinder extruding into a fluid at rest, the comparison is reasonably encouraging.

Introduction

Transverse curvature effects on boundary layer development are of importance in many situations encountered in the engineering and artificial fibre industries. The turbulent boundary layer on a stationary slender cylinder placed with its axis parallel to a uniform stream has been analysed on a number of occasions and a comprehensive list of references is given by White [1]. His analysis is one of the few based on a velocity profile shape which has some experimental verification. White [1] used the profile shape suggested by Rao [2] and included a comparison between Rao's [2] hypothesis and the available experimental velocity profile data. The comparison appeared promising, although subsequently the data used have been criticised (see, for example, Afzal and Narasimha [3]). However, the present work is not so much concerned with that aspect of the problem as with two points in White's [1] work. The first is that two algebraic errors occur in White's [1] analysis and each has serious consequences for the results. We shall show, however, that for most circumstances the two errors tend to cancel each other. The second point concerns the application of White's [1] results and we shall return to this presently.

It was felt that results based on serious mathematical errors should be corrected and this is done in the next section. However, rather than use White's [1] method, we adopt the rather more straightforward approach used by Tsou et al. [4] in their study of the extrusion of a flat sheet into a fluid at rest. A corrected form of White's [1] method is given separately in an Appendix, the errors in White's [1] original method being discussed in detail there.

In the methods of both White [1] and Tsou et al. [4] relationships are obtained between skin friction and boundary layer development length in the form of double integrals which usually are evaluated numerically. As we shall show in the next section, however, interchange of the sequence of integration reduces the problem to that of the numerical evaluation of single integrals, with consequent saving of numerical labour. The next section also contains a reasonably encouraging comparison between Rao's [2] velocity profile hypothesis and the recent and most carefully obtained experimental data of Willmarth et al. [5], thus supporting White's [1] initial use of this hypothesis.

Our second point concerning White's [1] work is that he compares his results with the experimental drag data of Selwood [6]. However, the latter work is concerned with a different problem, that of the extrusion of a slender cylinder through an orifice into a fluid at rest. Laminar flow solutions to this problem have been given by Sakiadis [7] and by Crane [8] but, to the author's knowledge, only Sakiadis [7] has attempted a turbulent flow analysis based on an assumed power law velocity profile. It is argued later that Rao's [2] hypothesis, extended along lines suggested by the experimental work of Tsou et al. [4], might provide a more realistic velocity profile shape. The present method of analysis therefore can be extended to include the extruding cylinder case and this is done later.

The recent experimental data for drag on a cylinder in a uniform axial stream provided by Gould and Smith [9] and the experimental drag data of Selwood [6] are compared with the analyses in the last section.

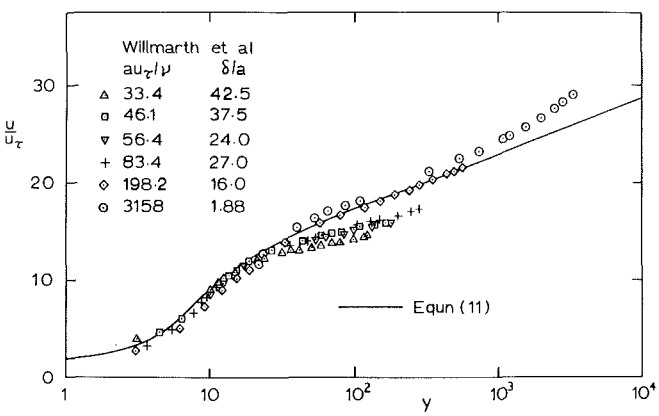

Fig. 1 Graphs of u/u_τ against Y

Contributed by the Fluids Engineering Division for publication in the JOURNAL OF FLUIDS ENGINEERING. Manuscript received by the Fluids Engineering Division, April 30, 1980.

Flow Along a Cylinder in a Uniform Stream

For this case Glauert and Lighthill [10] have shown that the integral momentum equation is

$$\frac{d\theta}{dz} = \frac{2\pi a}{\rho U^2}\tau_w, \tag{1}$$

where the momentum defect area, θ, is defined as

$$\theta = 2\pi\int_a^\delta \frac{u}{U}\left(1-\frac{u}{U}\right)rdr. \tag{2}$$

We define

$$\frac{c_f}{2} = \frac{\tau_w}{\rho U^2} = \frac{u_\tau^2}{U^2} = \frac{1}{\lambda^2}, \tag{3}$$

where u_τ is the friction velocity. Following White [1], we assume that the velocity profile has the form

$$\frac{u}{u_\tau} = f(Y),\ Y = \frac{au_\tau}{\nu}\ln\left(\frac{r}{a}\right). \tag{4}$$

We shall consider the assumptions of equations (4) and the specific form of $f(Y)$ presently.

With the aid of equations (3) and (4), we obtain equation (1) in the form

$$\left.\begin{aligned} &\frac{d\mathrm{Re}_z}{dI} = \lambda^2, \\ &\text{where } \mathrm{Re}_z = \frac{Uz}{\nu}, \\ &I(\lambda;\ \mathrm{Re}_a) = \int_0^\lambda \frac{f(\lambda-f)}{\lambda}e^{2Y\lambda/\mathrm{Re}_a}\frac{dY}{df}df \\ &\text{and } \mathrm{Re}_a = \frac{Ua}{\nu}. \end{aligned}\right\} \tag{5}$$

Integration by parts yields equations (5) in the form

$$\mathrm{Re}_z = \lambda^2 I(\lambda;\ \mathrm{Re}_a) - 2\int_0^\lambda \lambda_1 I(\lambda_1;\ \mathrm{Re}_a)d\lambda_1, \tag{6}$$

where we assume that $c_f \to \infty$ as $z \to 0$. This result has the form obtained by Tsou et al. [4] with the exception that the integral I, for the present problem, is defined by equations (5). Rather than carry-out the numerical double integration contained in equation (6) directly, we reverse the sequence of integration and reduce the problem to that of the numerical evaluation of a single integral, i.e.

$$\mathrm{Re}_z = \lambda^2 I(\lambda;\mathrm{Re}_a) - 2\int_0^\lambda f\frac{dY}{df}\left(\int_f^\lambda(\lambda_1 - f)e^{2Y\lambda_1/\mathrm{Re}_a}d\lambda_1\right)df \tag{7}$$

$$= \int_0^\lambda f\frac{dY}{df}\left((\lambda-f)\left(\lambda-\frac{\mathrm{Re}_a}{Y}\right)e^{2Y\lambda/\mathrm{Re}_a} + \frac{\mathrm{Re}_a^2(e^{2Y\lambda/\mathrm{Re}_a} - e^{2Yf/\mathrm{Re}_a})}{2Y^2}\right)df. \tag{8}$$

It is convenient to carry-out the above integrations with respect to f, rather than Y, since when $r = \delta$, $f = \lambda$. Furthermore, we shall use an inverse relation for the velocity profile in the form $Y = Y(f)$.

The corresponding result for the frictional drag force, D, is

$$D = \rho U^2\theta_L, \tag{9}$$

where $z = L$ is the axial length of the cylinder. Thus,

$$C_D = \frac{D}{\rho U^2 \pi aL} = \frac{2}{\mathrm{Re}_L}I(\lambda_L;\ \mathrm{Re}_a),\ \mathrm{Re}_L = \frac{UL}{\nu}. \tag{10}$$

Clearly, the validity of the above method depends on the correctness of the assumption, originally due to Rao [2], for the velocity profile embodied in equations (4). Note that this assumption is intended to apply to all but the outer region of the boundary layer. White [1] reviewed the data available at the time and made a convincing case for the above assumption. Subsequently, other investigators have questioned the data used by White [1] (see, for example, the detailed discussion of Afzal and Narasimha [3]) on the grounds that c_f had not been known accurately and that some data had perhaps been obtained in flows which were not in a fully developed turbulent state. More recently, data which apparently do not suffer from these defects have been provided by Willmarth et al. [5] and these are presented in Fig. 1, in the form suggested by Rao [2]. The intention of Rao's [2] correlation is to transform axisymmetric flow velocity profiles to two-dimensional flow profiles, the latter being represented by the solid line in Fig. 1. While the case for Rao's [2] correlation presented in Fig. 1 looks at first sight less convincing than did the corresponding figure in White [1], one should recall that outer region data need not follow this correlation. As can be seen in Fig. 1, departures from the solid

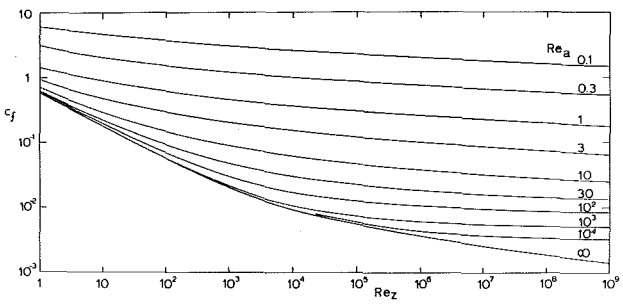

Fig. 2 Cylinder in uniform stream: c_f against Re_z

Nomenclature

- a = cylinder radius
- c_f = local skin friction coefficient, equations (3) and (16)
- C_D = drag coefficient, equations (10) and (23)
- D = drag force, equations (9) and (22)
- f = law of the wall function, equation (4)
- G = integral function, equation (30)
- I = integral function, equations (5) and (19)
- L = cylinder length
- r,z = radial and axial coordinates
- Re = Reynolds number based on length scale given by suffix
- u,v = axial and radial velocity components
- U = free stream or cylinder velocity
- u_τ = friction velocity, equations (3) and (16)
- Y = law of the wall variable, equation (4)
- Z = z, equation (27)
- δ = boundary layer thickness
- θ = momentum defect and excess thicknesses, equations (2) and (18)
- λ = friction variable, equations (3) and (16)
- ν = kinematic viscosity
- ρ = density
- τ = shear stress
- ϕ = law of the wall function, equation (11)

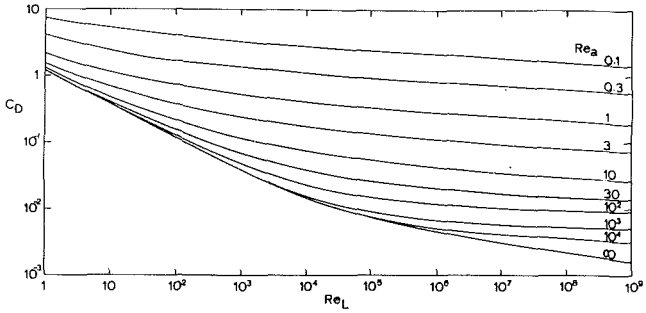

Fig. 3 Cylinder in uniform stream; C_D against Re_L

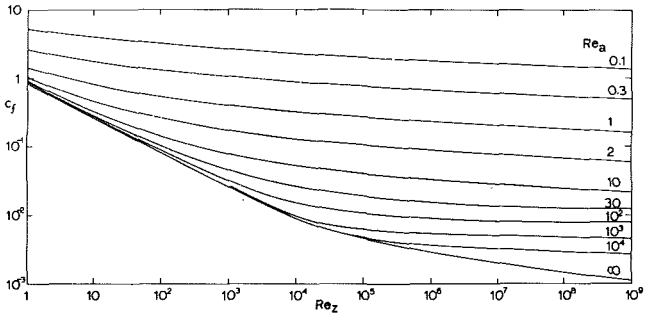

Fig. 4 Extruding Cylinder; c_f against Re_z

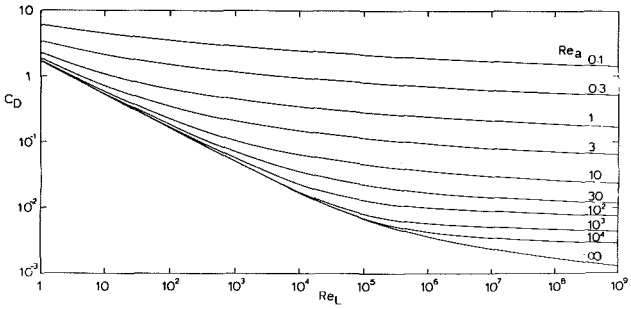

Fig. 5 Extruding Cylinder; C_D against Re_L

line occur entirely in the outer portion of the boundary layers. Although entirely acceptable correlations for these boundary layers have yet to be provided, nevertheless, it appears that the correlation of Rao [2] used by White [1] remains as good as, or even superior to, those alternatives reviewed more recently by Afzal and Narasimha [3]. Consequently, as in White's [1] analysis, we use the two-dimensional flow relation of Spalding [11] for the velocity profile $f(Y)$, i.e.

$$\left.\begin{aligned} Y &= f + 0.1108\left(e^{\phi} - 1 - \phi - \frac{\phi^2}{2} - \frac{\phi^3}{6} - \frac{\phi^4}{24}\right) \\ \phi &= 0.4f. \end{aligned}\right\} \tag{11}$$

Equations (8) and (10) have been integrated numerically using the Runge-Kutta-Merson method. Unfortunately, the integrand of equation (8) is singular at $f = 0$ but equation (7) does not suffer from this difficulty. It is possible to show from equations (7) and (10) that

$$\lim_{f\to 0}\left(\frac{d\mathrm{Re}_z}{df}\right) = \lim_{f\to 0}\left(\frac{d(C_D \mathrm{Re}_L \lambda_L}{df}\right) = 0, \tag{12}$$

these results being required to initiate the numerical integration. Estimates of numerical errors provided by the Merson method were at most of order 10^{-3} of the values calculated for Re_z and $C_D\mathrm{Re}_L$. This order of error occurred only at the highest values of c_f; for lower values of c_f, errors were very considerably reduced.

Equations (8) and (10) provide relations between Re_z and λ (or Re_L and λ_L) and C_D and λ_L, respectively, for a given value of Re_a. From the former relation Fig. 2 has been prepared using equations (3) to relate λ to c_f. This, in combination with the second relation, allows the construction of Fig. 3 which shows the variation of C_D with Re_L for fixed values of Re_a. As discussed in the Appendix, the algebraic errors in White's [1] analysis result in numerical errors in the final results of no more than ten percent. Consequently, to the scale adopted in Fig. 2, and within the more limited range of White's [1] results, the present curves are indistinguishable from those of White [1].

For $\mathrm{Re}_a \to \infty$, the above results should reduce to those for the case of the flat plate in a uniform stream. Expansion of the exponential terms in equations (8) and (10) gives for the limiting case, $\mathrm{Re}_a \to \infty$,

$$\mathrm{Re}_x = \int_0^{\lambda} f^2(\lambda - f)\frac{dY}{df}\,df, \tag{13a}$$

$$C_D = \frac{2}{\lambda_L \mathrm{Re}_L}\int_0^{\lambda_L} f(\lambda_L - f)\frac{dY}{df}\,df, \tag{13b}$$

where x here denotes the distance from the plate leading edge and C_D is evaluated for one surface of the plate only. A separate analysis of the case of the flat plate yields identical results. Results from equations (13) are incorporated in Figs. 2 and 3.

From Fig. 1 we see that as $\mathrm{Re}_a \to 0$, $f \simeq Y$, in which case the analysis reduces to that performed for laminar flow by Glauert and Lighthill [10], using the integral momentum method. Using equations (5) and (10), we find that as $\mathrm{Re}_a \to 0$,

$$c_f \frac{\mathrm{Re}_a}{4}\ln\left(4\frac{\mathrm{Re}_z}{\mathrm{Re}_a{}^2}\right) \to 1,\ C_D \frac{\mathrm{Re}_a}{4}\ln\left(4\frac{\mathrm{Re}_L}{\mathrm{Re}_a{}^2}\right) \to 1. \tag{14}$$

Although this quasi-laminar behaviour was noted by White [1], the physical significance remains obscure.

Flow Along An Extruding Cylinder in a Fluid at Rest

In this case the cylinder moves with constant velocity U through a fluid at rest, the point of extrusion of the cylinder and of the boundary layer origin being fixed in space. This case cannot be related to that of the cylinder in a uniform stream discussed in the previous section, since the imposition of a velocity $-U$ to the complete flow about an extruding cylinder, so as to reduce the cylinder surface to rest, results in the origin of the boundary layer moving uniformly with velocity $-U$.

Before considering the extruding cylinder flow, we shall consider briefly the case of the extruding two-dimensional sheet. Application of Millikan's [12] functional arguments shows that for the latter case the form of the turbulent velocity profile should be identical to that of the boundary layer on a flat plate in a uniform stream, provided that the u velocity component is measured relative to the moving sheet. The experimental work of Tsou et al. [4] confirms this and, furthermore, shows that most of the constants in the functional relationships (the outer region was not discussed) are identical to those for the turbulent boundary layer on a flat plate in a uniform stream.

Turning now to the extruding cylinder case, examination of the surface sub-layer suggests a velocity profile of the form

$$\frac{U-u}{u_\tau} = f(Y),\ Y = \frac{au_\tau}{\nu}\ln\left(\frac{r}{a}\right), \tag{15}$$

the function f being equal to its argument very close to the surface. Here, U is the uniform surface velocity and u_τ is defined now as

$$\frac{c_f}{2} = -\frac{\tau_w}{\rho U^2} = \frac{u_\tau^2}{U^2} = \frac{1}{\lambda^2}. \tag{16}$$

It is seen that equation (15) for $U - u$ is consistent with the behaviour described above for the extruding sheet.

Since there are, to the author's knowledge, no experimental data for turbulent velocity profiles around extruding cylinders, we assume that Rao's [2] hypothesis can be applied here, i.e. that equations (15) apply to all but the outer region of the boundary layer and that the function $f(Y)$ is given by equation (11).

Crane [8] has shown that the integral momentum equation for this case is

$$\frac{d\theta}{dz} = -\frac{2\pi a}{\rho U^2}\tau_w \tag{17}$$

where the momentum excess area, θ, is defined as

$$\theta = 2\pi\int_a^\delta \left(\frac{u}{U}\right)^2 r dr. \tag{18}$$

Use of equations (15)-(18) results in equation (6) but now I is defined by

$$I(\lambda; \mathrm{Re}_a) = \int_0^\lambda \frac{(\lambda - f)^2}{\lambda} e^{2Y\lambda/\mathrm{Re}_a} \frac{dY}{df} df, \tag{19}$$

instead of by equations (5). Interchange of the sequence of integration gives

$$\mathrm{Re}_z = \lambda^2 I(\lambda; \mathrm{Re}_a)$$
$$-2\int_0^\lambda \frac{dY}{df}\left(\int_f^\lambda (\lambda_1 - f)^2 e^{2Y\lambda_1/\mathrm{Re}_a} d\lambda_1\right) df \tag{20}$$

$$= \int_0^\lambda \frac{dY}{df}\left((\lambda - f)\left((\lambda - f)\left(\lambda - \frac{\mathrm{Re}_a}{Y}\right) + \frac{\mathrm{Re}_a^2}{Y^2}\right) e^{2Y\lambda/\mathrm{Re}_a}\right.$$
$$\left. - \frac{\mathrm{Re}_a^3}{2Y^3}(e^{2Y\lambda/\mathrm{Re}_a} - e^{2Yf/\mathrm{Re}_a})\right) df. \tag{21}$$

The corresponding result for the frictional drag force, D, on a cylinder of length L is

$$-D = \rho U^2 \theta_L, \tag{22}$$

the negative sign indicating that the force opposes the motion. Thus,

$$C_D = -\frac{D}{\rho U^2 \pi a L} = \frac{2}{\mathrm{Re}_L} I(\lambda_L; \mathrm{Re}_a). \tag{23}$$

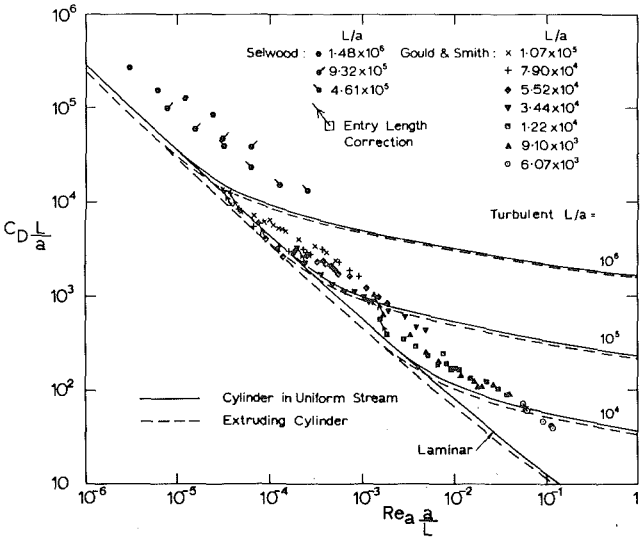

Fig. 6 Graphs of $C_D L/a$ against $\mathrm{Re}_a a/L$

It is seen that the form of the results differs little from that obtained for the case of the cylinder in a uniform stream and the numerical integration procedure used was identical to that used in that case. However, in the present case, using equations (20) and (23), it was necessary to deduce that the limiting values

$$\lim_{f\to 0}\left(\frac{d\mathrm{Re}_z}{df}\right) = \frac{\lambda^3}{3}, \lim_{f\to 0}\left(\frac{d(-C_D\mathrm{Re}_L\lambda_L)}{df}\right) = 2\lambda_L^2, \tag{24}$$

in order to initiate numerical integration.

As $\mathrm{Re}_a \to \infty$ the case of the extruding sheet is recovered and expansion of the exponential terms in equations (21) and (23) yields

$$\left.\begin{aligned} \mathrm{Re}_x &= \int_0^\lambda \left(\frac{\lambda^3}{3} + \frac{2}{3}f^3 - \lambda f^2\right)\frac{dY}{df} df, \\ C_D &= \frac{2}{\mathrm{Re}_L}\int_0^{\lambda_L} \frac{(\lambda_L - f)^2}{\lambda_L}\frac{dY}{df} df, \end{aligned}\right\} \tag{25}$$

the drag force being that for one surface of the sheet only.

Once again, as $\mathrm{Re}_a \to 0$ we expect to recover results obtained for laminar flow. The latter can be deduced[1] from an analysis by Sakiadis [7] and are identical to equations (14).

The results obtained from equations (21) and (23) for c_f against Re_z and for C_D against Re_L are shown in Figs. 4 and 5, respectively.

Comparison Between Analyses and Experiment

In comparing his analysis with the available experimental data for drag, White [1] commented that the correlation was, in general, reasonably good, except in the case of the data of Selwood [6]. This remark prompted the present author to undertake the analysis given in the preceding section on the grounds indicated in the introduction. We shall return to the question of Selwood's [6] data presently. More recently, extensive data for drag on a cylinder in a uniform axial stream have been provided by Gould and Smith [9] and it is these data with which we shall be concerned.

In comparing the present analyses with the experimental data, it is useful to do this in terms of the variables which occur naturally in the laminar analyses. In the latter, $C_D L/a$ is a function of $\mathrm{Re}_a a/L$ only and these variables have been plotted in Fig. 6 for the cases of a cylinder in a uniform stream and a cylinder extruding through a fluid at rest. The analytical results shown are obtained, in the former case, from the analysis of Glauert and Lighthill [10] and, in the latter case, from the analyses of Crane [8] and Sakiadis [7]. The results obtained from the present analyses, for turbulent flow, could be obtained, in principle, by interpolation from Figs. 3 and 5. However, this has been found to be highly inaccurate. Consequently, what has been done is to use a linear iterative method which uses equations (8) and (21) to estimate, for a specified value of Re_a, the value of λ_L which yields a specified value of Re_L, to within an error of 0.01 percent in Re_L. Simultaneously, equations (10) and (23) are used to calculate the corresponding values of $C_D\mathrm{Re}_L$. Thereafter, values for $C_D L/a$ and $\mathrm{Re}_a a/L$ follow immediately and these are included in Fig. 6. It is seen in that figure that the various analyses for the two different flow geometries do not produce significantly different results.

[1] Crane [8] has deduced this behaviour from the analysis of Sakiadis [7]. Unfortunately, a factor of 2 has been omitted from Crane's [8] equations (36) and (39) for $\theta/(\pi a^2)$.

Before comparing the experimental data with the analyses, it should be recognised that errors exist in the latter because of the over-simplification used in the description of the velocity profiles, i.e. equations (4) and (11). To the author's knowledge, no satisfactory correlation for the outer region exists so that any estimate of the error introduced by the use of equation (11) in the outer region must be necessarily qualitative. However, examination of the data given in Fig. 1 suggests an error of similar small order to that mentioned by White [1]. Furthermore, as $\mathrm{Re}_a \rightarrow 0$, the data in Fig. 1 suggest that this error should reduce progressively.

The results of Selwood's [6] experiments for the extruding cylinder case are included in Fig. 6 and although the trend appears to be in reasonable agreement with the analysis, the magnitudes of C_D differ greatly. Despite the possible shortcomings of the present analysis, doubts raised by both White [1] and Gould and Smith [9] regarding the accuracy of Selwood's [6] measured drag force seem justified. Gould and Smith [9] also have demonstrated experimentally that transverse motion of the cylinder (a flexible nylon thread in both their and Selwood's [6] experiments) can produce a significant increase in the drag force.

The experimental data of Gould and Smith [9] for the case of the cylinder in a uniform stream, shown in Fig. 6, appear rather more promising. The data for a given value of L/a appear to follow the laminar flow analysis (or the "turbulent" analysis for small values of Re_a) at the lower values of $\mathrm{Re}_a a/L$ and drift toward the appropriate curve of the turbulent flow analysis at the higher values of $\mathrm{Re}_a a/L$. Unfortunately, the range of the experimental data is limited and it is not possible to demonstrate conclusive agreement with the entirely turbulent flow analysis. Furthermore, discrepancies remain and it is seen that generally C_D appears to be rather higher than analyses predict. Although the analyses are approximate, the experimental data of Gould and Smith [9] also can be criticised. The experimental data were obtained in a fairly short vertical pipe, the air flow entering the pipe at its upper end. The cylinder was placed along the pipe centre line and the flow velocity was measured with a pitot-static tube near the centre of the lower end of the pipe. The boundary layer growth on the pipe wall would produce an increase in the pipe centre line velocity above its value at the pipe mouth and this pipe entry flow would introduce two sources of error in the reduction of the experimental data. Firstly, the nonuniformity of the centre line velocity along the length of the cylinder would expose the cylinder to a lower average velocity than that used in the calculation of C_D and Re_a. Secondly, the favourable pressure gradient in the pipe might be expected to yield a higher drag force than that obtained in a uniform stream. While it is very difficult, at this stage, to correct for the second effect, we can make a reasonable estimate of the error introduced by the first effect. What has been done is to use the experimental data for the laminar entry flow in a pipe quoted by Schlicting [3] to estimate the maximum variation in centre line velocity which might occur at a particular value of L/a. We then find the average velocity along the length of the cylinder and use that to adjust the values of C_D and Re_a. This has been done for the lowest and highest values only of $\mathrm{Re}_a a/L$ for each value of L/a shown in Fig. 6. The change produced at the highest values of $\mathrm{Re}_a a/L$ is insignificant and, therefore, has not been included in Fig. 6, whereas the change at the lowest values of $\mathrm{Re}_a a/L$ is quite large, as may be seen in that figure. The correction indicates that experimental data lying below the laminar curve can, with some justification, be moved to lie above the curve. Nevertheless, discrepancies remain and these could be due to the effects of the favourable pressure gradient in the experimental data as well as to shortcomings in the analyses.

Conclusions

Two mathematical errors in the analysis of White [1] for the turbulent flow about a cylinder in a uniform axial stream have been corrected. Although each error is significant in itself, it has been found that the overall correction is not very significant because the two errors tend to cancel each other. The method of analysis has been extended to include turbulent flow along a cylinder extruding through an orifice into a fluid at rest in an attempt to explain the experimental data of Selwood [6]. In this latter respect, the analysis has not been successful, although it is recognised that the fault may lie in the experimental data.

Comparison of the analyses for laminar and turbulent flows about cylinders in a uniform stream with the recent experimental data of Gould and Smith [9] is encouraging. Corrections carried out on the data of Gould and Smith [9] for the effects of flow non-uniformity suggest, in certain respects, a better correlation between the analyses and the experiments.

Both in White's [1] and the present investigations, the analyses have depended heavily on Rao's [2] method of experimental data reduction for the turbulent flow velocity profile. Relevant experimental data are not extensive and, whilst the data of Willmarth et al. [5] have been found to show reasonable agreement with Rao's [2] hypothesis, the necessarily required empirical profile could be improved only by further extensive experimental measurement. In this connection, it should be emphasised that a conclusive investigation of the behaviour of the outer region has yet to be undertaken. It is important for this to be achieved before a more accurate analysis along the lines suggested here could be undertaken.

Acknowledgments

The author is grateful to I. M. Hall for his excellent advice and to T. H. Bull, F. Smith and M. Wilson of ICI Fibres, Harrogate, for their helpful discussion of their work.

References

1 White, F. M., "An Analysis of Axisymmetric Turbulent Flow Past a Long Cylinder," ASME *Journal of Basic Engineering*, Vol. 94, 1972, pp. 200–206.

2 Rao, G. N. V., "The Law of the Wall in a Thick Axisymmetric Turbulent Boundary Layer," ASME *Journal of Applied Mechanics*, Vol. 34, 1967, pp. 237–238.

3 Afzal, N. and Narasimha, R., "Axisymmetric Turbulent Boundary Layer along a Circular Cylinder at Constant Pressure," *Journal of Fluid Mechanics*, Vol. 74, 1976, pp. 113–128.

4 Tsou, F. K., Sparrow, E. M., and Goldstein, R. J., "Flow and Heat Transfer in the Boundary Layer on a Continuous Moving Surface," *International Journal Heat Mass Trans.* Vol. 10, 1967, pp. 219–235.

5 Willmarth, W. W., Winkel, R. E., Bogar, T. J., and Sharma, L. K., "Axially Symmetric Turbulent Boundary Layers on Cylinders," Rep. No. 021490-3-T, 1975, Dept. Aerospace Engng., Univ. Michigan.

6 Selwood, A., "The Axial Air-drag of Monofilaments," *Trans. of the Journal of the Textile Institute*, Vol. 53, 1962, p. 576.

7 Sakiadis, B. C., "Boundary Layer Behaviour on Continuous Solid Surfaces: III The Boundary Layer on a Continuous Cylindrical Surface," *A. I. Ch. E. Journal*, Vol. 7, 1961, pp.467–472.

8 Crane, L. J., "Boundary Layer Flow on a Circular Cylinder Moving in a Fluid at Rest," *ZAMP*, Vol. 23, 1972, pp. 201–212.

9 Gould, J., and Smith, F. S., "Air-drag on Synthetic-Fibre Textile Monofilaments and Yarns in Axial Flow at Speeds of up to 100 m/s," *Journal of the Textile Institute*, Vol. 71, 1980, pp. 38–49.

10 Glauert, M. B., and Lighthill, M. J., "The Axisymmetric Boundary Layer on a Long Thin Cylinder," *Proc. Roy. Soc. A*, Vol. 230, 1955, pp. 188–203.

11 Spalding, D. B., "A Single Formula for the Law of the Wall," ASME *Journal of Applied Mechanics*, Vol. 28, 1961, pp. 455–458.

12 Millikan, C. B., Proceedings of the Fifth International Congress of Applied Mechanics, 1938, pp. 386–392.

13 Schlichting, H., *Boundary Layer Theory*, 4th ed., McGraw-Hill, New York, 1960, p. 257.

APPENDIX

White's [1] analysis contains two algebraic errors, the effects of which, as we shall see, nearly cancel each other. Each error, made alone, would have produced considerable errors in the final results.

Using axisymmetric co-ordinates z, r with corresponding velocity components, u, v, we follow White [1] and write the continuity equation as

$$rv = -\frac{\partial}{\partial z}\left(\int_a^r ur_1 dr_1\right), \tag{26}$$

since $v = 0$ at $r = a$. It is convenient to change the independent variables from z, r to Z, Y where Y is given by equations (4),

$$Z = z, \tag{27}$$

and we assume that velocity profiles for u are of the form given in equations (4). Thus, since $u_\tau = u_\tau(z)$, whilst a and ν are constants, we have

$$\left.\begin{aligned} rv = -a\nu\left(\left(\frac{\partial}{\partial Z}\right)_y + \left(\frac{\partial Y}{\partial z}\right)_r \left(\frac{\partial}{\partial Y}\right)_Z\right)\left\{\int_0^Y fe^{2Y_1\nu/(au_\tau)} dY_1\right\}, \\ \left(\frac{\partial Y}{\partial z}\right)_r = \frac{Y}{u_\tau}\frac{du_\tau}{dZ} \end{aligned}\right\} \tag{28}$$

and this gives

$$rv = -\frac{\nu}{a}\left(\frac{\partial Y}{\partial z}\right)_r \left(r^2 f - \frac{2\nu}{au_\tau}\frac{1}{Y}\int_0^Y fr^2 Y_1 dY_1\right). \tag{29}$$

Only the first term on the right-hand side of equation (4) was obtained by White [1] in his equation (6). Paradoxically, the correct result was suggested in the published discussion which follows White's [1] paper, only to be rejected as incorrect.

White's [1] approach can now be repeated and at each stage of the analysis it is found that terms additional to those given in White's [1] equations (7), (8), and (10) are obtained. In particular, the final result, which can be compared with White's [1] equation (10), is

$$\mathrm{Re}_z = \int_0^\lambda G(\lambda_1) d\lambda_1, \tag{30a}$$

$$G(\lambda_1) = \int_0^{\lambda_1} f\frac{dY}{df} e^{2Y\lambda_1/\mathrm{Re}_a}\left(f + \frac{2Y\lambda_1}{\mathrm{Re}_a}(\lambda_1 - f)\right) df. \tag{30b}$$

It is at this stage of the analysis that the second error is introduced into White's [1] analysis. We note that

$$\frac{\lambda}{\mathrm{Re}_a} = \frac{\nu}{au_\tau} \tag{31}$$

and White [1] claims that the double integration contained in his (incorrect) form of equations (30) was performed numerically for fixed values of au_τ/ν. Clearly, this procedure is incorrect since it is Re_a which is constant, whereas λ is a variable. We shall return to this second error presently. Meanwhile, we note that interchange of the sequence of integration simplifies the numerical integration required in equations (30);

$$\mathrm{Re}_z = \int_0^\lambda f\frac{dY}{df}\left(\int_f^\lambda \left(f + \frac{2Y\lambda_1}{\mathrm{Re}_a}(\lambda_1 - f)\right) e^{2Y\lambda_1/\mathrm{Re}_a} d\lambda_1\right) df. \tag{32}$$

The integration with respect to λ_1 can be performed analytically (treating f, Y and Re_a as constants) and the resulting expression for Re_z is that given in equations (7).

In order to obtain some idea of the scale of the numerical errors introduced by the above two algebraic errors, we can take White's [1] incorrect form of equation (30),

$$\mathrm{Re}_z = \int_0^\lambda \left(\int_0^{\lambda_1} f^2 e^{2Y\lambda_1/\mathrm{Re}_a}\frac{dY}{df} df\right) d\lambda_1, \tag{33}$$

and interchange the sequence of integration to yield

$$\mathrm{Re}_z = \frac{\mathrm{Re}_a}{2}\int_0^\lambda \frac{f^2}{Y}\frac{dY}{df}\left(e^{2Y\lambda/\mathrm{Re}_a} - e^{2Yf/\mathrm{Re}_a}\right) df. \tag{34}$$

This is the result which White [1] would have obtained by the present single integral method had he made the first error only. However, as already noted, White [1] evaluated the double integral (33) keeping the exponent of the exponential, λ/Re_a, fixed. If we repeat this procedure whilst interchanging the sequence of integration, we obtain

$$\mathrm{Re}_z = \int_0^\lambda f^2(\lambda - f) e^{2Y\lambda/\mathrm{Re}_a}\frac{dY}{df} df. \tag{35}$$

This is the result which White [1] would have obtained by the present single integral method. Thus, equation (35) allows a repetition of White's [1] numerical results for comparison with the present results, using a single numerical integration. The errors are found to be negligibly small at the lowest values of c_f and increase with increasing c_f to a maximum of ten per cent. On the other hand, use of equation (34) (incorporating the first error only) yields numerical results which are in error by amounts lying between ten and sixty per cent over the same range of c_f.

On the Scaling of Impulsively Started Incompressible Turbulent Round Jets

T.-W. Kuo
Graduate Student.

F. V. Bracco
Associate Professor.

Department of Mechanical & Aerospace Engineering, Princeton University, Princeton, N.J. 08544

A scaling law for transient, turbulent, incompressible, round jets is reported. Numerical solutions of the Navier-Stokes equations were obtained using a k-ϵ model for turbulence. The constants of the k-ϵ model were optimized by comparing computed centerline velocity, mean radial velocity distribution, longitudinal kinetic energy distributions with those measured by other authors in steady round jets. The resulting constants are those also used in computations of steady planar jets except for the one that multiplies the source term in the ϵ-equation. After optimization, the agreement is satisfactory for all mean quantities but is still rather poor for the kinetic energy distribution. Parameteric studies of the transient were performed for $9 \cdot 10^3 \leq Re_D \leq 10^5$. *Then the definition was adopted that a jet reaches steady state between the nozzle and an axial location when, at that location, the centerline velocity achieves 70 percent of its steady state value, and characteristic steadying length and time scales* ($D \cdot Re_D^{0.053}$ *and* $D \cdot Re_D^{0.053}/u_{\ell,0}$ *respectively*) *were determined as well as a unique function that relates dimensionless steadying time to dimensionless steadying length. This function changes in a predictable way if a percent other than 70 is selected but the characteristic length and time scales do not. It is found that the 70 percent threshold is reached within the head vortex of the transient jet. Thus a transient jet, practically, is a steady jet except within its head vortex. This, in part, justifies our use of steady state k-ϵ constants in our transient computations. The computed jet tip arrival times are shown to compare favorably with measured ones.*

Introduction

It would appear that the transient of turbulent, or even laminar, incompressible jets has been considered only limitedly, probably because of difficulties in making reliable measurements in unsteady flows and of the large computation time required to solve the unsteady Navier-Stokes equations [1].

Hengrussamee et al. [2] reported experimental and theoretical studies of an impulsively started turbulent air-into-air injection with emphasis on the evaluation of the three different numerical integration techniques they used to solve the equations for a particular set of experimental measurements at $Re_D \simeq 10^6$. Their main purpose was to test the prediction capability of the numerical techniques in preparation for application to the case of non-uniform density. A two-equation k-ϵ turbulence model was also evaluated with a set of model constants designed for the prediction of confined, steady state, duct flow. The jet penetration rate they predicted was much higher than the measured one. Recently, Witze [3] measured steady and transient centerline axial velocity distributions and transient jet arrival time and other quantities in impulsively started air-into-air jets. His transient jet arrival time will be used for comparison with our calculations.

By looking at photographic records, one gets the impression that impulsively started turbulent round jets scale up in time. But the specific law of such scaling does not seem to have been previously identified and reported. Through numerical computations we have derived the scaling rules and we discuss them in this paper.

The general organization of the paper is as follows. First, the governing differential equations and the corresponding initial and boundary conditions are given together with the method of solution used and comments on the numerical accuracy of the results.

Second, brief reviews of similar applications of the k-ϵ model and of the available information on the physics of the transient of round jets are given. The reviews are followed by an optimization study of the constants of the k-ϵ model using the detailed experimental measurements of Bogustawski et al. [4] in steady round jets. The need for the optimization study is due to the established inadequacy of the k-ϵ model to reproduce steady round jets properly with the set of constants that are usually adequate in wall boundary layer calculations.

Finally, we report the results of our parametric studies of steady and transient round jets. In particular, two scaling parameters, one for space and the other for time, were ob-

Contributed by the Fluids Engineering Division for publication in the JOURNAL OF FLUIDS ENGINEERING. Manuscript received by the Fluids Engineering Division, April 28, 1981.

Table 1 Governing differential equations

$$\frac{1}{r}\left[\frac{\partial}{\partial x}(r\rho u\phi)+\frac{\partial}{\partial r}(r\rho v\phi)\right]+\frac{\partial \rho\phi}{\partial t}=\frac{1}{r}\left[\frac{\partial}{\partial x}\left(rb\frac{\partial\phi}{\partial x}\right)+\frac{\partial}{\partial r}\left(rb\frac{\partial\phi}{\partial r}\right)\right]+S_\phi$$

Conservation of	ϕ	b	S_ϕ
Mass	1	0	0
Axial momentum	u	μ_{eff}	$\frac{\partial}{\partial x}\left(\mu_{\text{eff}}\frac{\partial u}{\partial x}\right)+\frac{1}{r}\frac{\partial}{\partial r}\left(\mu_{\text{eff}} r\frac{\partial v}{\partial x}\right)-\frac{\partial p}{\partial x}$
Radial momentum	v	μ_{eff}	$\frac{\partial}{\partial x}\left(\mu_{\text{eff}}\frac{\partial u}{\partial r}\right)+\frac{1}{r}\frac{\partial}{\partial r}\left(\mu_{\text{eff}} r\frac{\partial v}{\partial r}\right)-2\mu_{\text{eff}}\frac{v}{r^2}-\frac{\partial r}{\partial p}$
Turbulent kinetic energy	k	$\frac{\mu_{\text{eff}}}{\sigma_k}$	$G-C_D\rho\epsilon$
Rate of turbulent energy dissipation	ϵ	$\frac{\mu_{\text{eff}}}{\sigma_\epsilon}$	$\frac{\epsilon}{k}(C_1 G-C_2\rho\epsilon)$

$$G=\mu_{\text{eff}}\left[2\left(\left(\frac{\partial u}{\partial x}\right)^2+\left(\frac{\partial v}{\partial r}\right)^2+\left(\frac{v}{r}\right)^2\right)+\left(\frac{\partial u}{\partial r}+\frac{\partial v}{\partial x}\right)^2\right]$$

$$\mu_{\text{eff}}=\mu_l+\mu_t$$

$$\mu_t=C_\mu\rho k^2/\epsilon$$

tained. Their validity is supported by comparisons with experimental data.

The Model

1. Governing Equations. The equations of conservation of mass and momentum, and the two equations of the k-ϵ turbulence model [5], are solved simultaneously to obtain the mean dependent variables during the transient of the two-dimensional, incompressible, turbulent, free jet. In cylindrical coordinates, the governing differential equations

Nomenclature

b = coefficient in conservation equations, see Table 1
C_1, C_2
C_3, C_D
C_μ = turbulence model constants. For value of specific application, see Table 2
D = jet orifice diameter
f = retardation parameter, defined in Table 2
G = turbulence generation, expression, see Table 1
k = turbulence kinetic energy $\left(=\frac{1}{2}\overline{u'_i u'_i}\right)$
l_0 = characteristic length scale in turbulence modelling. ($\epsilon = k^{3/2}/l_0$)
l = nozzle passage length
L = length of calculation domain
r = radial coordinate
R = width of calculation domain
R_0 = jet orifice radius
Re_D = $u_{\mathfrak{L},0}/\nu_l$
S_ϕ = source term of conservation equations, see Table 1
S_{ij} = $\frac{1}{2}\frac{k}{\epsilon}\left(\frac{\partial u_i}{\partial x_j}+\frac{\partial u_j}{\partial x_i}\right)$
t = time. Also jet tip arrival time
u = axial component of velocity
U = jet exit velocity profile
U_e = coflow velocity
v = radial component of velocity
χ = stretching parameter. Defined in Table 2.
x = coordinate in the direction of jet axis
$y_{1/2}$ = half the width at half the depth
μ = dynamic viscosity
ν = kinemtic viscosity
ρ = density of jet fluid
ϵ = rate of turbulent energy dissipation
ϕ = general dependent variable of the conservation equations
σ_k = turbulent Prandtl number for k
σ_ϵ = turbulent Prandtl number for ϵ
ω_{ij} = $\frac{1}{2}\frac{k}{\epsilon}\left(\frac{\partial u_i}{\partial x_j}-\frac{\partial u_j}{\partial x_i}\right)$
δ_{ij} = Kronecker delta

Subscript

i = index used in tensor notion. (see Table 2)
j = " "
k = " "
ℓ = laminar
0 = jet exit plane
t = turbulent
in = initial value specified at jet exit plane
$\mathfrak{L}$ = location on jet centerline
eff = effective quantity

Superscript

$\bar{}$ = mean value
$'$ = turbulent fluctuation quantity

Table 2 Survey of k-ϵ turbulence model constants

	Wall boundary layer and planar jet						
	C_μ	C_D	C_1	C_2	σ_k	σ_ϵ	C_3
Commonly used value	0.09	1.0	1.43 ~ 1.45	1.90 ~ 1.92	1.0	1.3	
	Axisymmetric jet						
Sources	C_μ	C_D	C_1	C_2	σ_k	σ_ϵ	C_3^{***}
Simple modification [13, 14]	0.09	1.0	1.57 ~ 1.60	1.90	1.0	1.3	
Launder et al. [10]	0.09-0.04f*	1.0	1.43	1.92-0.0667f	1.0	1.3	
Launder et al. [10]	0.09 g($\bar{P}/\epsilon$)** − 0.0534f	1.0	1.40	1.94-0.1336f	1.0	1.3	
McGuirk et al. [11]	0.09	1.0	1.14-5.31 $\left(\frac{y_{1/2}}{u_\ell}\frac{du_\ell}{dx}\right)_x$	1.90	1.0	1.3	
Morse, A.P. [14]	0.09	1.0	1.4-3.4 $\left(\frac{k}{\epsilon}\frac{\partial u}{\partial x}\right)^3_{\ell,x}$	1.90	1.0	1.3	
Pope, S. B. [14]	0.09	1.0	1.45	1.90	1.0	1.3	0.79

$$*f=\left\{\frac{y_{1/2}}{2u_\ell}\left(\left|\frac{du_\ell}{dx}\right|-\frac{du_\ell}{dx}\right)\right\}^{0.2}$$

$$**(\bar{P}/\epsilon)\equiv\int_{y_1}^{y_2}\rho\,\bar{u}'v'(P/\epsilon)\,y^j dy\Big/\int_{y_1}^{y_2}\rho\,\bar{u}'v'y^j dy$$

$$***D\epsilon/Dt=\frac{\partial}{\partial x_i}\left(\frac{\nu_{\text{eff}}}{\sigma_\epsilon}\frac{\partial\epsilon}{\partial x_i}\right)+\frac{\epsilon^2}{K}(C_1P/\epsilon-C_2+C_3\chi)\ \text{where}$$

$$P=(-\overline{u'_iu'_j})\frac{\partial u_i}{\partial x_j},\ \overline{u'_iu'_j}=\frac{2}{3}k\,\delta_{ij}-\nu_{\text{eff}}\left(\frac{\partial u_i}{\partial x_j}+\frac{\partial u_j}{\partial x_i}\right),\ \nu_{\text{eff}}\equiv C_\mu k^2/\epsilon$$

$$\chi\equiv\omega_{ij}\omega_{jk}S_{ki}$$

—including the semi-empirical turbulence model equations —can be put into the following general form [6, 7]

$$\frac{\partial\rho\phi}{\partial t}+\frac{1}{r}\left[\frac{\partial}{\partial x}(r\rho u\phi)+\frac{\partial}{\partial r}(r\rho v\phi)\right]=\frac{1}{r}\left[\frac{\partial}{\partial x}\left(rb\frac{\partial\phi}{\partial x}\right)+\frac{\partial}{\partial r}\left(rb\frac{\partial\phi}{\partial r}\right)\right]+S_\phi \quad (1)$$

The meaning and form of the general dependent variable ϕ, parameter b, and source term S_ϕ are given in Table 1. The turbulent viscosity μ_t used in the present calculation is modeled through k and ϵ as shown in the same table.

2. Boundary and Initial Conditions. The initial conditions were zero velocity everywhere except on the inlet boundary. The boundary conditions for the hydrodynamic variables u and v for all the calculations presented in this study are:

$$\text{at } r=0,\quad \partial u/\partial r=0,\ v=0 \quad (2)$$

$$\text{at } r=R,\quad \partial u/\partial x=0,\ \frac{1}{r}\frac{\partial(rv)}{\partial r}=0 \quad (3)$$

$$(u)_{r=R}=U_e \quad (4)$$

A detailed discussion of the above boundary conditions is given in reference [1]. At $x = 0$, two jet exit velocity profiles were used as discussed later. A small coflow velocity, U_e = 0.03 percent $u_{\ell,0}$ was used following Shirakashi et al, [8]. Numerically, it was found to have almost no effect on both the steady and the transient results

At $r = 0$, the total normal fluxes for k and ϵ were set equal to zero. At $r = R$, the values of k and ϵ depended on the problem studied. Usually, a small value of k was used to simulate the natural turbulence level in the free stream. At $x = 0$, the distribution of k was prescribed and that of ϵ was estimated through the expression [4]

$$\epsilon=k^{3/2}/l_0 \quad (5)$$

The outlet conditions were that the normal gradients be nil thus the computed flows are elliptic in space, but the results are not very sensitive to the boundary conditions at the outlet plane as long as the head of the jet is away from that plane. In all our transient studies the head vortex remained within the computational domain.

3. Method of Solution. A modified form of the computer code "TEACH" [9] was used. The laminar diffusivity ν_l was replaced by an effective diffusivity $\nu_{\text{eff}} = \nu_l + C_\mu k^2/\epsilon$ (see Table 1), calculated from k and ϵ, for which additional equations were provided. The staggered grid system [9] was retained. The transient calculation used a forward time marching technique. The value of the time step was changed during the course of the calculation to keep the additional jet penetration approximately constant as the jet slows down. A total of 42 × 32 cells in axial and radial directions was used. Inside the pipe the grid size was uniform radially and made up

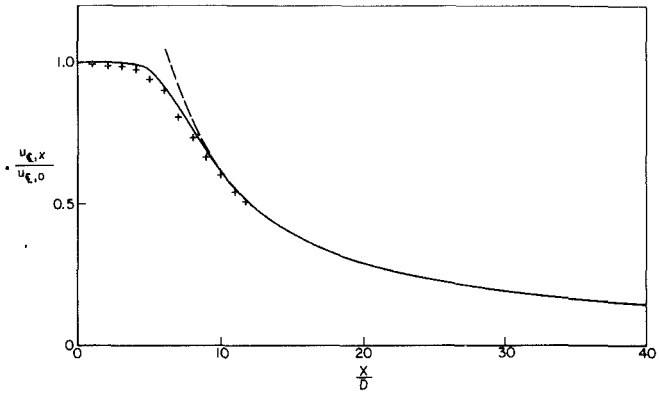

Fig. 1 Steady state centerline velocity using constant C_1 model
(*a*) ——— Calculation, $Re_D = 81100$, $C_1 = 1.5$, $k_{in}/(u_{\ell,0})^2 = 0.0012$
(*b*) + Exp., [4], $u_{\ell,0} = 30$ m/s, $0 \le x/D \le 12$
(*c*) ------ Proposed correlation, [4], $12 \le x/D \le 25$

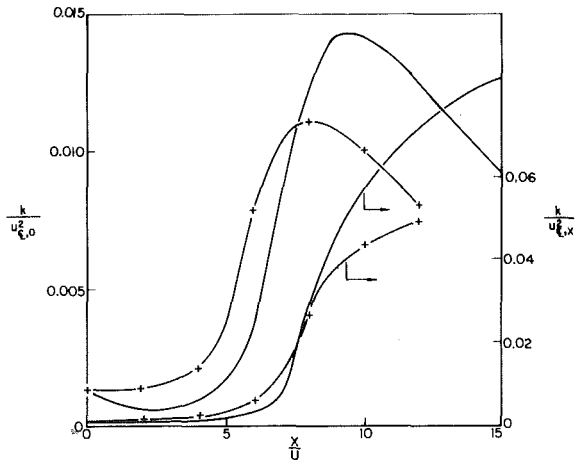

Fig. 2 Comparison of computed and measured centerline turbulence kinetic energy distribution using constant C_1 model.
(*a*) —+— Exp., [4], $u_{\ell,0} = 30$ m/s
(*b*) ——— Calculation, $Re_D = 81100$, $C_1 = 1.5$, $k_{in}/(u_{\ell,0})^2 = 0.0012$

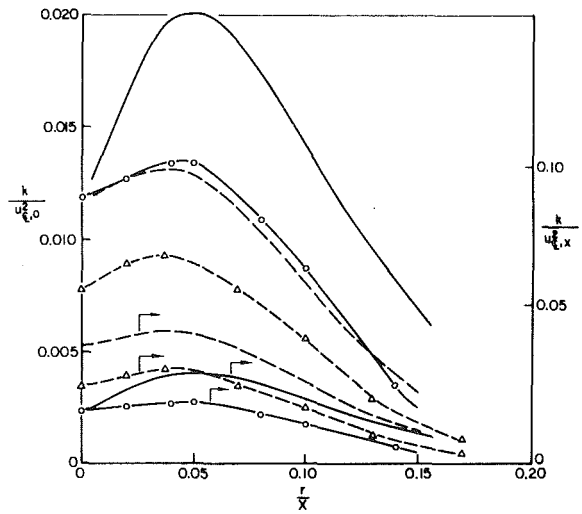

Fig. 3 Comparison of computed and measured lateral turbulence kinetic energy distribution using constant C_1 model.
(*a*) —0— Exp. [4], $x/D = 8$, $u_{\ell,0} = 30$ m/s.
(*b*) ——— Calculation, $x/D = 8$, $Re_D = 81100$, $C_1 = 1.5$, $k_{in}/(u_{\ell,0})^2 = 0.0012$
(*c*) --Δ-- Exp. [4], $x/D = 12$.
(*d*) ------ Calculation, $x/D = 12$, $Re_D = 81100$, $C_1 = 1.5$, $k_{in}/(u_{\ell,0})^2 = 0.0012$

of only one cell in the axial direction. Outside of the pipe, a grid expansion technique [1] was used with expansion factors of 3 percent axially and 7 percent radially. Accuracy of the numerical solution was checked by increasing the number of grid points as discussed later.

Optimization of k-ϵ Parameters for Steady Jets

1. Preliminary Considerations. Before performing the calculations, two surveys were made. One was of the two-equation k-ϵ model used to predict flows similar to the present one; and the other of the information available about the physics of steady round jets.

In the first study, it was found [5, 10–14] that the set of constants used in the k-ϵ model for steady wall boundary layers and two-dimensional planar jets, shown in Table 2, cannot predict the steady axisymmetric, round jet properly. In particular, the spreading rate of the round jet is overestimated by about 40 percent. A similar trend was also observed by Launder et al. [15] in a computation based on a 2nd order closure for the Reynolds stresses. The experimental examination by Yule [16], and Chandrsuda et al. [17] of the jet developing region very near the nozzle exit showed that, if the initial jet exit wall boundary layer is laminar, a large vortical structure is formed from the instability of the laminar free shear layer and propagates downstream. Subsequent vortices roll around each other and can persist to the end of the potential core. This pairing process was demonstrated to be the main mechanism for free shear layer growth and entrainment at least in the near field of both planar and round jets. The existence of large-scale structures casts doubts on the validity of a k-ϵ model to simulate the diffusive nature of the field. For this reason, a different approach, based on a discrete vortex dynamic method [18–20, 1] has also been explored in parallel to the present one and its results will be reported in a subsequent publication. However, in the fully developed region, the k-ϵ formulation is still expected to give reasonably accurate predictions [14]. Thus, there have been several attempts to fix the k-ϵ model to resolve the planar/round anomaly and to make it more universal [5, 10, 11, 13, 14] (see Table 2).

We selected two approaches. In the first one we simply adjusted the magnitude of one of the source term coefficients, C_1, in the dissipation equation, that is generally accepted to be conceptually weak [15, 21, 22]. We tried to establish if reasonable computational results for the near field of round jets ($0 \le x/D \le 30$) would result. In the second, a variable C_1 model proposed by Morse [23], which according to Pope [14] gave the best steady state near field velocity prediction of round jets, was adopted.

The second review concerned the physics of steady round jets. It has been pointed out that the round jets are influenced, especially very near the injector orifice, by the following factors [24–34]: initial turbulence intensity, initial exit velocity nonuniformity (boundary layer effect); nozzle exit geometrical configuration; jet exit Reynolds number; environmental boundary conditions; and the experimental apparatus used.

Recently there have been several experimental investigations [29, 30, 31, 33] of the quantitative effects of initial conditions on jet performance. However, highly controlled experiments are very difficult and often it is not feasible to change one initial parameter at a time while holding all others constant. Thus, we felt justified to see how these factors may possibly affect the jet properties by performing numerical experiments wherein the above mentioned restrictions of actual experiments do not exist, and even

though the quantitative accuracy of the model itself cannot be clearly assessed at this time. But the results of the parametric study will be mentioned only briefly due to space limitations.

In summary, three numerical tasks were undertaken: optimization of the constants of the turbulence model by comparisons with steady jet data; derivation of scaling parameters based on the computed results; and flow field sensitivity studies using the model.

2. Comparisons With Steady Jet Experiments. The constants used in the k-ϵ model were optimized by comparing the computed results with the experimental ones of Bogustawski et al. [4]. They used a pipe jet with a fully developed turbulent exit veolcity profile. They gave detailed near field measurements ($0 \leq x/D \leq 12$) including the turbulent kinetic energy distribution. Figure 1 gives the comparison of the steady-state center-line velocities for $U_{\ell,0} = 30$ m/s. The computation was based on the experimentally supplied initial value of k plus a value for ϵ estimated by equation (5) with $l_0 = 0.09\ R_0$. Except for C_1 that was set equal to 1.5, all the other constants of the k-ϵ model were the same as used for two-dimensional planar jets. In Fig. 1 it can be seen that the agreement is good for $0 \leq x/D \leq 12$ and excellent for $12 \leq x/D \leq 30$. Comparisons of other steady variables, such as radial mean velocity distribution, entrainment rate distribution, and location of virtual origin, also show adequate agreement.

But the calculated values of radial and longitudinal turbulent kinetic energy distributions tend to be much higher than the experimental ones as shown in Figs. 2 and 3. Variations of l_0 by a factor of three, did not change the results appreciably. A variable C_1 model, as suggested by Morse [23], gave very good agreement for the steady centerline velocity even in the transition region ($4 \leq x/D \leq 8$), but the predicted turbulent kinetic energy was still higher than the measured one [1]. Therefore it was decided to use the constant C_1 model for our transient studies and the variable C_1 model only occasionally for comparison. In this paper, only the results obtained with the constant C_1 model are presented. The variable C_1 model gives similar results for the steady state and 10 percent faster penetration in the transient [1].

In the foregoing optimization calculations, the grid size dependency of the results was assessed by doubling the grid points to 84×64. It resulted in a difference of no more than 3 percent in the computed dependent variables. For economic reasons and considering all other limitations of the model, it was decided to use the coarser grid, 42×32, for all the calculations.

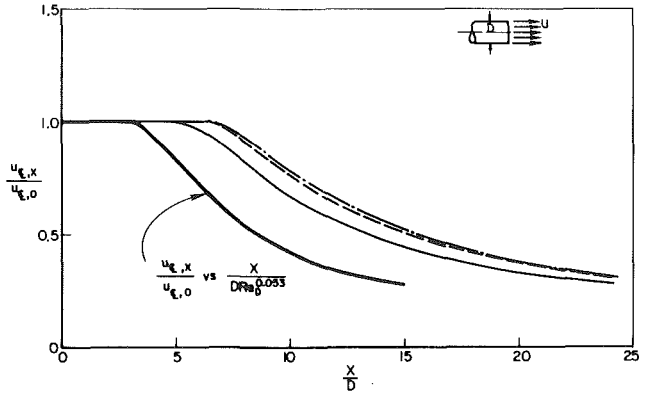

Fig. 4 Computed steady state centerline velocity distribution with three different Reynolds numbers. $C_1 = 1.5, k_{in}/(u_{\ell,0})^2 = 0.03$
(a) ——— $Re_D = 8{,}650$
(b) - - - - - - - $Re_D = 81{,}100$
(c) —·— $Re_D = 135{,}100$
(d) ——— $u_{\ell,x}/u_{\ell,0}$ versus $D\ Re_D^{0.053}$

Transient Jet Computations

1. Scaling Studies. Even though the optimization process was based on a comparison between *steady state* calculations and experiments with a *fully developed* turbulent exit velocity profile, the following *transient* computations were performed using a *uniform* exit velocity profile. This is because experimental data are available for the uniform exit velocity situation and all the analytical studies of free jets [26, 34] are based on the same assumption. Indeed, it will be of considerable advantage to use those results for comparison with our computations.

In Fig. 4 results are given for the steady state centerline velocity, with three different Reynolds numbers (based on the exit centerline velocity, orifice diameter, and kinematic laminar viscosity) and for the specified initial conditions. A systematic Reynolds number dependence is evidenced. However, it can be accounted for by scaling the axial distance with $D\ Re_D^{0.053}$ as shown by the heavy curve in the same figure. In Fig. 5, the transient results with three different

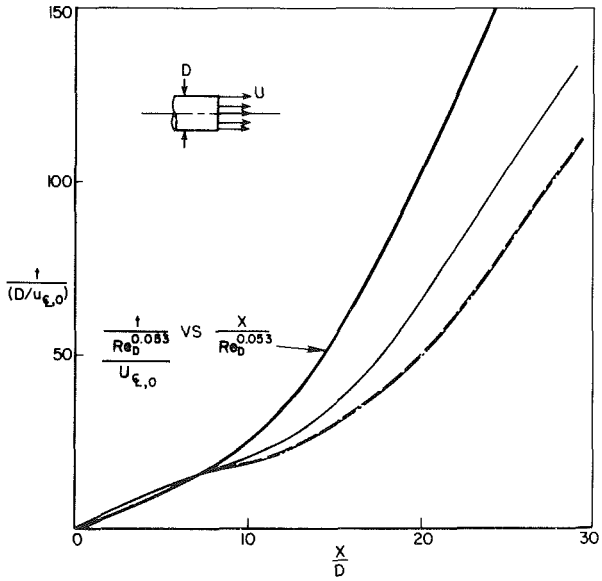

Fig. 5 Calculation results of transient jet tip penetration with three different Reynolds numbers. $C_1 = 1.5, k_{in}/(u_{\ell,0})^2 = 0.03$
(a) ——— $Re_D = 8{,}650$
(b) - - - - - - - $Re_D = 81{,}110$
(c) —·— $Re_D = 135{,}100$
(d) ——— $t/(DRe_D^{0.053}/u_{\ell,0})$ versus $x/DRe_D^{0.053}$

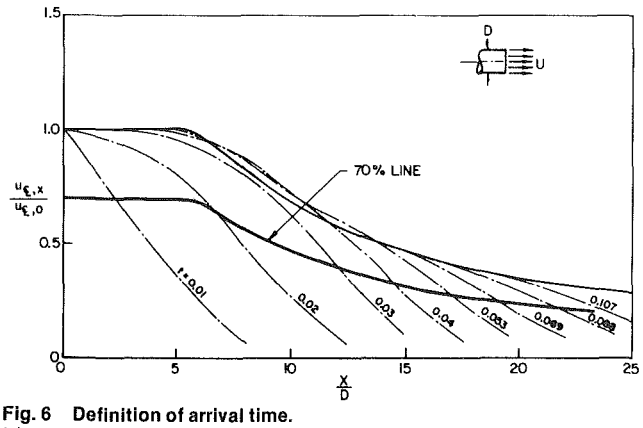

Fig. 6 Definition of arrival time.
(a) ——— Steady state centerline velocity distribution. $Re_D = 81{,}100, C_1 = 1.5, k_{in}/(u_{\ell,0})^2 = 0.0015$
(b) ——— 70 percent of steady state centerline velocity distribution curve
(c) —·— Transient centerline velocity decay at various time t after beginning of injection

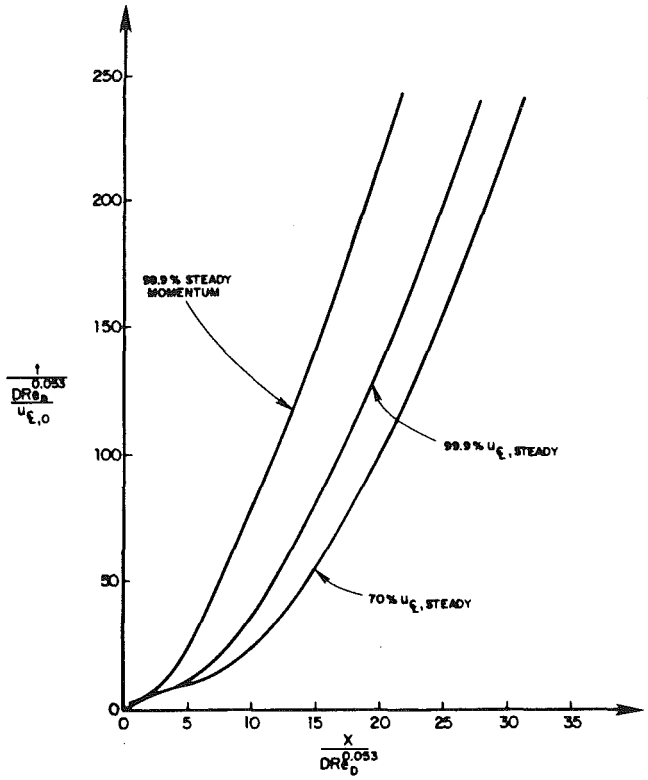

Fig. 7 Steadying time curves using different definitions for the achievement of steady state but the same length and time scales

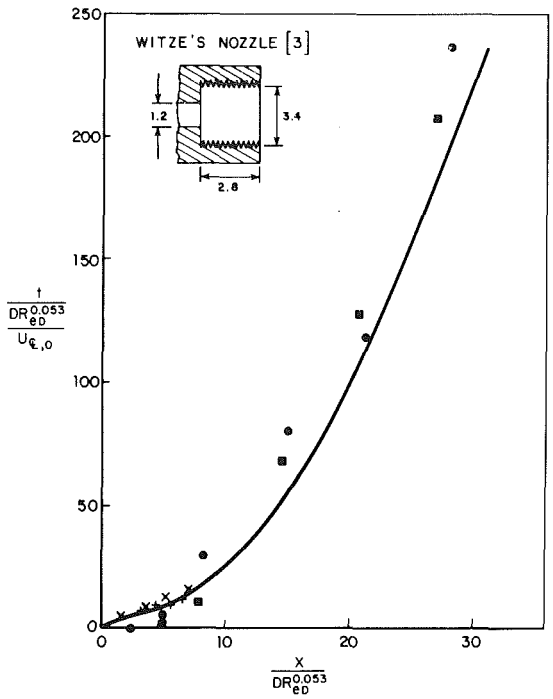

Fig. 8 Computed (continuous line) and measured (•, ■ by Witze [3]; +, by Rizk [38], Re_D = 40,000; X, by Dedeoglu [39], Re_D = 64,000) steadying time

Reynolds numbers are presented. Notice that the Reynolds number dependence disappearance for large values of Re_D, i.e., $Re_D > 10^5$. Also, the dependence of the transient on Re_D can be accounted for if the axial distance is scaled by $D\ Re_D^{0.053}$ and the steadying time by $D\ Re_D^{0.053}/u_{\ell,0}$ as shown in the same figure. The meaning of this scaling and how it was arrived at is explained in the following paragraphs.

In Fig. 5, t is the time needed for the axial velocity u to reach 70 percent of its steady state value at any point x on the centerline of the suddenly-started turbulent jet. To compute t, (see Fig. 6), we first plot the steady state centerline velocity and its corresponding 70 percent line in the $u_{\ell,x}/u_{\ell,0}$ versus x/D plane. Then the transient centerline velocities at subsequent times are added. The point of intersection of the transient velocity and the 70 percent steady state velocity defines the duration of the transient, t, and the penetration distance, x/D. For example, at the location x/D = 12, 70 percent of the steady state centerline velocity is reached after t = 0.03s.

Notice that if a percent other than 70 is selected, the universal curve of Fig. 5 changes but not the characteristic time and length scales. This is illustrated in Fig. 7 where the 70 percent curve is shown together with the 99.9 and 99.9 percent momentum curves. The latter is obtained imposing that the momentum reaches 99.9 percent of its steady value instead of the centerline velocity.

The dimensionless time $t/(D/u_{\ell,0})$ was obtained as follows We extended the results of our laminar jet study [1] and sought to find a characteristic diffusion time of the form D^2/ν_{eff} where ν_{eff} has been shown experimentally [35-37] to be nearly uniform across the jet in the downstream region. Thus it has been suggested that $\nu_{\text{eff}} \propto (u_{\ell,0}D)$ with the proportionality constant equal to 0.0116, 0.0144, 0.0162 according to Hinze [35], Schlichting [36] and Squire [37], respectively. The same expression for ν_{eff} is obtained also from our calculations [1].

After dividing D^2 by the limit value of ν_{eff}, the convection time $(D/u_{\ell,0})$ was obtained. It proved to be the correct scaling time at high Re_D, as shown in Fig. 5, and, when the length scale ($D\ Re_D^{0.053}$) is used instead of D, the resulting scaling time becomes adequate at all Reynolds numbers.

The universal curve of Fig. 5 can be represented by the equations

$$
\begin{aligned}
t^* &\equiv t u_{\ell,0}/D\ Re_D^{0.053} \\
x^* &\equiv x/D\ Re_D^{0.053} \\
t^* &= 2.0\ x^* \qquad \text{for } x^* \le 8 \\
t^* &= 0.25\ x^{*2} \qquad \text{for } x^* > 8
\end{aligned}
\tag{6}
$$

2. Parametric Studies. A parametric study of the effect of the turbulence constant C_1 and of the initial jet exit turbulence intensity on the steady state centerline velocity, unsteady penetration-time history and longitudinal centerline turbulent kientic energy distribution was also conducted [1]. It was found that for a fixed value of C_1, a slightly faster (10 percent) penetration can be achieved with the jet exit turbulence intensity increased by a factor of 10 ($(k_{\text{in}}/u^2_{\ell,0})$ changed from 0.0002 to 0.03). However, with a fixed jet exit turbulence intensity, a 10 percent variation of C_1 (from 1.45 to 1.60) causes a 45 percent decrease in the jet spreading rate. This sensitivity was also observed by Launder et al. [15] with a Reynolds stress closure model, and made the optimization study necessary.

Comparisons With Transient Jet Experiments

For steady state free round jet flows, considerable experimental information is available, even though it is not always adequately characterized. But for transient round jets it is very limited. Recently, Witze [3] made some measurements in impulsively started air-into-air injections by hot-film anemometry using two nozzle exit configurations. Only the jet arrival time he measured with one of the two nozzles was used for comparison with our transient computations because the second nozzle had two screens at its exit whose effects we cannot readily characterize.

In Fig. 8 the measurements of Witze at two Reynolds numbers (4500 and 9000) are seen to compare favorably with the proposed universal curve. The discrepancy is larger very

near the injector where the experimental measurements show weaker penetration but also broader scatter. Moreover Witze's near field transient data may have been affected by other factors. His experimental nozzle orifice geometry is complex (see Fig. 8) and his steady-state centerline velocity decay data [3] show a large reduction in jet potential core length and faster decay. This phenomenon was observed also by Hill and Jenkins [32] in their experiments with a whistler nozzle of geometry similar to that of Witze. They pointed out that, for certain values of the cavity l/D, acoustic resonance occurs that interacts with the jet and causes a higher mixing rate and faster decay. Also, the experimental measurements of Witze were made by hot-film anemometry. Due to the small jet orifice diameter (1.2 mm), the hot-film probe of 1.5 mmw may have affected the flow and presented spatial resolution limitations near the injector orifice.

A visual correlation based on two experimental transient jet penetration pictures of Rizk [38] and Dedeoglu [39] is also shown in Fig. 8. The center of the vortex shaped structure at the head of the jet photographed by them was chosen by us to identify the location and time at which 70 percent of the centerline steady state velocity is reached. These location and arrival times thus correspond to the computed ones with which they are seen to compare favorably. It may be of interest to point out that in the transient laminar jet experiments of Abramovich et al [40], 70 percent of the centerline steady state velocity was also used to define the penetration of the center of the head vortex. Finally, working with fuel sprays, Borman and Johnson [41] and Taylor and Walsham [42] pointed out that the spray tip penetration rate can be closely estimated using a value between 68 and 72 percent of the steady state centerline velocity of the spray.

In retrospect, we may not justify our use in the transient computations of a set of turbulence model constants determined by comparisons with steady state data, thus assuming that transient jets have essentially a steady state structure. It would appear that, at any given time, all but a small fraction of the jet (the head vortex) has already achieved its steady state configuration. It is also likely that the head vortex itself may obey scaling laws but we could not determine them due to difficulties in defining its structure from the numerical results.

Acknowledgments

This work was presented at the 2nd FIAT Combustion Workshop, FIAT Research Center, Orbassano, Italy, December 1979, the 11th DISC Meeting, Sandia Laboratories, Livermore, California, March 1980, and at the Spring Meeting of the Combustion Institute, Central States Section, General Motors Research Laboratories, Warren, Michigan, March 1981. It was supported by the Department of Energy under Contract EC-77-S-02-4192.A002.

References

1 Kuo, T.-W., "On the Scaling of the Impulsively Started Incompressible Laminar, Turbulent, and Spray Jets," Princeton University, MAE Department Ph.D. thesis. No. 1538, March, 1982.

2 Hengrussamee, D., Ma, A.S.C., and Ong, K. S., "Numerical Integration Techniques for an Impulsively Starting Incompressible Jet," Numerical Methods in Fluid Dynamics, *Proceedings of the International Conference*, Univ. of Southampton, England, 1973, p. 121.

3 Witze, P. O., "The Impulsively Started Incompressible Turbulent Jet," SAND 80-8617, 1980.

4 Bogustawski, L., and Popiel, C. O., "Flow Structure of the Free Round Turbulent Jet in the Initial Region," *Journal of Fluid Mech.*, Vol. 90, 1979, p. 531.

5 Launder, B. E., and Spalding, D. B., "The Numerical Computation of Turbulent Flows," *Comput. Methods Appl. Mech. Eng.*, Vol. 3, 1974, p. 269.

6 Khalil, E. E., Spalding, D. B., and Whitelaw, J. H., "The Calculation of Local Flow Properties in Two-Dimensional Furnace," *Journal of Heat Mass Transfer*, Vol. 18, 1975, p. 775.

7 Patankar, S. V., "Numerical Prediction of Three-Dmensional Flows," *Studies in Convection-Theory, Measurement and Application*, Launder, B. E. (Editor), Academic Press, 1975.

8 Shirakashi, M., Tomita, Y., "The Diffusion of Jets in Cross Flow," *Bulletin*, JSME, Vol. 21, 1978, p. 116.

9 Gosman, A. D., and Ideriah, F. J. K., "Teach-3p, A General Computer Program for Two-Dimensional, Turbulent, Recirculating Flows," Dept. of Mech. Engrg., Imperial College, London, 1976.

10 *Proceedings of Conference on Free Turbulent Shear Flows*, Langley Field, Hampton, NASA Report SP-321, 1972.

11 McGuirk, J. J., and Rodi, W., "The Calculation of Three Dimensional Free Jets," Symposium on Turbulent Shear Flows, Pennsylvania State Univ., Apr. 1977.

12 Lockwood, F. C., and Naguib, A. S., "The Prediction of Fluctuations in the Properties of Free, Round-Jet, Turbulent Diffusion Flames," *Combustion and Flame*, Vol. 24, 1975, p. 109.

13 Gosman, A. D., Lockwood, F. C., and Syed, S. A., "Prediction of a Horizontal Free Turbulent Diffusion Flame," Sixteenth Symposium (International) on Combustion, The Combustion Institute, MIT, Cambridge, Mass. 1976, p. 1543.

14 Pope, S. B., "An Explanation of the Turbulent Round-Jet/Plane-Jet Anomaly," AIAA Tech. Note 16, 1978, p. 279.

15 Launder, B. E., and Morse, A., "Numerical Prediction of Axisymmetric Free Shear Flows with a Reynolds Stress Closure," Turbulent Shear Flows I, selected papers from the 1st International Symposium on Turbulent Shear Flows, Pennsylvania State Univ., Univ. Park, Pa., 1977.

16 Yule, A. J., "Large Scale Structure in the Mixing Layer of a Round Jet," *J. Fluid Mech.*, Vol. 89, p. 413.

17 Chandrsuda, C., Mehta, R. D., Weir, A. D., and Bradshaw, P., "Effect of Free-Stream Turbulence on Large Structure in Turbulent Mixing Layers," *J. Fluid Mech.*, Vol. 85, 1978, p. 693.

18 Chorin, A. J., "Numerical Study of Slightly Viscous Flow," *J. Fluid Mech.*, Vol. 57, 1973, p. 785.

19 Chorin, A. J., "Vortex Sheet Approximation of Boundary Layers," *J. Computational Physics*, 1978, Vol. 27, p. 428.

20 Chorin, A. J., "Vortex Models and Boundary Layer Instability," *SIAM J. Scien. Comp.*, Vol. 1, 1980, pp. 1–21.

21 Pope, S. B., Whitelaw, J. H., "The Calculation of Near-wake Flows," *J. Fluid Mech.*, Vol. 73, 1976, p. 9.

22 Gosman, A. D., Khalil, E. E., and Whitelaw, J. H., "The Calculation of Two-Dimensional Turbulent Recirculating Flows," Symposium on turbulent shear flows, Pennsylvania State Univ., Univ. Park, Pa., Apr. 1977.

23 Morse, A. P., "Axisymmetric Turbulent Shear Flows with and without Swirl," Ph.D. thesis, London University, England, 1980.

24 Flora, Jr., J. F., and Goldschmidt, V. W., "Virtual Origin of a Free Plane Turbulent Jet," *AIAA*, Vol. 7, 1969, p. 2344.

25 Albertson, M. L., Dai, Y. B., Jensen, R. A., and Rouse, H., "Diffusion of Submerged Jets," *Transactions A.C.S.E.*, Paper No. 2409, Vol. 115, 1950, p. 639.

26 Abramovich, G. N., *The Theory of Turbulent Jets*, MIT Press, 1963.

27 Donaldson, C. Dup., and Gray, K. E., "Theoretical and Experimental Investigation of the Compressible Free Mixing of Two Dissimilar Gases," *AIAA*, Vol. 4, 1966, p. 2017.

28 Witze, P. O., "A Generalized Theory for the Turbulent Mixing of Axially Symmetric Compressible Free Jets," Fluids Mechanics of Mixing, Joint Meeting of the Fluid Engineering Division and the Applied Mechanics Division, ASME, June 1973.

29 Hussain, A. K. M. F., and Clark, A. R., "Upstream Influence on the Near Field of a Plane Turbulent Jet," *Phys. of Fluids*, Vol. 20, 1977, p. 1416.

30 Husain, Z. D., and Hussain, A. K. M. F., "Axisymmetric Mixing Layer: Influence of the Initial and Boundary Conditions," *AIAA*, Vol. 17, 1979, p. 48.

31 Hussain, A. K. M. F., "Initial Condition Effect on Free Turbulent Shear Flow," Structure and Mechanisms of Turbulence I, Symposium on Turbulence, Berlin, Germany, 1977.

32 Hill, W. G., Jr., and Jenkins, R. C., "Effects of Initial Conditions on Mixing Rate of Turbulent Jets," Workshop on Prediction Methods for Jet v/Stol Propulsion Aerodynamics, Institute for Defense Analysis, 1975.

33 Oster, D., Wygnanski, I., Dziomba, B., and Fiedler, H., "On the Effect of Initial Conditions on the Two Dimensional Turbulent Mixing Layer," Structure and Mechanisms of Turbulence I, *Proceedings of the Symposium on Turbulence*, Berlin, Germany, 1977.

34 Rajaratnam, N., *Turbulent Jets*, Elsevier Sci. Pub., 1976.

35 Hinze, J. O., *Turbulence*, 2nd ed., McGraw-Hill, 1975, p. 540.

36 Schlichting, H., *Boundary Layer Theory*, 6th ed., McGraw-Hill, 1968.

37 Squire, H. B., "The Round Laminar Jet," *Q.J. Mech., Appl. Math.*, Vol. 4, 1950, p. 321.

38 Rizk, W., "Experimental Studies of the Missing Processes and Flow Configurations in Two-Cycle Engine Scavenging," *Proc. of I. Mech. E.*, Vol. 172, 1958, No. 1, p. 417.

39 Dedeoglu, N., "Scavenging Model Solves Problems in our Burning Engine," *Trans. SAE*, 710579, p. 1930.

40 Abramovich, S., and Solan, A., "The Initial Development of a Submerged Round Jet," *J. Fluid Mech.*, Vol. 59, p. 791.

41 Borman, G. L., and Johnson, J. H., "Unsteady Vaporization History and Trajectories of Fuel Drops Injected into Swirling Air," Paper 598B presented at SAE National Fuels and Lubricants, Powerplants, and Transportation Meeting, Philadelphia, Pa., Oct. 1962.

42 Taylor, D. H., and Walsham, B. E., "Combustion Processes in a Medium Speed Diesel Engine," Symposium on Diesel Engine Combustion, *Proc. I. Mech. E.*, London, Part 3, 1967, p. 1970.

Plug Flow of Coarse Particles in a Horizontal Pipe

Y. Tsuji
Y. Morikawa

Department of Mechanical Engineering
for Industrial Machinery,
Faculty of Engineering,
Osaka University, Osaka, Japan

Plug flow of coarse particles was investigated experimentally in a horizontal pipe, in which a sub-pipe for secondary air injection was installed. Measurements were made about the plug motion, pressure drop, and transportation properties, and the roles of the main and sub-pipe air flow were clarified. The main air flow increases the number of plugs, while the sub-pipe air flow increases the plug velocity. The higher the main pipe air flow rate, the more regular the motion. The height of a stationary layer of deposited particles, which is built on the bottom of the main pipe, decreases with increasing the sub-pipe air flow rate. The pressure drop in the moving plug is quantitatively much smaller than that in the stationary packed bed of same particles.

1 Introduction

Low velocity and dense phase conveying is becoming increasingly important in pneumatic transport technology, because it has many merits compared with suspension transport systems. For example, pipe wear and breakage of conveyed materials are greatly reduced, and power consumption is expected to be reduced. In fact, several enterprises have put the plug flow conveying facilities on sale on a commercial basis and their pamphlets illustrate how well the plug flow is realized in the pipe line. There is also qualitative information available which explains the mechanism of plug formation. However, so far as earlier publications are concerned, fundamental research studies are scarce and most have dealt with practical problems such as transport efficiency, overall pressure drop, and other global properties [1]-[4].

In general, dense phase conveying is greatly affected by particle properties and given conditions. Particle flow patterns are sometimes very different according to the sort of particles. For example, a plug of fine particles with cohesive force dominant moves like a rigid body but such motion is not observed in the case of coarse particles. Therefore, technical progress up to present has been made by trial and error in accordance with a given situation. However, it should be noted at present that fundamental and quantitative approaches to the problem are required for development of the plug flow conveying technique. As an attempt at such an approach, we noted the behavior of individual plugs and investigated what phenomena really happen in the pipe.

The methods to make regular plugs are classified into two kinds. In one of them, air and/or particles are pulsatingly supplied to the pipe. The other makes use of air injection from a sub-pipe set inside or outside the main pipe. In the present work, we adopted the latter with an inside-set sub-pipe, i.e., a double pipe structure which has been developed by Gattys Co. of West Germany. The present work dealt with the case of coarse particles. This paper shows the role of the main and sub-pipe air flow in connection with the plug motion, pressure drop, and transportation properties.

2 Experimental Arrangement

2.1 Equipment. Figure 1 shows a sketch of the experimental equipment. The main pipe was a transparent acrylic pipe with 50 mm inner diameter and about 6.2 m in length from the mixing point to the receiver. The sub-pipe, set on the bottom of the main pipe as shown in the upper left of Fig. 1, was made of vinyl, of which outer and inner diameters are 10 mm and 8 mm, respectively. The secondary air was injected from it through six small holes of about 4 mm in diameter. The intervals of the holes are shown in Fig. 2.

A blower (4.8 m^3/min., 2.8 $\times$ 10^4 N/m^2) and compressor (0.4 m^3/min., 7 $\times$ 10^5 N/m^2) continuously supplied the air to the main and sub-pipes. The downstream outlets of both main and sub-pipes were open to the atmosphere. In the present experiment, only one kind of solid particles was used, of which properties are shown in Table 1. The particles were supplied to the main pipe at the mixing point through two electromagnetic feeders. To prevent the effect of electrostatic charging caused by friction between particles and pipe wall,

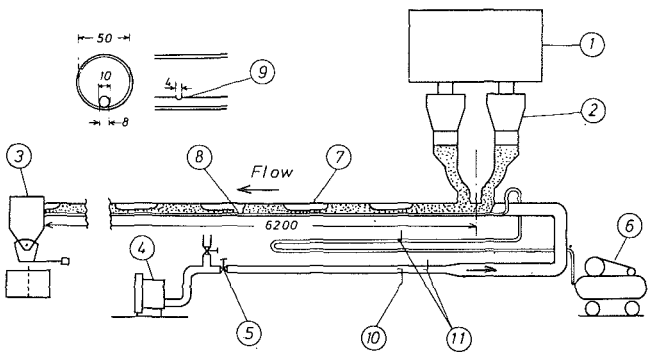

Fig. 1 Experimental equipment: ① Solid particles storage bunker, ② electromagnetic feeder, ③ receiver, ④ blower, ⑤ flow adjusting valve, ⑥ compressor, ⑦ main pipe, ⑧ sub-pipe, ⑨ hole for secondary air injection, ⑩ hot wire probe, ⑪ pitot tube

Contributed by the Fluids Engineering Division for publication in the JOURNAL OF FLUIDS ENGINEERING. Manuscript received by the Fluids Engineering Division, August 25, 1980.

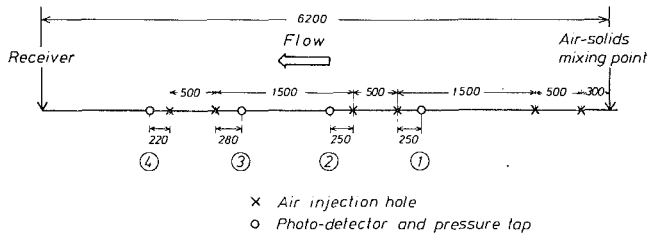

Fig. 2 Longitudinal location of the air injection holes, photo-detectors, and pressure taps

surfaces of the particles were coated with a charging preventive substance which is used for clothes. A packed bed was built up above the mixing point when plug conveying was realized. The height of the bed was kept constant during the experiment by adjusting the voltage to the feeders. Therefore, the condition at the air-solids mixing point remained the same during the measurement. This point is characteristic of our experiment. In most earlier experiments of the dense phase conveying particles were supplied to the pipe directly from a pressure vessel such as a blow tank. In those cases, the condition of particle feeding may change as the amount of stored particles decreases, so that steadiness could not always be assured during measurement.

2.2 Measurement. Measured quantities in this experiment were air flow rates in the main and sub-pipes (G_b and G_c), particle flow rate (G_s), passing periods of plugs (T) and pressure drop in the plug (Δp). The last two quantities were detected at four longitudinal points. The air flow rate in the main pipe was measured by a hot wire probe set at the center of the pipe. The calibration of the hot wire was frequently made by the use of a Pitot tube set in the downstream of the hot wire probe. The air flow rate in the sub-pipe was measured by a Pitot tube. The relation between the air flow rate and center velocity was obtained in a preliminary experiment. Particle flow rate per unit time was measured by the use of a stop watch and a platform scale.

In order to obtain the pressure drop in the individual moving plug, three transducers for the pressure difference were set between the pressure taps along the main pipe as well as four photo-detectors, as shown in Fig. 2. Although the static pressure fluctuated violently in the main pipe, it was not random but exactly correlated to the movement of the plug. The setting of the photo-detector is shown in Fig. 3. The passing period and velocity of the plug can be obtained from the signals of the photo-detectors.

Electromagnetic recorders were used to record simultaneously nine signals, that is, three pressure transducers and four photo-detectors together with the dynamic pressure of the Pitot tube and hot wire signal. The experimental uncertainty of these data is estimated as follows; G_b, G_c and G_s, ± 5 percent, Δp, ± 100 N/m^2, T, ± 0.02 s. However, the present phenomena are highly irregular, which is shown in Figs. 7, 8, and 14, and one of the present purposes is to see how irregular they are. Therefore, time average properties for one combination of G_b and G_c were obtained by averaging data of fifty plugs.

Table 1 Properties of solids particles

Material	Polyethylene
Shape	Sphere
Mean diameter (mm)	1.1 ± 1
Density (kg/m^3)	1030 ± 10
Bulk density (kg/m^3)	646 ± 5
Angle of repose (deg)	22 ± 1
Angle of internal friction (deg)	28 ± 2

At an earlier stage of this work the authors were not sure whether a regular and steady plug flow would be realizable for non-cohesive coarse particles. Air injection with various pitches of holes was attempted in a preliminary experiment, and the pitch shown in Fig. 2 seemed proper for inducing a relatively regular plug flow. Thus, we decided to investigate the plug flow in detail in the case of that pitch, and leave systematic investigations about various pitches for a future study. Instead, the air flow rates from the blower and compressor were changed systematically and each role was clarified in this work.

3 Motion of the Plug

3.1 Visual Observation. The present facilities realized the plug flow from the case where only a single plug was transported along the pipe to the case where five or six plugs were transported simultaneously, which depended on the air flow rate. If we observe the plug, the flow of particles is that shown in Fig. 4. Coarse particles do not form a rigid plug like a moving bed but they show a wavy motion. In this respect, the plug flow of coarse particles is quite similar to a liquid-gas slug flow in a horizontal pipe [5]. Observing the particle motion in detail, we notice that it is rather involved. That is, there exists a stationary settling layer of deposited particles in the lower half of the pipe, and particles consisting of the plug alternate with the deposited particles as the plug moves along the pipe. The stationary layer is distributed just in front of the plug and some particles spring out from the layer and form a cloud. In the front part of the plug the flow of particles shows a kind of vortex motion. On the rear side particles of the plug form a smooth curve and they deposit one by one, forming the stationary layer again. When the exchange of particles takes place at the same rate in the front and the rear of the plug, the plug flow is steady along the pipe. The presence of the stationary layer does not result from the double pipe structure

Nomenclature

D = pipe diameter
d = particle diameter
f = friction coefficient between the plug and pipe wall
g = gravitational constant
G_b = air flow rate in the main pipe
G_c = air flow rate in the sub-pipe
G_s = particle flow rate
H = height of the layer of deposited particles
l = plug length
Δp = pressure drop in the plug
Q = total volume air flow rate = $(G_b + G_c)/\rho_a$
S = pipe cross section
S_p = cross section of the plug above the deposit layer
T = periodic time with which plugs pass through a photo-detector, defined in Fig. 6
U = bulk air velocity
U_b = air velocity = G_b/S
U_c = air velocity = G_c/S
V = plug velocity
X = longitudinal distance measured from the air-solids mixing point
ϵ = porosity = $1 - \rho'/\rho_s$
η = transport efficiency defined by equation (11)
λ = coefficient of the pressure drop
μ = loading ratio = $G_s/(G_b + G_c)$
ν = kinematic viscosity of air
ρ_a = density of air
ρ_s = density of particle
ρ_s' = bulk density of particles
τ = length of time when one plug passes through a photo-detector, defined in Fig. 6

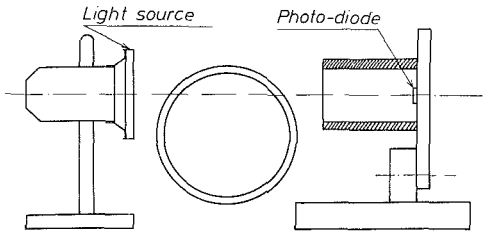

Fig. 3 Setting of the photo-detector

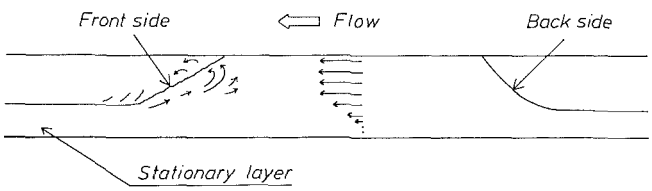

Fig. 4 Motion of particles

but it is inevitable in the case of coarse particles with low internal friction, for it has been observed in other experiments.

3.2 Recorded Signals. Figure 5 shows examples of wave forms recorded. Figure 5(*a*) shows the case when only one plug moves along the pipe and Fig. 5(*b*) the case when a number of plugs move one after another with close intervals. Upper two signals, A and B, represent the air flow rates in the main and sub-pipes, respectively. Signals C represent the ouptuts from the photo-detectors which detect the passing of the plug. Signals D represent instantaneous pressure differences between pressure taps. The numerals indicated in the figure correspond to those in Fig. 2. It is found that the air is supplied continuously, although the phenomena are highly unsteady in the main pipe as shown in Signals C. The relation between the signals of pressure and photo-detectors is well understood in Fig. 5(*a*). When the plug front begins to pass the pressure tap the pressure signal begins to increase. While the whole plug is between the taps the pressure signal indicates a maximum value. When there is no plug between the pressure taps the pressure difference is negligibly small, so that the above maximum value is the pressure drop in the plug. It is also noted that the pressure increases or decreases linearly with time when the plug is passing through the pressure tap, which means a linear distribution of pressure within the plug. When the interval between the plugs is close as in Fig. 5(*b*), the pressure signals, look irregular but the pressure drop in each plug can be determined by comparing the signals carefully with those from the photo-detectors.

Plug velocity and length change along the pipe. Moreover, the velocities of the front and rear of the plug are sometimes different because the plug is not a rigid body. Therefore, t_1, t_2, and τ which are defined in the wave forms of the photo-detectors differ according to the measuring position. See Fig. 6. Hence, the velocity and length of individual plugs were obtained by using the following assumptions.

(i) The plug length l is unchangeable during the time when it is moving between two measuring points of the photo-detectors.

(ii) The plug velocity V is defined as the average velocity of the front and rear velocities, $V_f = L_i/t_1$ and $V_r = L_i/t_2$, respectively, where L_i is the distance between the measuring points.

Therefore,

$$V = (V_f + V_r)/2 \tag{1}$$

and

$$l = L_i - V(t_1 - \tau). \tag{2}$$

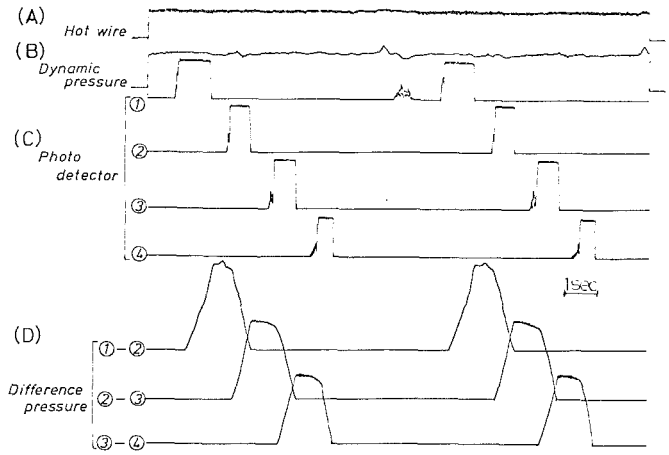

Fig. 5(*a*) Recorded signals in the case of small number of plugs

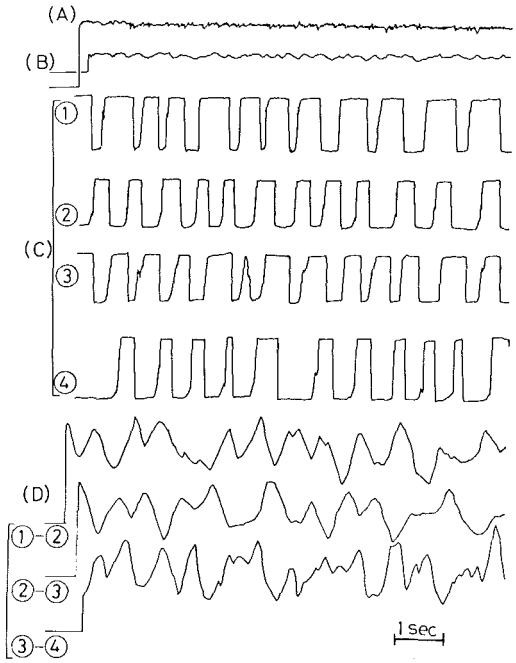

Fig. 5(*b*) Recorded signals in the case of large number of plugs

Fig. 5

3.3 Passing Period. As long as we observed the plug motion with only our naked eyes, it looked regular and little difference was observed between cases of small and large air flow rates. However, when the results are treated statistically, the motion of the plug is found to depend largely on the flow rate. Figure 7 and Fig. 8 show frequency distributions of the passing period measured at the most upstream and downstream measuring points, where the air flow rate in the sub-pipe, G_c, is kept constant ($G = 3.5 \times 10^{-3}$ kg/s) and the air flow rate in the main pipe, G_b, is changed. Figure 7, representing the results of relatively small G_b, shows that the distributions are more diverse and the period is larger on the average than Fig. 8. Comparing Figs. 7(*a*) and 7(*b*), we find that the average period becomes large at the downstream point. This means that some plugs detected at the upstream collapse as the flow moves downstream and they do not appear at the downstream point. On the other hand, in Fig. 8 which represents the case of higher G_b, the plugs pass at about the same period from the upstream to downstream. Therefore, the higher the air flow rate G_b, the more regular the motion, and the influence of G_b upon the passing period is remarkable in the downstream.

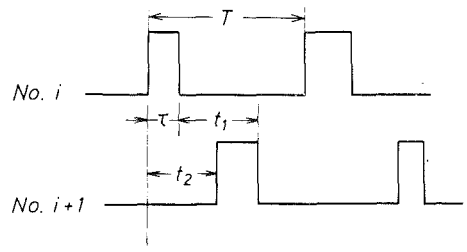

Fig. 6 Signals from photo-detectors

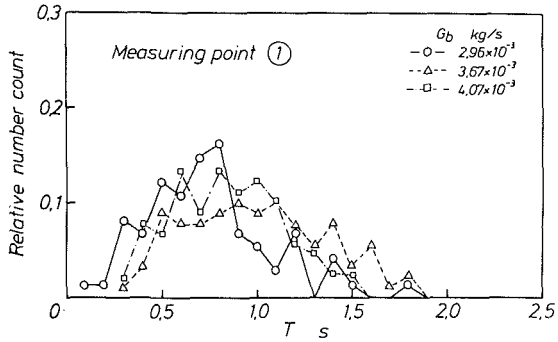

Fig. 7(*a*) Frequency distribution of the passing period in the case of small air flow rates G_b

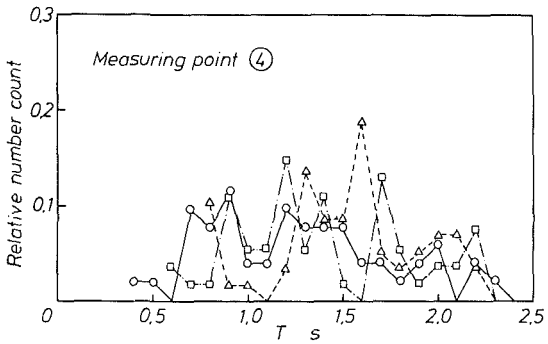

Fig. 7(*b*) Frequency distribution of the passing period in the case of small air flow rates G_b

Figure 9 shows the relation between the average period and the air flow rate G_b, where the effect of G_c is found to be within scattering of measurements. Decrease in the passing period means increase in the number of plugs per unit time, because the plug velocity is not influenced by the air flow rate G_b, as will be shown in the later section. The ratio of the plug passing time τ to the period T was about 0.2 to 0.6, and the larger the air flow rate G_b, the larger the ratio τ/T.

3.4 Plug Velocity and Length. Local velocity of the plug is shown in Fig. 10, where plotted values were obtained by averaging data of fifty plugs. It can be seen that the velocity varies along the pipe in the same manner. This variation is caused by the air injection. The location of the injection is shown by the arrow on the abscissa in the figure. Plugs move against large resistance and the injected air supplies energy to the plugs, so that the plug velocity decreases where the interval of injection holes is long.

Figure 11 shows the relation between the plug velocity and air flow rate G_c measured in the region ③-④, in which G_b ranges from a small to large value. The figure indicates that the velocity depends only on G_c and it increases in proportion to G_c.

Figure 12 shows the average plug length measured in the region ③-④. The length is not so influenced by G_b and G_c as the velocity except the case of the largest G_c. The distance

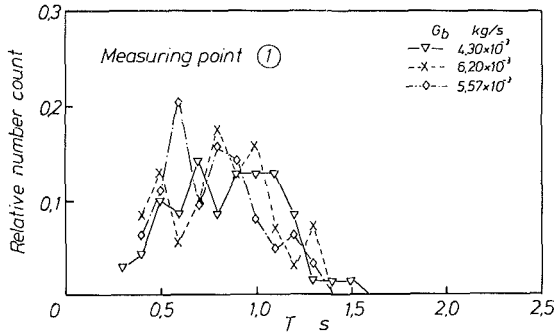

Fig. 8(*a*) Frequency distribution of the passing period in the case of large air flow rates G_b

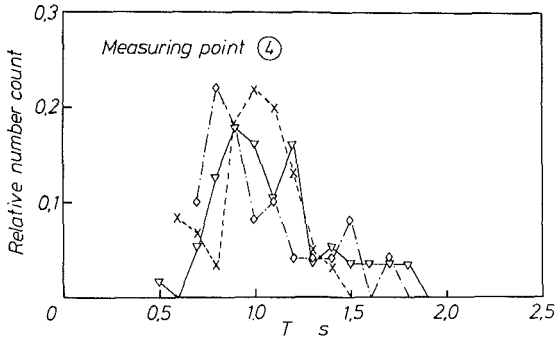

Fig. 8(*b*) Frequency distribution of the passing period in the case of large air flow rates G_b

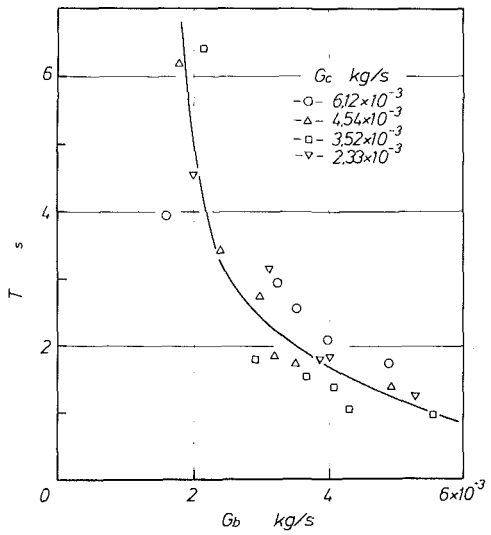

Fig. 9 Relation between the average period and air flow rate at the measuring point 4. (Uncertainty of T is ± 0.20 and G_b is ± 0.05)

between plugs changes largely depending on T, V, and l. In the present experiment, the minimum distance was about 0.5 m.

3.5 Cross-Sectional Area of the Plug. As shown in Fig. 4, a stationary layer of deposited particles always exists in the pipe. Thus, the total pipe cross section S is divided into the cross section of the plug above the deposit layer, S_p, and the cross section of the deposit layer S_d. As the sub-pipe was always within the deposit layer in the present experiment, the sub-pipe cross section is included in S_d. These cross sections were obtained from the height of the deposit layer H which was measured by photographing the plug. As a result, the height was found to depend on G_c but not on G_b, that is, the cross section of the plug S_p depends on G_c. Figure 13 shows

the height and cross section, where the cross section ratio increases with increasing G_c but it seems to have an asymptotic value below one.

The foregoing sections indicate that both G_b and G_c have large influence on the plug behavior. However, each role is clearly distinguished, that is, G_b increases the number of plugs and G_c increases the velocity and cross sectional area of the plug.

4 Pressure Drop and Transportation Properties

While behavior of the plug, which is shown in section 3, is a basic property in the plug flow, power consumption and efficiency of transport is more interesting in considering a practical use. Pressure drops are the most important quantities to estimate the required power. Most of the pressure drop occurs within the plug, but there is very little data available about it. Therefore, when plug conveyance facilities are designed, empirical relations established in packed beds have been applied to the pressure drop in the moving plug. This application is questionable in the case of coarse particles because the particles move very dynamically in real plug flow as shown in the previous section. The present section shows the difference in pressure drops between stationary packed beds and moving plugs, and transportation properties such as the loading ratio, efficiency and particle flow rate per unit time.

4.1 Pressure Drop. Figure 14 shows the pressure drop in the individual plugs measured in the regions ①-②, ②-③ and ③-④. The length of the plug changes from 0.2 to 0.6 m in spite of constant supply of the air and particles, because the phenomena are more or less irregular as mentioned before. The figure indicates that the pressure drop is proportional to the length as in a packed bed of the same sort of particles. Systematic measurements showed that the pressure drop depends on the air flow rate G_c and not on G_b. This is shown in Fig. 15, where the pressure gradient in the plug is plotted against the plug velocity which corresponds to G_c. The ratio of cross sections Sp/S defined in Fig. 13 is also known to be one of the quantities depending on G_c. As an attempt to relate the present result with another plug flow, the pressure gradient is plotted against Sp/S in Fig. 16. The points in the figure represent values averaged over G_b and all measuring regions. The point corresponding to $Sp/S = 0$ comes from another experiment. The authors measured pressure drops required to blow off a stationary packed bed in a horizontal pipe [6]. At the incipient stage of the motion, a number of small scale plugs were produced which occupied

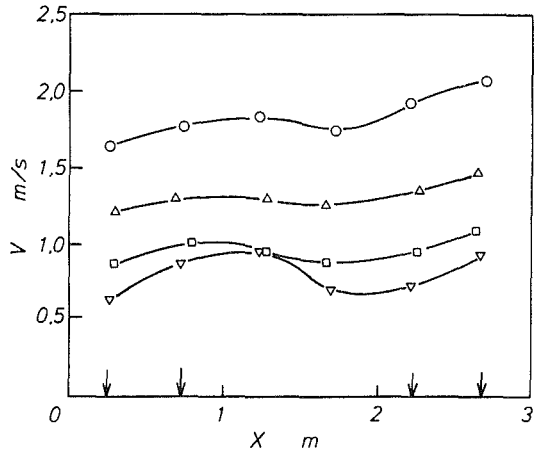

Fig. 10 Variation of the plug velocity. For legend, see Fig. 9 (Uncertainty of V is ± 0.05)

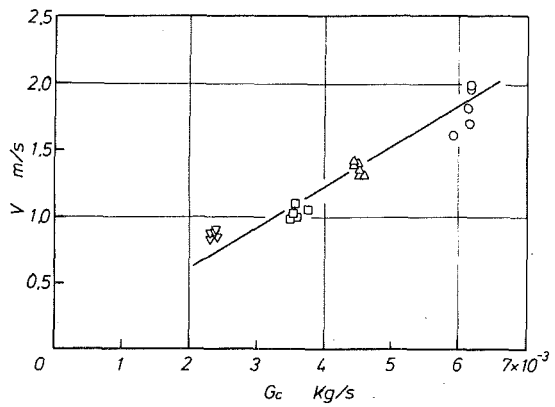

Fig. 11 Relation between the plug velocity and air flow rate G_c (○: $G_b = 20 - 5.1$ kg/s, △: $G_b = 1.5 \cdot 5.1$ kg/s, □: $G_b = 2.2 - 5.6$ kg/s, ▽: $G_b = 1.9 - 5.0$ kg/s) (Uncertainty of V is ± 0.05 and G_c is ± 0.05)

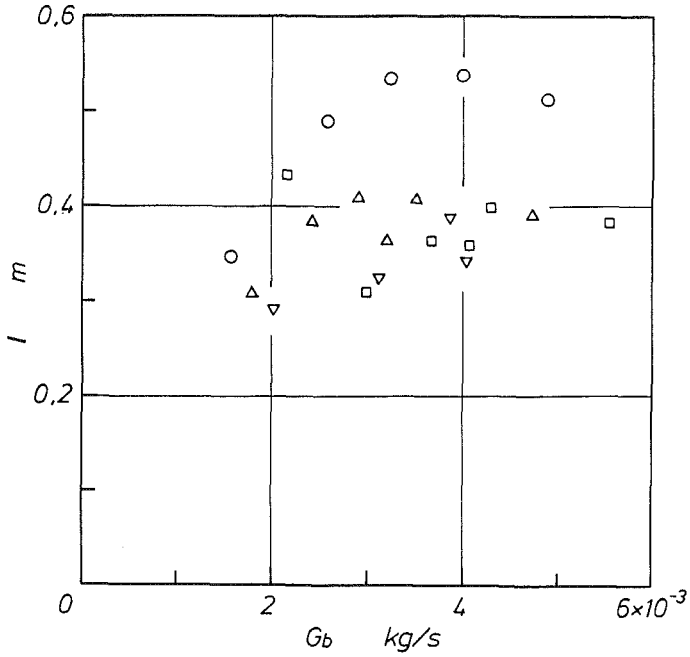

Fig. 12 Relation between the plug length and air flow rate Gb. For legend, see Fig. 9 (Uncertainty of l is ± 0.05 and G_b is ± 0.05)

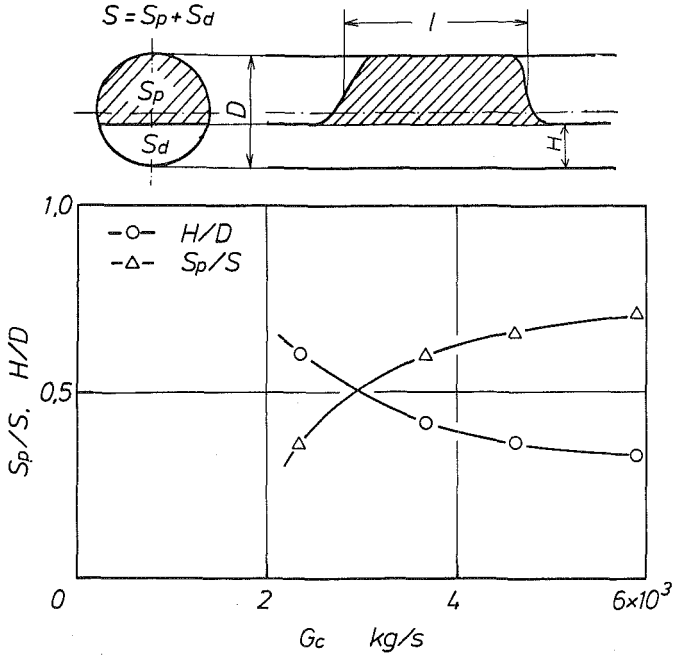

Fig. 13 Height H and cross sectional area S_p of the plug (Uncertainty of H/D or S_p/S is ± 0.02 and G_c is ± 0.05)

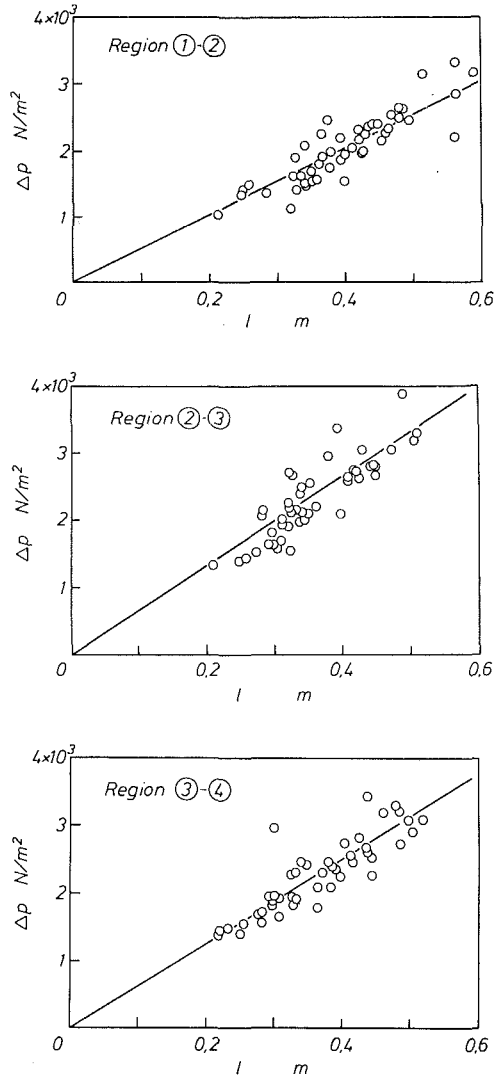

Fig. 14 Pressure drop in the moving plug (Uncertainty of Δp is 0.05 and l is ± 0.05)

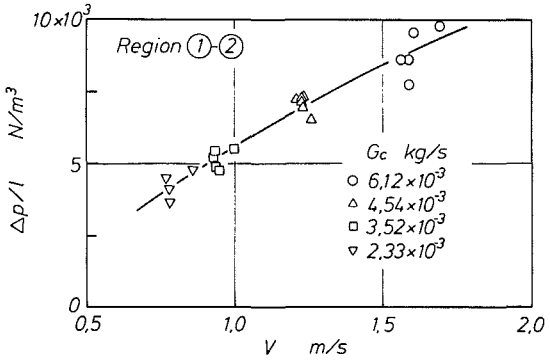

Fig. 15 Relation between the pressure gradient and plug velocity (Uncertainty of $\Delta p/l$ is ± 0.04 and V is ± 0.05)

only the top portion of the pipe section. The particles except those consisting of plugs were in the stationary state. If this plug is regarded as an asymptotic form of the present plug, the pressure drop at the incipient stage can be regarded as the pressure drop with Sp/S being nearly zero. The cited result at $Sp/S = 0$ was that obtained in the measurement of the same particles and pipe diameter that were used in the present experiment. The figure shows that the extrapolation of the present results agrees with the result of small plugs, and moreover the relation between $\Delta p/l$ and Sp/S is linear.

Next, the mechanism is considered how to maintain the

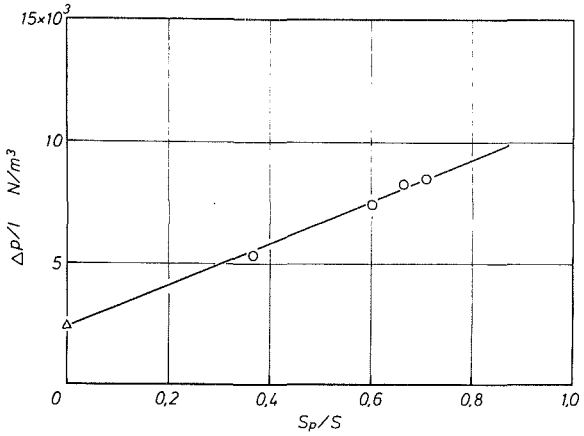

Fig. 16 Relation between the pressure gradient and cross sections ratio a: Present experiment △: Reference ——: Equation (7). $f = 1.2$ (Uncertainty of $\Delta p/l$ is ± 0.02 and S_p/S is ± 0.02)

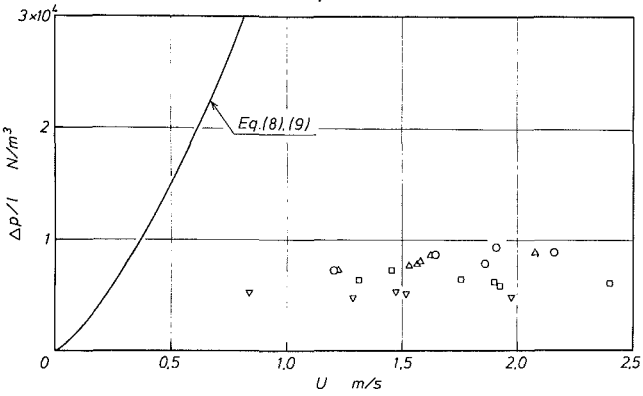

Fig. 17 Comparison of the pressure gradient between the packed bed and moving plug. For legend, see Fig. 15 (Uncertainty of $\Delta p/l$ is ± 0.04 and U is ± 0.05)

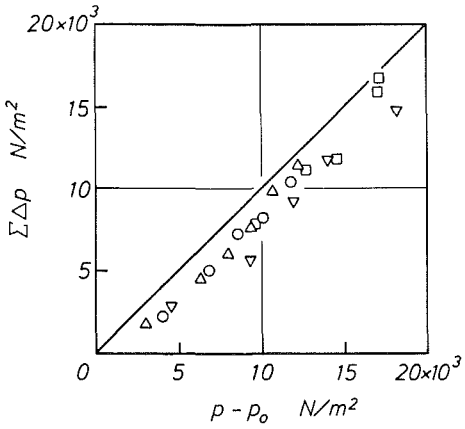

Fig. 18 Comparison of total pressure drops between equation (10) and direct measurement (Uncertainty of $\Sigma\Delta p$ is ± 0.03 and $p - p_0$ is ± 0.01)

plug flow in coarse particles. After that, a formulation which gives good agreement with measurements will be attempted. For maintaining the plug flow, there must be some force which lifts up the group of particles. If the pressure difference across the plug is the same to the difference in the layer just under the plug, the force due to the pressure acts on the deposited particles ahead. That is, the deposited particles in front of the plug are pushed by the particles behind. However, the pushed particles are not able to move forward because there lies a large amount of deposited particles. Thus, they must be lifted up and make a new plug. Particles in the plug are again desposited in the stationary layer in sequence from the rear side. When the deposit rate and entrainment rate are equal a stable plug flow is possible.

If the plug flow is maintained according to the mechanism

mentioned above, the smaller the cross section of the deposit layer, S_d, the larger the pressure difference Δp must be, because $\Delta p\ S_d$ is the force to push and lift up the particles ahead. Here, the product $\Delta p\ S_d$ is assumed to be constant with a given diameter and sort of particles. That is,

$$\Delta p\ S_d = \text{constant}.$$

When the above equation is applied to an asymptotic case of $Sp = 0$,

$$\Delta p\ S_d = \Delta p_0\ S, \tag{3}$$

where Δp_0 represents the pressure drop at the incipient stage of blowing off the stationary packed bed.

Here, a very simple model is adopted about the force acting on the plug. That is, $\Delta p\ Sp$ which is the force working on the plug is assumed to be equal to the dynamic friction concerned with the plug motion. The dynamic friction is expressed as the product of the weight W and the friction coefficient f in general. Thus,

$$\Delta p\ Sp = f\ W. \tag{4}$$

Adding equations (3) and (4),

$$\Delta p\ S = f\ W + \Delta p_0\ S. \tag{5}$$

The weight of the plug is given as

$$W = \rho_s'\ g\ l\ Sp, \tag{6}$$

where ρ_s' is the bulk density of particles. Substituting equation (6) into equation (5),

$$\Delta p/l = f\ \rho_s'\ g\ Sp/S + \Delta p_0/l. \tag{7}$$

The above equation shows a lineaar relationship between Sp/S and $\Delta p/l$, which agrees with Fig. 16. The value of $f = 1.2$ gives quantitatively good agreement with measurements. The authors propose this analysis as an attempt for dealing with the plug flow of coarse particles. The analysis should be examined by a number of experiments with different conditions.

4.2 Comparison With the Stationary Packed Bed. The pressure drop in a stationary packed bed is usually expressed as

$$\Delta p/l = \lambda\{(1-\epsilon)/\epsilon^3\}\rho_a U^2/(2d). \tag{8}$$

Ergun's empirical formula [7] is widely used in the coefficient λ.

$$\lambda = 300/\mathrm{R}_{ed} + 3.5, \tag{9}$$

where $\mathrm{R}_{ed} = U\ d/(1-\epsilon)\nu$. Pressure drops in the moving plug are compared with equations (8) and (9) in Fig. 17, where the results obtained in the most downstream measuring region ③-④ are shown. We measured the pressure drop in the stationary packed bed in the same pipe with the same particles and confirmed that Ergun's formula gives good agreement with the results. Figure 17 shows that the pressure gradient in the moving plug is much smaller than that in the packed bed. This means that the relation established in the packed bed can not be applied to the moving plug like the present one. The above result is significant in the plug flow analysis from now on. Therefore, further discussion is given in section 4.6 to examine the present results.

4.3 Pressure Drop Per Unit Pipe Length. Almost all of the pressure drop is caused by the part of the plug, so that the pressure drop per unit length $\Delta p/\Delta L$ is obtained by dividing the pressure drop Δp in the plug by the length period $\Delta L = T\ V$. Then, the total pressure drop in the whole pipe length is given by

$$\Sigma\Delta p = L\ \Delta p/(T\ V), \tag{10}$$

where L is the distance between the mixing point and receiver which was 6.2 m in the present experiment. The total pressure drop $\Sigma\Delta p$ obtained by equation (10) is compared with the direct measurement $(p - p_0)$ in Fig. 18. Since the quantities Δp, T and V vary along the pipe, the values averaged over the region ①-④ were used in substituting them into equation (10). The figure indicates that the total pressure drop $\Sigma\Delta p$ nearly agrees with the directly measured one, which proves the soundness of the pressure measurement in the present experiment.

Figure 19 shows the relation between the pressure drop per unit length and air velocity U_b. The velocity U_b is the velocity corresponding to the main pipe air flow rate G_b. Actual air velocity in the main pipe is larger than U_b because the air was also supplied from the sub-pipe into the main pipe. Thus, the air velocity obtained by dividing G_c by the main pipe cross section is shown in the figure. The numerals attached to the plotted points are the loading ratio $\mu = G_s/(G_b + G_c)$. The figure shows that $\Delta p/\Delta L$ increases monotonically with U_b and that dependence on the sub-pipe air flow rate does not appear. The pressure drop per plug shows the tendency different from the above one, that is, it depends mainly on the sub-pipe air flow rate as shown in section 4.1. The reason of this difference is as follows. The pressure drop per unit pipe

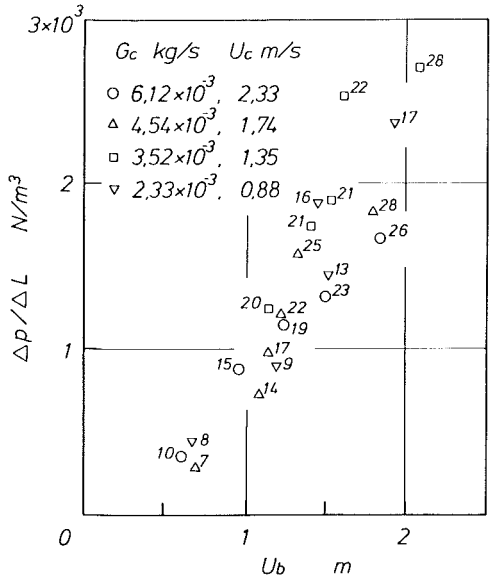

Fig. 19 Pressure drop per unit pipe length (Uncertainty of $\Delta p/\Delta L$ is ± 0.10 and U_b is ± 0.05)

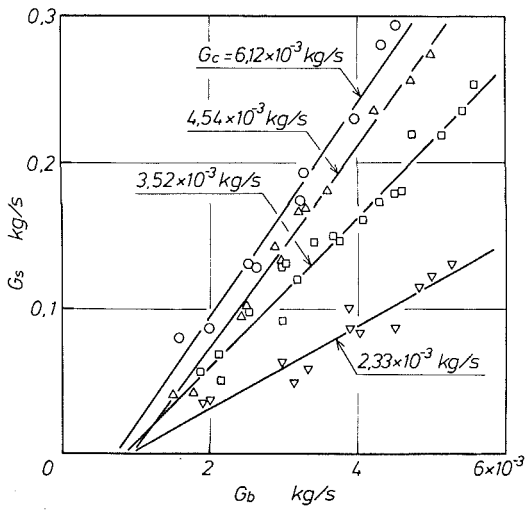

Fig. 20 Relation between the particle and air flow rates (Uncertainty of G_s is ± 0.05 and G_b is ± 0.05)

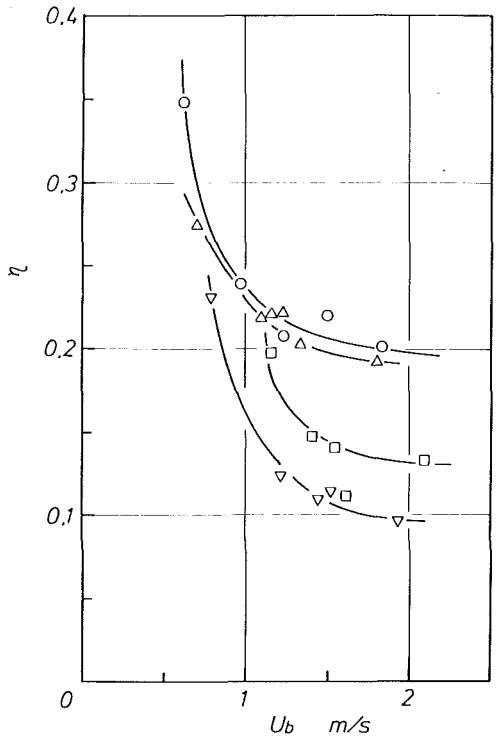

Fig. 21 Transport, efficiency. For legend, see Fig. 20 (Uncertainty of η is ± 0.05 and U_b is ± 0.05)

length is largely affected by the passing period which depends on the main pipe air flow rate, so that the effect of U_b is remarkable in Fig. 19.

4.4 Transportation Properties. In the double pipe method, the particles flow rate G_s depends on two kinds of air flow rates, G_b and G_c. Figure 20 shows the relation between G_s and G_b with G_c as a parameter. Both G_b and G_c contribute to the increase in G_s. This can be explained in connection with the results in section 3 as follows. G_b increases G_s by increasing the number of the plugs, and G_c by increasing the plug velocity and the cross sectional area of the plug. A linear relationship between G_s and G_b is observed in the figure. The gradient of the lines increases with increasing G_c. The extrapolation of these lines to the point of $G_s = 0$ gives the bulk air velocity U_{b0} being about 0.3 to 0.4 m/s. The bulk air velocity U' in the stationary packed bed at the incipient stage of blowing off motion was about 0.25 m/s in the same particles and pipe. Therefore, it can be said that U_{b0} and U' are the same order of magnitude. This means that the condition necessary to make the plug flow is related to the incipient motion of the stationary packed bed, which was already indicated in Fig. 16.

The loading ratio was about 8 to 28 in the present experiment as shown in Fig. 19. This value is low compared with the values gained in earlier dense phase conveying. Even a conventional pneumatic conveying of the suspension type has the loading ratio of about 10. The reason of the low loading ratio is that the sectional area of the plug is reduced by the presence of the stationary deposit layer. Therefore, the particles are not transported effectively.

4.5 Transport Efficiency. The transport efficiency η is usually defined by the following equation,

$$\eta = g\, G_s / (Q\, \Delta p / \Delta L), \tag{11}$$

where Q is the volume flow rate of air being $(G_b + G_c)/\rho_a$. The efficiency η defined by equation (11) is the ratio of the work by the gravitational force to the one given by the air in a vertical pipe. However, in a horizontal pipe, η does not have

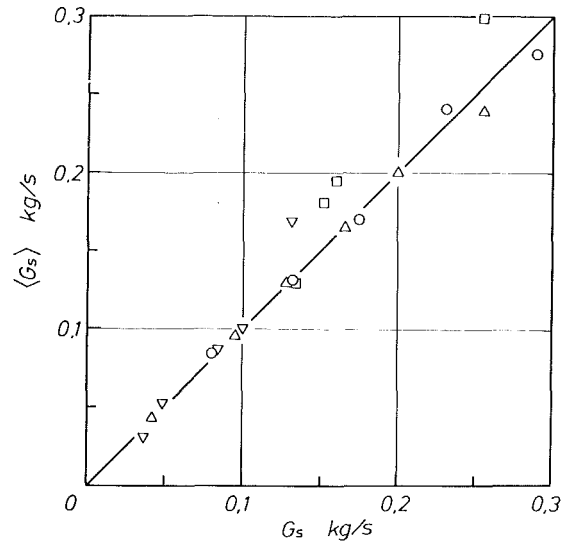

Fig. 22 Comparison of particle flow rates between equation (12) and direct measurement (The Uncertainty of $\langle G_s \rangle$ is ± 0.10 and G_s is ± 0.05)

such a definite meaning as an efficiency. The value of η can sometimes exceed 1 in the horizontal pipe. We have no other proper definition now, and thus the equation (11) is applied to the horizontal pipe. Figure 21 shows the results. The efficiency tends to become higher as the air velocity U_b decreases. The figure also shows that the larger the rate G_c, the higher the efficiency. However, the maximum value of η is about 0.35 which is not so high in comparison with a maximum value in usual suspension transport. For example, the experiment by Welschof [8] shows that the maximum value of η is 1.0. The reason of low efficiency is the same that was mentioned before for the low loading ratio.

4.6 Discussion. The most notable result in section 4 is the large difference in pressure drops in the moving plug and stationary bed. This large difference may occur if the porosity ϵ defined by $\epsilon = 1 - \rho_s'/\rho_s$ becomes much larger in the moving plug. The purpose of this subsection is to check whether such assumption is acceptable. The assumption can be checked by calculating the particle flow rate from the volume of the individual plug and bulk density assumed, and by comparing it with direct measurement. The particle flow rate is obtained by the equation.

$$\langle G_s \rangle = \rho_s'\, l\, Sp / T \tag{12}$$

The length l, sectional area Sp and passing period T were measured in detail in the present experiment. As an attempt to see the possibility of difference in the porosity or bulk density, the same bulk density to that in the stationary bed was substituted in equation (12) and $\langle G_s \rangle$ was calculated. $\langle G_s \rangle$ is compared in Fig. 22 with G_s measured by the use of a platform scale and stop watch. The figure shows that both flow rates agree quite well with each other, which means that the bulk density or porosity is not changed even in the moving plug. Therefore, the above assumption does not hold good.

The authors have no idea why the pressure drop is so small in the present plug. If the low pressure drop is caused by the secondary air, the double pipe method is advantageous in transport distance compared with others. At any rate, further study is to be desired.

5 Conclusions

A plug flow of coarse particles was measured in a horizontal pipe in which secondary air was injected from subpipe set inside the main pipe. The role of the main and subpipe air flow was clarified in connection with the plug motion,

pressure drop and transportation properties. The results are summarized as follows.

1. The plug of coarse particles accompanies a stationaly layer of deposited particles at the bottom of the pipe. The plug moves on this layer, showing a wavy motion. The height of the layer decreases with increasing the sub-pipe air flow rate.

2. The higher the main pipe air flow rate, the more regular the plug motion.

3. The main pipe air flow increases, the number of the plugs and the sub-pipe air flow increases the plug velocity.

4. The pressure drop in the plug is proportional to the plug length and its gradient increases with increasing sub-pipe air flow rate.

5. The pressure drop in the plug is quantitatively much smaller than that in the stationary packed bed of the same particles.

6. The pressure drop per unit pipe length increases as the main pipe air flow increases.

7. Both main and sub-pipe air flow rates increase the particle flow rate. The relation between the main pipe air flow rate and particle flow rate is linear.

8. Transport efficiency defined by equation (11) increases as the main pipe air flow decreases and the sub-pipe air flow increases.

Acknowledgment

The authors are very grateful to Mr. H. Honda who made the experiment with great competence and enthusiasm.

References

1 Lippert, A., "Pneumatic Transport of Highly Concentrated Materials," *Chemie-Ing.-Techn.*, Vol. 38, No. 3, 1966, pp. 350–355 (in German).

2 Muschelknautz, E., and Krambrock, W., "Simplified Calculations on Horizontal Pneumatic Feed Pipes at High Loading with Finely Divided Granular Products," *Chemie-Ing.-Techn.*, Vol. 41, No. 21, 1969, pp. 1164–1172 (in German).

3 Flatt, W., and Allenspach, W., "Capacity and Efficiency Increase of Pneumatic Conveying Systems," *Chemie-Ing.-Techn.*, Vol. 41, No. 21, 1969, pp. 1173–1176 (in German).

4 Tsunakawa, H., Nakai, J., and Aoki, R., "Pneumatic Conveying of Solid Plugs," *J. Soc. Powder Technology*, Japan, Vol. 16, No. 5, 1979, pp. 249–254, (in Japanese).

5 Haywood, N. I., and Richardson, J. F., "Slug Flow of Air-Water Mixtures in a Horizontal Pipe: Determination of Liquid Holdup by γ-Ray Absorption," *Chem, Eng. Sci.*, Vol. 34, No. 1, 1979, pp. 17–30.

6 Tsuji, Y., and Morikawa, Y., "A Study on Blowing Off a Stationary Plug of Coarse Particles in a Horizontal Pipe," *Proceedings of the International Conference* on Pneumatic Conveying, London, Jan. 1979.

7 Zenz, F. A., and Othmer, D. F., "*Fluidization and Fluid-Particle Systems*," Reinhold, New York, 1960. p. 187.

8 Welschof, G., "Pneumatic Conveying at High Particle Concentrations," VDI-Forsch.-Heft 492, 1962 (in German).

T. Sarpkaya
Professor,
Department of Mechanical Engineering,
Naval Postgraduate School,
Monterey, Calif. 93940
Fellow ASME

H. K. Kline
LCDR, U. S. Navy,
Executive Officer,
USS Oldendorf (DD-972),
FPO
San Francisco, Calif.
Assoc. Mem. ASME

Impulsively-Started Flow About Four Types of Bluff Body

Measurement of the forces acting on a circular cylinder and those on three other noncircular cylinders is reported. The results confirm and quantify the profound effects of the shedding of the first two or three vortices on all the characteristics of resistance and demonstrate that the evolution of the flow, and hence the forces, significantly depend on whether the separation points are fixed or mobile, or a combination thereof. The data are expected to form the basis of future numerical analysis based on refined discrete vortex models.

Introduction

Impulsively-started flow about a circular cylinder is a classic problem in fluid mechanics for which analytical and numerical solutions exist at least for small times and relatively low Reynolds numbers. The complexity of the phenomenon at relatively large Reynolds numbers stems partly from the difficulty of obtaining a solution of the equations of motion and partly from experimental difficulties [1].

Numerical solutions based on finite difference techniques and some form of the discrete vortex model require experimental verification and guidance. This is particularly important for impulsive flow about noncircular bodies for the delineation of the physics needed to determine whether the numerical solution is the real one for the given set of boundary conditions. Often the knowledge of where the separation points occur is lacking and this information could come only from experiments. The flow in the vicinity of the separation points exhibit time- and Reynolds-number dependent complex recirculation zones or secondary vortices [1–3]. The numerical simulation of the primary and secondary vortices by, for example, the discrete vortex model requires a clear understanding of these separation zones and the sources of vorticity feeding the shear layers. The discrete vortex model cannot help to discover such features of the flow or help to interpret their consequences unless they are incorporated into the model at the start of the numerical formulation. Thus, careful measurement of the forces and pressures and flow visualization are necessary to guide and complement the analytical efforts, particularly at large Reynolds numbers. All other alternatives such as the numerical solution of the unsteady Navier-Stokes equations or the development of empirical correlations are less attractive.

Aside from its intrinsic fluid mechanical interest, impulsively started flow is of direct relevance to many practical applications. These include the loading of bodies immersed in the pressure suppression pool of boiling water nuclear reactors during a loss-of-coolant accident (LOCA) and the loading and subsequent response of underwater vehicles, such as a submarine or torpedo undergoing a turn or dive. Also, the development of cross flow with distance along an inclined body of uniform diameter is thought to be analogous to the development with time of the flow on a cylinder set impulsively in motion from rest (the so-called cross-flow analogy). A critical review of the available theories and experimental data leads to the conclusion that this hypothesis yields a satisfactory first approximation over certain ranges of Mach number, Reynolds number, body length, and angle of attack, and makes the two-dimensional impulsive flow phenomenon a useful tool for the analysis of separated subsonic and moderately supersonic flow about slender lifting bodies [4].

This work is an attempt to provide data on the forces acting on four types of bluff bodies (a circular cylinder, a D-shaped cylinder, a T-shaped cylinder, and a flat plate). A wide range of angles of attack were used for the three non-circular cylinders. The Reynolds number ranged from about 20,000 to 30,000.

The body shapes and the ambient flow characteristics, although resulting in a much simpler flow than those encountered in the practical applications cited, have been arranged to provide a basis for the improvement of calculation methods and for a fuller understanding of the role played by the shedding of the first few vortices.

Experimental Apparatus

Water Tunnel. The vertical water tunnel used for these experiments was previously described in references [5 and 6]. It consists of a 12 ft (3.66 m) high, 2 ft by 2 ft (0.61 m × 0.61 m) cross-section tunnel, a quick-release valve, located at the base of the tunnel, and various force and displacement transducers.

The position of a mushroom-shaped seating surface, closing a large circular opening at the bottom of the tunnel, is controlled by a three-way valve, mounted beneath the tunnel. The stem extends downward from the mushroom valve and is directly coupled to the control valve assembly. Compressed

Contributed by the Fluids Engineering Division for publication in the JOURNAL OF FLUIDS ENGINEERING. Manuscript received by the Fluids Engineering Division, June 1, 1981.

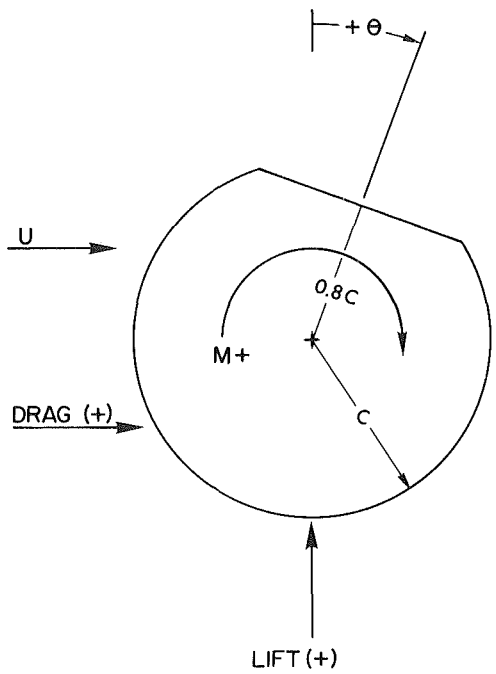

Fig. 1(a) D-shaped cylinder

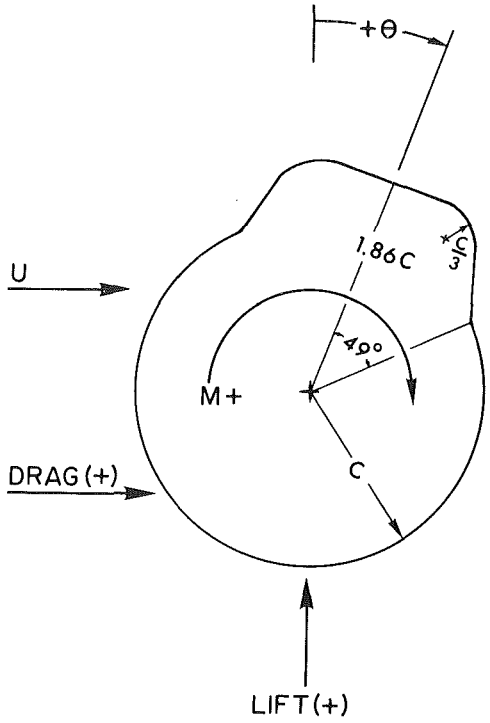

Fig. 1(b) T-shaped cylinder

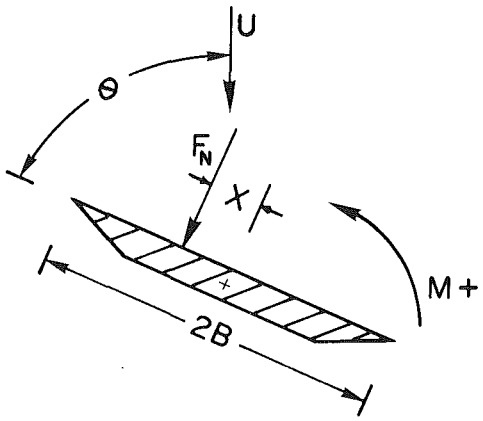

Fig. 1(c) Flat plate

air is provided to the two air chambers in the upper part of the valve. A two-way valve in the air-supply line provides on-off control of the quick release valve and, therefore, the flow itself. Upon opening the two-way air-supply valve, the differential pressure between the two air chambers in the upper part of the control valve initiates motion of the piston, rapidly opening the mushroom valve. Subsequent valve motion is regulated by the vertical motion of the piston in the lower part of the control valve and the viscosity of oil in the liquid chamber. The resistance which the piston encounters can be varied by opening or closing the dual ports in the piston and by suitably adjusting the supply-air pressure and the oil viscosity. These adjustments allow constant velocities at desired rates to be obtained. Following the rapid initial opening, which accelerates the flow in 0.1 seconds or less, slower further opening of the mushroom valve sustains a controlled drop of the tunnel water level at a constant velocity. Suffice it to note that, other than numerical experiments, there is no mechanical or traveling-shock system which is capable of generating a truly impulsive flow. Efforts to generate impulsive or uniformly-accelerated flow at high Reynolds numbers or accelerations in a liquid medium may be hampered by the generation of compression and rarefaction waves and regions of intense cavitation. These are some of the difficulties of the experiments with impulsive flows. [1].

Measurement System. Velocity was measured through the use of a variable resistance probe. A seven foot (2.14 m) long platinum wire, placed vertically in the tunnel and mounted away from the walls, provided water-level indication to an amplifier-recorder assembly. Three force transducers were used to measure the instantaneous lift and drag forces and moment on the test bodies. Special housings were built for each gage so that they could be mounted on the tunnel wall at each end of the test body. Prior to testing a new body, calibration of the drag, lift, and moment transducers was conducted. Furthermore, impulsive flow was initiated a number of times to verify that the velocity remained constant and the force signals were free from noise. Additional details are described in [6]. Unfiltered raw analog data were produced from the force and moment transducers and the variable resistance probe. The data were then digitalized with

Nomenclature

B = half width of flat plate
C_d = drag coefficient, $F_d/(\rho cU^2)$
C_L = lift coefficient, $F_L/(\rho CU^2)$
C_m = moment coefficient, $M/(\rho c^2 U^2)$
C_n = normal force coefficient, $F_n/(\rho BU^2)$
c = radius of base circle, see Fig. 1
F_d = drag force
F_L = lift force or transverse force
F_n = normal force
f_v = vortex shedding frequency
M = moment
Re = Reynolds number, $2Uc/\nu$
St = Strouhal number, $2f_v c/U$
T = time
T^* = normalized time, UT/c or UT/B
U = velocity of the ambient flow
X = distance to normal force from plate axis
θ = angle of attack, see Fig. 1
ν = kinematic viscosity of fluid
ρ = density of fluid

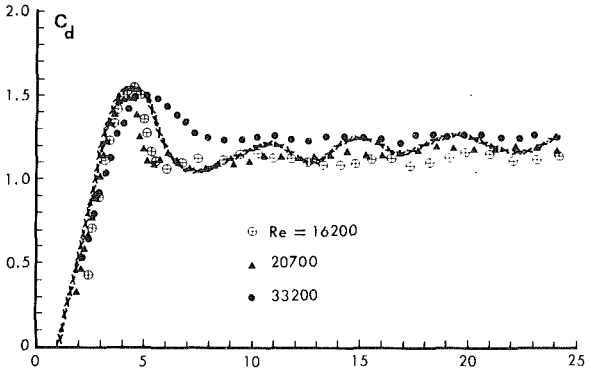

Fig. 2 Drag coefficient versus UT/c for the circular cylinder, (points: experiment, xxxxx discrete vortex model [7-9])

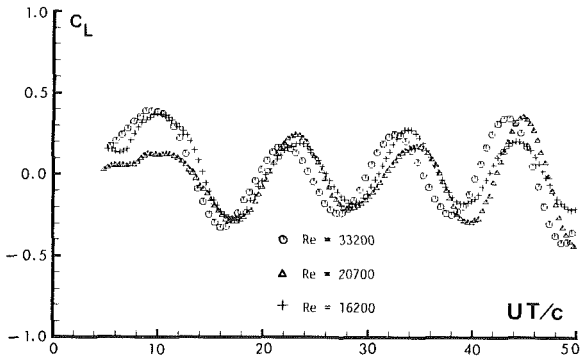

Fig. 3 C_L versus UT/c for the circular cylinder (experiment)

an HP-9874A digitizer coupled to an HP-9845B desk-top computer. Each run was repeated at least three times.

Test Bodies. Three cylinders [a circular cylinder with $c = 1.5$ in (3.81 cm), a D-shaped cylinder with $c = 1.75$ in (4.44 cm), a T-shaped cylinder with $c = 1.75$ in (4.44 cm)] and a flat plate with $B = 1.5$ in (3.81 cm) were used in the experiments. Figures 1(a) through 1(c) show the cross-sectional profiles of the D- and T-shaped cylinders and the flat plate together with the directions of forces, moments, and the angle of attack.

Each test body was mounted horizontally in the middle of the 2 ft by 2 ft (0.61 m × 0.61 m) test section, 6 ft (1.83 m) above the bottom of the tunnel and 5 ft (1.52 m) below the free surfaces. The length of each cylinder was cut so that a gap of approximately 0.06 in (1.5 mm) was present between the tunnel wall and each end. The gaps were filled with foam, glued to the ends of the cylinder.

The maximum possible error associated with the measurement of forces and moments was 5 percent. The variation of velocity during a given run was less than 0.5 percent for times larger than 0.1 second after the initiation of motion, i.e., for $T^* > 0.5$.

Results

The results are discussed in four sections which relate to the four body shapes.

Circular Cylinder. The variation of the drag and lift coefficients with $T^* = UT/c$ is shown in Figs. 2 and 3. C_d reaches a maximum at about $T^* = 4.5$ and then rapidly decreases to its ultimate value of about 1.2 (in the range of Reynolds numbers shown in Fig. 2). The fluctuations of C_d have a frequency twice the vortex shedding frequency. The overshoot of the drag coefficient is a direct consequence of the rapid accumulation of vorticity in the first two symmetrically growing vortices. Also shown in Fig. 2 is the drag coefficient predicted through the use of the discrete vortex model, based on the rediscretization of the shear layers, boundary-layer-wake interaction, and a heuristic model of circulation dissipation. Mathematical and numerical details of the model are described in [7-9]. The agreement between the experimental and numerical results is quite good in spite of the fact that the discrete vortex model does not deal with the complex recirculation zones near the separation points. Two shear layers, connected to two mobile separation points, represented the separated flow about the circular cylinder (see Fig. 4).

The lift coefficient shown in Fig. 3 may be compared with the predictions of the discrete vortex model shown in Fig. 5. The measured lift coefficient has a mean amplitude of about 0.3 and a frequency of $f_v = 0.10$, corresponding to a Strouhal number of 0.2. The calculated lift coefficient has a mean

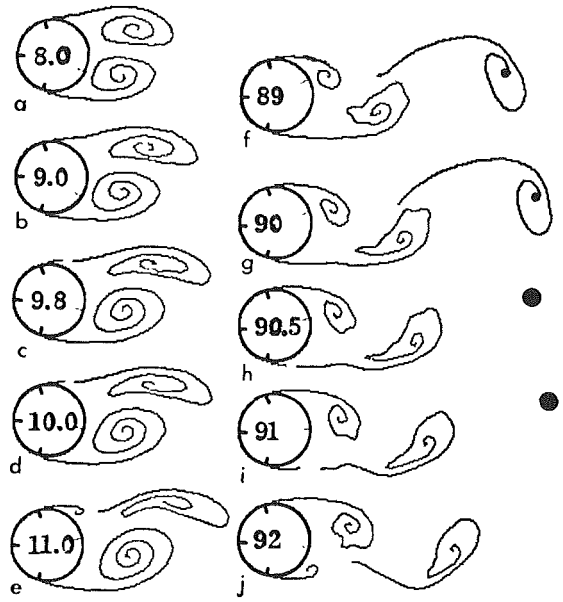

Fig. 4 Discrete vortex model representation of the vortex shedding in implusive flow [7], (numbers in circles represent UT/c)

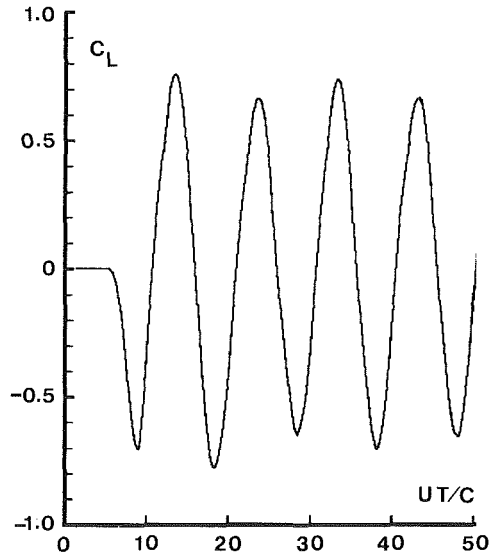

Fig. 5 Transverse force on a circular cylinder via the discrete vortex model [7]

amplitude of about 0.65 and a frequency of $f_v = 0.1025$, corresponding to a Strouhal number of 0.205. The imperfect spanwise coherence of the vortices in the experiments may partly account for the smaller lift coefficient. One must also bear in mind the fact that the discrete vortex model has not yet evolved into a method of prediction. It is possible to match the observed and calculated separation points and the lift and drag coefficients with some retrofitting to experiments through the use of one or more judiciously-selected disposable parameters. Hopefully, additional calculations and comparisons will improve the predictive powers of the discrete vortex model.

The onset of lift and its relation to the evolution of drag are of some importance. Figures 2 and 3 show that the drag overshoot reaches its maximum shortly before the onset of lift (vortex asymmetry). The shedding of the first vortex decreases C_d dramatically. However, the shedding of subsequent vortices cause only minor oscillations in C_d. Finally, it should be noted that the time evolution of C_d for $T^* < 1$ differs from numerical results obtained by numerical solution of the Navier-Stokes equations (see e.g., Thoman and Szewczyk [10]). This is partly due to the inertial forces associated with the impulsive start of the motion and partly due to the differences in the generation of flow between the experiments and numerical analysis. The numerical calculations can simulate a truly impulsive start whereas the experiments must necessarily reflect the history effects of the period of initial acceleration. Calculations have shown that [7, 10] $T^* \leq 1$ corresponds to the time interval during which the separation point moves rapidly from the rear stagnation point to about $\theta_s \pm 109$ deg. The particular time dependence of the ambient flow during the time interval $0 < T^* < 1$ dictates the evolution of the separation points and the total resistance. As to the discrete vortex model, the calculation normally begins at about $T^* = 1$, with the placement of two symmetrical nascent vortices near the separation pionts at $\theta_s = \pm 109$ deg. Thus it already excludes the time interval $T^* < 1$.

D-Shaped Cylinder. This body was tested at angles of attack of 0, ± 10, ± 20, ± 30, ± 45, and -90 degrees. The drag, lift, and moment coefficients are shown in Figs. 6 through 8 for Re = 28,000 and $\theta = 0$ degrees.

Dramatic effects are associated with the growth and shedding of the first two or three vortices. At the start of the motion the flow separates almost immediately at the flat side of the D-shape and a single vortex grows rapidly at a rate of growth such that the vorticity accumulates to an amount far in excess of that found in the later stages of motion. This excess vorticity reduces the base pressure and causes a large drag overshoot. Shortly after the development of the first vortex, the flow separates from the round side of the cylinder and a second vortex begins to grow. The growth of this vortex gives rise to another drag overshoot (see Fig. 6). Note that in the case of the circular cylinder two vortices grow symmetrically and this leads to a drag overshoot with a single hump spanning over a time period of about half that for the D-shaped cylinder. In other words, the shedding of each of the first two vortices from a noncircular cylinder gives rise to a drag overshoot whose magnitude and duration depend on the particular details of the asymmetry of the body and the time interval between the shedding of the vortices. The shedding of the subsequent vortices causes only minor changes in the asymptotic value of the drag coefficient.

Also shown in Fig. 6 is the drag coefficient predicted through the use of the discrete vortex model together with a suitable conformal transformation to map the points on and outside the D-shaped body to the points on or outside a circle [11]. With the exception of the said transformation, the details of the numerical analysis are nearly identical to those described in [7–8]. Apparently, the predictions of the discrete

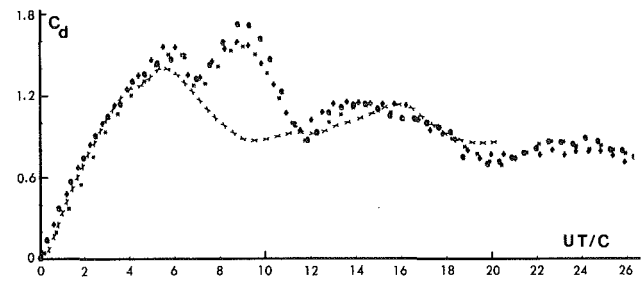

Fig. 6 Drag coefficient for the D-shaped cylinder, (points: experiment, xxxxxx discrete vortex model [11])

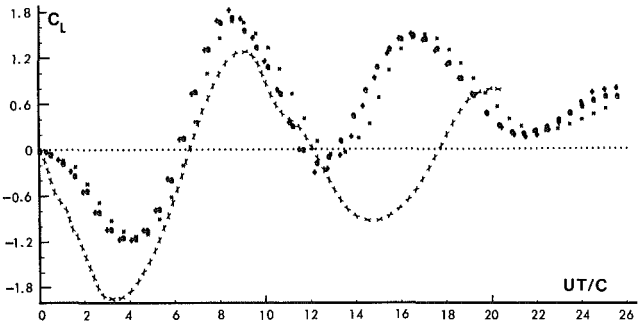

Fig. 7 Lift coefficient for the D-shaped cylinder, (points: experiment, xxxxx discrete vortex model [11])

vortex model are encouraging but there are significant differences between the measured and calculated C_d values, particularly in the range $7 < T^* < 12$. The numerical model does not account for the second drag overshoot resulting from the shedding of the second vortex from the round side of the D-shaped body. This is primarily due to the fact that the time difference between the evolutions of the first two vortices is not correctly modeled. This points out some of the difficulties associated with the applicatoin of the discrete vortex model to noncircular bodies with fixed and mobile separation points.

Figure 7 shows that at the start of the motion the lift force is directed toward the flat surface of the D-shaped body. This is in conformity with the shedding of the first vortex from the flat side of the cylinder and suggests that a D-shaped submerged vehicle (with the flat surface horizontal) turning left or right is subjected to a vertical force which tends to submerge the body for T^* less than about 6 (assuming no other vortices are present and the three-dimensionality of the body may be ignored). In general other body- and control-surface generated vortices tend to interact with the first vortex resulting from the impulsive motion of a submarine's turn. Thus, the right or left turn of a submarine with a D-shaped cross-section does not necessarily and always result in a force which tends to generate a diving motion.

The subsequent shedding of vortices results in a transverse force alternating about a positive mean value (see Fig. 7) with a frequency of $f_v = 0.19$ $(U/(2c)$ which corresponds to a Strouhal number of $\mathrm{St} = 2f_v c/U = 0.19$. The previous experiments (see e.g., [12]) do not deal with the case of $\theta = 0$ deg, (see Fig. 1(*a*)). Mujumdar and Douglas [12] who determined the Strouhal number for a number of non-circular cylinders in steady flow found $\mathrm{St} = 0.21$ for $\theta = 90$ deg, and $\mathrm{St} = 0.14$ for $\theta = -90$ deg at the corresponding Reynolds numbers (maximum Re in [12] was about 20,000). Evidently, the case of $\theta = 0$ deg yields a Strouhal number close to that for a circular cylinder. In other words, with the ambient flow parallel to the flat face of the D-shaped body, the flow "sees" the body more or less as a circular cylinder.

A comparison of Figs. 3 and 7 shows that C_L for the D-

shaped body is considerably larger than that for the circular cylinder. This is partly due to the increased spanwise coherence of vortices emanating first from a fixed then a mobile separation point, alternatingly, and partly, and more importantly due to the asymmetric evolution and shedding of the first two vortices. The latter enhances the clockwise or counter-clockwise circulation imposed on the body, thereby increasing the lift or the transverse force. This is also the reason for the development of lift right from the start of the motion (see Fig. 7). In the case of a circular cylinder, the first two vortices evolve symmetrically. Thus, the net circulation imposed on the cylinder remains practically zero until the asymmetry sets in (see Figs. 3 and 5). In other words, the time interval between the reaching to full strength of the first two vortices is extremely important in the initiation, growth, and magnitude of the transverse force. These, in turn, are directly related to the shape of the body and the angle of attack.

Also shown in Fig. 7 is the lift coefficient predicted through the use of the discrete vortex model [11]. As noted earlier in connection with the discussion of the drag coefficient, the predictions of the discrete vortex model are encouraging but there are significant differences between the measured and calculated lift coefficients, particularly for $T^* > 12$.

Figure 8 shows the moment coefficient. The sign of the moment is such that it tends to bank the body in a direction opposite to the direction of heel that normally occurs during the initial phase of the turn, i.e., a submarine rolls inboard during a turn. Thus, the moment created by the impulsive cross-flow of the turn helps to stabilize the heeling position of the body. The discrete vortex model of Shoaff and Franks [11] did not predict any moment for this particular body.

T-Shaped Body. The drag, lift, and moment coefficients are shown in Figs. 9 through 11 for Re = 24,500. As in the case of the D-shaped body, the first vortex begins to grow immediately on the side where geometrical symmetry is disturbed, i.e., at the side of the flat-topped protrusion. The rapid accumulation of vorticity first in the vortex shedding from the side of the protrusion and then in the vortex shedding from the round side of the body results in a large drag overshoot, spanning over a period covering the shedding of the first two vortices. At large values of T^*, C_d approaches a value of about 1.5.

The direction of the lift force during the development and shedding of the first vortex (for $T^* > 0.6$) is from the protrusion toward the axis of the cylinder. For T^* smaller than about 0.6, the flow does not quite separate. This results in a small but positive lift force of brief duration since the unseparated flow on the side of the protrusion must have larger velocities and hence lower pressures relative to the other side.

Motion pictures have revealed that the first lift maximum occurs at the time when the first vortex is still attached to (and about to be separated from) its shear layer ($T^* \simeq 5$) and the second vortex has not yet grown sufficiently. As time or the relative displacement of the fluid increases the second vortex grows and the lift coefficient passes through zero at $T^* = 8$. At this time, the net circulation imposed on the body is nearly zero. A study of the subsequent stages of motion has shown that the second vortex reaches its full strength at $T^* = 10.3$ and then the third vortex begins to develop from the protruding side of the body (where the first vortex was initiated).

Also shown in Figs. 9 and 10 are the drag and lift coefficients predicted through the use of the discrete vortex model [11]. Evidently, there are significant differences between the measurements and the model predictions. The understanding of the causes of these differences may lead to the improvement of the discrete vortex model.

Unlike the D-shaped body, the shedding of the vortices causes significant changes in the moment acting on the T-shaped body (see Fig. 11). This is primarily due to the fact that the protrusion increases the available moment arm whereas, with the D-shaped cylinder, the flat face decreases the moment arm. Consequently, underwater bodies with protrusions are more likely to undergo larger amplitudes of moment fluctuations as a result of an impulsive turn. This may give rise to greater stability problems. It is noted in passing that the discrete vortex model of Shoaff and Franks [11] did not yield any moment for the T-shaped body.

It follows from the discussion of the results for the D- and T-shaped cylinders that the asymmetry of the body relative to the direction of the flow removes the randomness from the

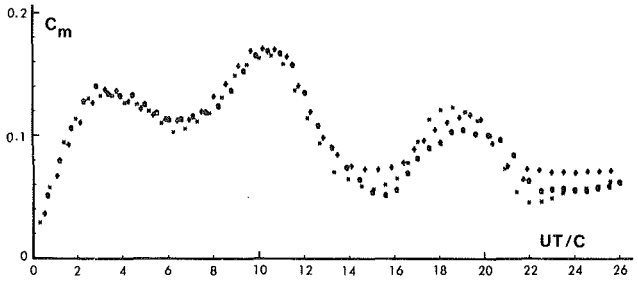

Fig. 8 Moment coefficient for the D-shaped cylinder (experiment)

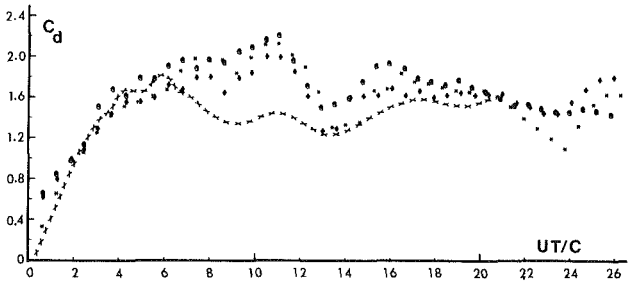

Fig. 9 Drag coefficient for the T-shaped cylinder ($\theta = 0$ degrees), (points: experiment, xxxxx discrete vortex model [11])

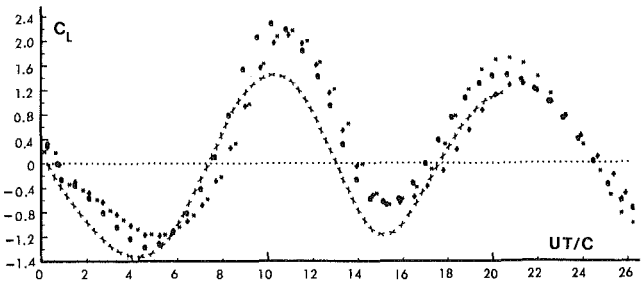

Fig. 10 C_L for the T-shaped Cylinder ($\theta = 0$ degrees), (points: experiment, xxxxx discrete vortex model [11])

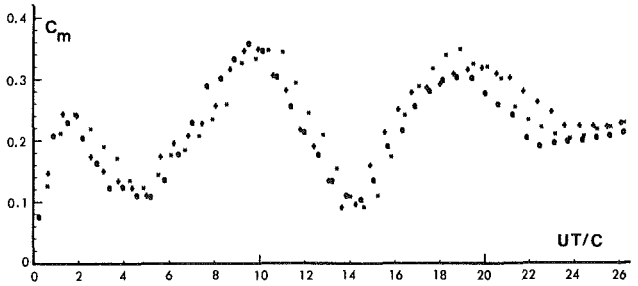

Fig. 11 C_m for the T-shaped cylinder ($\theta = 0$), (experiment)

position of the growth of the first vortex. In the case of a circular cylinder the first vortex may shed from either side, at random. The introduction of a geometric deformity to the otherwise axisymmetric shape of the cylinder fixes the direction of the lift force and the position of the first vortex. Thus, the shedding of the first vortex is not a consequence of an instability in two symmetrically growing vortices, as in the case of the circular cylinder. The alternate shedding of the vortices right from the start of the motion gives rise to a drag overshoot over a longer time period, with two pronounced peaks corresponding to the first two vortices.

Flat Plate. The Reynolds number for this body was kept at a nearly constant value of Re = 21,000. The results are discussed with respect to two representative angles of attack ($\theta = 90$ and 60 degrees) in order to accentuate the differences brought about by the shedding of the vortices on the normal force coefficient C_n and the position of the resultant force X/B.

Figure 12 shows the normal force coefficient for $\theta = 90$ degrees. As anticipated, the symmetric growth of the vortices causes a large normal force to develop during the early stages of motion. The shedding of the vortices does not cause significant oscillations in C_n for this particular case where the flow is normal to the plate. This is attributed to the absence of the transverse force (no after-body). For UT/B larger than about 12, C_n reaches a near constant value of about 2.2. No discrete vortex model predictions exist for this particular angle of attack.

Figure 13 shows C_n for $\theta = 60$ degrees. One of the three sets of data shown in Fig. 13 was obtained by measuring the normal force directly and the other two sets were obtained by summing vectorially the independently-measured lift and drag forces. It is apparent that at the early stages of motion C_n increases dramatically to values never before noted in the relevant literature. The shedding of the first vortex at $T^* = 9$ brings about an abrupt change in C_n. A subsequent maximum in C_n occurs at $T^* = 14$, as a result of the shedding of the second vortex.

Also appearing in Fig. 13 are the discrete vortex model predictions of Kiya and Arie [13] and of Sarpkaya [14]. Sarpkaya's results are based on the methods described in [14] but modified to take into account the circulation dissipation described in [8]. Comparisons of the predicted and measured normal force coefficients show relatively poor agreement. This is rather surprising in view of the fact that the flat plate with fixed separation points appears to be more amenable to numerical treatment via the discrete vortex model.

The normalized moment arm X/B for $\theta = 60$ degrees is shown in Fig. 14. The fluctuations of the moment arm are directly related to the shedding of the vortices and are more severe than for either the D-shaped or the T-shaped body. This is partly due to the fact that the vortex strength for a plate is relatively larger and partly because the sharp edges of the plate fix the separation points and increase the spanwise coherence along the plate.

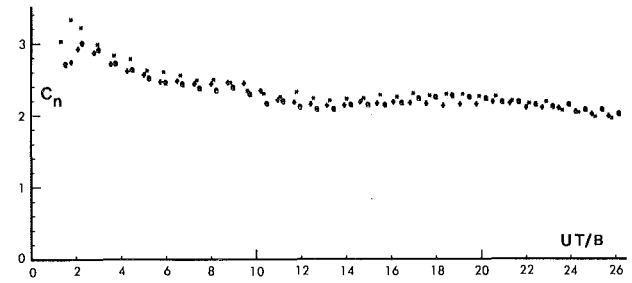

Fig. 12 C_n for the flat plate with $\theta = 90$ degrees, (experiment)

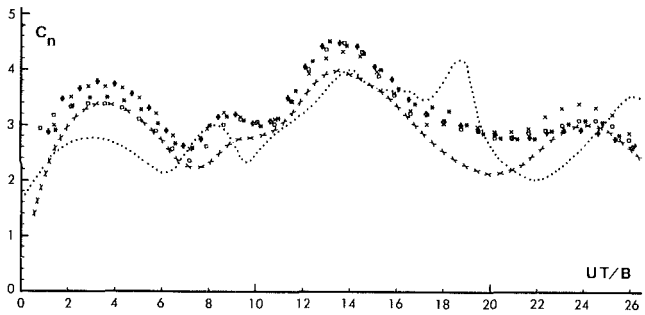

Fig. 13 C_n for the flat plate with $\theta = 60$ degrees, (points: experiment, ... [13], xxxxxx [14])

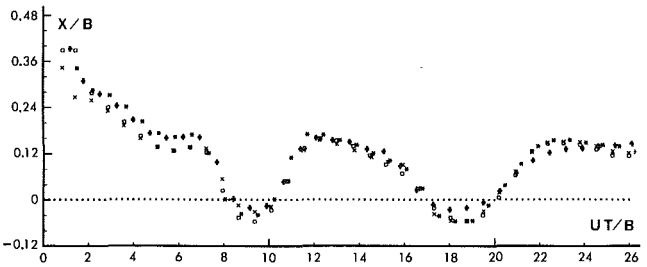

Fig. 14 Moment arm versus UT/B for the flat plate with $\theta = 60$ degrees, (experiment)

Concluding Remarks

It has been shown that the impulsively-started flow gives rise to significant drag overshoot. This is true whether the vortices develop symmetrically at first, as in the case of a circular cylinder, or asymmetrically, as in the case of D- and T-shaped cylinders. For noncircular cylinders, the asymmetric separation of flow, at different points and times, and the subsequent alternate shedding of the first two vortices result in overlapping drag overshoots for each vortex. The combined drag overshoot spans over a period of T^* considerably larger than that for a circular cylinder. Asymmetry of the body relative to the direction of the impulsive flow removes the randomness from the shedding of the first vortex and fixes the initial direction of the transverse force. Any geometrical deformity which precipitates the occurrence of asymmetric separation necessarily leads to a preferential shedding of the first vortex and to the determination of all other features of the flow.

There are at present no reliable analytical techniques which accurately predict the behavior of the impulsive flow about bluff bodies. Most of the numerical models are restricted to small Reynolds numbers and relative displacements. The discrete vortex model is not free from deficiencies and requires some retrofitting to experimental results even for a circular cylinder or simple flat plate. Attempts to use the discrete vortex model for non-circular cylinders through the use of suitable conformal transformations meet with additional difficulties regarding separation points, sources of oppositely-signed vorticity, and the interaction of the boundary layers with the large scale motion of the wake. The data presented herein should provide guidance and means of comparison for future analytical efforts.

Acknowledgment

This work has been supported by David W. Taylor Naval Ship Research and Development Center, Bethesda, Maryland. Special thanks are due Mr. Jack McKay for his skillful and

industrious efforts which were essential to the experimental process described herein. The authors also wish to express their appreciation to Dr. Ray L. Shoaff for his support.

References

1 Sarpkaya, T., and Isaacson, M., *Mechanics of Wave Forces on Offshore Structures*, Van Nostrand Reinhold, New York, 1981, pp. 73–85.

2 Bouard, R., and Coutanceau, M., "The Early Stage of Development of the Wake Behind an Impulsively Started Cylinder for $40 < Re < 10{,}000$," *Journal of Fluid Mechanics*, Vol. 101, Part 3, 1980, pp. 583–607.

3 Ta Phuoc Luc, "Numerical Analysis of Unsteady Secondary Vortices Generated by an Impulsively Started Circular Cylinder," *Journal of Fluid Mechanics*, Vol. 100, Part 1, 1980, pp. 111–128.

4 Sarpkaya, T., "Separated Flow About Lifting Bodies and Impulsive Flow About Cylinders," *AIAA Journal*, Vol. 4, 1966, pp. 414–420.

5 Sarpkaya, T., "Impulsive Flow About a Circular Cylinder," Naval Postgraduate Technical Report No. NPS-69SL78-008, Monterey, Calif., 1978.

6 Kline, H. K., "Impulsively-Started Flow About Submarine-Shaped Bodies," M.S. thesis submitted to the Department of Mechanical Engineering, Naval Postgraduate School, Monterey, Calif., 1981.

7 Sarpkaya, T., and Shoaff, R. L., "A Discrete Vortex Analysis of Flow About Stationary and Transversely Oscillating Circular Cylinders," Naval Postgraduate School Technical Report No. NPS-69SL79011, Monterey, Calif., 1979.

8 Sarpkaya, T., and Shoaff, R. L., "Inviscid Model of Two-Dimensional Vortex Shedding by a Circular Cylinder," *AIAA Journal*, Vol. 17, No. 11, 1979, pp. 1193–1200.

9 Sarpkaya, T., "Vortex-Induced Oscillations—A Selective Review," ASME *Journal of Applied Mechanics*, Vol. 46, 1979, pp. 241–258.

10 Thoman, D. C., and Szewczyk, A. A., "Time-Dependent Viscous Flow Over a Circular Cylinder," *Physics of Fluids Supplement*, Vol. 12, p. II-76–II-80; also Tech. Report 66-14, Univ. of Notre Dame, Ind., 1966.

11 Shoaff, R. L. and Franks, C. B., "A Discrete Vortex Analysis of Flow About Non-Circular Cylinders," *Proceedings of the Third International Conference on Numerical Ship Hydrodynamics*, Vol. 3, 1981, pp. V-2-1–V-2-15.

12 Mujumdar, A. S., and Douglas, W. J. M., "Vortex Shedding from Slender Cylinders of Various Cross Sections," ASME JOURNAL OF FLUIDS ENGINEERING, Sept. 1973, pp. 474–476.

13 Kiya, M., and Arie, M., "A Contribution to an Inviscid Vortex-Shedding Model of an Inclined Flat Plate in Uniform Flow," *Journal of Fluid Mechanics*, Vol. 82, Part 2, 1977, pp. 223–240.

14 Sarpkaya, T., "An Inviscid Model of Two-Dimensional Vortex Shedding for Transient and Asymptotically Steady Separated Flow Over an Inclined Flat Plate," *Journal of Fluid Mechanics*, Vol. 68, Part 1, 1975, pp. 109–128.

Numerical Solution for Laminar Two Dimensional Flow About a Cylinder Oscillating in a Uniform Stream

S. E. Hurlbut
Graduate Research Assistant.

M. L. Spaulding
Associate Professor.
Mem. ASME

F. M. White
Professor.
Mem. ASME

Department of Ocean Engineering,
University of Rhode Island,
Kingston, R. I. 02881

A finite difference model is presented for viscous two dimensional flow of a uniform stream past an oscillating cylinder. A noninertial coordinate transformation is used so that the grid mesh remains fixed relative to the accelerating cylinder. Three types of cylinder motion are considered: oscillation in a still fluid, oscillation parallel to a moving stream, and oscillation transverse to a moving stream. Computations are made for Reynolds numbers between 1 and 100 and amplitude-to-diameter ratios from 0.1 to 2.0. The computed results correctly predict the lock-in or wake-capture phenomenon which occurs when cylinder oscillation is near the natural vortex shedding frequency. Drag, lift, and inertia effects are extracted from the numerical results. Detailed computations at a Reynolds number of 80 are shown to be in quantitative agreement with available experimental data for oscillating cylinders.

Introduction

The vibration of structures immersed in a fluid flow has received much experimental, analytical, and numerical study, as reported in review articles [1–4], a recent text [5], and a recent symposium [6]. Flow induced vibrations can be caused by vortex shedding which occurs in the wake of a bluff body at Reynolds numbers above about 40. The natural shedding frequency is expressed as a Strouhal number $S_s = f_s D/V$. The vortices induce a periodic transverse or lift force at the shedding frequency and a periodic drag force at twice the shedding frequency.

Numerical studies of vortex shedding have primarily addressed the flow of a uniform stream normal to a rigid circular cylinder, in either two [7–9] or three [10] dimensions. Since the cylinder is fixed, no information about vibration interaction is thus obtained. If the cylinder is vibrating, either in forced or natural motion, a nonlinear interaction occurs as the cylinder frequency approaches the vortex shedding frequency. This interaction has two major characteristics. First, the natural shedding frequency is suppressed and vortex shedding occurs instead at the cylinder vibration frequency over a range of flow velocities. This is known as the lock-in or "wake capture" phenomenon. Second, the transverse or lift force increases greatly, with maximum response occurring near the mid-point of the lock-in range. These effects occur when the cylinder is vibrating either in-line or transverse with the freestream direction. The lock-in range is somewhat dependent on Reynolds number and cylinder amplitude, and the maximum range is approximately ±40 percent of the mid-point frequency [11].

The major problem associated with a numerical simulation of viscous flow around an oscillating cylinder is describing boundary conditions at the continuously accelerating solid wall within a discrete finite difference or finite element grid system. The present study transforms the Navier-Stokes equations to a non-inertial reference frame following the cylinder, thus simplifying the boundary condition specification. Results are computed for a range of Reynolds numbers and cylinder amplitudes and compared to experimental data for in-line and transverse oscillation at $Re_0 = 80$ and 100.

Numerical Technique

This study is an extension to the two dimensional oscillatory case of a three dimensional rigid-cylinder model developed by Swanson and Spaulding [10]. The model uses the Marker and Cell (MAC) finite difference method to solve the incompressible continuity and Navier-Stokes equations in terms of pressure and velocity. For each time step, the momentum equations are solved explicitly for a tentative velocity field. These velocities are successively recalculated based on a relaxation of the pressure field until continuity is satisfied at each cell. A complete discussion of the MAC method is given in references [12] and [13].

The present model uses cylindrical coordinates with logarithmically spaced radial cells which provide a fine grid scale near the cylinder walls and a coarse grid in the far field. The distance from the cylinder to the outer boundary is fifty-

Contributed by the Fluids Engineering Division and presented at the Winter Annual Meeting, San Francisco, Calif., December 10–15, 1978, of THE AMERICAN SOCIETY OF MECHANICAL ENGINEERS. *Manuscript received by the Fluids Engineering Division, November 21, 1979.*

five cylinder diameters. Due to the oscillating nature of the flow, a uniform freestream condition was imposed at both upstream and downstream boundaries. More complete details of the model specifications are given by Hurlbut [14].

Noninertial Transformation

A discrete Eulerian grid system will not readily accommodate arbitrarily moving solid boundaries. One remedy, used by Cheng [15] is to translate the grid system at each time step and interpolate the variables to new locations. In the present study the Eulerian grid system remains attached to the oscillating cylinder by use of a noninertial coordinate transformation. The absolute velocity of a moving fluid particle is divided into velocity V_f relative to the moving cylinder plus velocity V_r relative to an inertial reference frame. Newton's law thus becomes

$$\rho \frac{d}{dt}(V_f) = \Sigma F - \rho \frac{d}{dt}(V_r) \tag{1}$$

where V_r in the present case is a known function of time representing the cylinder motion. The MAC method may then be used in fixed coordinates with no-slip at the cylinder and an oscillating velocity at the outer boundaries. The Navier-Stokes equations are modified by an acceleration term which is uniform over the field at each time step.

Results

Calculations were made for three types of cylinder oscillation conditions: (*a*) oscillation in a still fluid; (*b*) "in-line" oscillation parallel to a flowing stream; and (*c*) "transverse" oscillation normal to a flowing stream.

Still-Fluid Cases. Initial calculations were made with zero freestream velocity and the cylinder oscillating normal to its axis at amplitude A and frequency ω. The relevant parameters are thus a Reynolds number, either based on maximum velocity $u_m D/\nu$ or frequency $\omega D^2/\nu$ (also called frequency parameter) and an amplitude ratio A/D or period parameter $u_m T/D$ (Keulegan Carpenter number). In harmonic oscillation $u_m T/D = 2\pi A/D$ and $\omega D^2/\nu = D/A\,(u_m D/\nu)$. These parameters are used in various combinations by different investigators [ex: 16, 17, 18]. The maximum velocity Reynolds number and amplitude ratio are used in this study.

Cases were run for Re = 1, and 10, at $A/D = 0.1$ and for Re = 100 at A/D = 0.1, 1.0, and 2.0. The drag and lift coefficients were defined using cylinder projected area DL and maximum oscillation velocity $u_m = \omega A$:

$$C_{D,L} = \frac{F_{D,L}}{\frac{1}{2}\rho D L u_m |u_m|} \tag{2}$$

For a given Re and A/D these coefficients will be periodic functions of dimensionless time tu_m/D.

Figure 1 shows the computed still-fluid cylinder acceleration and drag at $A/D = 0.1$ for Re = 1, 10, and 100. The shear and pressure drag components are also shown, with the shear contribution decreasing and becoming nearly negligible above Re = 100. The computed lift forces were nearly zero in all these cases. Note that the drag variation is approximately sinusoidal at all Reynolds numbers. At this small amplitude ratio, $A/D = 0.1$, there is no flow separation or wake formation.

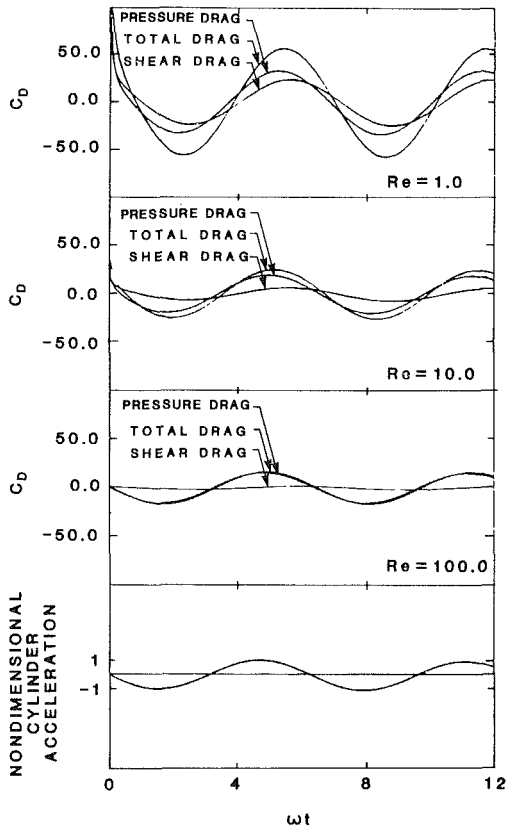

Fig. 1 Computed cylinder drag and acceleration time histories in a still fluid at $A/D = 0.1$, for various Reynolds numbers

Figure 2 shows the computed acceleration and drag time history at Re = 100 for A/D = 0.1, 1.0, and 2.0. As A/D increases the dimensionless drag decreases and its phase angle shifts away from the acceleration toward the velocity oscillation. Additional off-fundamental frequency components are faintly visible at $A/D = 1.0$ and clearly so at A/D = 2.0. Computer plots of the instantaneous streamlines (see reference [14]) show vortex wake formation at $A/D = 1.0$ and 2.0, and the cylinder collides on its return stroke with previously formed vortices. This is in agreement with the experimental observation of Nath et al. [19] and Sarpkaya

Nomenclature

A = cylinder oscillation amplitude
$C_{D,L}$ = dimensionless drag and lift forces, equation (2)
C_d = drag coefficient, equation (3)
C_m = inertia coefficient, equation (3)
D = cylinder diameter
F = force
f_c = cylinder oscillation frequency
f_s = vortex shedding frequency
L = cylinder length
Re = oscillation Reynolds number, $\omega AD/\nu$
Re_0 = freestream Reynolds number, $= VD/\nu$
S_c = dimensionless oscillation frequency, $= f_c D/V$
S_s = Strouhal shedding frequency, $= f_s D/V$
t = time
T = oscillation period
u = instantaneous cylinder velocity
V = freestream velocity
V_f = fluid velocity in noninertial coordinates
V_r = velocity of noninertial coordinate system
ρ = density
ω = cylinder angular frequency, $= 2\pi f_c$
ν = kinematic viscosity

[17] that wake formation effects are important for A/D greater than about 0.75 ($u_m T/D > 4$).

The still-fluid cases provide an estimate of the average drag and inertia coefficients by comparison to the well known Morison equation approximation [20]:

$$F = C_m \rho \frac{\pi}{4} D^2 L \frac{du}{dt} + \tfrac{1}{2} C_d \rho D u |u| \tag{3}$$

where u is the relative velocity between cylinder and fluid and C_m and C_d are the inertia and drag coefficients, respectively. The coefficients were evaluated in two ways: 1) the maximum value method; and 2) the least squares method. In the former technique, C_m is evaluated from equation (3) when du/dt is a maximum ($u = 0$), and similarly C_d is computed when u is maximum ($du/dt = 0$). In the least squares method, the coefficients are adjusted to create minimum square error between equation (3) and the computed force history $F(t)$. For a discussion of this technique see Garrison [16].

The results of these two estimates of force coefficients are given in Table 1 for all still-fluid cases. As Re and A/D increase, C_d approaches the steady state drag for uniform velocity u_m. As Re increases, C_m approaches its potential flow value of 1.0, but there is a significant viscous effect at the large amplitude ratio $A/D = 2.0$.

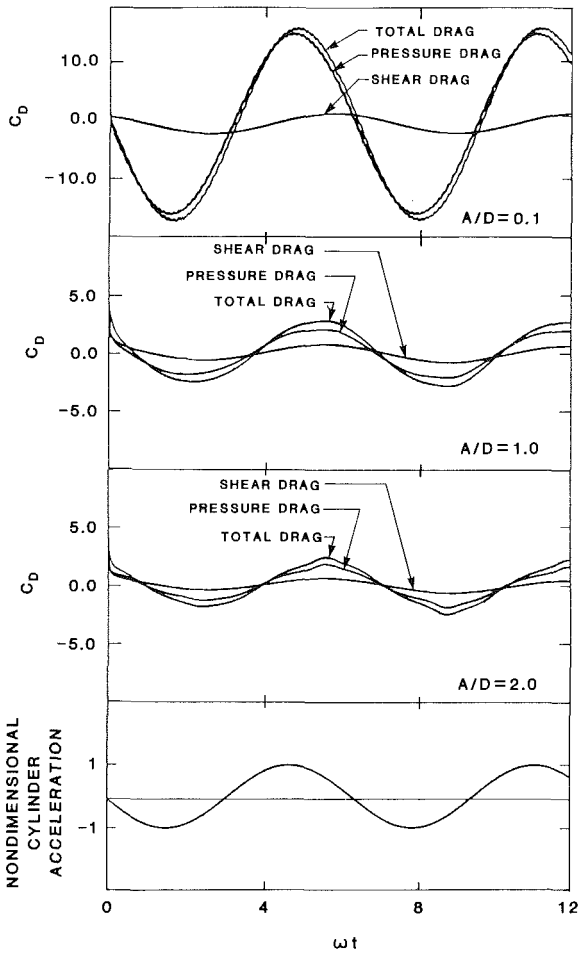

Fig. 2 Computed cylinder drag and acceleration time histories in a still fluid at Re = 100, for various amplitude ratios

The amplitude dependence of C_m has been noted in several experimental investigations [16, 17, 22]. Increasing amplitudes (A/D .3–.7) generally result in a decrease in C_m. This is contrary to the present observation, however, the experimental results involved much higher Reynolds numbers.

It is reasonable to assume from laminar boundary layer considerations that for small amplitudes and a given frequency of oscillation the drag force experienced by a cylinder will be proportional to the velocity rather than the square of the velocity as is typical for separated flows [see for example 23]. For this reason some investigators of hydrodynamically damped oscillations have chosen to reduce their data in terms of a linear drag formulation [ex: 18, 24]. Skop et al. [18] measured hydrodynamic damping on plucked linearly sprung cylinders over a range of vibratory Reynolds number ($\beta_s = \omega D^2/4\nu$) which coincides with the Re = 100, $A/D = 0.1$ case of the present study. Modifying the drag coefficient to reflect the linear (viscous) drag formulation results in the following values $C_v = 3.52$ and $C_m = 1.03$ which compares favorably with their values of $C_v = 3.44$ and $C_m = 1.15$, particularly considering the relatively large scatter in their C_m values.

In-Line Oscillation. A series of simulations were run in a uniform stream at $Re_0 = VD/\nu = 80$ and 100 for constant $A/D = 0.14$ and cylinder driving frequencies varying in the range $S_c = f_c D/V = 0.0$ to 0.4. The value $A/D = 0.14$ matches available experimental data [25]. For a rigid cylinder the natural shedding frequency is $S_s = 0.16$ at $Re_0 = 80$ and 0.17 at $Re_0 = 100$ [10]. For in-line oscillation, lock-in should occur at an oscillation frequency about twice the shedding frequency, $S_c \simeq 0.32$.

Two examples of non-resonant computed time histories at $Re_0 = 100$ are shown for in-line oscillation below lock-in (Fig. 3, $S_c = 0.1$) and above lock-in (Fig. 4, $S_c = 0.4$). In each case the drag history has a steady component approximately equal to the rigid cylinder value plus an oscillatory component at the cylinder driving frequency f_c. The oscillatory amplitude increases with driving frequency. One would also expect an oscillatory drag component at twice the natural shedding frequency, such as occurs in the rigid cylinder case [10], but here it is negligibly small and masked by the driving frequency component.

In Figs. 3 and 4, which are off-resonance, vortex shedding is independent of cylinder oscillation and occurs at the natural Strouhal frequency f_s. The cylinder oscillation and shedding interact to create an extremely complex periodic lift coefficient history. Since these cases appear to have no easily definable steady state, it is difficult to decide when a simulation should be terminated. In general, the simulations were continued until obvious transients died out and then for a time roughly equivalent to the time required for steady state in the lock-in cases. Fourier analysis of the lift records in Fig. 3 ($S_c = 0.1$) and Fig. 4 ($S_c = 0.4$) require five and seven

Table 1 Drag and added-mass coefficients for the still-fluid cases

		Maximum Value Method		Least Squares Method		Steady State Drag C_d(Re)[24]
Re	A/D	C_m	C_d	C_m	C_d	C_d
1	0.1	2.58	39.0	2.59	40.2	11.1
10	0.1	1.47	10.7	1.45	11.0	2.9
100	0.1	1.03	3.6	1.03	3.5	1.3
100	1.0	1.07	2.25	1.08	2.3	1.3
100	2.0	1.68	1.64	1.7	1.7	1.3

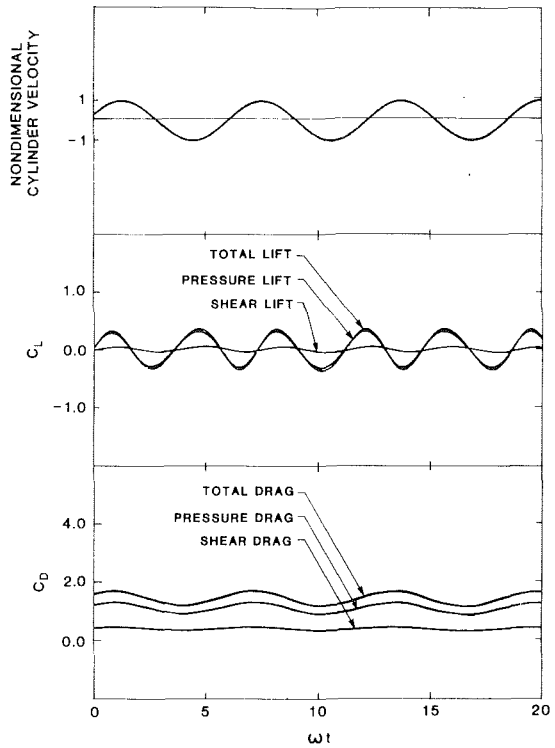

Fig. 3 Computed cylinder velocity, lift, and drag at $Re_0 = 100$ for in-line oscillation below lock-in, $S_c = 0.1$

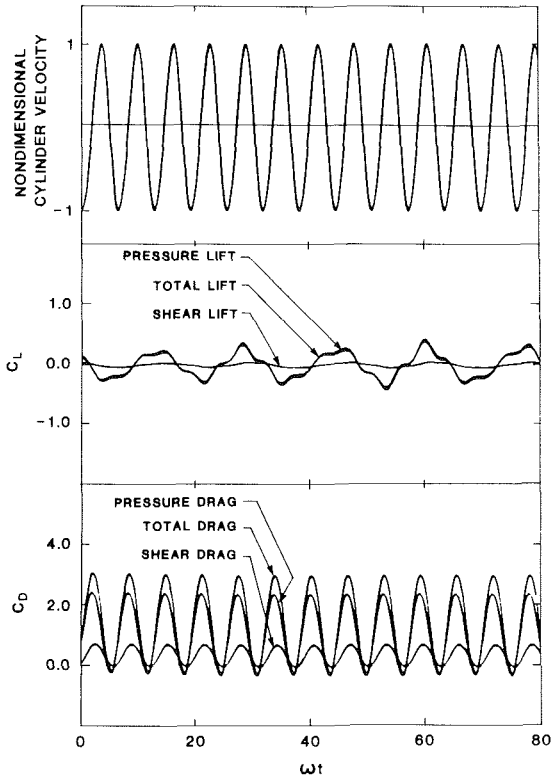

Fig. 4 Computed cylinder velocity, lift, and drag at $Re_0 = 100$ for in-line oscillation above lock-in, $S_c = 0.4$

components, respectively, to adequately approximate the time series. In contrast, the lift record during lock-in essentially consists of a first plus a third harmonic related to the driving frequency.

Figure 5 shows the lift and drag during lock-in ($S_c = 0.32$)

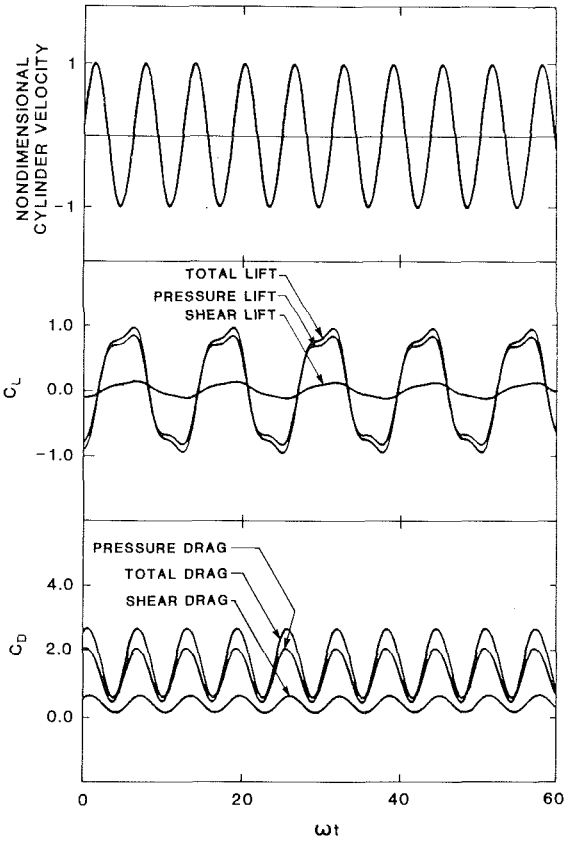

Fig. 5 Computed cylinder velocity, lift, and drag at $Re_0 = 100$ for in-line oscillation at lock-in, $S_c = 0.32$

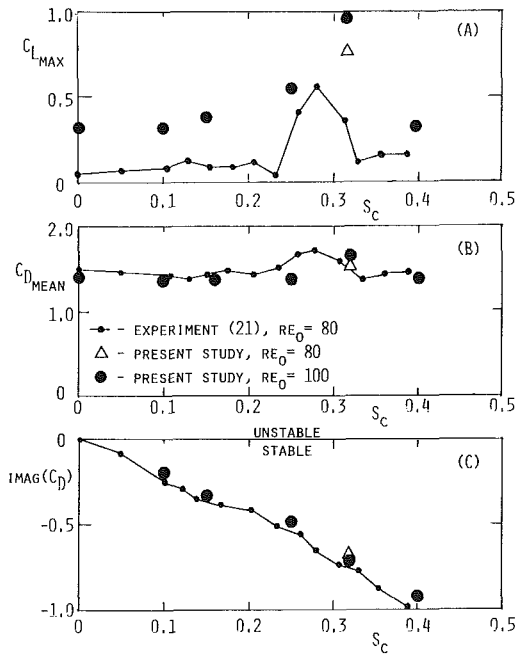

Fig. 6 Comparison of experiment and computations for lift and drag amplitudes versus cylinder oscillation frequency, in-line

where the wake is "captured" by the cylinder oscillation. The lift record is periodic with two dominant components: $f_c/2$ and $3f_c/2$, all other components being negligible from Fourier analysis. This predominance of the first and third harmonics during lock-in is in agreement with experiment [26, 27]. During lock-in the computed lift amplitude is approximately three times that obtained for a rigid cylinder at the same Re_0.

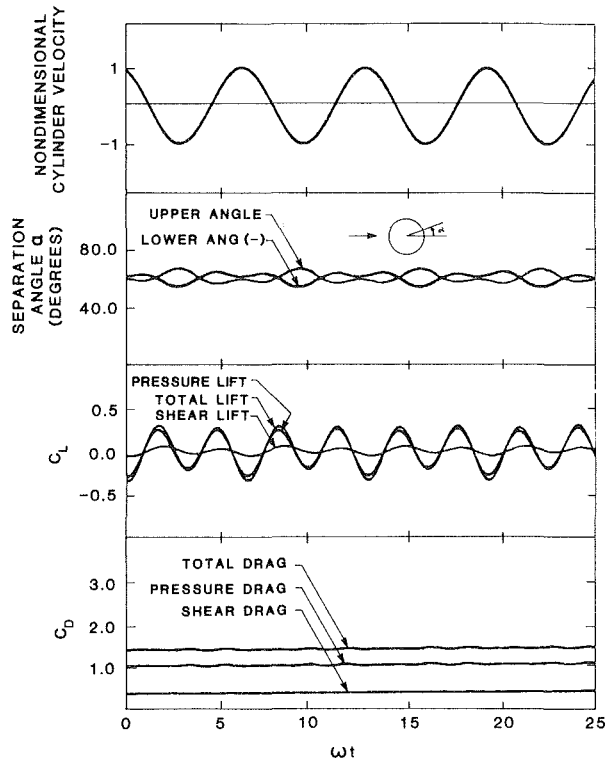

Fig. 7 Computed cylinder velocity, separation angle and distance, lift, and drag for transverse oscillation below lock-in, $Re_0 = 80$, $A/D = 0.14$, $S_c = 0.076$

The lock-in drag history in Fig. 5 is similar to the off-resonance cases, Figs. 3 and 4, with a mean plus a fundamental oscillation component. The sole noticeable difference is a slight increase in mean drag over the rigid or nonresonance values.

The effect of oscillation frequency on lift and drag amplitudes is shown in Fig. 6. Computations were made for $Re_0 = 80$. Figure 6(*a*) shows the numerical and experimental maximum lift coefficient. Both show an increase in lift in the same lock-in range, but the numerical results are consistently higher. This agrees with other rigid-cylinder computations, where maximum lift is in the range of 0.25 to 0.70 [8,9,28,29] compared with an experimental value of about 0.08. It is thought that one reason for the discrepancy is the three-dimensionality inherent in the experiments, which would reduce the coherence of spanwise shedding and hence reduce the integrated transverse or lift force. If this reason is correct, one would expect better agreement between numerical and experimental results in the lock-in range, where a decrease in three-dimensional effects is reported [30, 31]. Figure 6(*a*) does show relatively less discrepancy at lock in. Further discussion is given by Sarpkaya and Shoaff [32].

Figures 6(*b*) and 6(*c*) compare the computed drag with Tanida's experiments, with good agreement for both the mean drag and the imaginary component. In Fig. 6(*b*) the maximum increase in the mean drag during lock-in is approximately 20 percent. Due to the experimental difficulties associated with measuring the fluid forces in the direction of cylinder oscillation Tanida et al. only measured the forces in phase with the oscillating velocity (the imaginary component) and, therefore, determined the aerodynamic stability of the oscillating system. For purposes of comparison the data in this study is analyzed in a similar manner.

Figure 6(*c*) can be interpreted as the aerodynamic stability of the oscillating cylinder. The imaginary component of the drag force (in phase with the cylinder velocity) is negative throughout the lock-in range, which makes self-excited oscillations impossible. A second region of possible instability has been reported for higher Reynolds numbers ($Re_0 \doteq 10^4$) [4]. This instability is not associated with a definite lock-in phenomenon and occurs at frequencies between 2.1 and 2.9 times the Strouhal number, which in this case corresponds to a value of S_c between 0.34 and 0.46. It appears that this regime, at least to $S_c = 0.40$ is stable at $Re_0 = 80$.

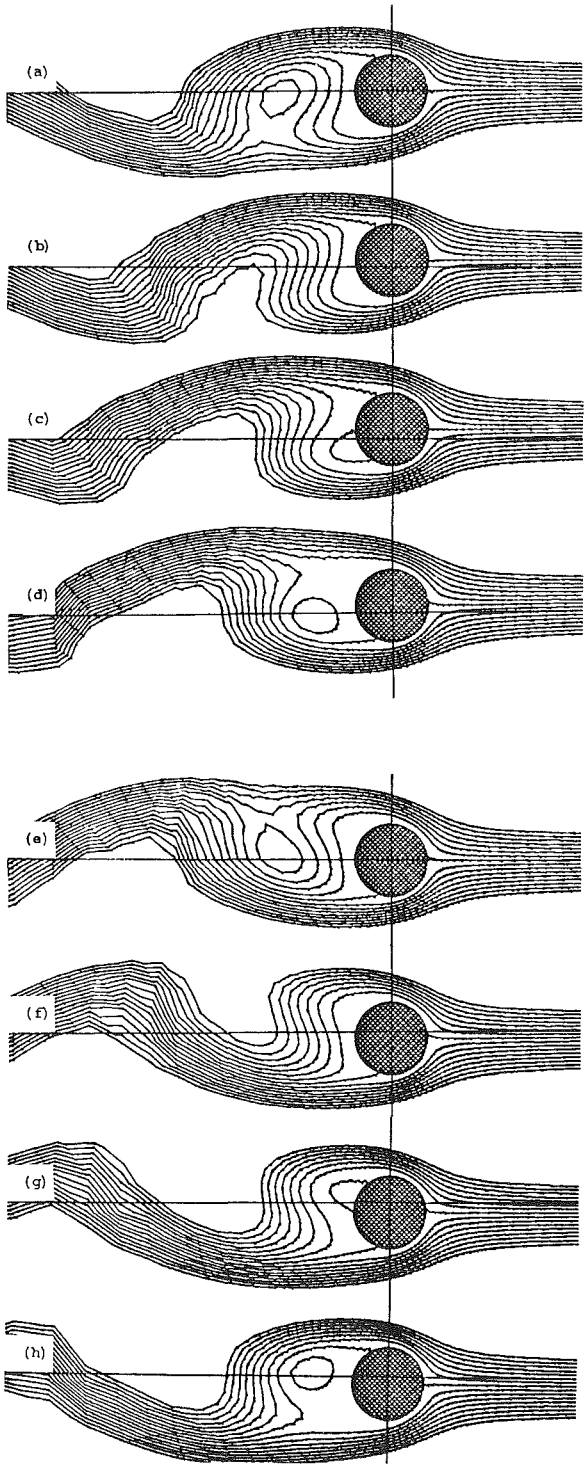

Fig. 8 Computed stream function contours every one-eighth cycle for transverse oscillation near lock-in, $Re_0 = 80$, $A/D = 0.14$, $S_c = 0.14$

Transverse Oscillation. Three transverse oscillation cases were run at $Re_0 = 80$, $A/D = 0.14$, for comparison with the

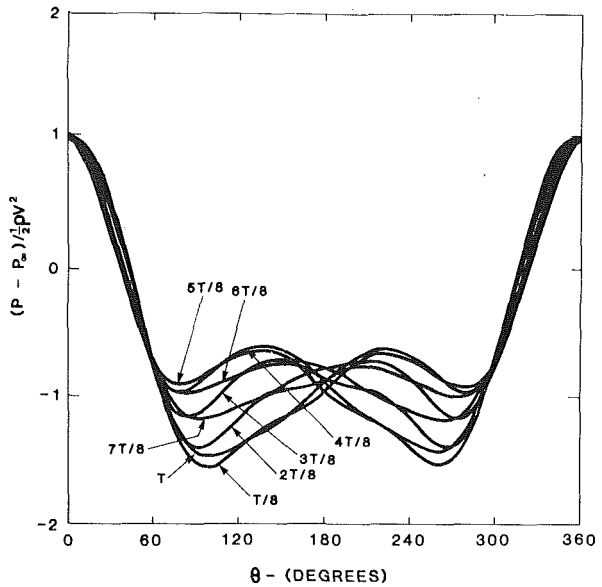

Fig. 9 Computed cylinder wall pressure coefficients for one-eighth cycle increments for transverse oscillation near lock-in, $Re_0 = 80$, $A/D = 0.14$, $S_c = 0.16$

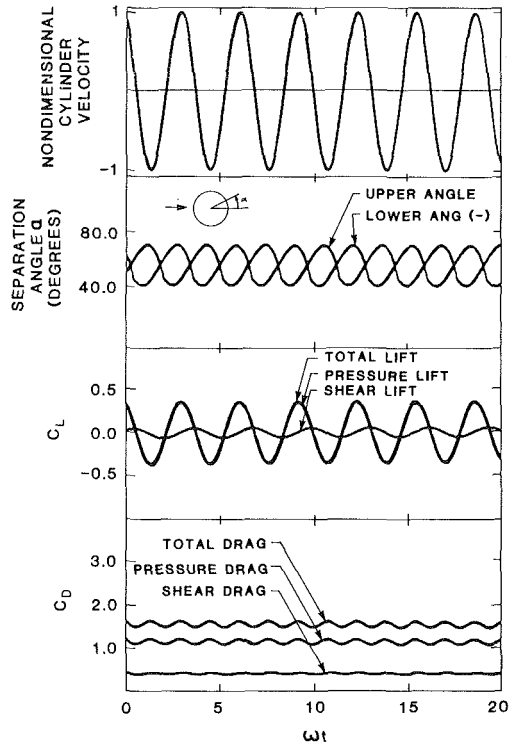

Fig. 10 Computed cylinder velocity, separation angle and distance, lift, and drag for transverse oscillation at lock-in, $Re_0 = 80$, $A/D = 0.14$, $S_c = 0.16$

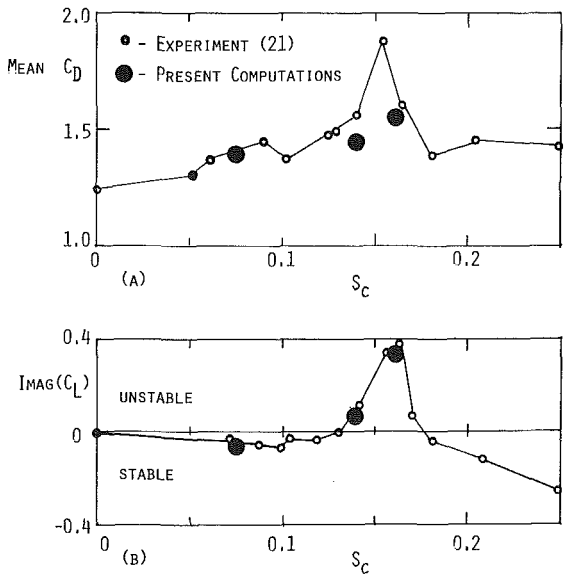

Fig. 11 Comparison of experimental and computed drag and imaginary lift components versus oscillation frequency for transverse oscillation at $Re_0 = 80$, $A/D = 0.14$

experimental data of Tanida et al. [25]. There are two cases within the lock-in range $S_c = 0.14$ and 0.16.

In transverse oscillation, as with the in-line cases, lock-in occurs in a range of frequencies around the Strouhal shedding point, and shedding is captured by the cylinder frequency. Outside lock-in, shedding occurs at the Strouhal frequency [31], and the cylinder force is a complex combination of shedding and forcing motions. This is illustrated in Fig. 7 for $S_c = 0.076$. The drag record is nearly constant with a superimposed small oscillation at twice the cylinder frequency. The lift record is basically periodic at the shedding frequency, modulated by the cylinder frequency. This modulation is also evident in the record of the separation angle (the angle of the point of flow separation relative to downstream).

In a lock-in condition the wake synchronizes with the cylinder oscillation. Figure 8 shows stream function contours at $S_c = 0.14$ for every one-eighth cycle of cylinder oscillation. Figure 9 is the cylinder pressure distribution for $S_c = 0.16$ also at eighth-cycle increments. The symmetry in Figs. 8 and 9 between the first and second half of the cycle indicates lock-in at the cylinder frequency.

Figure 10 shows the computed time series for a resonant case, $S_c = 0.16$. The drag shows slightly more oscillation than the off-resonance case and slightly higher mean value. The mean drag is plotted versus cylinder frequency in Fig. 11(*a*) and compared with Tanida's data. The maximum lock-in increase is not as great as experimentally observed, although the peak may have been missed by the choice of S_c values.

Fourier analysis of the lift time series for both resonant cases indicate they are almost perfectly sinusoidal at the cylinder driving frequency. All higher harmonics have amplitude less than 0.5 percent of the fundamental. The stability of the transverse oscillation is shown in Fig. 11(*b*), which is the imaginary component of the lift record (in phase with cylinder velocity). The agreement with Tanida's data is excellent. In passing through lock-in the lift undergoes a large phase shift, as observed experimentally by Bishop and Hassan [33]. From the computations at $S_c = 0.076$, the lift leads the velocity by 154 deg, and the imaginary component is negative, indicating positive damping and stability. Near the shedding frequency the phase lead angle drops significantly to 67 deg at $S_c = 0.14$ and to only 2.7 deg at $S_c = 0.16$. In the lock-in range in Fig. 11(*b*) the imaginary component is positive, indicating negative damping and possible self-excited oscillations [25, 34].

Computer Run Times

The present numerical model was implemented on the ITEL-AS5 computer at the University of Rhode Island. Computer average run times for these simulations were three hours for the still-fluid cases, ten hours for the in-line cases, and up to thirty hours for the transverse oscillation cases. Further discussion is given in references [14 and 35].

Conclusions

The use of a noninertial coordinate transformation leads to a successful finite difference simulation of accelerating rigid-wall boundaries in a viscous fluid. The technique is verified by application to a cylinder oscillating in a still fluid and also oscillating parallel to and normal to a uniform stream. Two dimensional computations for Reynolds numbers between 1 and 100, with amplitude ratios from 0.1 to 2.0 are in reasonable agreement with available data. Drag, lift, and inertia effects extracted from the computations are shown to be strongly dependent upon Reynolds number, oscillation amplitude, and driving frequency.

The model in its present form is limited to the simulation of low Reynolds number flows by computer run time requirements. This limit could be extended by the use of large vector processing computers, which in the authors' experience can reduce the run times quoted here by as much as twenty times, or through the use of a smaller dedicated computer system. The utility of this technique is not as a design tool but once completely verified, as a source of very complete basic data. The entire flow field is reproduced synoptically which allows study of the fluid structure interaction phenomenon in a level of detail not possible with experimental techniques.

Acknowledgment

This study was supported by the Naval Underwater Systems Center, New London, Connecticut, under Contract N66604-77-M-8952. The assistance of the URI Academic Computer Center is also gratefully acknowledged.

References

1 Parkinson, G. V., "Mathematical Models for Flow-Induced Oscillations of Bluff Bodies," *Flow-Induced Structural Vibrations*, E. Naudascher, ed., Springer-Verlag, N. Y., 1974, pp. 81–127.

2 Savkar, S., "A Survey of Flow-Induced Vibrations of Cylindrical Arrays in Cross Flow," ASME JOURNAL OF FLUIDS ENGINEERING, Vol. 99, No. 3, 1977, pp. 517–519.

3 Sarpkaya, T., "Vortex Induced Oscillations, A Selective Review," ASME *Journal of Applied Mechanics*, Vol. 46, No. 2, June 1979, pp. 241–258.

4 King, R., "A Review of Vortex Shedding Research and its Application," *Ocean Engineering*, Vol. 4, 1977, pp. 141–172.

5 Blevins, R., *Flow-Induced Vibration*, Van Nostrand Reinhold Company, New York, 1977.

6 Crow, D. E., and Miller, J. A. (Ed.), *Symposium on Nonsteady Fluid Dynamics*, ASME, New York, 198, 252 pp.

7 Bratanow, T., Ecer, A., and Kobiske, M., "Finite-Element Analysis of Unsteady Incompressible Flow Around an Oscillating Obstacle of Arbitrary Shape," *AIAA Journal*, Nov. 1973, pp. 1471–1477.

8 Dawson, C., and Marcus, M., "DMC-A Computer Code to Simulate Viscous Flow Around Arbitrarily Shaped Bodies," *Proceedings of the 1970 Heat Transfer and Fluid Mechanics Institute*, Stanford Press, Stanford, 1970.

9 Jordan, S. K., and Fromm, J. E., "Oscillating Drag, Lift and Torque on a Circular Cylinder in Two Uniform Flows," *Physics of Fluids*, Vol. 15, 1972, pp. 371–376.

10 Swanson, J. C., and Spaulding, M. L., "Three Dimensional Numerical Model of Vortex Shedding from a Circular Cylinder," in *Symposium on Non-steady Fluid Dynamics*, ASME, New York, 1978, pp. 207–216.

11 Griffin, O., and Ramberg, S., "Vortex Shedding from a Cylinder Vibrating in Line with an Incident Uniform Flow," *Journal of Fluid Mechanics*, Vol. 75, No. 2, 1976, pp. 257–271.

12 Welch, J., Harlow, F., Shannon, J., and Daly, B. J., "The MAC Method—A Computing Technique for Solving Viscous, Incompressible, Transient Fluid-Flow Problems Involving Free Surfaces," Report No. LA 3425, Los Alamos Scientific Laboratory, 1965.

13 Hirt, C., and Cook, J., "Calculating Three-Dimensional Flows Around Structures and Over Rough Terrain," *Journal of Computational Physics*, Vol. 10, 1972, pp. 324–340.

14 Hurlbut, S. E., "A Numerical Model of Fluid-Structure Interaction for Circular Cylinders," M. S. thesis, Dept. of Ocean Engineering, University of Rhode Island, Kingston, R. I., 1978..

15 Cheng, R., "The Interaction Between a Solid Body and Viscous Fluid by Marker-and Cell Method," Technical Report 76-CL, School of Engineering, Old Dominion University, 1976.

16 Garrison, C. J., Field, J. B., and May, M. D., "Drag and Inertia Forces on a Cylinder in Periodic Flow," *Journal of the Waterway, Port, Coastal and Ocean Division*, ASCE, May 1977, pp. 193–204.

17 Sarpkaya, T., "In-Line and Transverse Forces on Cylinders in Oscillatory Flow at High Reynolds Numbers," *Journal of Ship Research*, Vol. 21, No. 4, Dec. 1977, pp. 200–216.

18 Skop, R. A., Ramberg, S. E., and Ferer, K. M., "Added Mass and Damping Forces on Circular Cylinders," Naval Research Laboratory Report 7970, May 19, 1976.

19 Nath, J. H., Yamamoto, T., and Wright, J. C., "Wave Forces on Pipes Near the Ocean Bottom," *Proc. of the Offshore Technology Conference*, OTC 2496, Houston, May 1976, pp. 741–747.

20 Morison, J. R., O'Brien, M. P., and Schaff, S. A., "The Force Exerted by Surface Waves on Piles," *Petroleum Transactions*, AIME, TP 2846, Vol. 189, 1950, pp. 149–154.

21 Clift, R., Grace, J. R., and Weber, M. E., *Bubbles, Drops, and Particles*, Academic Press, New York, 1978.

22 Yamamoto, T., and Nath, J. H., "High Reynolds Number Oscillating Flow by Cylinders," *Proceedings ASCE 15th Coastal Engineering Conference*, Chapter 136, 1976, pp. 2321–2340.

23 Batchelor, G. K., *An Introduction to Fluid Dynamics*, Cambridge University Press, 1967.

24 Verley, R. L. P., "An Investigation into the Damping of Oscillations of a Cylinder in Still Water," Norwegian Institute of Technology Report. STF60-A78046, 1978.

25 Tanida, Y., Okajima, A., and Watanabe, Y., "Stability of a Circular Cylinder Oscillating in Uniform Flow or Wake," *Journal of Fluid Mechanics*, Vol. 61, 1973, pp. 769–784.

26 Durgin, W. W., March, P. A., and Lefebvre, P. J., "Lower Mode Response of Circular Cylinders in Cross Flow," in *Symposium on Nonsteady Fluid Dynamics*, ASME, New York, 1978, pp. 192–200.

27 King, R., "A Review of Vortex Shedding Research and its Application," *Ocean Engineering*, Vol. 4, 1977, pp. 141–171.

28 Sallet, D., "On the Prediction of Flutter Forces," *Flow-Induced Structural Vibrations*, E. Naudascher, ed., Springer-Verlag, New York, 1974.

29 Chen, Y., "Fluctuating Lift Forces of the Karman Vortex Streets on Single Circular Cylinders and in Tube Bundles, Part 2—Lift Forces on Single Cylinders," ASME *Journal of Engineering for Industry*, Vol. 94, 1972, pp. 613–622.

30 Feng, C. C., "The Measurement of Vortex-Induced Effects in Flow Past Stationary and Oscillating Circular and D Section Cylinders," M.A.Sc. thesis, Univ. British Columbia, 1968.

31 Koopman, G. H., "The Vortex Wakes of Vibrating Cylinders at Low Reynolds Numbers," *Journal of Fluid Mechanics*, Vol. 28, No. 3, 1967, pp. 501–512.

32 Sarpkaya, T., and Shoaff, R. L., "A Discrete-Vortex Analysis of Flow About Stationary and Transversely Oscillating Circular Cylinders," Report NPS-69SL79011, Naval Postgraduate School, Monterey, Jan. 1979, 166 pp.

33 Bishop, R. E. D., and Hassan, A. Y., "The Lift and Drag Forces on a Circular Cylinder Oscillating in a Flowing Fluid," *Proc. Royal Society*, Series A, Vol. 277, 1964, pp. 51–75.

34 Griffin, O. M., and Koopmann, G. H., "The Vortex-Excited Lift and Reaction Forces on Resonantly Vibrating Cylinders," *Journal of Sound and Vibration*, Vol. 54, No. 3, 1977, pp. 435–448.

35 Hurlbut, S., Spaulding, M. L., and White, F. M., "Numerical Solution of the Time-Dependent Navier Stokes Equations in the Presence of an Oscillating Cylinder," in *Symposium on Non-steady Fluid Dynamics*, ASME, New York, 1978, pp. 201–206.

N. W. M. Ko
Reader.

W. L. Leung
Student.

H. Au
Graduate Student.

Department of Mechanical Engineering,
University of Hong Kong,
Hong Kong

Flow Behind Two Coaxial Circular Cylinders

The flow behind two circular cylinders of different diameters, which were joined coaxially has been examined at the Reynolds number of 8×10^4. The detailed pressure spectral measurements indicate the shedding and the distributions of the pressure fluctuations of the vortex wakes associated with the big and small cylinders. The effect of the presence of the small vortex wake on the vortex shedding of the big cylinder and the interaction between them is presented. The wake formed behind the plane of discontinuity has been isolated and presented.

Introduction

Flow around a stationary circular cylinder has been very extensively investigated [1-3]. Coupled with the immense interest on the flow over tall buildings or structures, as could be seen from the organization of the International Conference on Wind Engineering, the behavior of the flow over cylinders or bluff bodies and the mechanism of vortex formation and shedding were better understood. Basically, the effect of the Reynolds number, surface roughness, local turbulence, blockage of the wind tunnel, and aspect ratio on the flow have been established. Based on the Reynolds number, the flow could be divided into the subcritical, critical, and supercritical regimes [1, 3]. In the critical regime, surface roughness could alter the effective critical Reynolds number by one-order-of-magnitude. Similarly, on the flow over two-dimensional rectangular cylinders, the flow was sensitive to turbulence intensity but almost immune to changes in turbulence scale [4]. These findings, as with other effects, really suggested the sensitivity of the boundary layer and the vortex-shedding mechanism to external disturbances.

The aim of this study was to obtain experimental data on the effect of the presence of another circular cylinder on the formation and shedding of vortex wake. Two circular cylinders of different diameter were joined coaxially to produce a plane of discontinuity. Measurements were made of the local pressure fluctuations and their spectra in the wakes of the two cylinders and in the three-dimensional regime behind the discontinuity.

Experimental Arrangement

The experiments were carried out inside a wind tunnel with a test section measuring 56 cm by 56 cm. The big cylinder tested has a diameter D of 50.4 mm and the small cylinder has a diameter d of 25.0 mm, giving a diameter ratio D/d of 2. The two cylinders were joined coaxially and the junction or the plane of discontinuity occurred at the centerline of the test section (Fig. 1). The cylinders were mounted stationary in the mid of the test section and their surfaces were polished. The origin of the coordinates was chosen at the centers of the two cylinders with x, y, and z as the streamwise, lateral, and spanwise coordinates, respectively. The combined cylinders occupied 7 percent of the total cross-section area.

The tunnel was run at a mean velocity U_0 of 23 m/s. At this mean velocity the free stream turbulence intensity was 0.8 percent. The Reynolds numbers based on the diameters of the big and small cylinders were $R_{e_D} \simeq 8\times10^4$ and $R_{e_d} \simeq 4\times10^4$, respectively. Thus the flow over the two cylinders was within the subcritical regime [3]. The free stream turbulence of the present investigation was the same as the lowest range of Petrie [5] in which further increase in the turbulence intensity resulted in the amplification of the vortex shedding motion.

The pressure fluctuations of the vortex wake downstream were obtained by using a standard Brüel and Kjaer 1/8 in condenser microphone with the proper nose cone. The condenser microphone was found suitable to measure the fluctuating static pressure in a flow [6, 7]. Spectral analysis of the pressure signal from the microphone was performed by means of a Brüel and Kjaer narrow band spectrum analyzer Type 2031. At each microphone position an average of 128 samples was adopted.

The domain of investigation was within the spanwise distance of $-3.0 \le z/D \le 1.0$. Lateral traverses across the

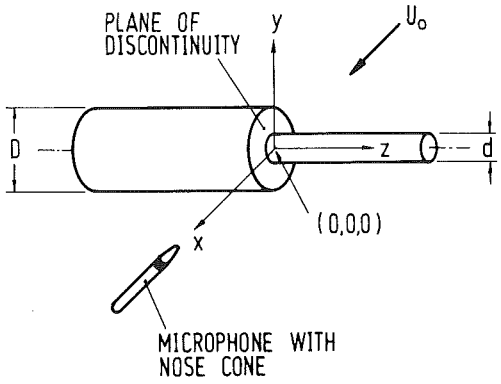

Fig. 1 Schematic layout of the two coaxial cylinders

Contributed by the Fluids Engineering Division for publication in the JOURNAL OF FLUIDS ENGINEERING. Manuscript received by the Fluids Engineering Division, April 1981.

wake of the cylinder at each spanwise position were obtained. Streamwise measurements at $y/D=0.25$ and $z/D=0$ for $1 \le x/D \le 2.5$ have shown that the pressure coefficients were nearly constant. Thus, for the present investigation, the microphone was fixed at the streamwise position of $x/D=1.5$.

The experimental uncertainty of the data was as follows: the mean velocity ±1 percent and linear dimension ±0.1 mm. The uncertainty of the non-dimensional groups such as distance ratio ±1 percent and pressure coefficient ±0.1.

Results

Before presenting the spectral results at and near the discontinuity, the results at the regions which are not affected are presented first. Figure 2 shows the spectra behind the big and small cylinders with the microphone at $y/D=0.5$, $z/D=-2.0$ and $y/d=0.5$, $z/d=1.0$, respectively. The dominant spectral peak of the big cylinder is at 85 Hz with a pressure coefficient $C_p' \approx 0.12$ and the Strouhal number St_D is 0.19. The peak at the double frequency of 170 Hz is due to the combined contributions of the vortices from both sides of the vortex street. It is supported by the findings that the lateral distribution of the relevant pressure coefficient C_p' is highest at $y/D=0$.

For the small cylinder the dominant peak is at 180 Hz with a pressure coefficient $C_p' \approx 0.055$. The Strouhal number St_d is 0.19. Similarly, the broader peak at the double frequency of 360 Hz is also due to the combined contributions of the vortices from both sides of the vortex street.

Another peak at the frequency of 198 Hz is due to the fan noise of the wind tunnel. Thus it is neglected in the following presentation.

Behind the plane of discontinuity, $z/D=0$, the spectrum obtained at $y/d=0.5$ is shown in Fig. 3. Only the spectral peak at 180 Hz, which is due to the vortex wake of the small cylinder, is found. The spectral peak associated with the vortex wake of the big cylinder is absent from the spectrum, suggesting the complete absence of the big vortex wake behind the discontinuity plane. In addition, the vortex wake of the small cylinder is found to have lower pressure fluctuations. The variation of the pressure coefficients will be discussed later.

The vortex wake of the big cylinder starts to appear only from $z/D=-0.25$. At this position the spectral peak is only marginally bigger than the background pressure level. A little bit further away from the discontinuity the spectrum obtained at $y/D=0.5$, $z/D=-0.5$ indicates clearly the two peaks which are associated with the big and small cylinders (Fig. 3). However, even at this spanwise position of $z/D=-0.5$ the vortex wake of the small cylinder is much more dominant than that of the big cylinder.

Because of this phenomenon, detailed traverses of the pressure fluctuations of the individual vortex wake at and near the discontinuity have been obtained and are shown in Figs. 4 and 5. The distribution of the big cylinder, as shown in Fig. 4, indicates that two-dimensional conditions exist for $z/D \le -2.0$. For $z/D > -2.0$ the effect of the discontinuity becomes obvious. This involves a gradual reduction of the pressure coefficient C_p' as the discontinuity is approached.

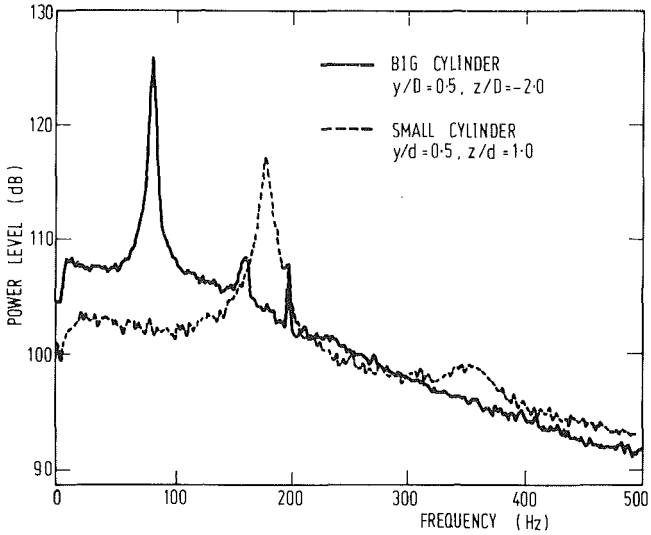

Fig. 2 Pressure spectra behind big and small cylinder (uncertainty ±0.5 dB)

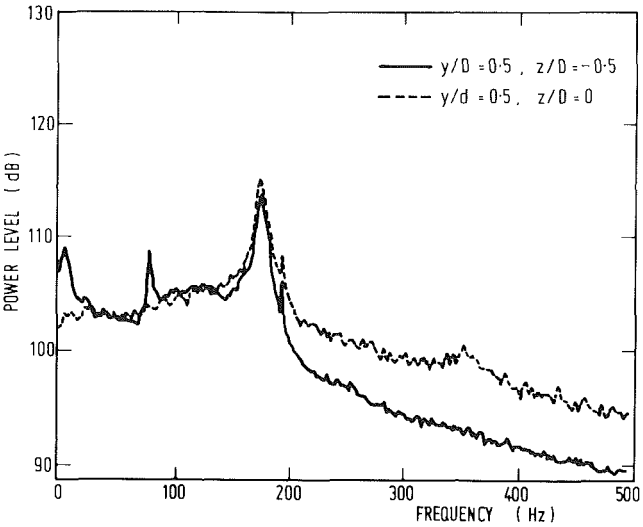

Fig. 3 Pressure spectra behind and near the discontinuity (uncertainty ±0.5 dB)

For $z/D > -0.25$ it was impossible to separate the spectral peak associated with the vortex wake of the big cylinder from the background pressure fluctuations.

Besides the reduction in the pressure coefficients, the lateral distributions of the coefficients indicate a shift of the maximum coefficients toward the central axis. This shift seems to start from $y/D \approx \pm 0.5$ which is the edge of the big cylinder toward the lateral position of $y/D \approx \pm 0.25$ ($y/d \approx \pm 0.5$), which is the edge of the small cylinder. As is the case for the vortices of a jet [6, 7], the position of the maximum of the pressure fluctuations indicates the position of the vortices. Similarly, as has been reported by Bearman [8]

Nomenclature

C_p' = fluctuating pressure coefficient $p'/\frac{1}{2}\rho U_0^2$
D,d = diameter of big and small cylinder
p' = rms value of fluctuating static pressure at the peak of the spectrum
R_{e_D}, R_{e_d} = Reynolds number $U_0 D/\nu$, $U_0 d/\nu$
St_D, St_d = Strouhal number fD/U_0, fd/U_0
U_0 = free stream mean velocity
x,y,z = streamwise, lateral, and spanwise coordinates, respectively
ν = kinematic viscosity of fluid
ρ = fluid density
θ = angle from stagnation point

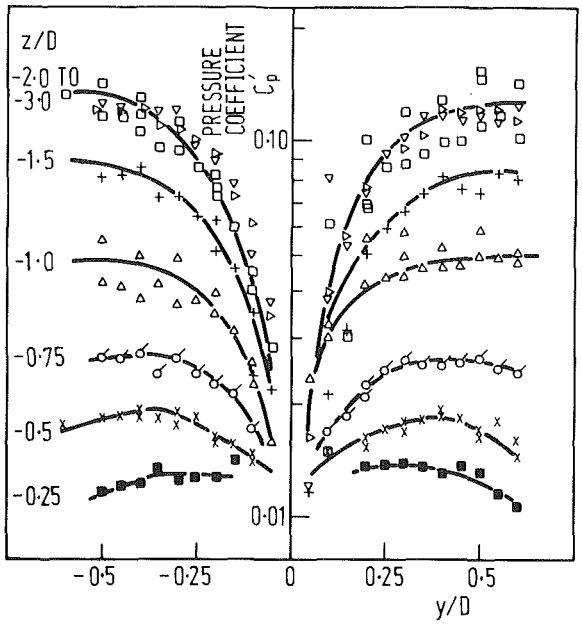

Fig. 4 Lateral distributions of pressure coefficients of vortex street associated with big cylinder (uncertainty on C_p' is ±0.1)

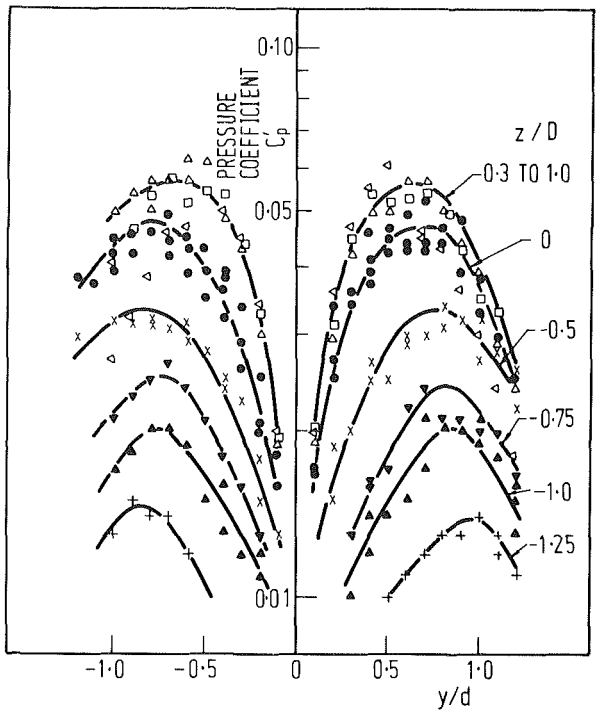

Fig. 5 Lateral distributions of pressure coefficients of vortex street associated with small cylinder (uncertainty on C_p' is ±0.1)

the maximum streamwise velocity fluctuations indicates the vortex formation position behind a blunt trailing edge. Thus, the shift of the position of the maximum pressure coefficients from $y/D \approx \pm 0.5$ toward $y/D \approx \pm 0.25$ ($y/d \approx \pm 0.5$) suggests that with the proximity of the small cylinder the vortex wake of the big cylinder shifts toward the central axis. At the spanwise position where the vortex wake starts to disappear its position corresponds to that of the vortex wake of the small cylinder.

The maximum pressure coefficient at which the vortex wake associated with the big cylinder disappears is 0.015 (Fig. 6). This is much lower than the two-dimensional coefficient of about 0.12. This reduction of the coefficient occurs within a spanwise distance of $\Delta z/D = 1.75$, starting from $z/D = -2$. The vortex wake disappears at $z/D = -0.25$. This means that within the first quarter of a diameter from the plane of discontinuity no vortex wake of the big cylinder is formed.

The lateral distributions of the pressure coefficients of the vortex wake of the small cylinder are shown in Fig. 5. As shown in Figs. 5 and 6, two-dimensional condition can be found even up to $z/D = 0.2$. This spanwise position is much nearer to the plane of discontinuity than that of the big cylinder ($z/D = -2$). The reduction of the maximum pressure coefficient of these small vortex wake from that of the two-dimensional level occurs mainly behind the big cylinder. This small vortex wake disappears at $z/D \approx -1.25$ which is near the two-dimensional regime of the big cylinder. This reduction from C_p' of 0.055 to 0.012 before the disappearance occurs within a spanwise distance of $\Delta z/D = 1.45$. This is only slightly smaller than that of the big cylinder of 1.75. The shorter distance may be due to the lower two-dimensional pressure coefficient of the vortex wake of the small cylinder. In addition, comparison of the rate of reduction of the two cylinders indicates that the rate of the small cylinder is lower than that of the large cylinder (Fig. 6).

The maximum pressure coefficients of the vortex wake associated with the small cylinder experience a shift from the lateral position $y/d \approx \pm 0.5$ at $z/D = 0.2$ to $y/d \approx \pm 1$ ($y/D \approx \pm 0.5$) at $z/D = -1.25$. The former lateral position corresponds to the edge of the small cylinder while the latter corresponds to that of the big cylinder. This observation is in the reverse order as that of the big cylinder pointed out above. Therefore, it seems to suggest that with the presence of the

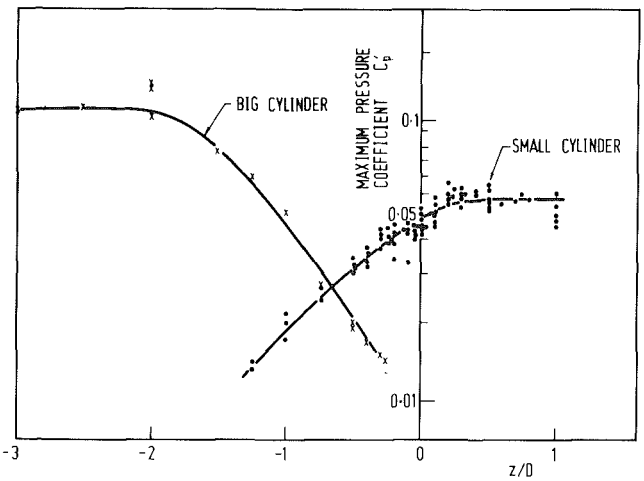

Fig. 6 Spanwise distributions of the maximum pressure coefficients of the two vortex streets (uncertainty on C_p' is ±0.1)

other cylinder, be it big or small, the vortex wake try to adjust to the condition imposed by the other cylinder.

The results presented above are interesting. The maintenance of the two-dimensional characteristics of the vortex wake associated with the small cylinder nearly right up to the plane of discontinuity suggests that this vortex wake is least affected by the change of configuration and the presence of the big cylinder. It may be because, in a certain sense, the end of the big cylinder acts like a small end-plate for the small cylinder. Thus it may help to stabilize the wake of the small cylinder.

The observation of the small vortex wake right inside the wake flow behind the big cylinder suggests its presence and propagation into this region. The propagation into the wake of the big cylinder is not really surprising. It is because the mean pressure coefficient measurements on the surface of the cylinder indicate a subatmospheric region [1, 9]. This subatmospheric region extends from an angle θ of about 30 to

about 330 deg. In other words, it extends right across the leeward side of the cylinder. For the same Reynolds number and blockage ratio of the present investigation the mean base pressure coefficient was found to be fairly uniform with a value of -1.0 [9]. The minimum pressure coefficient, which occurred at θ of about 70 deg, was -1.2 and was only marginally lower than that of the uniform base value. Because of the bigger size of the big cylinder and thus the bigger area where the subatmospheric condition exists, the smaller vortex wake of the small cylinder may fit into this region and may prefer convecting toward it. This convection may result in the partial annihilation of the subatmospheric region behind the big cylinder. With the partial annihilation of the subatmospheric region the flow characteristics of the big cylinder change, resulting in the suppression of the formation of the big vortex wake. However, as has been pointed out by the study on the effect of increase in turbulence due to the introduction of vortex spoilers [10], the effect of turbulence or the disturbances associated with the small vortices on the shear and separation of the flow of the big cylinder is not known.

The propagation of the small vortex wake into the wake of the big cylinder may be similar to that of the base bleed into the subatmospheric region behind a blunt trailing edge [8]. Increase in the bleed rate resulted in an increase in the base pressure. At sufficiently high bleed rate, a bleed coefficient of 10 to 15 percent, the increase in base pressure inhibited the regular vortex shedding.

The suppression of the vortex wake of the big cylinder, besides being due to the partial annihilation of the subatmospheric region, may also be due to the three dimensional end-effects on the interruption of vortex shedding from the big cylinder before the discontinuity. It may also be due to the presence of the small vortex wake within its wake flow. As has been investigated by Maull and Young [11] and Kuethe [12], it was found that with the introduction of longitudinal vortices into the wake of a body by placing vortex generators at the trailing edge, the vortex shedding was suppressed. However, this gives rise to a more significant jump in the peak frequency of the original vortices. In the present study the jump in the peak frequency is not readily observed. Thus it is not really known how significant is the effect of the presence of the small vortex wake on the suppression of the large vortices.

The occurrence of the vortex wake of the small cylinder behind the big cylinder up to $z/D=-1.25$ and the proximity of its two-dimensional characteristics at the discontinuity indicate that the vortex wake is basically intact. In addition, because of the subatmospheric region, one may expect a certain amount of acceleration of the vortices which are propagating against a negative pressure gradient. Although an analysis of the convection velocity of these vortex wakes has not been attempted in the present study, this acceleration effect may partly be the reason for the maintenance of the two-dimensional characteristics of the small vortex wake so near the discontinuity plane. Nevertheless, interaction with the wake flow behind the big cylinder results in its loss in pressure coefficient. However, one would not expect the small vortex wake propagating parallel to the axis; thus the reduction in the pressure coefficient may also partly be due to the propagation of the vortex wake at an angle with the direction of the uniform flow.

Unlike the investigation of the base bleed on the flow behind the blunt trailing edge in which a change of Strouhal number with bleed rate was found [8], the measurements of the present study have indicated constant values of St_D and St_d for the two types of vortex wakes, even within the region where interaction occurs. This implies that within the region near the discontinuity, though the two types of vortex wakes experience suppression of reduction in amplitude, the fundamental mechanism of vortex shedding and the dependence

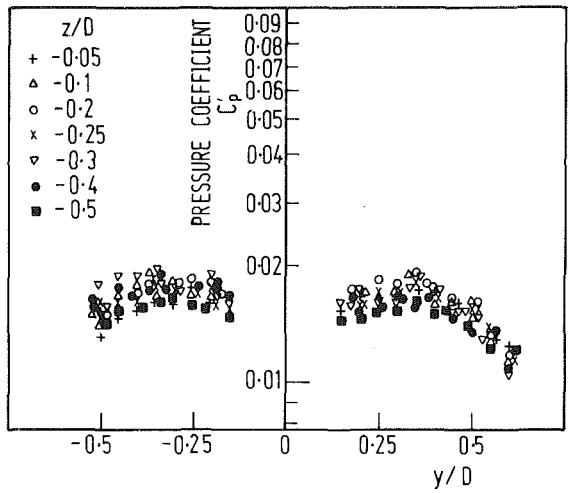

Fig. 7 Lateral distributions of pressure coefficients associated with the discontinuity (uncertainty on C_p' is ±0.1)

of the frequency on the cylinder diameter and free-stream mean velocity have not changed.

A closer look at the pressure spectrum obtained at $y/D=0.5$, $z/D=-0.5$, as shown in Fig. 3, indicates another broad peak at a frequency between those of the big and small cylinders. The peak frequency, because of its broadness, is estimated at about 128 Hz and is roughly equal to the mid frequency of 85 Hz and 180 Hz of the big and small vortex wakes. This peak, besides being broad in character, is very low in its pressure coefficient and is only slightly higher than that of the background level. A detailed charting of this broad peak has shown that it is mainly found for the spanwise positions of $-0.5\leq z/D\leq -0.05$ and the lateral positions of $0.6\geq y/D\geq 0.15$ $(1.2\geq y/d\geq 0.3)$ and $-0.15\geq y/D\geq -0.5$ $(-0.3\geq y/d\geq -1.0)$ (Fig. 7). The lateral positions, where this broad peak is found, occur mainly behind the discontinuity plane formed by the two cylinders (Fig. 1). Further, the pressure coefficients of this broad peak found within this whole area do not vary much with spanwise position (Fig. 7). However, maxima seem to be found in its lateral distribution and the position of these maxima is found at $y/D\approx\pm 0.35$. This is roughly at the mid lateral position of the discontinuity formed by the two cylinders of $y/D=0.375$.

The lateral positions, where this broad peak is found, suggest that it is due to the flow over the plane of discontinuity at $z/D=0$. The broad peak observed may be due to the separation of flow in the surface of the discontinuity and to the wake thus formed. The separation may result in vortices shed from the plane of discontinuity. These vortices are not discrete in nature and may depend on the formation of the bubble, shear-layer reattachment and burst [13].

The absence of this broad peak at $z/D=0$ and the appearance at $z/D=-0.5$ implies that the vortices propagate at an angle toward the big cylinder. Their presence can even be found up to $z/D=-0.95$.

Conclusions

Detailed measurements of the pressure fluctuations behind two coaxially-joined circular cylinders of diameter ratio of 2:1 indicate the effect of the discontinuity on the vortex wakes shed from the cylinders. Two-dimensional characteristics of the vortex wakes shed from the big and small cylinders have been observed. The Strouhal numbers of these two dimensional vortex wakes are in agreement with those of a single cylinder.

The spanwise position at which the two-dimensionality of

the vortex wake ends depends on the diameter of the cylinder. For the small cylinder it is found that the spanwise position occurs just next to the discontinuity at $z/D = 0.2$. For the big cylinder, however, the same spanwise position occurs far away from the discontinuity at $z/D = -2.0$.

The flow over the plane of discontinuity seems to introduce separation and the formation of another type of vortex wake. Though the pressure coefficients observed are only slightly higher than the background level, the positions where they are found suggests the deflection of the vortex wake toward the big cylinder.

From the findings of this paper it seems that further work will be required before fuller understanding of the interaction between the shedding of vortices from two coaxially-joined cylinders of different diameters can be obtained.

References

1 Morkovin, M. V., "Flow Around Circular Cylinder—A Kaleidoscope of Challenging Fluid Phenomena," *ASME Symposium on Fully Separated Flow*, 1964, pp. 102–118.

2 Bearman, P. W., and Graham, J. M. R., "Vortex Shedding from Bluff Bodies in Oscillatory Flows: A Report on Euromech 119," *Journal of Fluid Mechanics*, Vol. 99, 1980, pp. 225–245.

3 Ericsson, L. E., "Karman Vortex Shedding and the Effect of Body Motion," *American Institute of Aeronautics and Astronautics Journal*, Vol. 18, 1980, pp. 935–944.

4 Lanville, A., and Williams, C. D., "The Effect of Intensity and Large Scale Turbulence on the Mean Pressure and Drag Coefficients of 2D Rectangular Cylinders," Fifth International Conference on Wind Engineering, Colo., 1979, pp. IV-5-1–IV-5-8.

5 Petrie, A. M., "Effect of Free-Stream Turbulence on Vortex Shedding in the Wakes of Cylinders in Cross-Flow," *Journal of Sound and Vibration*, Vol. 34, 1974, pp. 287–290.

6 Fuchs, H. V., "Measurement of Pressure Fluctuations Within Subsonic Turbulent Jet," *Journal of Sound and Vibration*, Vol. 22, 1972, pp. 361–378.

7 Ko, N. W. M., and Kwan, A. S. H., "The Initial Region of Subsonic Coaxial Jets," *Journal of Fluid Mechanics*, Vol. 73, 1976, pp. 305–332.

8 Bearman, P. W., "The Effect of Base Bleed on the Flow Behind A Two-Dimensional Model with A Blunt Trailing Edge," *Aeronautical Quarterly*, Vol. 18, 1967, pp. 207–224.

9 Modi, V. J., and El-Sherbiny, S., "Effect of Wall Confinement on Aerodynamics of Stationary Circular Cylinders," Third International Conference on Wind Effects on Buildings and Structures, Tokyo, 1971, pp. 365–375.

10 Gartshore, I. S., Khanna, J., and Laccinole, S., "The Effectiveness of Vortex Spoilers on A Circular Cylinder in Smooth and Turbulent Flow," Fifth International Conference on Wind Engineering, Colo., 1979, pp. X-10-1–X-10-9.

11 Maull, D. J., and Young, R. A., "Vortex Shedding from Bluff Bodies in A Shear Flow," *Journal of Fluid Mechanics*, Vol. 60, 1973, pp. 401–409.

12 Kuethe, A. M., "Effect of Streamwise Vortices on Wake Properties Associated with Sound Generation," *Journal of Aircraft*, Vol. 9, 1972, pp. 715–719.

13 Melbourne, W. H., "Turbulence Effects on Maximum Surface Pressures—A Mechanism and Possibility of Reduction," Fifth International Conference on Wind Engineering, Colo., 1979, pp. V-5-1–V-5-11.

K. Imaichi
Professor.

Y. Tsujimoto
Research Associate.

Y. Yoshida
Researcher,
Mitsubishi Heavy Industry,
Takasgo Lab.,

Faculty of Engineering Science,
Osaka, University,
Toyonaka, Osaka, Japan

An Analysis of Unsteady Torque on a Two-Dimensional Radial Impeller

Unsteady flows around radial impellers are analyzed by the use of singularity methods. Unsteady torque is given for transient and/or sinusoidal flow rate and/or angular velocity fluctuation. It is shown that the unsteady torque can be divided into three components – quasisteady, apparent mass and wake – and the nature of each component is discussed. As a result of separating the torque into these three components, it is shown that the wake component is usually smaller than the others. A gross estimate of torque fluctuation can be made easily by using the apparent mass coefficient given in the paper for logarithmic impellers covering a wide range of blade angles, blade numbers and impeller diameter ratios.

Introduction

There have been many studies of the stationary characteristics of radial impellers but there are fewer studies of unsteady characteristics, owing to the complicated main flow. The theoretical studies of unsteady flows through radial impellers are needed not only for the prediction of unsteady characteristics of the impeller, but also for the prediction of unsteady forces on the impeller and for the prediction of noise and cavitation.

Most theoretical studies of unsteady flows in radial impellers make use of simplifying assumptions which reduce the complexity of the flows. These simplifications are: 1) simplification of shed vortices [1] 2) simplification of geometry: application of the results of unsteady flow analysis of isolated airfoil [2,3] or rectilinear cascades [4,5] 3) reduction to quasisteady analyses [6-8].

Singularity methods have been very powerful techniques for the analyses of stationary flows [9]. The methods have been used for the analysis of unsteady flow around isolated airfoils executing large amplitude oscillations [10, 11]. The methods are applied also to an analysis of flutter characteristics of straight radial impeller [12], and for an analysis of interaction effects of a volute casing and radial impeller [13], taking into account the unsteadiness of the flows.

This paper treats the unsteady torque on two-dimensional impellers when the flow rate and/or angular velocity of the impellers change periodically and/or nonperiodically by using a singularity method. For periodic disturbances it is assumed that the unsteady disturbances are small, but large disturbances are permitted for transient (i.e., nonperiodic) fluctuations. Unsteady torque is one of the most typical unsteady characteristics of impellers. A sort of unsteady head may be defined as the work done by the impellers by using the unsteady torque. And, more directly, it is required in order to predict the fatigue strength of shafts under periodic unsteady operation or to discuss the torsional vibration of shaft systems. In case of pump turbines, it will be necessary to know the hydraulic torque on the runner in order to predict run-away characteristics.

von Karman and Sears [14] have shown that the unsteady forces on an isolated airfoil can be divided into three components – quasisteady, apparent mass, and wake components. This paper shows that the same division is possible for unsteady torque on radial impellers and clarifies the nature of each component. The apparent mass coefficients are given for logarithmic impellers covering a wide range of geometrical parameters. It is shown that the wake component is smaller than the other components and that an approximate estimate of unsteady torque can be made easily by using apparent mass coefficients given in this paper.

We apply singularity methods directly in the physical plane. It is assumed that the flow is two-dimensional, inviscid and incompressible. The vane is assumed to be thin and without volute casing. We consider cases in which cavitation and flow separation are not present, and the fluids flow radially into the impeller in the absolute frame (without prerotation).

Basic Equations

Complex Conjugate Velocity. Relative velocity in radial impellers is rotational due to the rotation of the impellers. But the absolute flow can be assumed to be irrotational if prerotation is absent and the fluid is inviscid. We consider a frame $z = x + iy$ rotating with the impeller as shown in Fig. 1. Then the position of the vane surface is stationary in this frame and the irrotational absolute velocity can be expressed as follows. We put an unsteady source $Q(t)$ at the center of the impeller and represent the vortex distribution on the vanes by

Contributed by the Fluids Engineering Division of THE AMERICAN SOCIETY OF MECHANICAL ENGINEERS and presented at the Winter Annual Meeting, November 15-20, 1981, Washington, D.C. Manuscript received by the Fluids Engineering Division, March 9, 1981. Paper No. 81-WA/FE-30.

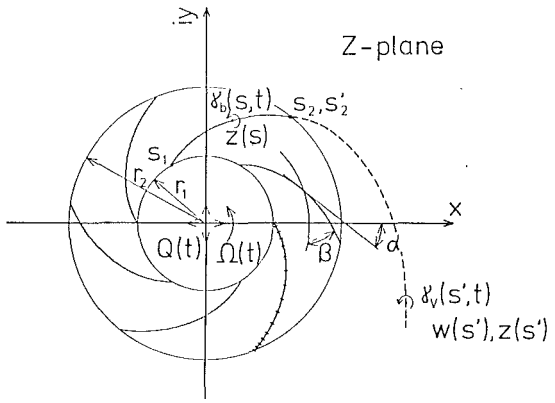

Fig. 1 Radial Impeller

$\gamma_b(s, t)$ and shed vortex distribution by $\gamma_v(s', t)$. Then the absolute complex conjugate velocity $u_x - iu_y$ at time t and position z can be written as follows.

$$u_x - iu_y|_{z,t} = \frac{Q(t)}{2\pi} \cdot \frac{1}{z} + \frac{1}{2\pi i} \sum^N \int_{S_1}^{S_2} \frac{\gamma_b(s,t)}{z - z(s)} ds + \frac{1}{2\pi i} \sum^N \int_{S_2'}^{\infty} \frac{\gamma_v(s',t)}{z - z(s')} ds' \quad (1)$$

Where Σ^N signifies the sum for all the vanes. The relative velocity can be given by simply adding the rotational velocity $i\Omega(t)\bar{z}$, where $\Omega(t)$ is the angular velocity of the impeller. Applying the unsteady Bernoulli equation in a rotating frame on both surfaces of a vane we get the relation

$$(p_2 - p_1)/\rho = -\frac{1}{2}(u_{r2} + u_{r1})(u_{r2} - u_{r1}) - \frac{\partial}{\partial t}(\Phi_2 - \Phi_1)$$

where subscripts 1 and 2 represent corresponding positions on the upper and lower surfaces of a vane. Assuming that the pressure is continuous at the trailing edge, the above equation can be reduced to:

$$\frac{d}{dt}\int_{S_1}^{S_2} \gamma_b(s,t) ds = -w(s_2)\gamma_b(s_2,t) = -w(s_2')\gamma_v(s_2',t) \quad (2)$$

where $w(s_2) = w(s_2')$ and is the average of the relative velocities on the upper and lower sides of the trailing edge. Equation (2) means that the amount of the change of the circulation of a vane is shed from the trailing edge as a free vortex distribution of strength $\gamma_v(s_2',t) = \gamma_b(s_2,t)$. Shed vortices sustain no external force and flow downstream with the local relative velocity. The strength and the position of the shed vortex distribution are determined by the conservation law of circulation.

Boundary Condition. The condition of vanishing relative normal velocity on the vane surfaces can be written as:

$$\mathrm{Im}\{e^{i\alpha}(u_x - iu_y + i\Omega(t)\bar{z})\} = 0 \quad (3)$$

where α is the angle made by the tangent of the vanes and x-axis. Then the problem can be reduced to solving an integral equation (1) with (3) for the vortex distribution on the vanes under unsteady Kutta condition (2). This integral equation can be reduced to a set of linear equations by specifying the values of $\gamma_b(s,t)$ at several discrete positions as unknowns and making the same number of equations by applying equation (3) at several points and equation (2) at the trailing edge.

Unsteady Torque. By applying the conservation law of angular momentum to a region between a circle of outer radius r_2 and an infinitely small circle around the center of the impeller, we can express the unsteady torque as follows for the case without prerotation [13].

$$T(t) = \frac{\rho Q(t)}{2\pi} \sum^N \int_{S_1}^{S_2} \gamma_b(s,t) ds + \rho\,\mathrm{Real}\left[\sum^N \int_{S_1}^{S_2} \gamma_b(s,t) \cdot z(s) \cdot \left\{\frac{1}{2\pi i}\sum^N \int_{S_2'}^{\infty} \frac{\gamma_v(s',t)}{z(s) - z(s')} ds'\right\} ds\right] + \frac{\rho}{2} r_2^2 \sum^N \frac{d}{dt}\int_{S_1}^{S_2} \gamma_b(s,t) ds - \frac{\rho}{2}\sum^N \int_{S_1}^{S_2} r^2(s)\frac{\partial}{\partial t}\gamma_b(s,t) ds \quad (4)$$

Separation of Unsteady Torque

In order to get a physical understanding of the unsteady torque T presented in the last section we separate the vortex distribution on the vanes into following four components:

1) Steady vortex distribution $\gamma_s(s)$ with total circulation Γ_s, relating to stationary flow rate Q_0 and stationary angular velocity Ω_0.

2) Vortex distribution $\gamma_0(s,t)$ which induces zero normal velocity on the vane surface and has total circulation Γ_0.

Nomenclature

$C_a^{\varphi}, C_a^{\Omega}$ = apparent mass coefficients for flow rate and angular velocity fluctuation
F = fluctuating torque coefficient
i,j = imaginary units with respect to space and time
k = frequency parameter, $= \omega/\Omega_0$
N = vane number
p = pressure
$Q(t), Q_0$ = flow rate, average flow rate
r_1, r_2 = inner and outer radius of the impeller
T = torque
t = time
u_x, u_y = velocity components in x and y-direction
x,y = Cartesian coordinate
z = complex coordinate, $= x + iy$
β = vane angle
γ_0, Γ_0 = circulatory quasisteady vortex distribution and its circulation
γ_1 = noncirculatory quasisteady vortex distribution
γ_2, Γ_2 = vortex distribution and its circulation cancelling the velocity induced by shed vortices
γ_b = total vortex distribution on the vanes
γ_s, Γ_s = steady vortex distribution and circulation
γ_v = shed vortex distribution
τ = accelerating time
Φ = velocity potential
$\varphi, \varphi_0, \Delta\varphi$ = flow coefficient, average flow coefficient and amplitude of flow coefficient fluctuation
ψ, ψ_s = head coefficient, shut-off head coefficient
$\Omega, \Omega_0, \Delta\Omega$ = angular velocity, average angular velocity, and amplitude of angular velocity fluctuation of the impeller
ω = angular velocity of fluctuation

Subscripts

s = steady component
a = apparent mass component
qs = quasisteady component
w = wake component

Superscripts

$*$ = nondimensional value
$-$ = complex conjugate

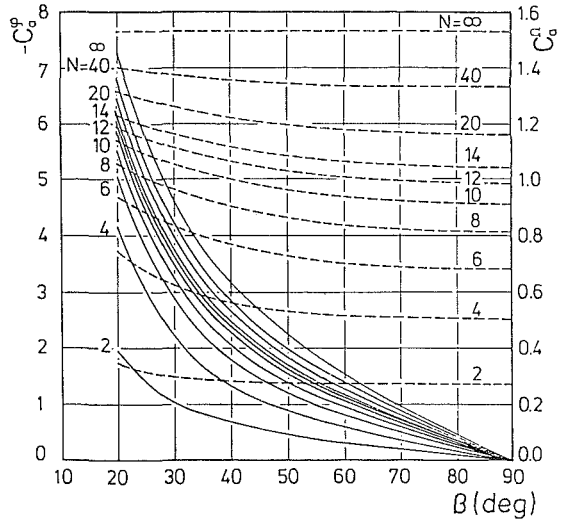

Fig. 2(a) $r_1/r_2 = 0.4$

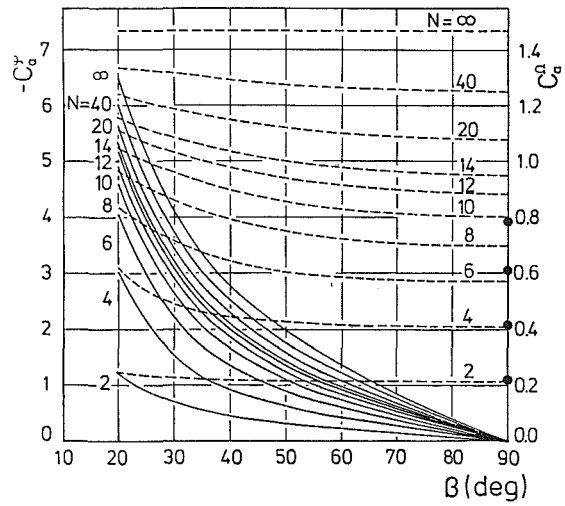

Fig. 2(b) $r_1/r_2 = 0.5$, • Kito [15]

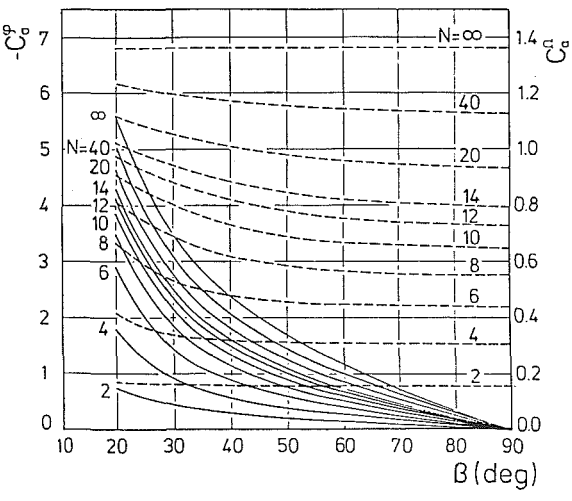

Fig. 2(c) $r_1/r_2 = 0.6$

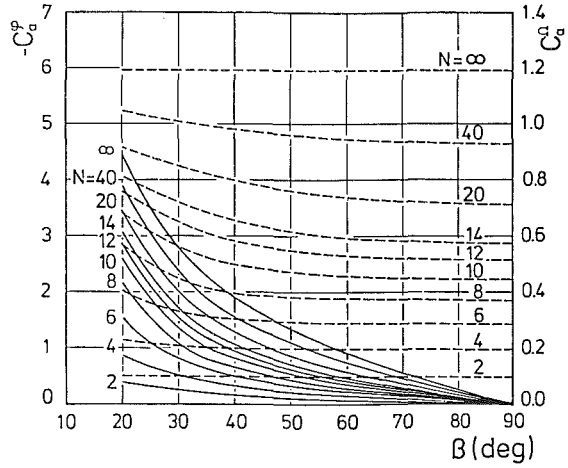

Fig. 2(d) $r_1/r_2 = 0.7$

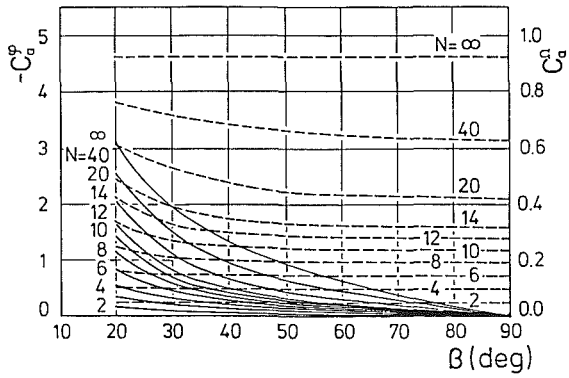

Fig. 2(e) $r_1/r_2 = 0.8$

Fig. 2 Apparent mass torque coefficients —C_{φ}^{a} – – –C_a^{Ω}

3) Vortex distribution $\gamma_1(s,t)$ which cancels the normal component of unsteady disturbance velocity due to flow rate fluctuation or angular velocity fluctuation, with zero total circulation.

4) Vortex distribution $\gamma_2(s,t)$ with total circulation Γ_2, which cancels normal component of the velocity induced by shed vortices and satifies the unsteady Kutta condition.

Circulation Γ_0 is evaluated so that the vortex distribution $\gamma_0(s,t)+\gamma_1(s,t)$ satisfies Kutta's condition for steady flow. That is, the vortex distribution $\gamma_0(s,t)+\gamma_1(s,t)$ is the quasisteady vortex distribution that cancels the normal component of unsteady disturbance velocity satisfying Kutta's condition on every moment.

In the classical von Karman-Sears analysis for isolated airfoil [14], the blade vorticity is divided into two components, i.e., $\gamma_0+\gamma_1$ and γ_2 in the present nomenclature. For radial impellers the steady vortex distribution cannot be assumed small in general and we include the steady component. Since the apparent mass contribution arises from noncirculatory flow component, it is generally necessary to distinguish the noncirculatory part γ_1 from the circulatory part γ_0 for the separation of the apparent mass component. In case of an isolated airfoil, the contribution of γ_0 drops out automatically in the estimation of apparent mass components because of the symmetry of γ_0 distribution. This is not the case for radial impellers, and we need to distinguish these two components.

After the separation of the blade vorticity γ_b into these four components we can separate the torque T into the following three components:

$$T = T_s + T_{qs} + T_a + T_w \tag{5}$$

$$T_s + T_{qs} = \frac{\rho Q(t)}{2\pi}\left(\sum^{N}\Gamma_s + \sum^{N}\Gamma_0\right) \tag{6}$$

$$T_a = -\frac{\rho}{2}\sum^{N}\int_{S_1}^{S_2} r^2(s)\frac{\partial}{\partial t}\gamma_1(s,t)ds \tag{7}$$

$$T_w = \text{ rest terms of equation (4)} \quad (8)$$

Component $T_s + T_{qs}$ is a quasi-steady torque component, which results from the instantaneous velocity disturbance on the blades. This component can easily be calculated from stationary $\varphi - \psi$ characteristics of the impeller.

Component T_a represents the effect of apparent mass since this term results from $\partial\Phi/\partial t$ and relates only to $\gamma_1(s,t)$ which has no circulation. This term depends only on the geometrical configuration of the impeller and instantaneous acceleration of disturbance velocity and is independent of flow rate, circulation and the history of the disturbance.

The terms of T_w depends on the circulation fluctuation of the vanes or on the shed vortices and represents the effect of vortex shedding. We call this "wake component." Since the shed vortices flow down with instantaneous local velocity, this term depends on the history of the flow field. But if the fluctuation is small, we may assume that the shed vortices flow on some averaged stream. In such cases it can be shown that this term is proportional to the amplitude of quasisteady circulation fluctuation and that the proportionality constant is independent of the types of the disturbance (fluctuations of flow rate or angular velocity) if the "averaged stream" and the frequency are the same. This is because this term is dependent on γ_0 and not on γ_1.

Apparent Mass Torque Component

In this paper we will discuss flow rate fluctuation and angular velocity fluctuation of the impeller. Since $\partial\gamma_1/\partial t = (\partial\gamma_1/\partial\varphi)(d\varphi/dt)$ for flow rate fluctuation and $\partial\gamma_1/\partial t = (\partial\gamma_1/\partial\Omega)(d\Omega/dt)$ for angular velocity fluctuation, equation (7) can be normalized as follows.

For flow rate fluctuation

$$T_a/\left(\rho r_2^4 \Omega_0 \frac{d\varphi}{dt}\right) = -\frac{1}{2}\sum^{N}\int_{S_1^*}^{S_2^*} r^{*2}\frac{\partial\gamma_1^*}{\partial\varphi}\,ds^* \equiv C_a^{\varphi} \quad (9)$$

For angular velocity fluctuation

$$T_a/\left(\rho r_2^4 \frac{d\Omega}{dt}\right) = -\frac{1}{2}\sum^{N}\int_{S_1^*}^{S_1^*} r^{*2}\frac{\partial\gamma_1^*}{\partial\Omega^*}\,ds^* \equiv C_a^{\Omega} \quad (10)$$

where the amounts with * represent quantities normalized with respect to length r_2 and velocity $r_2\Omega_0$. We define C_a^{φ} and C_a^{Ω} as "apparent mass torque coefficients." The values $\partial\gamma_1^*/\partial\Omega^*$ and $\partial\gamma_1^*/\partial\varphi$ are vortex distributions on the blade that cancel the normal relative velocity due to unit angular velocity and unit outflow respectively and have zero circulation.

These vortex distributions can be calculated by a singularity method. We specify the amount of vortex distribution at 16 points on the vane surface (vortex points) as shown in Fig. 1 and apply the boundary condition at 15 points between them (velocity points). Normal velocity induced by the vortex distribution is calculated by assuming that the vortex distribution is linear between the vortex points. Then the normal velocity at 15 velocity points can be represented by a linear sum of 15 unknown vorticities, which is set to cancel normal disturbance velocities. These 15 linear equations are used for the determination of 16 unknowns with the last condition that the total circulation is zero.

In order to check the accuracy of the singularity method, we solved a steady flow through a radial impeller using the same 16 vortex points and 15 velocity points and appeying Kutta's condition at the trailing edge. By comparing the result with those by conformal mapping method it was found that the present method can give satisfactory accuracy (within 2 percent error in total circulation) and we used 16 vortex points as the standard size throughout the present paper.

The resulting apparent mass coefficient are shown in Fig. 2 for logarithmic impellers. The figures show that $|C_a^{\varphi}|$ and $|C_a^{\Omega}|$ are larger for larger blade number N and smaller inner

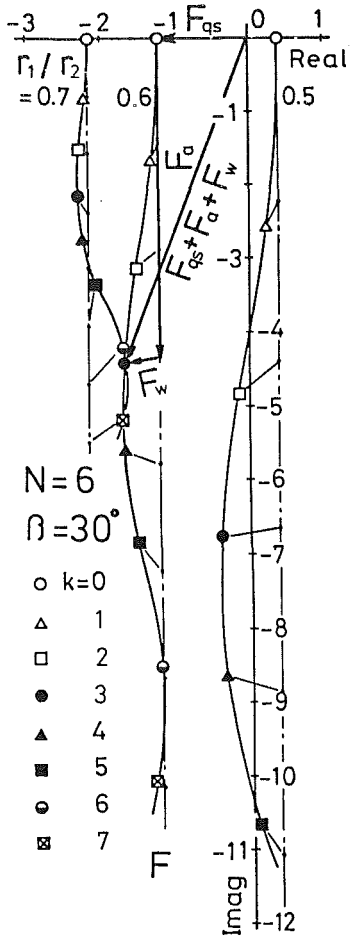

Fig. 3 Fluctuating torque coefficient F for sinusoidal flow rate fluctuation

to outer ratio r_1/r_2. The effect of vane angle β is small for C_a^{Ω} and C_a^{φ} grows larger for smaller vane angle. This is because the normal disturbance velocity is larger for smaller vane angle impellers.

Now let us consider the case in which the impeller executes small torsional oscillations in an otherwise stationary infinite fluid or the case that the impeller is stationary and the flow rate oscillates around zero. For these cases $T_w = T_s = T_{qs} = 0$ and T_a is just the unsteady torque on these impellers. Kito [15] has given an apparent mass coefficient relating to kinetic energy of surrounding fluid for the torsional oscillation of straight vaned radial impeller in otherwise stationary fluid. Since the work done by the torque equals the kinetic energy of the fluids we can deduce the relation of his apparent mass coefficient and ours. Comparison with Kito's results are made in Fig. 2(*b*).

In case of torsional oscillation, the fluid is assumed to execute the same motion as a rigid cylinder with inner to outer radius ratio r_1/r_2 in the limit $N \to \infty$. Then

$$C_{a\,N=\infty}^{\Omega} = \frac{\pi}{2}\left\{1 - \left(\frac{r_1}{r_2}\right)^4\right\}.$$

For flow rate fluctuation the fluid moves along the vane surfaces and the consideration of angular momentum gives

$$C_{a\,N=\infty}^{\varphi} = -\pi\left\{1 - \left(\frac{r_1}{r_2}\right)^2\right\}\cot\beta.$$

These values are plotted in Fig. 2. In this way the work done by the apparent mass component will be stored in the fluid near the impeller as kinetic energy and it will be necessary to

eliminate this component in estimating the unsteady head of working pumps from unsteady torque.

Numerical Examples

The foregoing procedure is applied to two types of unsteady flows.

The first type examples assume that the disturbances are small and sinusoidal in time. In these cases shed vortices are assumed to flow away on a steady relative flow which is a sum of the average rotational velocity $i\Omega_0\bar{z}$ and the velocity induced by an average source Q_0 and a concentrated vortex $N\Gamma_s$ at the origin representing the effects of steady flow rate and circulation of the vanes. The infinite integral in equation (1) relating to shed vortices is cut off at $r/r_2 = 3.5$, since it is confirmed that the truncation does not influence the resulting velocity.

The second type examples treat large transient disturbances and the flow field is solved stepwise in time applying the boundary conditions (2) and (3) at each time step. The positions of shed vortices are corrected by using the exact relative velocity at the previous time step.

In every case the vortex points and velocity points are the same as for the calculation of apparent mass coefficient, and the vortex distribution between the vortex points is assumed to be linear. The impeller is assumed to have logarithmic vanes, although the present method can be applied to any two-dimensional impellers.

Small Sinusoidal Fluctuations. We consider the case where the angular velocity of the impeller is constant and the flow rate fluctuates sinusoidally in time around the mean flow rate φ_0

$$\varphi = \varphi_0 + \Delta\varphi e^{j\omega t} \tag{11}$$

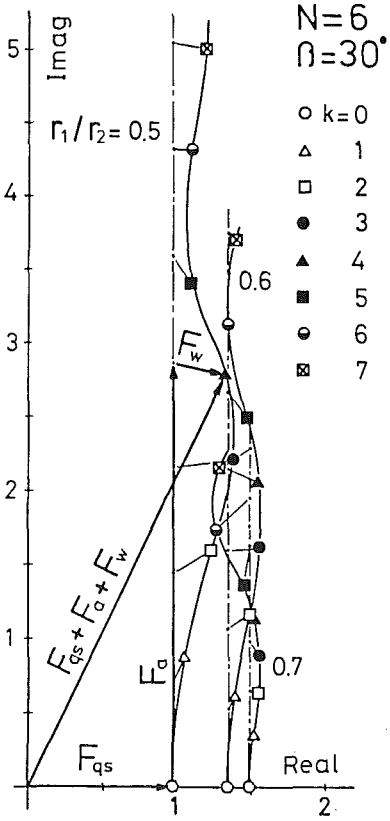

Fig. 4 Fluctuating torque coefficient F for sinusoidal angular velocity fluctuation

where $\varphi \equiv Q(t)/2\pi r_2^2\Omega_0$ and $\Delta\varphi << \varphi_0$. Only the first order fluctuating component in equation (4) are retained. All the fluctuating quantities are expressed as complex values with respect to the imaginary unit j, so as to include the phase of the fluctuation. Fluctuating torque coefficient F is defined as follows.

$$F = \Delta T/(\rho r_2{}^4\Omega_0{}^2\Delta\varphi) \tag{12}$$

where ΔT is the amplitude of torque fluctuation

$$T = T_s + \Delta T e^{j\omega t} \tag{13}$$

In these examples the mean flow rate is chosen to be shockless, but there is no necessity of using this rate.

The fluctuating torque coefficient F is shown in Fig. 3 as functions of normalized frequency $k \equiv \omega/\Omega_0$. In this figure the torque fluctuation is divided into the three components. The apparent mass component is given by:

$$F_a = \Delta T_a/(\rho r_2^4\Omega_0^2\Delta\varphi) = jk\,C_a^\varphi \tag{14}$$

using the apparent mass torque coefficient shown in Fig. 2. If we represent the $\varphi - \psi$ characteristics of the impeller by

$$\psi = \psi_s - A\varphi = gH_{th}/(r_2\Omega_0)^2$$

we can write the quasisteady torque component as follows.

$$F_{qs} = \Delta T_{qs}/(\rho r_2^4\Omega_0^2\Delta\varphi) = 2\pi(\psi_s - 2A\varphi_0) \tag{15}$$

The quasisteady torque for $k > 0$ coincides with the torque for $k = 0$ and the growth of the amplitude with k is mainly due to the apparent mass component. It can be seen that the small deviation of F with increasing k from straight lines is due entirely to the wake component. This component is smaller than the other two components.

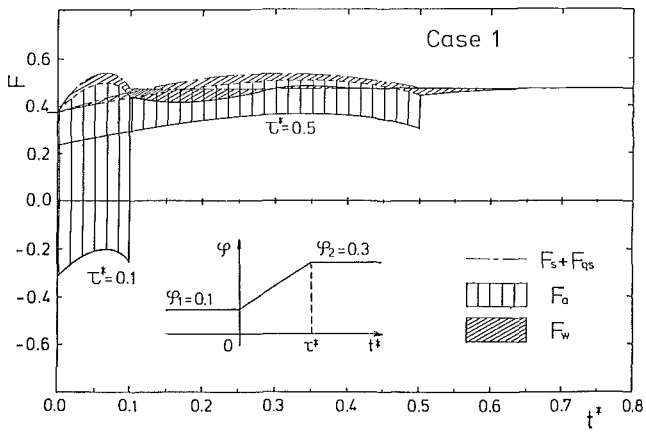

Fig. 5(a) Case 1

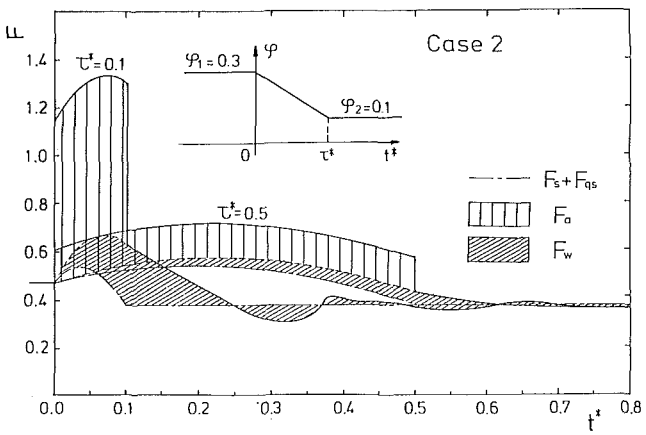

Fig. 5(b) Case 2

Fig. 5 Fluctuating torque coefficient F for transient flow rate fluctuation

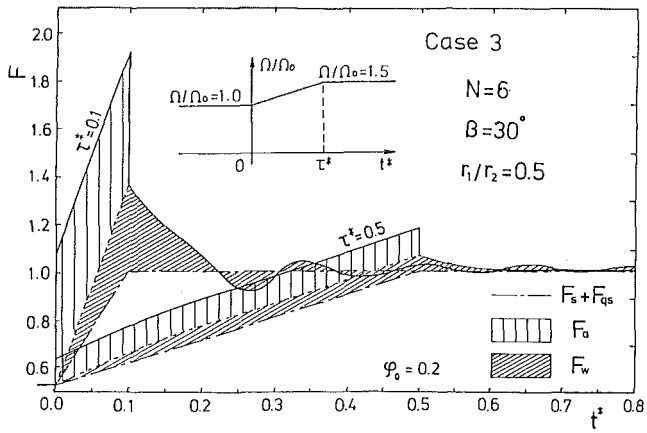

Fig. 6(a) Case 3

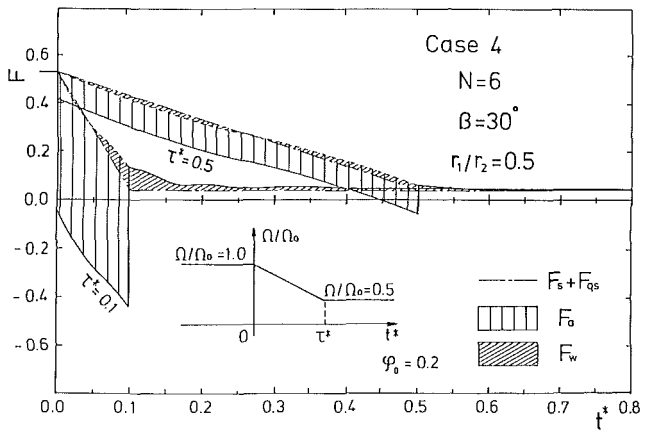

Fig. 6(b) Case 4

Fig. 6 Fluctuating torque coefficient F for transient angular velocity fluctuation

Next is considered the case when the flow rate is constant but angular velocity Ω of the impeller fluctuates as

$$\Omega = \Omega_0 + \Delta\Omega e^{j\omega t}, \quad \Delta\Omega << \Omega_0 \tag{16}$$

The apparent mass and quasisteady torque components are given by:

$$F_a = \Delta T_a/(\rho r_2^4 \Omega_0 \Delta\Omega) = jk\, C_a^{\Omega} \tag{17}$$

$$F_{qs} = \Delta T_{qs}/(\rho r_2^4 \Omega_0 \Delta\Omega) = 2\pi\psi_s \varphi_0 \tag{18}$$

Fluctuating torque coefficient

$$F = \Delta T/(\rho r_2^4 \Omega_0 \Delta\Omega) \tag{19}$$

is shown in Fig. 4. The tendencies are the same as for flow rate fluctuations except the sign of the apparent mass component. The wake component is again smaller than the other two components. It is verified that the ratio of the wake component to the amplitude of quasisteady circulation is the same as that for flow rate fluctuation.

Transient Fluctuations. Consider the cases in which the flow rate is largely changed as shown in Fig. 5. Corresponding torque fluctuation is shown in the same figures. Fluctuating torque coefficient F is defined as

$$F = T/(\rho r_2{}^4 \Omega_0{}^2) \tag{20}$$

and is shown as functions of nondimensional time $t^* = t/(2\pi/\Omega_0)$ for two accelerating time $\tau^* = \tau/(2\pi/\Omega_0)$. It is found that the time step $\Delta t^* = 0.01$ is sufficiently small for these and the next cases. Apparent mass and quasisteady components are given by

$$F_a = T_a/(\rho r_2^4 \Omega_0^2) = (1/2\pi)(d\varphi/dt^*) C_a^{\delta} \tag{21}$$

$$F_s + F_{qs} = (T_s + T_{qs})/(\rho r_2^4 \Omega_0^2) = 2\pi\varphi(\psi_s - A\varphi) \tag{22}$$

It can be seen that the discontinuities at $t = 0$ and $t = \tau$ are the result of sudden exertion and removal of apparent mass component. The amount of wake component differs significantly between Case 1 and 2. This is mainly because of the nonlinearity of equation (4), i.e., due to the difference of the amount of $\gamma_0(s,t) + \gamma_1(s,t)$ when the flow rate is increased or decreased. Except for the result of case 2, $\tau^* = 0.1$ the wake component is smaller than other two components. But this exceptional case is an example of very rapid and large fluctuation such that the flow rate is diminished to 1/3 of the initial value within 1/10 turn of the impeller.

We also solved the flows in which the angular velocity is largely increased or decreased keeping the net flow rate constant. The apparent mass and quasisteady components are given by:

$$F_a = T_a/(\rho r_2^4 \Omega_0^2) = (1/2\pi)(d/dt^*)(\Omega/\Omega_0) C_a^{\Omega} \tag{23}$$

$$F_s + F_{qs} = (T_s + T_{qs})/(\rho r_2^4 \Omega_0^2) = 2\pi\varphi_0(\psi_s \Omega/\Omega_0 - A\varphi_0) \tag{24}$$

where Ω_0 and φ_0 are the initial angular velocity and flow coefficient. Fluctuating torque coefficient F defined by equation (20) is shown in Fig. 6 for the angular velocity fluctuations shown in the figure. It can be seen that the general tendencies are the same as for flow rate fluctuation except the sign of the apparent mass components. The wake component is small except the cases of sudden and large fluctuation such as the case in which the angular velocity is raised to 3/2 of the initial value within 1/10 turn of the impeller.

Although only limited number of the results are shown here, we may conclude that the estimation of unsteady torque from the apparent mass and quasisteady components will not lead to large errors in the usual cases. Further sample calculations show that the contribution of the wake component is larger for impellers with larger inner to outer radius ratio, larger vane angle and smaller vane number, for which the apparent mass coefficient is smaller.

Conclusion

Unsteady torque on a radial impeller is analysed by the use of singularity methods. Several calculations are made for small sinusoidal fluctuations and for large transient fluctuations of flow rate and angular velocity of the impeller. In every case, it was shown that the fluctuating torque can be divided into three components: quasisteady, apparent mass and wake. The quasisteady component can be calculated from $\varphi - \psi$ characteristics of the impeller. The apparent mass component depends only on the impeller geometry and the types of the disturbance. This coefficient is calculated and plotted for a wide range of logarithmic impeller for angular velocity and flow rate fluctuations. This apparent mass coefficients can be used for any average flow rate and fluctuations of any time dependence.

By separating the unsteady torque into above three components it was shown that the wake component is smaller than other components except for sudden and large disturbances. On this observation, gross estimation of unsteady torque can be made easily by using the apparent mass coefficient and the formula for quasisteady component given in this paper.

Acknowledgments

The authors would like to express their appreciation to Prof. S. Murata of Osaka University for his fruitful discussions during development and to Prof. E. R. Lady and Prof. N. R. Scott of the University of Michigan who reviewed

the manuscript. Acknowledgements are also to Y. Morita of Mitsubishi Automobile Co. and to M. Sugai of Sanyo Electric Co. for their assistance in the numerical calculations.

References

1 Isay, W. H., "Die Strömung durch ein Schwingendes und rotierendes radiales Schaufelgitter," *Z. Flugwiss.*, Band 6, Heft 11, Nov. 1958, pp. 319–328.

2 Kemp, N. H., and Sears, W. R., "Aerodynamic Interference Between Moving Blade Rows," *J. Aero. Sci.*, Vol. 20, Sept. 1953, pp. 585–597.

3 Simpson, H. C., Clark, T. A., and Weir, G. A., "A Theoretical Investigation of Hydraulic Noise in Pumps," *J. Sound Vib.*, Vol. 5, No. 3, 1967, pp. 456–488.

4 Ohashi, H., "Studies on Dynamic Characteristics of Turbopumps," *Trans. Japan. Soc. Mech. Engrs.*, (in Japanese), Vol, 33, No. 255, Nov. 1967, pp. 1779–1788.

5 Tsukamoto, H., and Ohashi, H., "Transient Characteristics of Centrifugal Pumps at Starting," ASME JOURNAL OF FLUIDS ENGINEERING, Vol. 104, No. 1, 1982, pp. 6–14.

6 Corniglion, J., and Albano, G., "Theoretical and Experimental Study of Flow Through Centrifugal Pumps," *Proc. of 9th Symposium of I.A.H.R.*, Colorado, Vol. 2, 1978, pp. 67–71.

7 Kamimoto, G., Oshima, T., Mizutani, M., and Mizutani, H., "Applications of Singularity Method in Turbomachinery," *Proc. of 10th Symposium of I.A.H.R.*, Tokoyo, 1980, pp. 649–660.

8 Thompson, W. E., "Fluid Dynamic Excitation of Centrifugal Compressor Rotor Vibrations," ASME JOURNAL OF FLUIDS ENGINEERING, Vol. 100, No. 1, 1978, pp. 73–78.

9 Hess, J. L., and Smith, A. M. D., "Calculation of Potential Flow About Arbitrary Bodies," *Progress in Aeronautical Sciences*, Vol. 8, Pergamon Press, London, 1957, pp. 1–138.

10 Geising, J. P., "Nonlinear Two-dimensional Unsteady Potential Flow With Lift," *J. Aircraft*, Vol. 5, No. 2, 1968, pp. 135–143.

11 Basu, B. C., and Hancock, G. J., "The Unsteady Motion of a Two-dimensional Airfoil in Incompressible Inviscid Flow," *J. Fluid Mech.*, Vol. 87, No. 1, 1978, pp. 159–178.

12 Nishioka, K., Mitsunaka, Y., "On Unsteady Aerodynamic Forces and Moments of Radial Impeller Blades," *Bull. of Japan Soc. Mech. Engrs.*, Vol. 22, No. 173, 1979, pp. 1544–1551.

13 Imaichi, K., Tsujimoto, Y., and Yoshida, Y., "A Two-dimensional Analysis of the Interaction Effects of Radial Impeller in Volute Casing," *Proc. of 10th Symposium of I.A.H.R.*, Tokyo, 1980, pp. 635–647.

14 von Karman, Th., and Sears, W. R., "Airfoil Theory for Non-uniform Motion," *J. Aero. Sci.*, Vol. 5, No. 10, 1938, pp. 379–390.

15 Kito, F., "On Virtual Mass of Vane-wheel Having Radial Vanes, Which Makes Torsional Vibration in Water," *Trans. Japan Soc. Mech. Engrs.*, (in Japanese), Vol. 18, No. 66, 1953, pp. 127–131.

Measurements in a Motored Four-Stroke Reciprocating Model Engine

C. Arcoumanis

A. F. Bicen

J. H. Whitelaw

Imperial College of Science and Technology, Department of Mechanical Engineering, Fluids Section, London SW7 2BX, England

Measurements of ensemble-averaged axial and swirl velocities and the rms of the corresponding fluctuations obtained by laser-Doppler anemometry, are reported for the axisymmetric swirling flow in a four-stroke model engine motored at 200 rpm with a compression ratio of 3.5. A centrally located valve, incorporating a 60 degree seat angle and 30 degree swirl vanes resulting in a swirl number of 1.2, was used to draw in and exhaust seeded air. The piston-head configurations included a flat surface and a cylindrical bowl with and without a lip. Comparison of the results with those obtained previously, with a flat piston in the absence of compression, shows that the mean and rms profiles during the intake stroke are similar. In the axial plane a system of vortices is created which has almost disappeared by the time the inlet valve closes with a small vortex existing near the cylinder head at the early part of compression; later on this vortex breaks up and the mean velocities tend to become uniform. The intake generated turbulence decays gradually until the inlet valve closes; it then becomes uniform and remains constant in magnitude for the rest of the compression stroke. The mean swirl flow has a spiralling nature during intake but tends towards solid body rotation during compression with associated turbulence levels of similar magnitude to the axial ones. During the expansion stroke the rms velocities decrease further until the exhaust valve opens and new turbulence is generated. The influence of the piston bowl is generally small but the addition of a lip results, during the compression stroke, in inward movement of the air towards the bowl as the piston approaches TDC. The reverse squish effect, observed during the expansion stroke and due to the outgoing motion of the entrapped air inside the bowl, results in significant reversed velocities near the axis and increase in the turbulence levels close to the piston.

1 Introduction

The results presented in references [1-5] describe the mean velocity and normal stress distributions in piston-cylinder assemblies for a wide range of geometry and flow boundary conditions of relevance in internal-combustion engines. They were obtained in a plexiglass arrangement designed for the application of laser-Doppler anemometry and with open-port configurations rather than valves. The absence of compression allowed the use of comparatively thin-walled plexiglass and the associated constant-density flows a direct test of the accuracy of measurement by means of integration of the mean-velocity profiles at different radial planes for the same crank angle.

Investigations of the in-cylinder flow in motored and firing production engines have been carried out using hot wires and laser-Doppler anemometers, as for example in references [6-13]. The first studies of the fluid motion in engines used hot-wire anemometers, references [6-8], but problems were encountered in the interpretation of the signals due to uncertainties in the calibration of the instrument during the compression stroke. Some of the more recent investigations, references [9-13], used laser anemometers either in the forward-scatter or more often in the back-scatter mode to demonstrate the capabilities of the experimental technique and to throw more light on the in-cylinder fluid mechanics in internal combustion engines. Reference [13], for example, investigated the flow in a motored single-cylinder Diesel engine operating with a compression ratio of 17.5, but due to limited optical access, measurements of axial velocities were not reported. The results for the swirl and radial components gave rise to lower measurement precision than that of references [1-5] and showed that, in the compression stroke, the flow tends toward solid body rotation. During the intake process velocities show only a small dependence on compression in contrast to the rms velocities which are considerably lower under compressing conditions.

The difficulties associated with measurements in real engines and reported in reference [13] can be overcome by using model engines. This study and reference [14] represent a step in this direction. The present results were obtained in a four-stroke model engine made of plexiglass, with identical instrumentation to references [1-5], for one inlet arrangement and three piston configurations and quantify the influence of piston-head shape on the in-cylinder fluid motion with a

Contributed by the Fluids Engineering Division and presented at the Joint Applied Mechanics, Fluids Engineering, and Bioengineering Conference, Boulder, Colo., June 22-24, 1981, of THE AMERICAN SOCIETY OF MECHANICAL ENGINEERS. Revised manuscript received by the Fluids Engineering Division, December 1, 1981.

compression ratio of 3.5. Although the lack of knowledge of the density distribution precludes mass-balance checks, the accuracy of measurement can be presumed similar to that of the previous non-compressing flows and the range of measurements is much greater than can be achieved in real-engine configurations such as that of reference [13]. Thus, measurements of mean axial velocities and the corresponding rms values are reported in the form of radial profiles for crank angles of 90 deg in the intake stroke, 270 and 324 deg in the compression stroke, 380 and 450 deg in the expansion and 630 deg in the exhaust stroke. Temporal profiles of both axial and swirl velocities are also presented together with swirl radial profiles at crank angles of 36 and 270 deg. The experimental apparatus together with the uncertainties associated with the measurements are discussed briefly in Section 2; the results are presented in Section 3 followed by conclusions in Section 4.

2 Experimental Apparatus

A line diagram of the optical and signal processing arrangements is shown in Fig. 1 and a diagram of the piston-cylinder assembly in Fig. 2. A description of the model engine is given in the following subsection and a brief statement of optical and data reduction arrangements in subsections 2.2, 2.3, and of precision in 2.4.

2.1 Flow Configuration. The model engine was fabricated from plexiglass with the piston reciprocating inside the cylinder via a crank and motor arrangement. The motor speed was kept constant at 200 rpm within ± 0.5 percent. The engine was mounted with its axis horizontally, and, after flow symmetry had been confirmed, measurements of the axial and swirl velocity components were obtained with the laser beams in the horizontal and vertical planes, respectively.

A single, axisymmetrically located valve whose lift diagram is shown in Fig. 3(*a*), was used to intake and exhaust air seeded with silicone oil to increase the rate of Doppler signals. Seeding for the laser-Doppler anemometer was provided by spraying a low velocity jet of silicone particles from an atomizer into the plenum region upstream of the intake port of the model engine. Instead of using a helical port or masking part of the valve periphery to promote swirl in the intake airflow, swirl vanes were incorporated into the inlet port to result in an axisymmetric flow with a swirl number of 1.2. The swirl number is defined as the ratio of the angular and axial momentum fluxes at the entry to the cylinder, normalized by the width of the jet at the exit of the port. It was evaluated from a swirl and an axial profile measured close to the cylinder head and averaged over the intake stroke. Geometric details of the model engine are given in Table 1.

The compression ratio of 3.5 corresponds to peak-cycle isentropic pressure and temperature of 580 KPa and 483°K, respectively. Cooling water coils were wound round the lower region of the cylinder to maintain outside wall temperatures less than 413°K. The pressure inside the cylinder, was monitored by a pressure transducer and a charge amplifier as a check on the satisfactory sealing of the pressure rings. The pressure traces were monitored on an oscilloscope and confirmed a peak-cycle pressure of 520 KPa, as shown in Fig. 3(*a*). The difference between the theoretical and the measured value can be attributed to the closing of the intake value 44 deg after BDC and heat losses through the walls.

2.2 Optical Arrangement. The laser-Doppler anemometer comprized a 5 mW helium-neon laser, a focusing lens, a rotating diffraction grating, a system of lenses which focused the first order diffracted beams to an intersection region forming the fringe volume, a light collecting lens and a photomultiplier which controlled the diameter of the probe volume. The laser and the transmitting and receiving optics

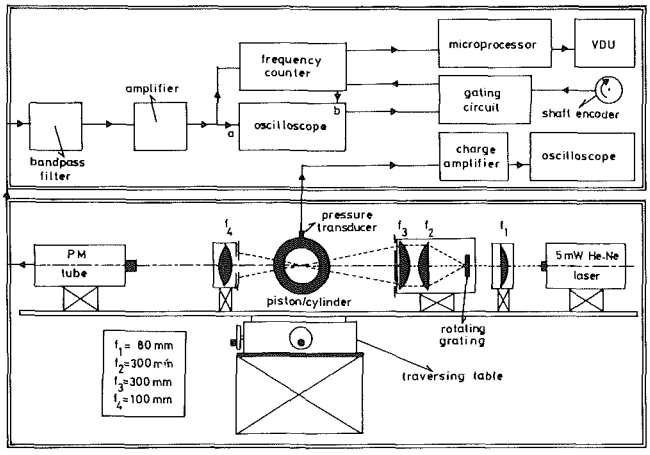

Fig. 1 Block diagram of optical and signal processing arrangements

Table 1 Geometric details of model engine

Bore, mm	75
Stroke, mm	94
Compression ratio	3.5
Connecting rod length, mm	363.5
Intake-exhaust valve	
Diameter (D), mm	34.0
Maximum lift (L), mm	7.3
Dimensionless lift (*L/D*)	0.21
Seat angle, degrees	60
Overlap, degrees	12
Intake valve	
Opens at	6° BTDC*
Closes at	44° ABDC
Exhaust valve	
Opens at	44° BBDC
Closes at	6° ATDC*
Piston bowl configurations	
Diameter, mm	43
Depth, mm *	23
Lip diameter, mm	16.5

* Extrapolated crank angles from intake and exhaust lift diagrams.

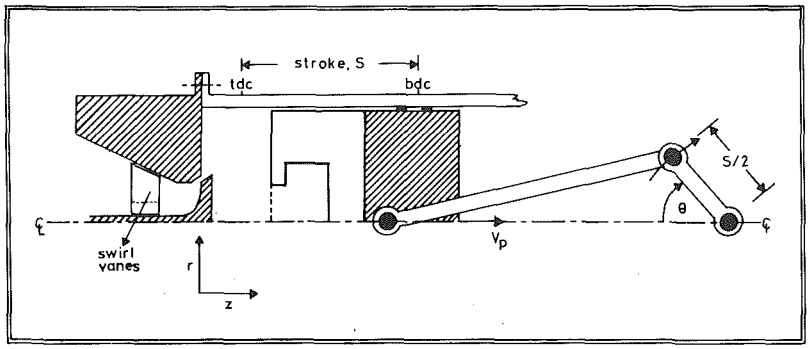

Fig. 2 Diagram of piston-cylinder assembly

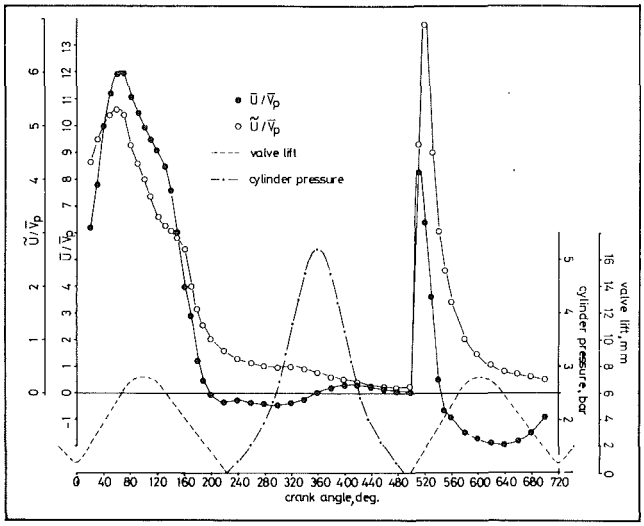

Fig. 3(*a*) Axial velocity, valve lift and pressure diagrams

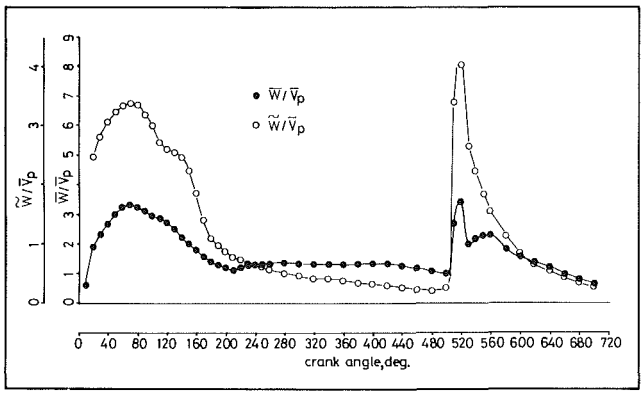

Fig. 3(*b*) Swirl velocity

Fig. 3 Temporal profiles of mean and rms velocities at $z = 15$ mm, $r = 25$ mm, flat piston

were mounted on a traversing table with two degrees of freedom in the horizontal plane. The main characteristics of the optical arrangement are summarized in Table 2.

Table 2 Characteristics of laser-doppler anemometer

Half angle of intersecting beams	6.4 deg
Fringe spacing	2.8 μm
Diameter of intersection region at the $1/e^2$ intensity locations	93 μm
Length of intersection region at the $1/e^2$ intensity locations	830 μm
Number of stationary fringes	33
Frequency shift	1.83 MHz

2.3 Data Acquisition and Processing. The Doppler signals from the photomultiplier were band-pass filtered to remove low frequency pedestal and high frequency electronic noise, amplified and displayed on an oscilloscope prior to their input to a computing frequency counter. The triggering mechanism of the oscilloscope was used to accept signals with amplitudes above a certain level and to send an arming pulse to the counter for every acceptable Doppler burst. Setting the trigger level to -6db together with the characteristics of the band-pass filter implied an effective bandwidth of 0.16 to 5.5 MHz corresponding to the range of the expected velocities. The arming pulses, prior to the counter input, were sent to a gating circuit which identified the part of the engine cycle at which measurements were made. The gate of this circuit was opened and closed after a preset number of pulses, corresponding to the crank angle window of interest, were received from an optical shaft encoder coupled to the engine half-speed shaft. For each pulse within the crank angle window, a d-c logic

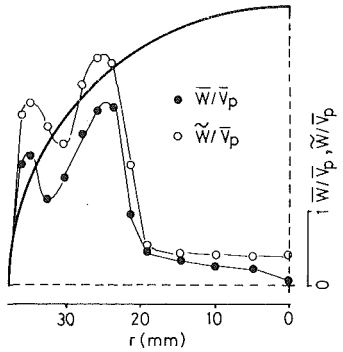

Fig. 4(*a*) $\theta = 36$ deg

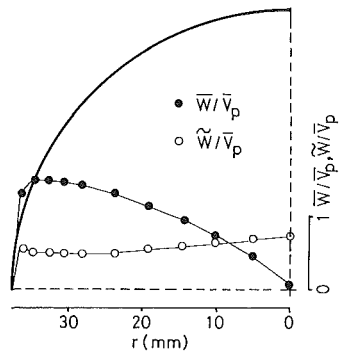

Fig. 4(*b*) $\theta = 270$ deg

Fig. 4 Swirl mean and rms velocity profiles at $z = 15$ mm, flat piston

signal was returned from the counter to the oscilloscope to display the part of the burst whose frequency was measured and to verify that the measurement had been carried out properly.

The binary-coded-decimal frequency output from the counter was interfaced to a microprocessor which was controlled by a 6502 machine language code with a software dependent maximum sampling rate of 5 Hz corresponding to a 200 ms time interval. The frequency counter had a minimum cycle time of 3 ms which incorporated a variable measurement time of 2-4 μs. The function of the gating circuit, on the other hand, was determined by the motor speed; it opened every 600 ms and stayed open for approximately 8 ms corresponding to a 10 degree crank angle window. During this time no more than 3 samples were counted but only one was processed to provide frequency information due to the low sampling rate of the microprocessor. The data reduction program was written in BASIC and performed a wide band filtering by accepting frequency values within three standard deviations in order to reject erroneous, noise-induced counts; validation of the Doppler frequencies by this method was of the order of 99 percent. For each ensemble within the 10 degree crank angle window, sample sizes in the range of 700–2000 were used depending on the point in the cycle and the location inside the cylinder.

2.4 Precision The possible sources of experimental uncertainty have been discussed in detail in references [1, 3, and 5]. The present measurement system is similar to that of reference [5] where mass balances obtained by integration of the velocity profiles at each axial location were within 15 percent with the imbalances attributed mainly to uncertainties in the integration procedure and to velocity-gradient broadening; both effects were significant in the region close to the cylinder head where velocity gradients were steepest. In the present study, based on data provided in the previous section, filter biasing was insignificant and sampling bias minimized according to reference [15] by adjusting the time between samples to be longer than the average particle arrival

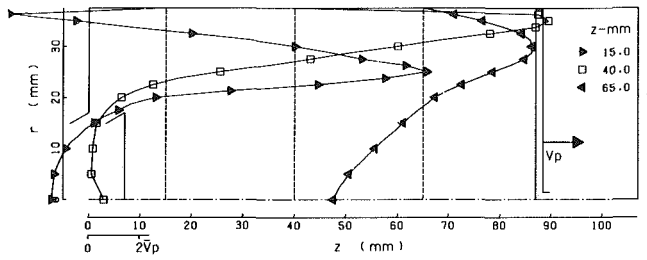

Fig. 5(a) $\theta = 90$ deg

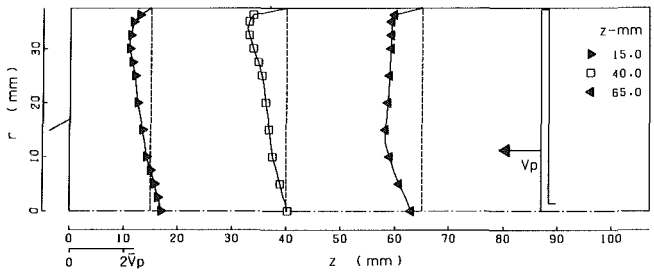

Fig. 5(b) $\theta = 270$ deg

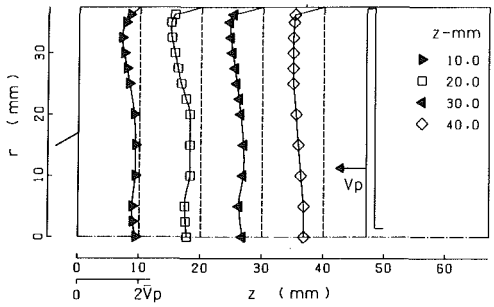

Fig. 5(c) $\theta = 324$ deg

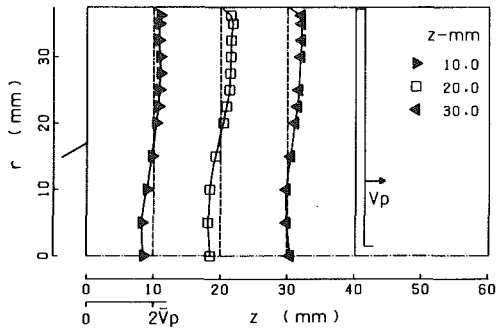

Fig. 5(d) $\theta = 380$ deg

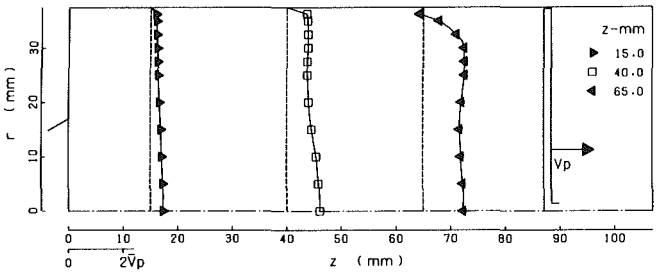

Fig. 5(e) $\theta = 450$ deg

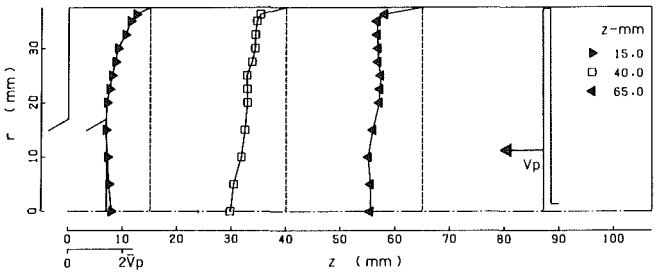

Fig. 5(f) $\theta = 630$ deg

Fig. 5 Mean axial velocity profiles, flat piston

interval and turbulent time scale. In addition, the small velocity gradients measured in the compression and expansion strokes are expected to improve the experimental precision, in terms of mean and rms velocities, to better than 5 and 10 percent respectively. The overall uncertainty associated with the measurements does not influence the implications of the results and the related conclusions.

3 Results and Discussion

The results are presented in radial and temporal profile form and are a representative sample of measurements chosen to show the more important flow phenomena. Figure 3 presents temporal profiles for both axial and swirl velocities obtained with the flat-piston; radial profiles of swirl mean and rms velocities for selected crank angles are shown in Fig. 4 and of axial mean and rms velocities in Figs. 5 and 6, respectively. Axial mean and rms velocities, obtained with a piston bowl of 23 mm depth, are shown in Figs. 7 and 8 for two crank angles in the compression and expansion strokes and the effect of a lip is indicated by the results of Figs. 9 and 10. The mean and rms values are normalized by the mean piston speed $\bar{V}_p = 0.627$ ms^{-1}. In most figures an outline of the cylinder, piston head configuration, the valve and piston positions and the normalized instantaneous piston speed corresponding to the angle under consideration are shown.

The Reynolds number on the intake stroke based on the maximum piston speed and the cylinder bore was calculated to be 5.2×10^3.

3.1 Flat-Piston Configuration. Temporal profiles of swirl and axial velocities obtained at a point in the jet region near the cylinder head ($z = 15$ mm, $r = 25$ mm) are shown in Fig. 3 and radial profiles of swirl velocity in Fig. 4. During the intake stroke, both mean velocity components reach maximum values at about 70 deg crank angle and decay rapidly until the closure of the valve; turbulence levels follow similar trends indicating the close correspondence between the inlet jet flow and turbulence. The mean swirl profile at $\theta = 36$ deg, shown in Fig. 4(*a*), exemplifies the spiraling nature of the inlet flow with low velocity region near the axis corresponding to the wake formed behind the valve. During compression the mean flow in the axial plane is suppressed by the action of the piston, Fig. 3(*a*), contrary to the swirling flow which is conserved and organized into solid body type of rotation according to Figs. 3(*b*) and 4(*b*), respectively; turbulence decays gradually and remains nearly constant during the second half of the stroke. In the expansion stroke the decay of both axial mean velocity and turbulence and the persistence of the solid body rotation are interrupted by the valve opening at about 500 deg crank angle; this results in fluid surge into the cylinder and consequent generation of turbulence which decays steadily during the rest of the cycle.

Figure 5 shows the mean axial velocity profiles obtained with the flat piston at crank angles of 90 deg in the intake stroke, 270 and 324 deg in the compression stroke, 380 and 450 deg in the expansion and 630 deg in the exhaust stroke; Fig. 6 shows the corresponding rms velocity profiles.

During the intake stroke, which has been investigated in detail in references [1-5] for the case of an open valve in the absence of compression, the flow pattern consists of a system

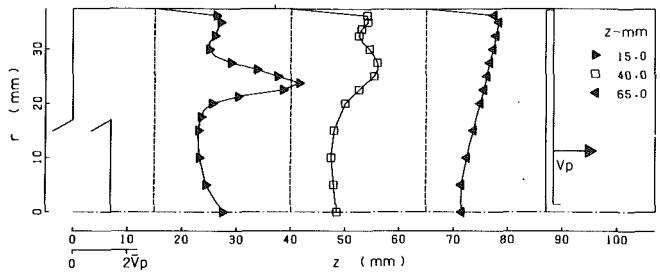

Fig. 6(*a*) $\theta = 90$ deg

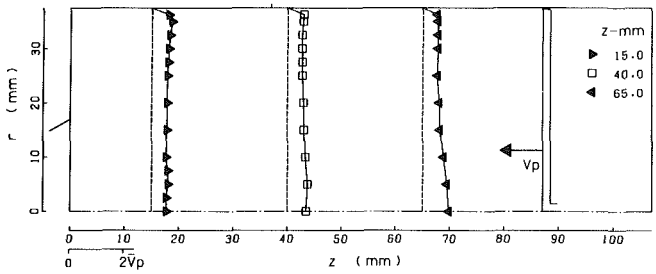

Fig. 6(*b*) $\theta = 270$ deg

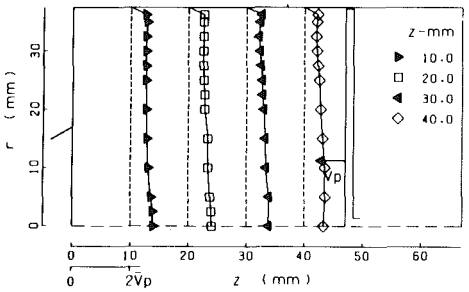

Fig. 6(*c*) $\theta = 324$ deg

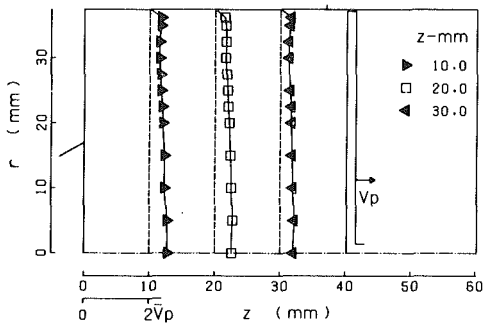

Fig. 6(*d*) $\theta = 380$ deg

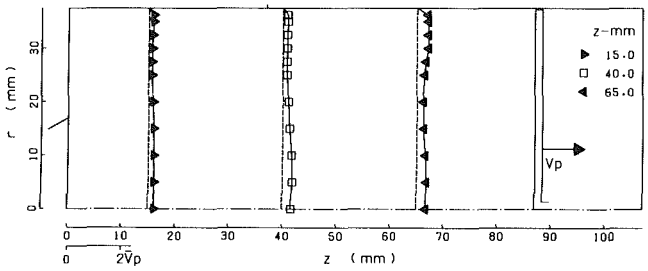

Fig. 6(*e*) $\theta = 450$ deg

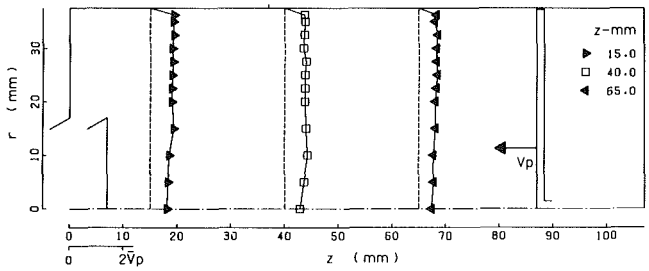

Fig. 6(*f*) $\theta = 630$ deg

Fig. 6 Axial rms velocity profiles, flat piston

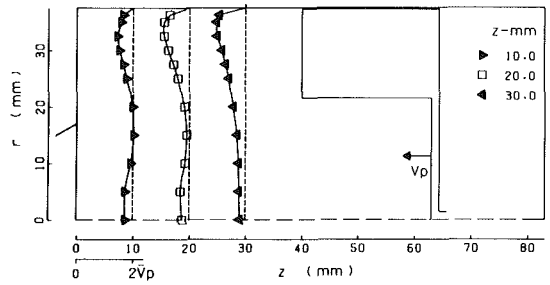

Fig. 7(*a*) $\theta = 324$ deg

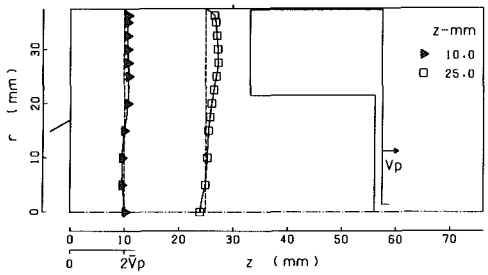

Fig. 7(*b*) $\theta = 380$ deg

Fig. 7 Mean axial velocity profiles, piston with bowl

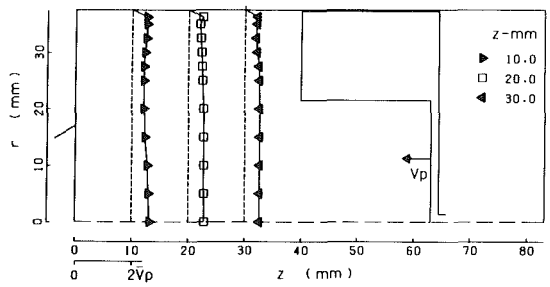

Fig. 8(*a*) $\theta = 324$ deg

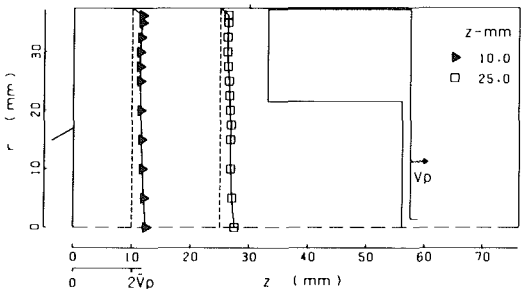

Fig. 8(*b*) $\theta = 380$ deg

Fig. 8 Axial rms velocity profiles, piston with bowl

of vortices with a large vortex occupying most of the flow space and smaller vortices in the corners between the wall, piston, and cylinder head. The results of reference [14] suggest that there is no significant difference in the mean axial velocity profiles for the cases of an operating valve with a compression ratio of 7 and a valve with constant lift at 31 rpm. The present results of Figs. 5(*a*) and 6(*a*) show similar trends; at mid-stroke the high velocity jet drawn in by the

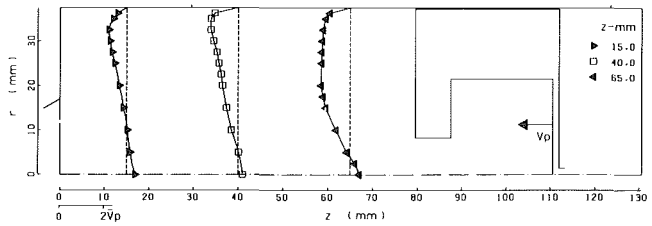

Fig. 9(a) $\theta = 270$ deg

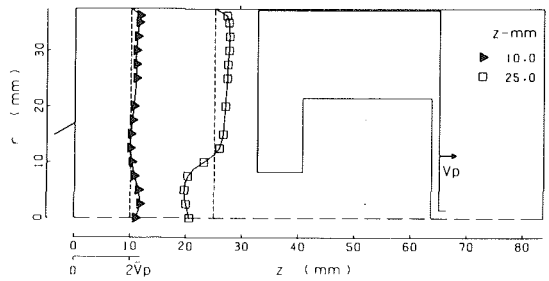

Fig. 9(c) $\theta = 380$ deg

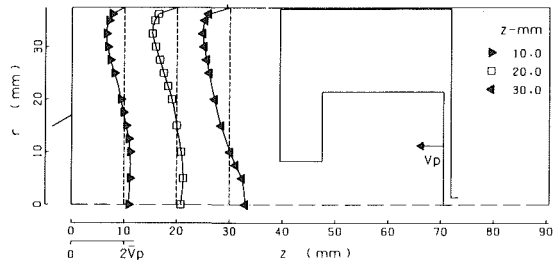

Fig. 9(b) $\theta = 324$ deg

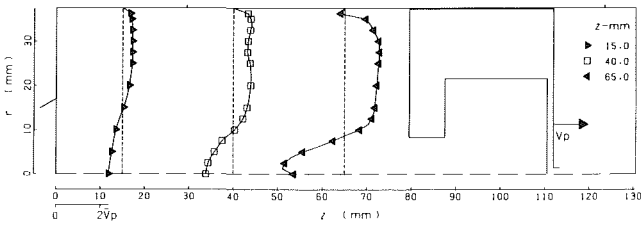

Fig. 9(d) $\theta = 450$ deg

Fig. 9 Mean axial velocity profiles, piston-bowl with lip

piston creates, due to the shearing action between the jet and the slower moving fluid inside the cylinder, high turbulence levels near the jet region.

During the compression stroke with the intake valve already closed, Fig. 5(*b*), the mean flow decays and a vortex is present near the cylinder head which may have persisted from intake. Figure 6(*b*) shows that turbulence also decays considerably and becomes homogeneous at a level of about 0.5 $\bar{V}_p$. Near TDC, at $\theta = 324$ deg, mean velocities are further reduced tending to become uniform, with higher velocities of the order of 1.0 $\bar{V}_p$ close to the piston and lower ones about 0.3 $\bar{V}_p$ near the cylinder head. As a consequence of further compression, the vortex existing at mid-stroke has disappeared. The rms levels remain uniform and of the same magnitude as in Fig. 6(*b*) with no further decay of turbulence. The results obtained are in qualitative agreement with previous investigations, for example references [7 and 10], in that the intake generated mean and rms velocities decay gradually and the nearly homogeneous turbulence remains constant during the second half of the compression stroke.

At the beginning of the expansion stroke, Fig. 5(*d*), as the piston reverses its direction a counter-rotating vortex is formed which occupies most of the flow space. The mean velocities have decreased in magnitude but changed in direction near the wall relative to $\theta = 324$ deg. The rms levels, as Fig. 6(*d*) shows, have decreased considerably to about 0.3 $\bar{V}_p$. At mid-expansion, Fig. 5(*c*), the fluid accelerates following the piston motion with considerably higher velocities of the order of 1.5 $\bar{V}_p$ close to the piston. However, the near homogeneous turbulence decays even further to about 0.2 $\bar{V}_p$, according to Fig. 6(*e*).

The flow patterns in the exhaust stroke were investigated in references [1–5]. According to reference [2], any structure present in the flow during expansion is likely to be destroyed before the next intake stroke; the same trends are observed here, as Fig. 5(*f*) indicates. In the exhaust stroke the fluid shows a tendency to move directly from the piston face towards the open valve. As Fig. 6(*f*) shows, the turbulence levels have increased considerably, compared to their values at mid-expansion, due to the generation of turbulence associated with the sudden incoming flow at the exhaust valve opening.

3.2 Piston-Bowl Configurations. Figures 7 and 8 show the axial mean and rms velocity profiles obtained with a cylindrical bowl and Figs. 9 and 10 those with a bowl-lip configuration.

As reported in references [1 and 5], the piston configuration in the absence of compression does not have a significant effect on the flow patterns and turbulence levels. Therefore, detailed investigation of the intake stroke was not carried out here and the conclusions of references [1 and 5] are considered to be valid due to the similarities of the operating and geometric boundary conditions.

During the compression stroke and at $\theta = 324$ deg, as Fig. 7(*a*) indicates, the cylindrical bowl configuration results in lower mean velocities near the cylinder axis than those of Fig. 5(*c*) with the flat piston. The rms velocity profiles of Fig. 8(*a*) show similar trends and magnitude to those of Fig. 6(*c*). Preliminary results obtained with a cylindrical bowl of 15 mm depth showed almost identical profiles at $\theta = 324$ deg. The addition of a lip to the bowl results in very small differences at mid-compression, Fig. 9(*a*), but significant ones at the second half of the stroke especially in the region close to the cylinder axis, due to inward bulk motion of the air toward the piston bowl, Fig. 9(*b*); the rms levels outside the bowl, shown in Figs. 10(*a*) and 10(*b*), are not influenced by the presence of the lip.

In the expansion stroke the influence of bowl configuration becomes even more important. Comparison between the results obtained with the cylindrical bowl and flat piston shows small differences in both the mean flow and turbulence. Results obtained with a smaller cylindrical bowl confirmed the observation made previously about the insignificant influence of the bowl depth in the resulting flow patterns and turbulence levels during the compression stroke. The addition of a lip to the bowl, however, resulted in reverse squish effect. As Figs. 9(*c*), 9(*d*) and 10(*c*), 10(*d*) show, the fluid which was forced inside the bowl during the compression stroke expands to form a jet with consequent increase in the reversed velocities near the axis and the associated turbulence levels. At $\theta = 380$ deg the maximum reversed velocity of magnitude 1.0 $\bar{V}_p$ is observed near the piston and increases to about 3 $\bar{V}_p$ by mid-expansion. Rms values follow the trend of the mean velocities reaching a peak of about 1.3 $\bar{V}_p$ at $\theta = 450$ deg in the vicinity of the bowl exit. Comparison with Figs. 6(*d*) and 6(*e*) shows that the bowl-lip configuration increases the turbulence levels by a factor of 3 in the region close to the axis. Preliminary results with a smaller lip indicated that the influence of the size of the lip is only quantitative; it reduces

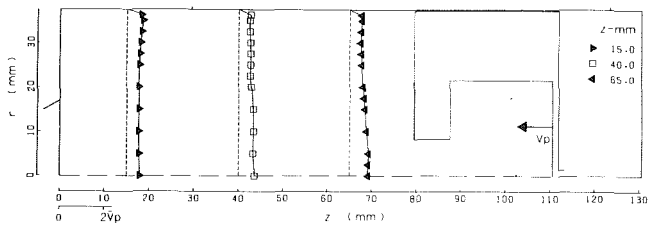

Fig. 10(*a*) $\theta = 270$ deg

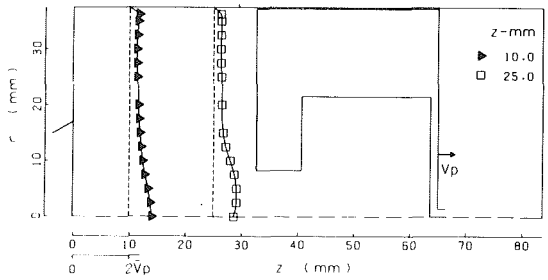

Fig. 10(*c*) $\theta = 380$ deg

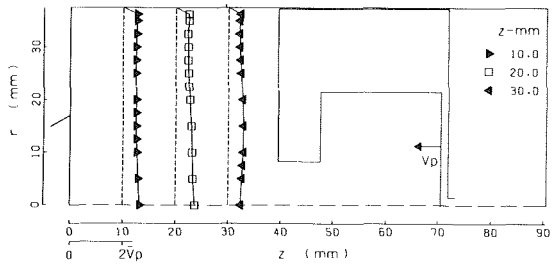

Fig. 10(*b*) $\theta = 324$ deg

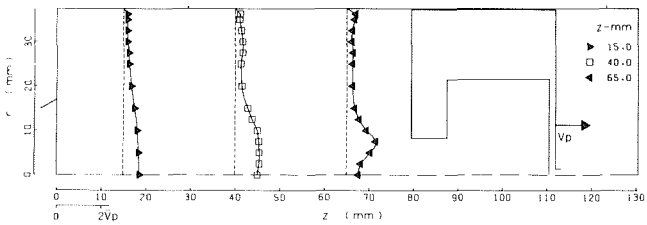

Fig. 10(*d*) $\theta = 450$ deg

Fig. 10 Axial rms velocity profiles, piston-bowl with lip

the reversed velocities without altering the trends of the flow patterns.

In the exhaust stroke, with the valve open, the flow patterns are not expected to be influenced by the piston configuration according to references [5]; therefore, the results obtained with the flat piston, Figs. 5(*f*) and 6(*f*) are expected to be also valid in the case of the cylindrical bowl with and without a lip.

4 Concluding Remarks

The investigation by laser-Doppler anemometry of the in-cylinder swirling flow in an axisymmetric four-stroke reciprocating model engine motored at 200 rpm with a compression ratio of 3.5 revealed the following:

1. The flow structure during the intake stroke is dominated by the inlet geometry conditions with small dependence on whether compression is applied and negligible dependence on piston configuration. It consists of a system of vortices created by a high velocity spiralling jet with associated turbulence levels which decay steadily after mid-stroke.

2. In the early part of the compression stroke the intake generated flow structure in the axial plane is no longer apparent with only a small vortex present near the cylinder head. Mean swirl motion, however, is conserved and organizes into solid body type of rotation. Both axial and swirl turbulence levels decay considerably and tend to become homogeneous. In the second half of the stroke the piston configuration becomes increasingly important. The flat piston results in almost constant axial and swirl turbulence levels and of equal magnitude suggesting that turbulence during compression is not only homogeneous but also isotropic. The presence of a cylindrical bowl has no significant effect on the flow characteristics, independent of the bowl depth within the practical range. However, the addition of a lip causes a substantial inward motion of the air toward the bowl but with no apparent effect on the turbulence levels outside the bowl.

3. In the expansion stroke and until the exhaust valve opening, the flat piston results in the creation of a weak vortex and considerable reduction in turbulence. Later in the stroke, the sudden surge of fluid through the valve generates new turbulence which decays rapidly. The bowl-lip configuration results in a reverse squish effect with a consequent increase in the mean and rms velocities near the axis.

4. Piston configuration is not important during the exhaust stroke; the fluid moves towards the open valve with further decay of the lately generated turbulence.

Acknowledgment

The authors are glad to acknowledge the financial support for this work provided by the Atomic Energy Research Establishment (A.E.R.E.), Harwell, the Science Research Council, the U.S. Department of Energy and the U.S. Army Research Office. They would also like to express their appreciation to Dr. N. S. Vlachos and Mr. M. Yianneskis for their contribution to the development of the engine and to Mr. N. Frost for its construction and maintenance.

References

1 Morse, A. P., Whitelaw, J. H., and Yianneskis, M., "Turbulent Flow Measurements by Laser-Doppler Anemometry in Motored Piston-Cylinder Assemblies," ASME JOURNAL OF FLUIDS ENGINEERING, Vol. 101, 1979, p. 208.

2 Bicen, A. F., Vlachos, N. S., and Whitelaw, J. H., "The Creation and Destruction of Vortices in Unsteady Flows," *Letters in Heat and Mass Transfer*, Vol. 7, 1980, p. 77.

3 Morse, A. P., Whitelaw, J. H., and Yianneskis, M., "The Influence of Swirl on the Flow Characteristics of a Reciprocating Piston-Cylinder Assembly," ASME JOURNAL OF FLUIDS ENGINEERING, Vol. 102, 1980, p. 478.

4 Morse, A. P., Whitelaw, J. H., and Yianneskis, M., "The Flow Characteristics of a Piston-Cylinder Assembly with an Off-Centre, Open Port," *Proc. I. Mech. E.*, Vol. 194, 1980, p. 291.

5 Arcoumanis, C., Bicen, A. F., Vlachos, N. S., and Whitelaw, J. H., "Effects of Flow and Geometry Boundary Conditions on Fluid Motion in a Motored I.C. Model Engine," to be published in *Proc. I. Mech. E.*

6 Semenov, E. S., "Studies of Turbulent Gas Flow in Piston Engines," NASA Technical Translation F-97, 1963.

7 Lancaster, D. R., "Effects of Engine Variables on Turbulence in a Spark-Ignition Engine," S.A.E. Paper 760159, Detroit, Feb. 1976.

8 Witze, P. O., "Measurements of the Spatial Distribution and Engine Speed Dependence of Turbulent Air Motion in an I.C. Engine," S.A.E. Paper 770220, Detroit, Feb. 1977.

9 Witze, P. O., "Application of Laser Velocimetry to the Measurement of Turbulence in a Motored Internal Combustion Engine," Third International Workshop on Laser Velocimetry, Purdue University, July 1978.

10 Johnston, S. C., Robinson, C. W., Rorke, W. S., Smith, J. R., and Witze, P. O., "Application of Laser Diagnostics to an Injected Engine," S.A.E. Paper 790092, Detroit, Feb. 1979.

11 Rask, R. B., "Laser-Doppler Anemometer Measurements in an Internal Combustion Engine," S.A.E. Paper 790094, Detroit, Feb. 1979.

12 Asanuma, T., and Obokata, T., "Gas Velocity Measurements of a Motored and Firing Engine by Laser Anemometry," S.A.E. Paper 790096, Detroit Feb. 1979.

13 Morse, A. P., and Whitelaw, J. H., "Measurement of the In-Cylinder Flow of a Motored 4-Stroke Reciprocating Engine." *Proc. Roy. Soc.*, A377, 1981, p. 309.

14 Gany, A., Larea, J. J., and Sirignano, W. A., "Laser-Doppler Velocimetry Measurements in a Motored I.C. Engine Simulator," A.I.A.A. Paper 80-0079, 1980.

15 Durao, D. F. G., Laker, J., and Whitelaw, J. H., "Bias Effects in Laser Doppler Anemometry," *J. Phys. E.: Sci. Instrum.*, Vol. 13, 1980, p. 442.